COUPLED ELECTRICAL AND ACOUSTIC MODELING OF VISCOUS FLUID EJECTORS

A Dissertation
Presented to
The Academic Faculty

By

Drew Allan Loney

In Partial Fulfillment
Of the Requirements for the Degree
Doctor of Philosophy in the
School of Mechanical Engineering

Georgia Institute of Technology
December 2014

COUPLED ELECTRICAL AND ACOUSTIC MODELING OF VISCOUS FLUID EJECTORS

Approved by:

Dr. Andrei G. Fedorov, Advisor
School of Mechanical Engineering
Georgia Institute of Technology

Dr. F. Levent Degertekin, Advisor
School of Mechanical Engineering
Georgia Institute of Technology

Dr. David Rosen
School of Mechanical Engineering
Georgia Institute of Technology

Dr. Massimo Ruzzene
School of Aerospace Engineering
Georgia Institute of Technology

Dr. William Hunt
School of Electrical and Computer Engineering
Georgia Institute of Technology

Approved Date: June 24, 2014

To my mother, Debra Arlene Loney

ACKNOWLEDGEMENTS

I would like to thank my grandparents, Wayne and Betty Pues, without whose love and support I would not have accomplished so much. I am also thankful for the many friends I have made during my time working on the research presented here, whose constant encouragement and faith helped me through even the most difficult times.

My advisors, Dr. Andrei Fedorov and Dr. Levent Degertekin, have my deepest gratitude for their guidance, encouragement, and patience throughout my graduate career. Their commitment to the success of their students is only matched by their dedication and devotion to the advancement of science. Their combined energies continue to motivate my dedication to engineering.

Financial support for the project was provided through the U.S. National Science Foundation, through award DMI-0900322.

TABLE OF CONTENTS

ACKNOWLEDGEMENTS ..... **IV**
LIST OF TABLES ..... **VIII**
LIST OF FIGURES ..... **X**
SUMMARY ..... **XIX**
CHAPTER 1 : INTRODUCTION **1**
CHAPTER 2 : DEVICE BACKGROUND AND MOTIVATION **5**
2.1 Review of inkjet fluid ejector devices 6
2.3 Horn-based ultrasonic atomizer concept and design 11
2.4 Viscosity limitations on atomization in inkjet fluid ejectors 12
2.4.1 Acoustic losses in cylindrical capillaries and horns 14
2.4.2 The effect of high viscosity working fluids on ejector behavior 16
2.5 Previous modeling of fluid ejectors 18
2.6 Concluding remarks on device background 20
CHAPTER 3 : DEVELOPMENT AND VALIDATION OF ANALYTICAL MODELS **22**
3.1 Description of the micromachined fluid ejectors to be modeled 22
3.1.1 Identification of common ejector components 25
3.2 Development of piezoelectric transducer models 27
3.2.1 Planar transducers 27
3.2.2 Annular transducers 29
3.3 Development of the acoustic pipe models 33
3.3.1 Development of the acoustic pipe without a wall model 34
3.3.2 Development of the acoustic pipe with a wall model 35
3.3.3 Applicability of the pipe models in various ejector regimes 48
3.4 Derivation of the horn models 50
3.4.1 Continuous variation in horn shape through the Webster Wave Equation 51
3.4.2 Discretization of the acoustic pipe models 53
3.5 Development of an electro-mechanical model for horn-based ultrasonic atomizers 56
3.5.1 Model validation 59
3.6 Development of an electro-mechanical model for squeeze type inkjets 67

3.6.1 Model validation 71
3.7 Concluding remarks on model development 79
CHAPTER 4 : OPTIMIZATION OF HORN-BASED ULTRASONIC ATOMIZER GEOMETRY 81
4.1 Performance of current horn-based ultrasonic atomizers 81
4.2 Geometric optimization of horn-based ultrasonic atomizers 86
4.2.1 The effect of horn shape on the generated pressure gradient 87
4.2.2 The effect of horn and reservoir length on the generated pressure gradient 92
4.2.3 The effect of transducer thickness on the generated pressure gradient 99
4.3 Application of the ejection threshold to determine fluid ejectability 104
4.4 The ejectability of physical fluids 108
4.5 The importance of heating effects to device operation 111
4.5.1 Heating due to power dissipation in the acoustic field 115
4.5.2 Heating due to power dissipation in the piezoelectric transducer 119
4.5.3 Comments on experimental results presented in literature 123
4.6 The transition to nonlinear device operation 127
4.7 Concluding remarks on fluid ejectability 131
CHAPTER 5 : EXPLORATION OF ALTERNATIVE HORN-BASED ULTRASONIC ATOMIZER DESIGNS 134
5.1 Alternative horn-based ultrasonic atomizer designs 134
5.2 Modification of the horn-based ultrasonic atomizer with a low viscosity fluid reservoir 137
5.2.1 Development of the low viscosity reservoir model 137
5.2.2 Application of the low viscosity reservoir model 140
5.3 Modification of the horn-based ultrasonic atomizer with a second acoustic horn 145
5.2.1 Development of the double acoustic horn model 147
5.2.2 Application of the secondary acoustic horn model 154
5.4 Concluding remarks on ejector design alternatives 160
CHAPTER 6 : CHARACTERIZATION OF SQUEEZE EJECTORS 161
6.1 Overview of squeeze type ejectors 161
6.2 Bogy devices loaded with high viscosity working fluids 163
6.3 The effect of ejector and driving section lengths on the generated pressure gradient 179
6.4 The effect of ejector radius on the generated pressure gradient 186

6.5 The effect of transducer thickness on the generated pressure gradient 187
6.6 Concluding remarks on squeeze type ejectors 192
CHAPTER 7 : CONCLUSIONS AND RECOMMENDATIONS FOR FUTURE WORK 194
APPENDIX A : MATERIAL PROPERTIES UTILIZED IN THE ANSYS AND ANALYTICAL MODELS 203
APPENDIX B : TECHNICAL DETAILS OF THE SIMULATIONS PERFORMED IN ANSYS 206
APPENDIX C : DEFINITION OF COMMONLY USED SYMBOLS 209
BIBLIOGRAPHY 212

LIST OF TABLES

Table 3.1: A comparison of the fluid cavity resonant frequencies predicted by the modified Dijksman, WWE, and ANSYS models for water as the working fluid. 61

Table 3.2: The driving pulse parameters used by Bogy and Talke for squeeze type ejectors of varying lengths.[2] 76

Table 4.1: Maximum values of the pressure gradient generated by the atomizer as a function of the working fluid viscosity and fluid cavity resonance mode. The examined geometry consisted of a 2.1 mm fluid reservoir, a 500 μm horn, and 1.5 mm transducer driven at its dielectric breakdown voltage. 85

Table 4.2: The maximum pressure gradient magnitude produced by a horn-based ultrasonic atomizer for increasing viscosity in the artificial working fluid. The atomizer geometry was allowed to vary in order to generate the largest pressure gradient possible when the fluid cavity was driven at the dielectric breakdown voltage of the coupled transducer. 106

Table 4.3: Configurations yielding the largest pressure gradient magnitude at the horn aperture for various working fluids when the piezoelectric transducer is driven by a voltage signal limited by its dielectric breakdown field. 108

Table 4.4: Physical data used to calculate the Namhe number for working fluid of increasing glycerol percentage by mass.[117, 119] A linear interpolation was utilized to obtain unavailable property values for mixtures between pure water and pure glycerol. 114

Table 4.5: Local temperature increase at the horn aperture due to viscous shear stresses as a function of working fluid viscosity. 120

Table 4.6: Experimental operating temperatures as reported by Meacham et al. for pulsed operation trials with glycerol/water mixtures.[28] 125

Table 4.7: Parameters utilized for the nonlinearity analysis. B/A ratios are those given by Hamilton and Blackstock.[121] The maximum velocity for each fluid is the velocity at the aperture when each fluid is driven by its optimal atomizer configuration. 128

Table 5.1: Reynolds numbers and sound speeds at the entrance and exit of the low viscosity acoustic horn. A frequency of 1 Hz was assumed with a maximum velocity of 500 m/s. The inlet wall thickness was taken to be 25 μm with an exit thickness of 387.5 μm. 150

Table 6.1: Geometric properties utilized in the simulation of each of the geometries given by Bogy and Talke. [2] 164

Table 6.2: The fluid cavity resonance frequencies and maximum pressure gradient magnitudes predicted in the squeeze ejector for artificial working fluids of increasing viscosity when driven by a 500 μm thick piezoelectric transducer at the dielectric breakdown voltage. The sound speed and density of the working fluid are taken to be equal to those of glycol. The ejector length is 12.3 mm, composed of two 3 mm spacer sections, a 125 μm horn, and a 6.175 mm driven section. 176

Table 6.3: The fluid cavity resonance frequencies and maximum pressure gradient magnitudes predicted in the squeeze ejector for artificial working fluids of increasing viscosity when driven by a 500 μm thick piezoelectric transducer at the dielectric breakdown voltage. The sound speed and density of the working fluid are taken to be equal to those of glycol. The ejector length is 18.7 mm, composed of two 3 mm spacer sections, a 125 μm horn, and a 12.575 mm driven section. 177

Table 6.4: The fluid cavity resonance frequencies and maximum pressure gradient magnitudes predicted in the squeeze ejector for artificial working fluids of increasing viscosity when driven by a 500 μm thick piezoelectric transducer at the dielectric breakdown voltage. The sound speed and density of the working fluid are taken to be equal to those of glycol. The ejector length is 33.9 mm, composed of two 3 mm spacer sections, a 125 μm horn, and a 27.775 mm driven section. 178

Table A.1: Component directions for the piezoelectric transducer properties for the planar and annular geometries.....203

Table A.2: Properties used to model silicon in the ANSYS simulations and analytical models.[124].....203

Table A.3: Properties used to model nickel in the analytical models[125] 204

Table A.4: Properties used to model lead zirconate titanate (PZT-5) in the ANSYS simulations and analytical models.....204

Table A.5: Properties used to model the working fluids in the ANSYS simulations and analytical models[2, 117, 126, 127] 205

LIST OF FIGURES

Figure 2.1: Common thermal inkjets. Left: Roof shooter geometry. Right: Side shooter geometry.[1] 8

Figure 2.2: Common piezoelectric inkjets. Top left: Bending mode top shooter. Top right: Bending mode side shooter. Bottom left: Push mode. Bottom right: Squeeze mode.[1]11

Figure 2.3: Schematic of the horn-based ultrasonic atomizer showing multiple unit cells.12

Figure 3.1: Representation of the modeled horn-based ultrasonic atomizer geometry.[3] The device consists of a fluid filled acoustic horn, a fluid reservoir, and a driving planar piezoelectric transducer. 24

Figure 3.2: Representation of the modeled squeeze ejector geometry. The device consists of a fluid filled cavity which tapers to a small aperture, a glass capillary which confines the fluid in a cavity, and a driving annular piezoelectric transducer. The left side is bounded by the fluid reservoir (not shown) used to fill the capillary. 25

Figure 3.3: A schematic of a horn-based ultrasonic atomizer with its constitutive components identified. The device can be modeled as an individual planar piezoelectric transducer, an acoustic pipe without a wall, and a horn coupled together with the appropriate boundary conditions. 26

Figure 3.4: A schematic of a squeeze ejector with its constitutive components identified. The device can be modeled as an individual annular piezoelectric transducer, acoustic pipes with a wall, a driven acoustic pipe with a wall, and a horn coupled together with the appropriate boundary conditions. 26

Figure 3.5: The annular piezoelectric transducer geometry as modeled by Liang.[4] The transducer is assumed to be infinite in axial length. The inner and outer surfaces are active and poling is in the radial direction. 29

Figure 3.6: A comparison of the predicted electrical impedance magnitude for an annular transducer using both ANSYS and the Liang impedance matrix. The geometry is taken to have a 9 mm inner radius and a 11.54 mm outer radius. Material properties are taken as PZT5. 31

Figure 3.7: Left: Geometry of the acoustic pipe without a wall model. Right: The boundary conditions and components of the acoustic field within the acoustic pipe without a wall. 35

Figure 3.8: Left: Geometry of the acoustic pipe with a wall model. Right: The boundary conditions and components of the acoustic field within the acoustic pipe with a wall.36

Figure 3.9: A representation of a thin cylinder of radius R and thickness h loaded on the interior with a pressure P. The cylinder has length L into the page. The stress and strain are assumed to be uniform due to the thinness of the wall. 40

Figure 3.10: A regime map for the operation of acoustic pipes based on the dimensionless parameter groups produced during model formulation. Four operating regions exist

from balancing the radial component of the viscous stress, the axial component of the viscous stress, and spatial pressure gradient. 49

Figure 3.11: Geometry of a conical horn modeled with the WWE. 51

Figure 3.12: The boundary conditions and components of the conical horn modeled with the WWE. 52

Figure 3.13: Left: Diagram of the discretization of the acoustic pipe without a wall model. Right: Diagram of the discretization of the acoustic pipe with a wall model. Elements in both models are coupled together by matching pressure and volume velocity at the interface between elements. 55

Figure 3.14: A schematic diagram of the ultrasonic atomizer based on the acoustic horn structure and its decomposition into the components used to develop the analytical acoustic models of the atomizer. 57

Figure 3.15: The magnitude of the electrical input impedance as predicted by the modified Dijksman, WWE, and ANSYS models with water as the working fluid. 62

Figure 3.16: A comparison of the pressure amplitude along the atomizer axis as predicted by the modified Dijksman, WWE, and ANSYS models for 500kHz in water as a function of the distance from the transducer surface. The amplitude of the voltage signal applied to the transducer was 10V. 64

Figure 3.17: A comparison of the pressure amplitude along the atomizer axis as predicted by the modified Dijksman, WWE, and ANSYS models for the first order cavity resonance mode in water as a function of the distance from the transducer surface. The amplitude of the voltage signal applied to the transducer was 10V. The frequencies for each model are as given in Table 3.1. 64

Figure 3.18: The magnitude of the electrical input impedance as predicted by the modified Dijksman, WWE, and ANSYS models with glycerol as the working fluid. .66

Figure 3.19: A comparison of the pressure amplitude along the atomizer axis as predicted by the modified Dijksman, WWE, and ANSYS models for the first order cavity resonance mode in glycerol as a function of the distance from the transducer surface. The amplitude of the voltage signal applied to the transducer was 10V. 66

Figure 3.20: A decomposition of the squeeze ejector into the basic components utilized for developing an analytical model. 67

Figure 3.21: Comparison of the predicted pressure and axial velocity magnitudes on the inner glass tube surface of the squeeze ejector model when driving the piezoelectric transducer with sinusoidal 1V amplitude voltage signal at 10kHz. Glycol was utilized as the working fluid. 73

Figure 3.22: Comparison of the predicted pressure and axial velocity magnitudes on the inner glass tube surface of the squeeze ejector model when driving the piezoelectric transducer with sinusoidal 1V amplitude voltage signal at 250kHz. Glycol was utilized as the working fluid. 74

Figure 3.23: Comparison of the predicted pressure and axial velocity magnitudes on the inner glass tube surface of the squeeze ejector model when driving the piezoelectric

transducer with sinusoidal 1V amplitude voltage signal at 500kHz. Glycol was utilized as the working fluid. 74

Figure 3.24: The squeeze ejector geometry as investigated by Bogy and Talke.[2] The device consists of a glass tube surrounded by an annular piezoelectric transducer connected to undriven tube segments on either side. The tube opens to the environment through a nozzle plate on the right and to a large fluid reservoir on the left. 75

Figure 3.25: Meniscus displacement at the ejector aperture as measured by Bogy and Talk for squeeze ejectors of various lengths. The duration of driving pulse for each geometry is indicated at the left[2] 75

Figure 3.26: Model result corresponding to the conditions of the Bogy and Talke experiment which measured meniscus displacement in various ejector operating configurations. The tube inner diameter was taken to be 1 mm with an outer diameter of 2 mm. The transducer outer diameter was taken as 3 mm. The time in μm at which the first several peaks occur is indicated. 77

Figure 3.27: Model results corresponding to the conditions of the Bogy and Talke experiment for the meniscus velocity using squeeze ejector model. The tube inner diameter was taken to be 1 mm with an outer diameter of 2 mm. The transducer outer diameter was taken as 3 mm. The ejector ends are assumed to be pressure release conditions. 78

Figure 4.1: Left: A schematic of the ultrasonic atomizer based on an array of acoustic horn structures. The cell under consideration is defined by the dashed lines. Right: A magnified view of atomizer unit cell horn geometry. The horn has a fixed aperture radius, $rapt$=25 μm, and horn entrance radius, $rent$ = 387.5 μm. The entrance flat region, $rspa$, is set equal to the aperture radius. The horn length, $hhorn$ and flare constant m are varying parameters of the horn model. 81

Figure 4.2: The regime map for horn-based ultrasonic atomizer operating with common working fluids. The considered fluids fall into the region where the discretized acoustic pipe with wall model applies for the horn. The multiple points for each considered fluid represent all fluid cavity resonant modes occurring below 1MHz. 82

Figure 4.3: Variation in the predicted pressure gradient at the horn aperture for each fluid cavity resonance as a function of viscosity when driven by a sinusoidal voltage input of 1V. The sound speed and density of the working fluid are taken to be equal to those of water. The fluid cavity resonant frequencies are adjusted to account for their change as a function of working fluid viscosity. 84

Figure 4.4: Pressure gradient magnitude in the horn as a function of frequency and diameter reduction when driven by sinusoidal pressure input of 1 Pa. The horn aperture diameter is 50 μm with a varying entrance diameter. The sound speed and density of the working fluid are taken to be equal to those of water. Top left: 500 μm horn with 1 mPas working fluid viscosity. Top right: 500 μm horn with 10 Pas working fluid viscosity. Bottom left: 2500 μm horn with 1mPas working fluid viscosity. Bottom right: 2500 μm horn with 10 Pas working fluid viscosity. 90

Figure 4.5: Pressure gradient magnitude in the horn as a function of frequency and horn flare when driven by sinusoidal pressure input of 1 Pa. The horn entrance is 775 micrometers with an aperture diameter of 50 micrometers. The sound speed and density of the working fluid are taken to be equal to those of water. The legend values next to the exponential are the flare constant of the horn, with higher numbers indicating greater flare. Top left: 500 μm horn with 1 mPas working fluid viscosity. Top right: 500 μm horn with 10 Pas working fluid viscosity. Bottom left: 2500 μm horn with 1mPas working fluid viscosity. Bottom right: 2500 μm horn with 10 Pas working fluid viscosity. 91

Figure 4.6: Pressure amplitude in the atomizer fluid cavity as a function of distance from the cavity inlet for the first six cavity resonance modes in the artificial test fluid with 1 mPas viscosity when driven by a constant amplitude (1 m/s) sinusoidal velocity inlet condition. 93

Figure 4.7: Representative maps of the pressure gradient magnitude ($\log_{10}$(Pa/m)) at the fluid cavity aperture for the artificial working fluid with 1mPas viscosity as a function of reservoir length and operating frequency. Top left: Horn length is 0.1 mm. Top right: Horn length is 1 mm. Bottom left: Horn length is 10 mm. The global maximum (not shown) occurs for a 258 μm horn and 649 μm reservoir operating at 1MHz, corresponding to the first order cavity resonance. 95

Figure 4.8: Representative maps of the pressure gradient magnitude ($\log_{10}$(Pa/m)) at the fluid cavity aperture for the artificial working fluid with 100mPas viscosity as a function of reservoir length and operating frequency. Top left: Horn length is 0.1 mm. Top right: Horn length is 1 mm. Bottom left: Horn length is 10 mm. The global maximum (not shown) occurs for a 271 μm horn and 642 μm reservoir operating at 1MHz, corresponding to the first order cavity resonance. 96

Figure 4.9: Representative maps of the pressure gradient magnitude ($\log_{10}$(Pa/m)) at the fluid cavity aperture for the artificial working fluid with 10 Pas viscosity as a function of reservoir length and operating frequency. Top left: Horn length is 0.1 mm. Top right: Horn length is 1 mm. Bottom left: Horn length is 10 mm. The global maximum (not shown) occurs for a 1.47 mm horn and 1 μm reservoir operating at 1 kHz. 97

Figure 4.10: Variation in the pressure gradient magnitude at the horn aperture for each fluid cavity resonant mode as a function of transducer thickness when driven with a sinusoidal voltage input of 1V and a transducer quality factor of 60. The horn is 1mm with a 4mm reservoir. The sound speed and density of the working fluid are taken to be equal to those of water. Left: Low viscosity (1mPas) fluids yield the highest pressure gradient at the highest 5^{th} cavity mode using a thinner transducer. Right: Higher viscosity (10Pas) fluids favor transducers that yield large displacements per applied volt at a given fluid cavity resonance. The absolute value is also an order of magnitude lower than that for the low viscosity fluid. 100

Figure 4.11: Left: Pressure gradient magnitude as a function of the resonance quality factor of the piezoelectric transducer when driven with 3.4mm transducer and a sinusoidal voltage input of 1V. The horn is 1mm with a 4mm reservoir. The sound speed and density of the working fluid are taken to be equal to those of water with a 100mPas viscosity. Right: Pressure gradient magnitude at the first order transducer

short circuit resonance as a function of the transducer resonance quality factor for various working fluid viscosities. The horn is 1mm with a 4mm reservoir. The sound speed and density of the working fluid are taken to be equal to those of water.....101

Figure 4.12: Variation in the pressure gradient magnitude at the horn aperture for each fluid cavity resonance as a function of transducer thickness when driven by a voltage signal limited by the transducer dielectric breakdown field threshold. The pressure gradient threshold for each viscosity is shown in gray, with configurations in white zone capable of producing a sufficient pressure gradient for fluid ejection. The horn is 1mm with a 4mm reservoir. The sound speed and density of the working fluid are taken to be equal to those of water. Top left: Working fluid viscosity is equal to 1mPas. Top right: Working fluid viscosity is equal to 100mPas. Bottom left: Working fluid viscosity is equal to 10Pas. 105

Figure 4.13: Variation in the pressure gradient magnitude per watt of input power to the transducer for each fluid cavity resonance as a function of transducer thickness. The sound speed and density of the working fluid are taken to be equal to those of water. The transducer area corresponds to the area of an individual atomizer cell. Left: Working fluid viscosity is equal to 1mPas. Right: Working fluid viscosity is equal to 100mPas. 107

Figure 4.14: The Nahme number predicted for glycerol/water mixtures as a function of operating frequency. 114

Figure 4.15: Time rate of temperature increase in glycerol/water mixtures due to electric power dissipation as obtained through scaling analysis. The considered atomizer geometry was a 2.1mm reservoir with a 0.5mm horn. The transducer thickness was taken to be 1.5mm. 123

Figure 4.16: Goldberg number as a function of Mach number for various working fluids at their optimal driving configuration. The maximum value predicted by the atomizer model is indicated by the dot. The utilized physical properties are given in Table 4.7 and the frequency corresponds to the optimal driving frequency of each fluid. 129

Figure 4.17: Shock distance as a function of Mach number for various working fluids at their optimal driving configuration. The maximum value predicted by the atomizer model is indicated by the dot. The utilized physical properties are given in Table 4.7 and the frequency corresponds to the optimal driving frequency for each fluid. 131

Figure 5.1: Alternative horn-based ultrasonic atomizer designs aiming to increase the maximum generated pressure gradient. The blue fluid indicates the high viscosity working fluid with the red fluid indicating the low viscosity working fluid. Left: The high viscosity horn is coupled to a low viscosity reservoir. The two fluids are separated by a thin membrane. Right: The high viscosity horn is coupled to a low viscosity horn. The two fluids are separated by a thin membrane. 136

Figure 5.2: A schematic diagram of the ultrasonic atomizer utilizing both a low and high viscosity fluid as propagation media. The model is decomposed into the individual components and the boundary conditions are shown. The low viscosity fluid is utilized in the reservoir with the high viscosity fluid in the horn. 138

Figure 5.3: The acoustic response of the dual fluid horn-based ultrasonic atomizer when driven by a constant velocity boundary condition of 1 m/s at the fluid cavity inlet for various working fluid combinations. The horn is 1mm with a 4mm reservoir. Upper left: The working fluid is the artificial test fluid with 10 Pas high viscosity in the horn and 1 mPas low viscosity in the reservoir. Upper right: The working fluid is the artificial test fluid with 1 Pas high viscosity in the horn and 1 mPas low viscosity in the reservoir. Lower left: The working fluid is glycerol for the high viscosity in the horn and water for the low viscosity fluid in the reservoir. Lower right: The magnitude of the fluid cavity inlet acoustic impedance as predicted by the model for the water/glycerol and glycerol/glycerol working fluid combinations. 143

Figure 5.4: Variation in the predicted pressure gradient magnitude and fluid cavity inlet impedance with the density of the working fluid in the low viscosity reservoir for glycerol. The driving condition is a 1 m/s velocity at the fluid cavity inlet. The horn is 1mm with a 4mm reservoir. All fluid properties, including the working fluid density in the high viscosity reservoir, remain fixed and the density in the reservoir region artificially reduced to that of water. 145

Figure 5.5: The acoustic response of the dual fluid horn-based ultrasonic atomizer when driven by a 1.5mm piezoelectric transducer for various working fluid combinations. The horn is 1mm with a 4mm reservoir. Upper left: The working fluid is the artificial test fluid with 10 Pas high viscosity and 1 mPas low viscosity. Upper right: The working fluid is the artificial test fluid with 1 Pas high viscosity and 1 mPas low viscosity. Lower left: The working fluid is glycerol for the high viscosity and water for the low viscosity fluid.....146

Figure 5.6: The acoustic response of the dual fluid horn-based ultrasonic atomizer when driven by a piezoelectric transducers of varying thicknesses driven by a 1V amplitude, sinusoidal signal. The horn is 1mm with a 4mm reservoir. Left: The working fluid is glycerol for the high viscosity and water for the low viscosity fluid. Right: The working fluid throughout the entire cavity is glycerol. 147

Figure 5.7: A schematic of a horn-based ultrasonic atomizer with dual acoustic horns, highlighting its constitutive components. The device can be modeled as an individual planar piezoelectric transducer and two acoustic pipes with wall components utilizing different working fluid properties in each. 148

Figure 5.8: A schematic diagram of the ultrasonic atomizer utilizing dual acoustic horns with a low and high viscosity fluids as propagation media. The model is decomposed into the utilized components and the boundary conditions are shown. The low viscosity fluid is utilized in the first acoustic horn component with the high viscosity fluid in the second acoustic horn component. 152

Figure 5.9: The acoustic response of the dual horn/dual fluid atomizer when driven by a constant amplitude of 1 m/s sinusoidal velocity boundary condition at the fluid cavity inlet for various working fluid combinations. The baseline atomizer refers to an atomizer without the second acoustic horn filled with the high viscosity working fluid throughout. Both the low and high viscosity fluid-filled horns are 1 mm in length. The fluid cavity entrance radius is 750 μm with a 362.6 μm interface radius and a 25 μm aperture radius. Upper left: The working fluids are the artificial test fluid with 10

Pas high viscosity and 1 mPas low viscosity. Upper right: The working fluids are the artificial test fluid with 1 Pas high viscosity and 1 mPas low viscosity. Lower left: The working fluids are glycerol for the high viscosity and water for the low viscosity fluid. Lower right: The magnitude of the fluid cavity inlet acoustic impedance as predicted by the model for the water/glycerol working fluid combinations. 157

Figure 5.10: Variation in the predicted pressure gradient magnitude at the ejection apex and fluid cavity inlet impedance with the diameter ratio across the low viscosity horn for glycerol as the working fluid. The driving condition is a 1 m/s amplitude sinusoidal velocity signal at the fluid cavity inlet. The high viscosity horn is 1mm with a 2mm low viscosity horn. The diameter ratio across the fluid cavity is fixed with an entrance radius of 750 μm and an aperture radius of 25 μm. 158

Figure 5.11: The acoustic response of the dual acoustic horn atomizer when driven by a 1.5mm piezoelectric transducer for various working fluid combinations. The baseline atomizer refers to an atomizer without the second acoustic horn filled with the high viscosity working fluid. Both the low and high viscosity horns are 1 mm in length. The fluid cavity entrance radius is 750 μm with a 362.6 μm interface radius and a 25 μm aperture radius. Upper left: The working fluids are the artificial test fluids with 10 Pas high viscosity and 1 mPas low viscosity. Upper right: The working fluids are the artificial test fluids with 1 Pas high viscosity and 1 mPas low viscosity. Lower left: The working fluids are glycerol for the high viscosity and water for the low viscosity fluid 159

Figure 6.1: A schematic of a squeeze ejector with its constitutive components and dimensions identified. The device can be modeled as an individual annular piezoelectric transducer, acoustic pipes with a wall, a driven acoustic pipe with a wall, and a horn coupled together with the appropriate boundary conditions. 162

Figure 6.2: Variation in the pressure gradient magnitude at the ejector aperture as a function of frequency for artificial working fluids of increasing viscosity when driven by a constant amplitude (1 m/s) harmonic velocity signal on the capillary exterior. The sound speed and density of the working fluid are taken to be equal to those of glycol. The ejector length is 18.7 mm, composed of two 3 mm spacer sections, a 125 μm horn, and a 12.575 mm driven section. 168

Figure 6.3: Variation in the mean (length averaged) acoustic impedance magnitude at the ejector driven section as a function of frequency for artificial working fluids of increasing viscosity. The sound speed and density of the working fluid are taken to be equal to those of glycol. The ejector length is 18.7 mm, composed of two 3 mm spacer sections, a 125 μm horn, and a 12.575 mm driven section. 168

Figure 6.4: Pressure and mean particle velocity amplitude in the ejector fluid cavity as a function of distance from the cavity inlet for the first two fluid cavity resonance modes. The working fluid is taken to be the artificial test fluid with 1 mPas viscosity and is driven by a constant amplitude (1 m/s) sinusoidal velocity signal on the capillary exterior. The shaded area indicates the portion of the fluid cavity to which the driving condition is applied. 169

Figure 6.5: Pressure and mean particle velocity amplitude in the ejector fluid cavity as a function of distance from the cavity inlet for the first two minima in the pressure gradient magnitude. The working fluid is taken to be the artificial test fluid with 1 mPas viscosity and is driven by a constant amplitude (1 m/s) sinusoidal velocity signal on the capillary exterior. The shaded area indicates the portion of the fluid cavity to which the driving condition is applied. 169

Figure 6.6: Variation in the pressure gradient magnitude at the ejector aperture as a function of frequency for artificial working fluids of increasing viscosity when driven by a constant amplitude (1 m/s) harmonic velocity signal on the capillary exterior. The sound speed and density of the working fluid are taken to be equal to those of glycol. The ejector length is 12.3 mm, composed of two 3 mm spacer sections, a 125 μm horn, and a 6.175 mm driven section 172

Figure 6.7: Variation in the pressure gradient magnitude at the ejector aperture as a function of frequency for artificial working fluids of increasing viscosity when driven by a constant amplitude (1 m/s) harmonic velocity signal on the capillary exterior. The sound speed and density of the working fluid are taken to be equal to those of glycol. The ejector length is 33.9 mm, composed of two 3 mm spacer sections, a 125 μm horn, and a 27.775 mm driven section 172

Figure 6.8: Variation in the pressure gradient magnitude at the ejector aperture as a function of frequency for artificial working fluids of increasing viscosity when driven by a 500 μm thick piezoelectric transducer with a sinusoidal input voltage of 1V. The sound speed and density of the working fluid are taken to be equal to those of glycol. Upper left: The ejector length is 12.3 mm, composed of two 3 mm spacer sections, a 125 μm horn, and a 6.175 mm driven section. Upper right: The ejector length is 18.7 mm, composed of two 3 mm spacer sections, a 125 μm horn, and a 12.575 mm driven section. Lower left: The ejector length is 33.9 mm, composed of two 3 mm spacer sections, a 125 μm horn, and a 27.775 mm driven section. 173

Figure 6.9: Variation in the pressure gradient magnitude at the ejector aperture as a function of frequency for artificial working fluids of increasing viscosity when driven by 5 mm long piezoelectric transducer with increasing spacer length. Each case was driven with a 500 μm transducer thickness and a 1V sinusoidal input voltage. The sound speed and density of the working fluid are taken to be equal to those of glycol. Upper left: Working fluid viscosity is equal to 1mPas. Upper right: Working fluid viscosity is equal to 100mPas. Lower left: Working fluid viscosity is equal to 10Pas.181

Figure 6.10: Variation in the pressure gradient magnitude at the ejector aperture as a function of frequency for artificial working fluids of increasing viscosity when driven by 15 mm long piezoelectric transducer with increasing spacer length. Each case was driven with a 500 μm transducer thickness and a 1V sinusoidal input voltage. The sound speed and density of the working fluid are taken to be equal to those of glycol. Upper left: Working fluid viscosity is equal to 1mPas. Upper right: Working fluid viscosity is equal to 100mPas. Lower left: Working fluid viscosity is equal to 10Pas.182

Figure 6.11: Variation in the pressure gradient magnitude at the ejector aperture as a function of frequency for artificial working fluids of increasing viscosity in a 15 mm ejector driven by transducers of various lengths. Each case was driven with a 500 μm

transducer thickness and a 1V sinusoidal input voltage. The sound speed and density of the working fluid are taken to be equal to those of glycol. Upper left: Working fluid viscosity is equal to 1mPas. Upper right: Working fluid viscosity is equal to 100mPas. Lower left: Working fluid viscosity is equal to 10Pas. 184

Figure 6.12: Variation in the pressure gradient magnitude at the ejector aperture as a function of frequency for artificial working fluids of increasing viscosity in a 25 mm ejector driven by transducers of various lengths. Each case was driven with a 500 μm transducer thickness and a 1V sinusoidal input voltage. The sound speed and density of the working fluid are taken to be equal to those of glycol. Upper left: Working fluid viscosity is equal to 1mPas. Upper right: Working fluid viscosity is equal to 100mPas. Lower left: Working fluid viscosity is equal to 10Pas. 185

Figure 6.13: Variation in the pressure gradient magnitude at the ejector aperture as a function of frequency for artificial working fluids of increasing viscosity in a 12.3 mm ejector with increasing capillary inner radius. Each case was driven with a 500 μm transducer thickness and a 1V sinusoidal input voltage. The sound speed and density of the working fluid are taken to be equal to those of glycol. Upper left: Working fluid viscosity is equal to 1mPas. Upper right: Working fluid viscosity is equal to 100mPas. Lower left: Working fluid viscosity is equal to 10Pas. 188

Figure 6.14: Variation in the pressure gradient magnitude at the ejector aperture as a function of frequency for artificial working fluids of increasing viscosity in a 18.7 mm ejector with increasing capillary inner radius. Each case was driven with a 500 μm transducer thickness and a 1V sinusoidal input voltage. The sound speed and density of the working fluid are taken to be equal to those of glycol. Upper left: Working fluid viscosity is equal to 1mPas. Upper right: Working fluid viscosity is equal to 100mPas. Lower left: Working fluid viscosity is equal to 10Pas. 189

Figure 6.15: Pressure amplitude in the ejector fluid cavity as a function of distance from the cavity inlet for varying capillary radius at the first order fluid cavity resonance (80kHz). The working fluid is taken to be the artificial test fluid with 10 mPas viscosity and is driven by a 500 μm thick piezoelectric transducer. The shaded area indicates the portion of the fluid cavity to which the driving condition is applied. 190

Figure 6.16: Variation in the pressure gradient magnitude at the horn aperture for each fluid cavity resonance as a function of transducer thickness when driven by a voltage signal limited by the transducer dielectric breakdown field. The pressure gradient threshold for each viscosity is shown in gray, with configurations in white zone capable of producing a sufficient pressure gradient for fluid ejection. The 12.3mm ejector geometry is utilized. The sound speed and density of the working fluid are taken to be equal to those of glycol. Top left: Working fluid viscosity is equal to 1mPas. Top right: Working fluid viscosity is equal to 100mPas. Bottom left: Working fluid viscosity is equal to 10Pas. 191

SUMMARY

The focus of this dissertation is the development of a fundamental understanding of the acoustics and piezoelectric transducer governing the operation of piezoelectric inkjets and horn-based ultrasonic atomizers when utilizing high viscosity working fluids. This work creates coupled, electro-mechanical analytical models of the acoustic behavior of these devices by extending models from the literature which make minimal simplifications in the handling terms that account for viscous losses. Models are created for each component of the considered fluid ejectors: piezoelectric transducers, acoustic pipes, and acoustic horns. The acoustic pipe models consider the two limited cases when either the acoustic boundary layer or attenuation losses dominate the acoustic field and are adapted to account for changes in cross-sectional area present in acoustic horns. A full electro-mechanical analytical model of the fluid ejectors is formed by coupling the component models using appropriate boundary conditions.

The developed electro-mechanical model is applied to understand the acoustic response of the fluid cavity alone and when combined with the transducer in horn-based ultrasonic atomizers. An understanding of the individual and combined acoustic response of the fluid cavity and piezoelectric transducer allow for an optimal geometry to be selected for the ejection of high viscosity working fluids. The maximum pressure gradient magnitude produced by the atomizer is compared to the pressure gradient threshold required for fluid ejection predicted by a hydrodynamic scaling analysis. The maximum working fluid viscosity of the standard horn-based ultrasonic atomizer and those with dual working fluid combinations, a low viscosity and a high viscosity working fluid to minimize viscous dissipation, is established to be on the order of 100mPas.

The developed electro-mechanical model is also applied to understand the acoustic response of the fluid cavity and annular piezoelectric transducer in squeeze type ejectors with high viscosity working fluids. The maximum pressure gradient generated by the ejector is examined as a function of the principle geometric properties. The maximum pressure gradient magnitude produced by the ejector is again compared to the pressure gradient threshold derived from hydrodynamic scaling. The upper limit on working fluid viscosity is established as 100 mPas.

CHAPTER 1: INTRODUCTION

Since the first practical devices were developed in the 1950's, inkjet printing with fluid ejectors has seen a rapid improvement in performance and diversification in areas of application.[5, 6] Inkjet fluid ejectors are now the preferred means to deposit small amounts of fluid due to their excellent controllability over droplet formation, inexpensive fabrication cost, and conservation of expensive working fluids. The advantages of inkjet printers has motivated the use of the technology in numerous application areas, the most familiar being the deposition of ink onto porous surfaces to produce text and images.[5] Recent work with inkjets has expanded this to include biotechnology[7-10], drug delivery[11-14], mass spectrometry[15, 16], electronics fabrication [17-20], and nanotechnology/materials science [21-23]. Useful reviews regarding the technological development of inkjet printing are given by Ford et al. and Wijshoff.[5, 6]

While inkjet ejectors are growing in popularity and are useful in many specific applications, there are challenges associated to applying the technology more generally. For example, working fluids which are thermally sensitive and degrade at high temperatures cannot be utilized with some inkjet devices due to the necessity of heating the working fluid during actuation.[24] Other limitations on inkjets stem from rheological limitations on the working fluid.[25] Most devices require a high surface tension, low viscosity working fluid. A low surface tension working fluid results in weeping of fluid from the fluid cavity aperture.[1] A large working fluid viscosity damps the driving acoustic field and prevents fluid ejection. While the surface tensions of most working fluids vary only slightly, the large variation in working fluid viscosity makes the

latter restriction a greater concern. Moreover, many processes utilize high viscosity fluids which would be conducive to inkjet printing, such as additive manufacturing with stereolithography resins and biological samples with biogels.[26, 27]

Previous research has demonstrated the ability of a new category of ultrasonic fluid ejector, the horn-based ultrasonic atomizer, to eject working fluids of high viscosity.[28] These devices use resonant operation to produce a large amplitude acoustic field to overcome the larger viscous dissipation and shear stresses that occur with high viscosity working fluids. Horn-based ultrasonic atomizers operate typically operate between 100 kHz and 5 MHz and utilize acoustic horns to further increase the amplitude of the acoustic field near the fluid cavity aperture. Ejection with working fluids as high as 3000 mPas have been experimentally demonstrated.[28] However, the underlying mechanism which permits the ejection of such fluids is not well understood.

The current research seeks to develop a fundamental understanding of the acoustics and piezoelectric transducer coupling underlying the operation of piezoelectric inkjets and horn-based ultrasonic atomizers with highly viscous working fluids. The understanding gained by this work can be applied to explore new concepts for piezoelectric transducer-driven fluid atomizers to achieve the ejection of high viscosity fluids. In particular, this research develops models for the acoustic behavior of inkjets and horn-based ultrasonic atomizers operating with high viscosity working fluids by extending models from literature with minimal simplifications in accounting for viscous losses. The analytical fluid cavity models consider two limiting cases when either the acoustic boundary layer or the attenuation losses dominate acoustic behavior in the cavity components. Furthermore, models of piezoelectric transducers that include losses have

been incorporated with the acoustic models to provide a comprehensive electro-mechanical modeling methodology of the entire device. This methodology, having been validated using analytical and experimental results from the literature, can be applied to various micromachined fluid ejectors to understand and optimize their acoustic response for use with high viscosity working fluids.

Chapter 2 provides a detailed discussion of inkjets and horn-based ultrasonic atomizers, including their operating principles and common device geometries. The major sources of viscous dissipation resulting from the acoustic boundary layer in the presence of a wall and bulk attenuation without a wall are discussed. Historical efforts at understanding the acoustic field in inkjets by a variety of experimental, numerical, and analytical approaches are also presented and serve to frame subsequent model development.

A modeling framework for fluid ejectors is introduced in Chapter 3, concentrating on modeling the electro-mechanical response of ejectors with viscous dissipation included in the acoustic field. Ejector models are created by considering each device component individually – the transducer, the acoustic pipe, and the acoustic horn – and coupling components together through appropriate boundary conditions to represent ejector physics. Moreover, scaling relationships that govern the viscous loss mechanisms within the fluid cavity are also explored. The acoustic response predicted by the developed analytical models is confirmed by comparison with finite element simulations and experimental data from literature.

Chapter 4 applies the developed analytical model for horn-based ultrasonic atomizers to understand the device acoustic response and optimize the device geometry

for operation with high viscosity working fluids. Each component of the atomizer is optimized in turn to produce the maximum possible pressure gradient magnitude. The upper limit on the working fluid viscosity able to be ejected by horn-based ultrasonic atomizer is established by the use of scaling arguments to create an order of magnitude estimate of the pressure gradient required for ejecting fluids of various viscosities. The predicted atomizer performance with physical fluids is also investigated.

In Chapter 5, potential modifications to the traditional, single fluid horn-based ultrasonic atomizer are investigated in an effort to further increase the pressure gradient magnitude generated by the device. The developed component models are utilized to examine dual fluid configurations, consisting of both a standard fluid reservoir and a secondary acoustic horn. The performance of each proposed design modification is evaluated against configurations loaded with only the high viscosity working fluid and the standard, unaltered horn-based ultrasonic atomizer.

The acoustic response of squeeze type piezoelectric inkjets is examined in Chapter 6, with an emphasis on understanding physical devices presented in the literature. The maximum pressure gradient generated by squeeze type ejectors is again compared to the required pressure gradient threshold derived from scaling analysis to predict the upper limit on fluid viscosity able to be ejected by squeeze ejectors. Key geometric parameters – fluid cavity length, transducer length, capillary radius, and transducer thickness – are also investigated for their effect on the maximum pressure gradient magnitude created by the ejector.

CHAPTER 2: DEVICE BACKGROUND AND MOTIVATION

Atomization, the production of liquid droplets from a large reservoir of fluid, is utilized in engineering applications ranging from additive manufacture and drug delivery to fuel injection and spray drying.[29] Atomization of high viscosity liquids is of particular concern in many engineering applications. For example, high viscosity liquids are important parts of additive manufacturing and biological material processing where the viscosity of the polymer and biogel working fluids can exceed several Pas.[26, 27] Atomization of high viscosity fluids has traditionally required special treatments, typically either preheating or imparting a large kinetic energy to the working fluid.[30] Preheat takes advantage of the inverse relationship between viscosity and temperature present in many liquids, increasing the temperature to reduce the viscosity of the liquid.[31] A common use of preheating is in applications such as injection molding of plastic polymers. Atomizers that impart kinetic energy to the working fluid apply a sufficiently large amount of energy to overcome the increased viscous dissipation and shear stresses in high viscosity liquids. Common forms are pneumatic atomizers, which utilize a coflowing stream of gas, and rotary atomizers, which utilize spinning disks to accelerate and disperse the liquid.[32] Such atomizers are commonly utilized when a spray of droplets is required from a jet of liquid. While these methods atomize highly viscous liquids, they are not applicable to all cases where droplets of high viscosity liquids are necessary. Working fluid preheat can damage thermally sensitive liquids, while kinetic atomizers lack fine control of droplet size and placement. For wide applicability, the following attributes are sought in a potential atomization method for high viscosity liquids:

- **A high degree of control over the timing of droplet creation**. Individual droplets must be produced only when necessary for the process into which the atomizer is integrated.
- **A high degree of control over the placement of droplets on the substrate.** Droplets must leave the atomizer in a controlled manner with a predictable velocity and impact characteristics on the substrate.
- **Low temperature operation.** Elevated temperatures should not be required to reduce working fluid viscosity as the working fluid may degrade.

Controlled atomization of high viscosity liquids thus poses an ongoing challenge requiring new atomization methods. Inkjet fluid ejectors have a high degree of control over atomization but have traditionally lacked to ability to eject working fluids of high viscosity.[25] However, a new form of fluid ejector called horn-based ultrasonic atomization has shown the potential to overcome the limitations on working fluid viscosity.[28] This dissertation research addresses the potential of fluid ejectors, and horn-based ultrasonic atomizers in particular, to eject high viscosity working fluids in a controlled, on-demand fashion.

2.1 Review of inkjet fluid ejector devices

Inkjet fluid ejection is an atomization method that has been integrated into many processes due to its excellent controllability and uniformity in atomizing low viscosity fluids.[33] Inkjet devices descend from the work of Lord Kelvin and Plateau, who first examined the breakup of liquid jets, and Weber, who considered the same behavior in viscous jets.[6] Elmquist of Siemens-Elma introduced the first practical inkjet device in 1951. This first device produced a continuous stream of charged droplets that were

directed based on an applied voltage. Further development throughout the 1980s led most users to move away from continuous inkjets in favor of drop-on-demand (DOD) inkjets that produce single droplets as needed. Droplet placement with DOD devices is not only more easily controlled than continuous inkjets, but DOD devices also significantly reduce the amount of working fluid required.[34] A full history of inkjet development is given by Ford et al.[5] Recent work continues to broaden the applications of inkjets; printing of biological tissues/samples, fabrication of electronics, and additive manufacturing have all been recent areas in which inkjets have been applied.[25, 35-37]

Fluid ejection from inkjet fluid ejectors is governed by the same physical processes regardless of actuation method and device geometry.[25] Inkjets confine a quantity of the working fluid targeted for ejection in a chamber to form a fluid cavity. A small aperture connects the fluid chamber to the ambient environment and provides a means for fluid to be ejected from the fluid cavity. Inkjets operate by producing a small displacement wave at a fluid cavity wall which travels from the wall to the fluid cavity aperture. Fluid is ejected from the aperture when a sufficiently large displacement occurs at the aperture following wave propagation. The amount of fluid ejected, as well as whether ejection takes place in a continuous jet or drop-on-demand (DOD) fashion, are determined by the geometry and operating parameters of the ejector.

Inkjets are can be broadly divided into classes based on the mechanism which imposes the displacement on the fluid cavity, the two most common being thermal bubbles and piezoelectric transducers.[6, 38] Thermal inkjets, shown in Figure 2.1, impose the displacement on the fluid cavity by heating a small volume of fluid until it

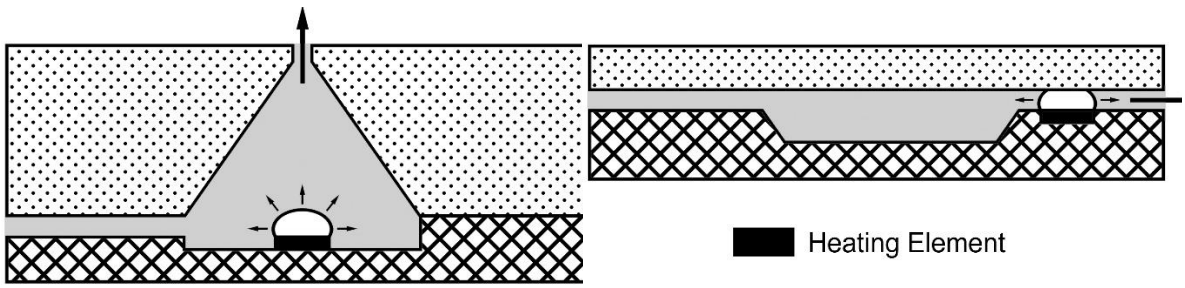

Figure 2.1: Common thermal inkjets. Left: Roof shooter geometry. Right: Side shooter geometry.[1]

vaporizes producing a gas bubble. As the bubble expands, the imposed displacement grows as a function of time. As the bubble contracts, the imposed displacement shrinks and returns to zero. Two common thermal inkjet geometries are the roof shooter and side shooter configuration. In the roof shooter geometry, the vapor bubble is produced at the bottom of the fluid cavity. As the wave propagates towards the aperture, the displacement is focused by the geometry of the ejector. In the side shooter geometry, the vapor bubble is produced and fills a small channel. The imposed displacement wave propagates to the aperture along the small channel without additional concentration from the geometry. Due to the simplicity of these devices, thermal inkjets were the first class of inkjets to gain widespread adoption and are used extensively in commercially available desktop printers from Hewlett-Packard and Canon.[5, 6, 39, 40] However, their simplicity also restricts their operation. Due to the need to heat the working fluid, such devices can only be utilized with working fluids that are not thermally sensitive and do not chemically breakdown at high temperatures. Also, because the displacement imposed on the fluid cavity is dependent on the growth and contraction of the vapor bubble, fine control of the imposed displacement waveform and amplitude is difficult.

As the roles of inkjets has expanded from two-dimensional printing of simple working fluids on paper to more complex roles, the restrictions associated with thermal inkjets has motivated the development of piezoelectric inkjets. Piezoelectric inkjets, shown in Figure 2.2, impose the displacement on the fluid cavity by the use of an applied voltage to a transducer. By controlling the voltage across the transducer, a displacement as a function of time can be imposed on the fluid cavity with fine temporal resolution. Moreover, as the working fluid is not directly heated, piezoelectric inkjets can be utilized with a wider variety of working fluids.

Piezoelectric inkjets can be broadly divided into four categories based on their geometry and the polarization of the transducer: bending mode top shooter, bending mode side shooter, bump mode, and squeeze mode. The bending mode top and side shooter geometries closely mirror the thermal inkjet designs with the vapor bubble replaced by the piezoelectric transducer. The transducer is polarized in the thickness direction with the voltage applied across the transducer thickness as well. The push type devices are in the side shooter style, with the transducer polarization and applied voltage in the thickness direction, but the displacement in the transverse direction is utilized. Due to their similarities outside of the transducer polarization, bending and push mode piezoelectric inkjets are often considered jointly. Most investigations of these inkjets center on the characteristics of the produced droplets and the optimal actuation voltage waveform in the particular geometry under investigation by the researcher. Voltage waveforms are studied so as to minimize the displacement of the free surface after the ejection of the primary droplet to prevent satellite droplet production, typically by experimental methods.[41-44] Droplets are an area of focus as they are the desired

output of the device.[45, 46] Commercially, Epson is a main producer of bending and push piezoelectric ejectors.[47] Due to the small length scales associated with bending and push mode inkjets as compared to the acoustic wavelength at the low operating frequencies characteristic of the devices, the pressure induced by the transducer motion equilibrates rapidly throughout the fluid cavity which permits a lumped-element description of these device types.[6, 38]

The fourth type of piezoelectric inkjet, the squeeze type, has a cylindrical fluid cavity bounded by an annulus of piezoelectric material that deforms radially inward when actuated. As squeeze type devices are typically long axially compared to the acoustic wavelength at the actuation frequency, the applied energy propagates as an acoustic wave. As for bending and push mode devices, the primary areas of investigation for the squeeze type ejectors remain the driving waveform and the shape of the produced droplets as these are the key input and output parameters for a given ejector geometry.[48-53] However, Bogy and Talke also experimentally examined the acoustic field governing the devices, showing that for the optimal duration of the driving pulse, the motion of the transducer reinforces the acoustic wave present in the fluid cavity.[2] However, the description provided by Bogy and Talke does not generalize to all squeeze ejector geometries and did not account for viscous dissipation mechanisms present in the fluid cavity. The various commercial ejectors produced by MicroFab Technologies use squeeze type piezoelectric inkjets extensively.[54]

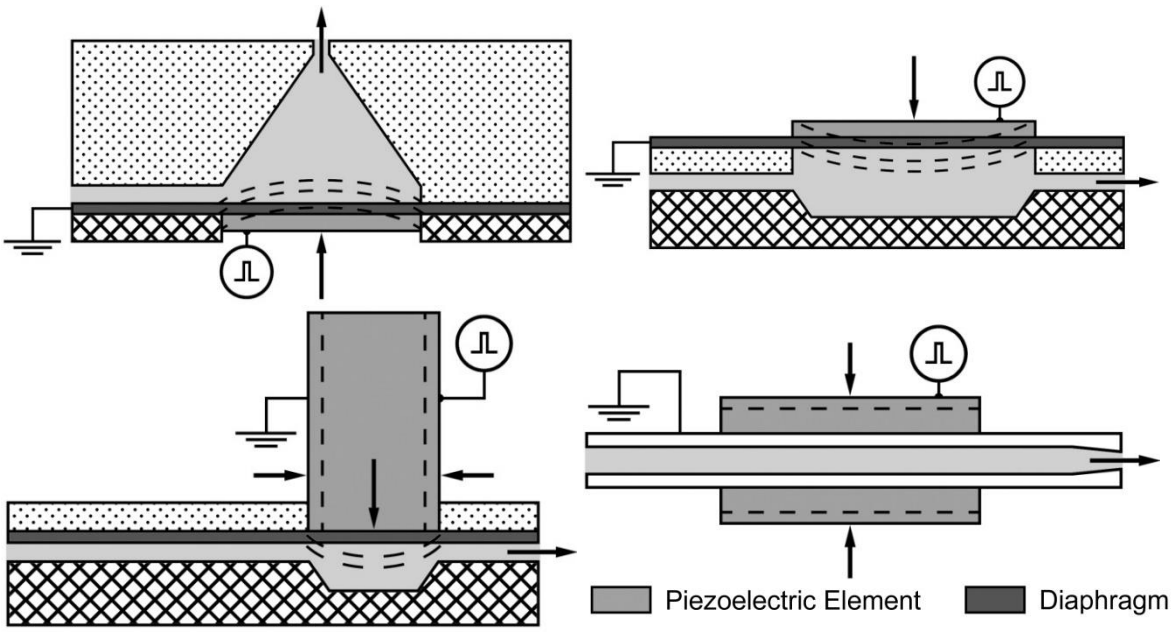

Figure 2.2: Common piezoelectric inkjets. Top left: Bending mode top shooter. Top right: Bending mode side shooter. Bottom left: Push mode. Bottom right: Squeeze mode.[1]

2.3 Horn-based ultrasonic atomizer concept and design

Resonant ultrasonic atomizers, a type of fluid ejector that produces droplets by means of resonant ultrasonic waves, range in form from surface wave atomizers to open pool devices.[55-57] Horn-based ultrasonic atomizers are a subgroup that enclose fluid in a cavity and utilize acoustic horns.[3, 58] These devices are composed of a piezoelectric transducer, a fluid reservoir, and a micromachined array of horns as shown in Figure 2.3. When the transducer is driven at one of the resonant frequencies of the fluid cavity, a high amplitude standing wave forms within the cavity. The acoustic horns act to increase the volume velocity of the standing wave near the horn aperture, resulting in a locally large pressure gradient and an efficient means for fluid ejection. [3] Horn-based ultrasonic atomizers typically operate in the frequency range between 100 kHz and several MHz depending on the dimensions of the fluid cavity which can vary in height from few millimeters to hundreds of micrometers. Fluid ejection occurs in either droplet-

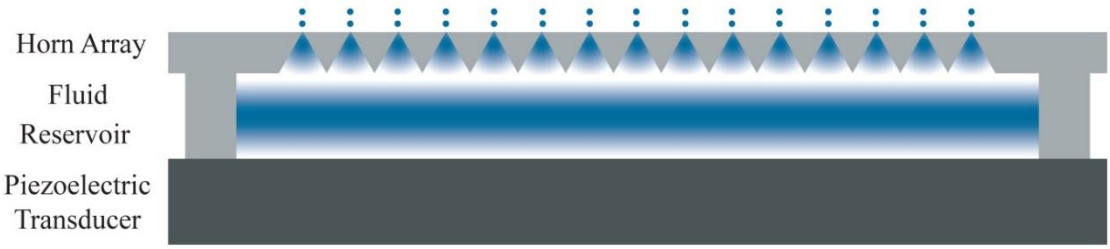

Figure 2.3: Schematic of the horn-based ultrasonic atomizer showing multiple unit cells.

mode or jet-mode as a function of the aperture size, operating frequency, and properties of the fluid.[59] Scalability is achieved by including multiple horns to form an array, the use of multiple arrays of horns, or by multiplexed operation of the device.[60] Horn-based ultrasonic atomization has been studied in various applications ranging from fuel injection to additive manufacturing.[61-63] Further work also examined effect of droplet charging on the behavior of horn-based ultrasonic atomizers for applications in electrospray generation.[64]

2.4 Viscosity limitations on atomization in inkjet fluid ejectors

Fluid ejection from current inkjet fluid ejectors is generally limited to working fluids which closely match the rheological properties of water, that is low viscosity (1 mPas) Newtonian fluids with high surface tension (72 mN/m). Atomization of working fluids which differ significantly from water encounter two principle challenges: the generation/propagation of the pressure wave within the fluid cavity and the droplet formation dynamics at the horn aperture. The former requires that the ejection-driving displacement in the form of an acoustic pressure wave propagates from the source (transducer) to the fluid cavity aperture while maintaining a sufficiently large intensity to expel fluid.[2] The latter necessitates control of the fluid mechanics at the fluid cavity aperture. The pressure field must be repeatable and of sufficient frequency to maintain uniformity between ejection cycles at the desired ejection mode, be it jetting or drop-on-

demand, while minimizing the production of satellite droplets.[37, 65, 66] Though an understanding of fluid mechanics is necessary to fully characterize droplet ejection from inkjet fluid ejectors, a prerequisite for fluid ejection is that the focused acoustic wave generates a sufficiently large pressure gradient to expel fluid from the aperture. As such, this work focuses on the acoustic field of fluid ejectors with an emphasis on evaluating the viscous effects on the acoustics of such devices and developing the guidelines for ejectability of high viscosity fluids by them.

High viscosity fluids rapidly dissipate, i.e. convert to heat, the mechanical energy of the propagating wave through two principle mechanisms, bulk attenuation and boundary layer losses. Bulk attenuation results from the shear stress in the propagating direction of the wave and occurs in direct proportion to the fluid viscosity.[67] Attenuation results in an exponential decay of the acoustic wave amplitude as a function of distance from the wave source.[68, 69] The attenuation effect of viscosity is often stated in terms of a complex wavenumber using the spatial attenuation coefficient, α_s with units of inverse meters, which accounts for both fluid viscous heat generation and heat dissipation by conduction and is also typically expressed as a frequency (f) independent value, α_s/f^2. The second means of viscous dissipation in fluid ejectors is the acoustic boundary layer. The acoustic boundary layer is present near device walls where the acoustic field must conform the no-slip condition at the wall surface. The boundary layer acts to transfer energy from the acoustic field to thermal energy due to tangential shear stress in the boundary layer, thereby reducing the amplitude of the acoustic field.[70]

For fluids of low viscosity or ejectors with small propagation distances, viscous losses from both dissipation mechanisms are insignificant and can be neglected in the acoustic analysis.[3] However, as the fluid viscosity or the propagation distance become large, significant decreases in the amplitude of the acoustic field will occur between the wave source and ejection point at the cavity aperture. This diminishes the pressure gradient magnitude produced by the ejector which is necessary to overcome the increased shear stress of high viscosity fluids near the horn aperture which grows linearly with the fluid shear stress/viscosity.[71] Thus, ejection of the high viscosity fluid presents a double challenge; not only do highly viscous fluids dampen the driving acoustic field but such working fluids also increase the required pressure gradient magnitude required for fluid ejection. The upper limit on working fluid viscosity able to be ejected by micromachined fluid ejectors is established when the ejector is no longer able to generate a sufficiently large amplitude acoustic field to overcome viscous dissipation and produce sufficient pressure gradient required for fluid ejection. The dominant viscous dissipation mechanism in any ejector is a function of working fluid properties, the device geometry, and the driving frequency.[72]

2.4.1 Acoustic losses in cylindrical capillaries and horns

The relatively simple geometries of most fluid ejectors parallel well studied standard acoustic components, namely capillaries/tubes and horns. This permits an understanding of the effect of working fluid viscosity on the acoustic field of each component. The acoustic field within tubes has been an intensive area of historical study. Kirchoff and Rayleigh were among the first to study the acoustic fields in tubes, developing solutions for limiting cases when the acoustic boundary layer was much

smaller and much larger compared to the tube radius.[73] The early twentieth century was also an era of significant research with Bogert, Lambert, and Beatty each developing analytical solutions for the acoustic field in a capillary under various conditions.[74-76] The result of their efforts is a series analytical descriptions for how the acoustic boundary layer behaves as a function of working fluid properties and operating frequency of which Tijdeman provides a review.[73] When the acoustic boundary layer is large compared to the radius of the tube, the axial flow profile reduces to a parabolic profile. As the acoustic boundary layer becomes smaller compared to the tube radius, the flow transitions to plug flow with the variation occurring only near the capillary walls. In this region near the wall, the flow reverses direction compared to the flow at the centerline during part of the cycle. As the working fluid viscosity is increased, the amplitude of acoustic field in the capillary goes through a maximum as the fluid initially becomes more stiff and then falls monotonically with increasing viscosity due to greater viscous dissipation. For most common working fluids (such as glycerol) operating below 1 MHz, the losses associated with the acoustic boundary layer will be several orders of magnitude greater than that due to bulk attenuation.[70, 72]

Viscous dissipation within horns is less well understood. For axisymmetric horns, the same physics governing cylindrical capillaries can be applied. However, this does not account for the change in cross-sectional area throughout the horn. The most common method of analyzing the acoustic field in horn structures is by the use of the Webster Wave Equation (WWE).[77] The WWE, first derived by Daniel Bernoulli but attributed to Webster, is able to relate the change in cross-sectional area to the change in amplitude of an acoustic wave to the first order.[78] Historically, the WWE has been extensively

utilized to understand the acoustic field within horns with numerous researchers employing it: Merkulov and Kharitonov to predict changes in amplitude across a horn connecting two different sized capillaries; Amza and Drimer to determine the gain of various horn structures; Stewart to explain his experimental results for conical horns; Lal to predict the wave amplitude in various solid horns; and Donskoy and Cray to form a transmission network model for various pipe sections connected together.[79-83] However, the WWE does not innately include viscous dissipation, requiring instead the use of a complex wavenumber to account for bulk attenuation losses. Furthermore, this method neglects the viscous dissipation associated with the boundary layer which is the dominant loss mechanism at low viscosities and frequencies in the presence of solid bounding surfaces. Work has also been done on ducts of varying cross-sections more generally, but these do not directly examine the effect of the viscosity of the medium on wave propagation or extend beyond small working fluid viscosity. [84-88]

2.4.2 The effect of high viscosity working fluids on ejector behavior

The influence of working fluid viscosity has been extensively studied in physical ejectors. Liu et al. maintained a fixed driving waveform in glycerol/water mixtures of increasing viscosity using a squeeze type ejector, demonstrating that as the working fluid viscosity grows the amplitude of the acoustic field declines.[89] Continued increases in working fluid viscosity ceased fluid ejection completely. Tai et al., Raman et al., and Jo et al. each reported a similar result in high viscosity glycerol/water concentrations in squeeze ejectors driven at a constant voltage, requiring a larger driving voltage to overcome the increase in viscous dissipation.[90-92] Each of these studies maintained a fixed voltage across the piezoelectric transducer below the dielectric breakdown value,

preventing them from examining the upper limit on working fluid viscosity able to be ejected from the devices. Jang et al. broaden their analysis to consider numerous working fluid mixtures and set the upper limit on working fluid viscosity as 12 mPas. Their limit was due to limited controllability of the ejected fluid and not on an inability to cause fluid ejection.[33] Sun et al. determined the minimum ejection voltage as a function of working fluid viscosity, again in glycerol/water mixtures.[93] At 1 mPas, the reported minimum ejection voltage is 20 V which increases minimally at 30 mPas to 30 V. Above 30 mPas, the minimum voltage for ejection increases rapidly to 150 V at 90 mPas. Extrapolating this curve to greater viscosities yields a driving voltage in excess of the dielectric breakdown voltage of the piezoelectric transducer. Due to the wide variability in ejector geometry, material properties, and working fluid properties, the upper limit on working fluid viscosity is generally taken to lie at 100 mPas.[6, 25]

Recent work has shown that horn-based ultrasonic atomizers may have the potential to overcome the historical limitation on the working fluid viscosity able to be ejected with micromachined fluid ejectors. Horn-based ultrasonic atomizers have experimentally shown the capability to eject high viscosity working fluids, including both pure glycerol with 1.4 Pas viscosity and proprietary photopolymer resins with a viscosity of 3 Pas.[28] This was done without external preheat, albeit for only short time periods at the higher range of viscosities.[62] Significant heating of the transducer was observed when ejecting high viscosity fluids, which may have resulted in heating of the fluid and reduction of its viscosity. Fundamentally, operation of horn-based ultrasonic atomizers, and inkjets more broadly, with high viscosity fluids and the basic physics governing

ejection of such fluids are still not well understood to provide definitive answers on their potential and limits for ejection of high viscosity fluids.

2.5 Previous modeling of fluid ejectors

The ability of fluid ejectors to eject high viscosity fluids is ultimately determined by effective generation and propagation of the acoustic wave in the fluid cavity. Previous efforts to understand the acoustic field present in the fluid cavity of piezoelectric fluid ejectors/inkjets have relied on a combination of empirical, numerical, and analytical approaches. The empirical acoustics description most often invoked is that given by Bogy and Talke.[2] By measuring the meniscus displacement in a squeeze type inkjet, Bogy and Talke were able to infer the reflection behavior of waves propagating in the device fluid cavity as well as to determine the optimal driving pulse duration to amplify the meniscus displacement leading to fluid ejection. A second often cited study of acoustic behavior is that of Antohe and Wallace who measured the electrical impedance of an inkjet with compliant cavity walls to determine resonance behavior, though they did not look explicitly at the acoustic field in the fluid cavity.[94] Empirical correlations to the fluid cavity acoustic properties can provide only limited insight into device behavior as the enclosed geometry and small tube diameter restrict one's ability to obtain detailed measurements. Horn-based ultrasonic atomizers have also been studied by experimental approaches. Meacham et al. studied the ejection of high viscosity fluids, developing empirical jettability criteria based on the plume height observed in the atomization of water/glycerol mixtures and a photopolymer resin.[28] This study clearly demonstrated that increasing working fluid viscosity was detrimental to fluid ejectability and eventually led to the cessation of ejection.

In contrast, numerical modeling permits exploration of the full acoustic field of the fluid cavity. Numerous numerical models of inkjets have been developed; however, the focus of most models has been on the characteristics of the ejected droplets rather than the acoustics of the fluid cavity.[43, 46, 92, 95] This is unsurprising as the final droplet characteristics are of principal interest in most applications. An exception to this is Pan et al. who simulated the entirety of the fluid cavity but assumes incompressible fluid thereby precluding any acoustic effects.[96] Chen et al. also included the influence of acoustics on device behavior and reported the pressure near the aperture.[97] Wijshoff performed the most extensive acoustic modeling for various inkjet geometries using finite-element based commercial software ANSYS but reported only limited results for each geometry.[6] Computational work with horn-based ultrasonic atomizers is more substantive. Previous investigations into fluid atomization with horn-based ultrasonic atomizers have centered on the device acoustic field and how it varies as a function of working fluid properties. Meacham et al. utilized ANSYS to study the acoustic field of a horn-based ultrasonic atomizer in the lossless case. [3] Tsai et al. modeled atomizers in single and multiple horn configurations, also with no accounting for acoustic power losses.[58] Percin et al. simulated atomizers driven by annular disks focusing on the droplet characteristics.[98, 99] While useful to understanding acoustic behavior and atomization of low viscosity working fluids, the computational tools employed in these studies cannot account for losses due to both the acoustic boundary layer and bulk attenuation. Moreover, finite-element based methods are computationally expensive which prohibits detailed parametric analyses and extensive optimization.

The limitations of numerical and empirical models have motivated the development of analytical models for understanding the acoustic behavior of piezoelectric droplet generators. Due to the simplifications necessary to analytically solve the governing equations, the available models consider device behavior in limiting cases with simplified geometries. The simplest models assume Hagen-Poiseuille flow to predict droplet volumes.[100] Lumped element and inviscid assumptions have also both been utilized to formulate models. [101-103] Narrow channel acoustics can be utilized in geometries with sufficiently small cross-sectional area.[6] More detailed models also exist for squeeze type devices that incorporate losses due to the acoustic boundary layer.[72] Furthermore, the WWE has been utilized to examine the acoustics of pipe/horn systems but has not been applied to atomizers.[77-80, 83] Analytical models provide significant advantages over numerical and empirical methods. First, analytical models yield the closed-form solutions to the problem that reveal the combination of parameters and scaling relationships that define device acoustic behavior. Additionally, analytical models are usually computationally less expensive than numerical models, allowing for fast exploration of a large parameter space. These benefits make analytical models useful tools for both an in-depth understanding and efficient design optimization of ultrasonic fluid ejectors.

2.6 Concluding remarks on device background

This chapter introduced various kinds of fluid ejectors, both piezoelectric inkjets and horn-based ultrasonic atomizers, the latter of which has shown the potential to eject high viscosity working fluids. The principle sources of viscous dissipation of wave mechanical energy were identified and attributed to the viscous boundary layer in the presence of bounding solid surfaces and bulk attenuation far from the walls. Historical

efforts toward understanding the acoustics of fluid ejectors were also presented. The characterization of ejectors consisted of experimental, numerical, and analytical approaches, none of which satisfactorily describe the fluid cavity acoustic field in sufficient detail to permit the design of ejectors which can overcome the increased viscous dissipation associated with high viscosity working fluids. Subsequent sections of this thesis analyze the performance of fluid ejectors, focusing on horn-based ultrasonic atomizers and squeeze type of ejectors, using comprehensive electromechanical modeling which includes both acoustics of the wave guiding/focusing cavity and transducer behavior with an ultimate goal to understand and define the capabilities and limits in using such devices for atomization of high viscosity fluids.

CHAPTER 3: DEVELOPMENT AND VALIDATION OF ANALYTICAL MODELS

Simplified electro-mechanical models are developed for micromachined fluid ejectors in order to investigate the ejection of high viscosity liquids. This effort concentrates on modeling the acoustic response of ejectors with viscous dissipation included in the fluid cavity acoustic field. The effect of the driving piezoelectric transducer on the fluid cavity acoustic field is obtained by coupling the fluid cavity acoustic field to a transducer model. Device models are created by considering each ejector component separately – the transducer, the acoustic pipe, and the acoustic horn – and coupling components together through appropriate boundary conditions to represent ejector physics. The scaling relationships that determine the acoustic behavior within the fluid cavity are also established to understand and account for the primary viscous loss mechanisms in the modeling framework. The developed analytical models are validated by comparison with finite element simulations and experimental data from literature.

3.1 Description of the micromachined fluid ejectors to be modeled

Two types of fluid ejectors will be considered during the subsequent model development, horn-based ultrasonic atomizers and squeeze ejectors, due to their demonstrated potential for ejecting high viscosity working fluids and the possibility to generalize the geometries across additional ejector types. The horn-based ultrasonic atomizer under investigation (Figure 3.1) consists of a piezoelectric transducer generating ultrasonic waves, a planar fluid reservoir, and an array of pyramidal nozzles etched in silicon acting as acoustic horns.[3] The displacement wave created by the transducer propagates through the fluid reservoir to the acoustic horn where it is

concentrated at the horn aperture. When the transducer is driven at the resonant frequencies of the fluid cavity, a locally increased pressure gradient results at the horn aperture producing an efficient means of fluid ejection. Micromachined horn-based ultrasonic atomizers consist of numerous horns ejecting in parallel from a shared fluid reservoir.[3] As the lateral dimensions of the fluid reservoir and number of horns become large, the acoustic field in the fluid reservoir becomes one-dimensional in the vertical direction as end effects at the reservoir walls become negligible. The acoustic response of the atomizer can then be simplified to the response of an individual cell, an enlarged version of which shown in Figure 3.1. Further simplification can be made by considering the atomizer cell to be axisymmetric about the center of the horn to aid in model formulation. This assumption modifies both the shape of the horn, which must be treated as circular rather than square, and the boundary condition on the exterior of the unit cell, which is symmetric in Cartesian but not in polar coordinates. The modification of the exterior boundary condition is unimportant as the acoustic field has been simplified to one-dimensional behavior in the axial direction which is unchanged by the transformation in coordinate systems; a change in the exterior boundary condition would only affect the acoustic field were a two-dimensional field permitted in the fluid cavity as the axisymmetric assumption would then influence the radial direction. The change in the horn shape affects both the surface area of the horn and acoustic impedance of the horn section; these are expected to differ from the pyramidal geometry only by a constant factor as the conical, axisymmetric horn closes approximates the pyramidal shape. Moreover, the horn taper between the entrance and aperture remains linear and a similar reduction in the cross-sectional area of the horn is achieved over the horn length. The

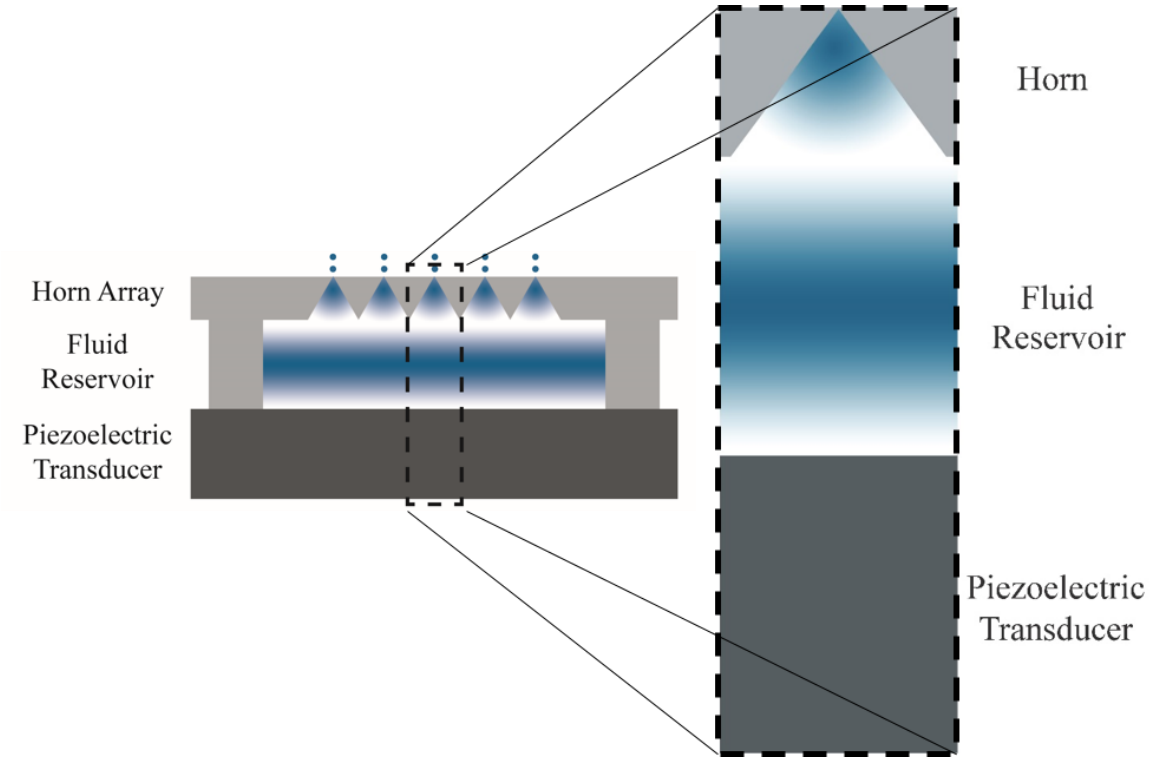

Figure 3.1: Representation of the modeled horn-based ultrasonic atomizer geometry.[3] The device consists of a fluid filled acoustic horn, a fluid reservoir, and a driving planar piezoelectric transducer.

axisymmetric atom izer cell model is therefore expected to be representative of large horn-based ultrasonic atomizers with many cells operating in parallel.

As squeeze type fluid ejectors can vary widely in geometry, selection of an archetypal form that is representative of the overall class of ejectors is necessary for modeling. The squeeze ejector geometry utilized by Bogy and Talke was selected, a reproduction of which is given in Figure 3.2.[2] The main part of the ejector is composed of a cylindrical, fluid-filled glass capillary divided into three sections. The left and right capillary sections are exposed to the atmosphere while the center section is surrounded by an annular piezoelectric transducer. When a voltage is applied to the transducer, it imposes a radial displacement on the glass capillary which is transmitted to the fluid cavity. As the diameter of the fluid cavity is much less its axial length, the resulting

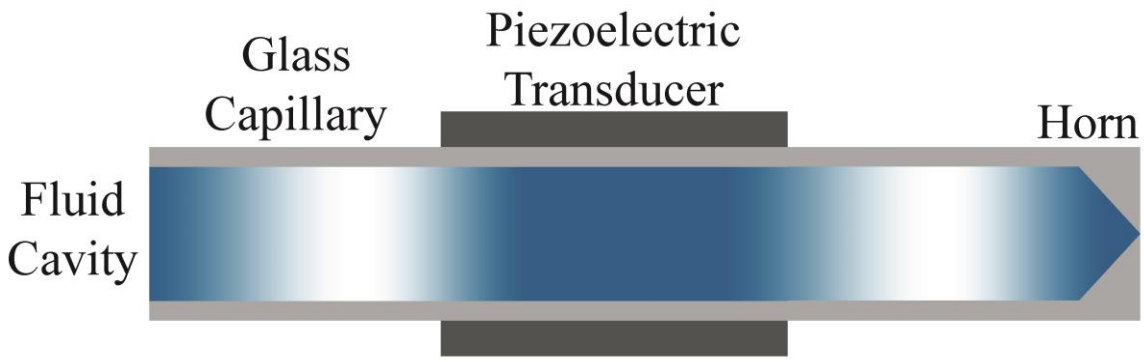

Figure 3.2: Representation of the modeled squeeze ejector geometry. The device consists of a fluid filled cavity which tapers to a small aperture, a glass capillary which confines the fluid in a cavity, and a driving annular piezoelectric transducer. The left side is bounded by the fluid reservoir (not shown) used to fill the capillary.

acoustic field is one-dimensional in the axial direction a short distance away from the transducer ends and transmits the displacement wave laterally from the transducer to the capillary ends. The capillary is bounded on one end by a large fluid reservoir used to fill the capillary and the other end by a short horn through which fluid is ejected.

3.1.1 Identification of common ejector components

Analytical model development can take advantage of common physical features shared between horn-based ultrasonic atomizers and squeeze ejectors. These features can be seen by breaking the devices into constitutive components based on the physics which govern each component. The structure of the horn-base ultrasonic atomizer cell (Figure 2.1) can be divided into three component sections as seen in Figure 3.3: a planar piezoelectric transducer, an acoustic pipe without a confining wall, and a horn section. The structure of squeeze ejectors (Figure 3.2) is similarly considered in Figure 3.4, yielding five components of four different types: an annular piezoelectric transducer, an acoustic pipe with a confining wall, a "driven" acoustic pipe with a confining wall, and a horn section. As the acoustic pipe with a confining wall exists in both "driven" and "undriven" states, a unified model capable of handling both cases will be developed. By

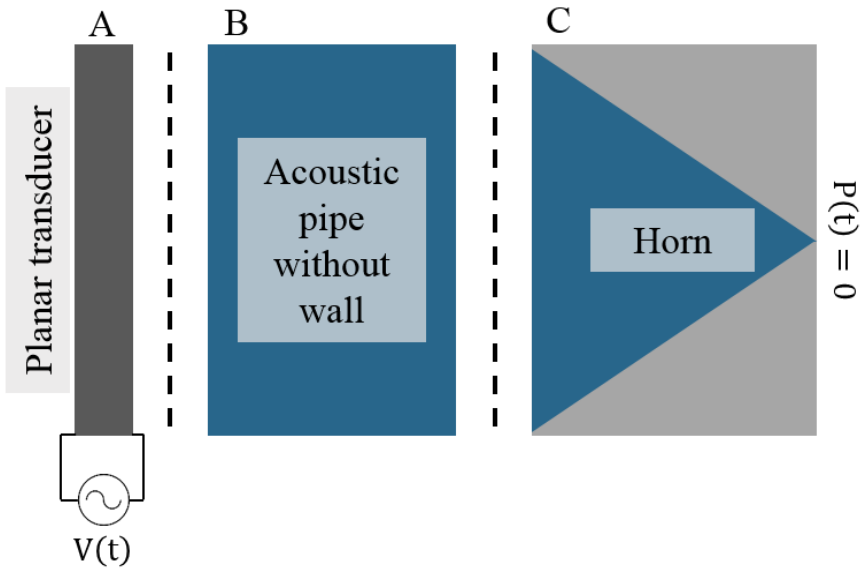

Figure 3.3: A schematic of a horn-based ultrasonic atomizer with its constitutive components identified. The device can be modeled as an individual planar piezoelectric transducer, an acoustic pipe without a wall, and a horn coupled together with the appropriate boundary conditions.

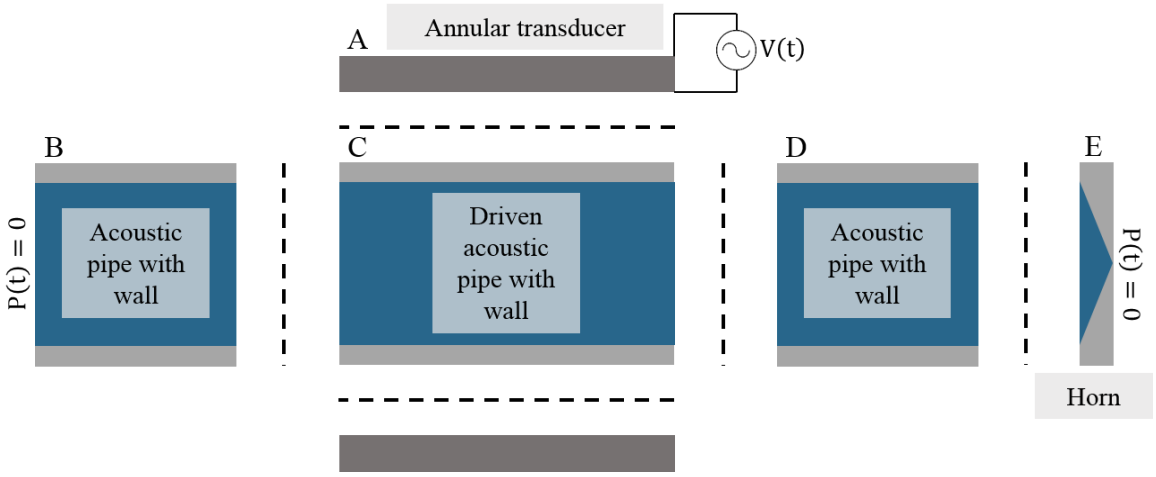

Figure 3.4: A schematic of a squeeze ejector with its constitutive components identified. The device can be modeled as an individual annular piezoelectric transducer, acoustic pipes with a wall, a driven acoustic pipe with a wall, and a horn coupled together with the appropriate boundary conditions.

examining constitutive components of the ejectors, five necessary models have been identified for the following components: a planar piezoelectric transducer, an annular piezoelectric transducer, an acoustic pipe without a confining wall, an acoustic pipe with a confining wall, and an acoustic horn. By developing each model independently,

incorporating viscous dissipation into each fluid cavity component, and joining the components together with appropriate boundary conditions, development of coupled electro-mechanical models of the fluid ejectors is possible.

3.2 Development of piezoelectric transducer models

The first type of component to be considered is the piezoelectric transducer. A transducer model for each of the planar and annular geometries is necessary to model the micromachined fluid ejectors under investigation. Development of a model for each transducer geometry draws on established impedance matrix methods commonly utilized in transducer design.

3.2.1 Planar transducers

The planar piezoelectric transducer geometry is modeled using an impedance matrix formulation as outlined by Auld.[104] The impedance matrix, given in Equation 3.1, characterizes the behavior of a one-dimensional, planar transducer by relating its mechanical and electrical properties. The formulation assumes the transducer has three ports, two mechanical consisting of the front and back planes and an electrical port across the planes. Polarization is assumed in the thickness direction between the planes. The system of equations is solved by dividing the force across the mechanical ports by their respective velocities to eliminate the force terms in favor of mechanical impedances. In reference to Figure 3.3, the front side of the transducer is then taken to be loaded by the fluid cavity impedance ($Z_{m,cav}$) and the backside by the impedance of air ($Z_{m,air}$). When one assumes a user specified sinusoidal voltage signal V driving the transducer, the system of equations can be solved given the material properties of the transducer:

$$\begin{bmatrix} F_1 \\ F_2 \\ V \end{bmatrix} = \begin{bmatrix} -jZ_c\cot(\beta l) & -jZ_c\csc(\beta l) & \frac{-jh_{33}}{\omega} \\ -jZ_c\csc(\beta l) & Z_c\cot(\beta l) & \frac{-jh_{33}}{\omega} \\ \frac{-jh_{33}}{\omega} & \frac{-jh_{33}}{\omega} & \frac{-j}{\omega C_0} \end{bmatrix} \begin{bmatrix} v_1 \\ v_2 \\ I_3 \end{bmatrix} \quad 3.1$$

where Z_c is the transducer characteristic impedance given by $S_{trans}\sqrt{\rho_{trans}c_{33}^D}$, β is the wavenumber in the transducer given by $\omega\sqrt{\rho_{trans}/c_{33}^D}$, l is the transducer thickness, h_{33} is the transmitting constant, C_0 is the clamped capacitance, and c_{33}^D is the elastic stiffness constant at constant displacement in the thickness direction. The specific material properties utilized for the model can be found in Appendix A. The area of the transducer S_{trans} is taken to be large such that one-dimensional behavior is maintained. Dielectric and mechanical losses can be incorporated into the model by modifying h_{33} with the loss tangent $\tan(\delta)$ and the wavenumber with the mechanical quality factor Q_m:

$$h_{33} = \frac{e_{33}}{\epsilon_{33}^s} = \frac{e_{33}}{\epsilon_r\epsilon_0(1 - jtan(\delta))} \quad 3.2$$

$$\beta = \omega\sqrt{\frac{\rho_{trans}}{c_{33}^D}}\left(1 - \frac{j}{2Q_m}\right) \quad 3.3$$

where e_{33} is the piezoelectric stress constant, ϵ_{33}^s is the clamped dielectric constant, ϵ_r is the relative permeability of the transducer, and ϵ_0 is the permeability of free space. The system of equations given in the impedance matrix formulation can be solved directly for the velocity associated with the front/fluid cavity side of the transducer which is then applied as the inlet boundary condition to the fluid cavity model. In addition, the electrical behavior of the transducer, such as its electrical impedance and energy loss, can be readily determined. As the behavior of the Mason impedance matrix formulation is well documented, a detailed verification of its validity is not required.[105-107]

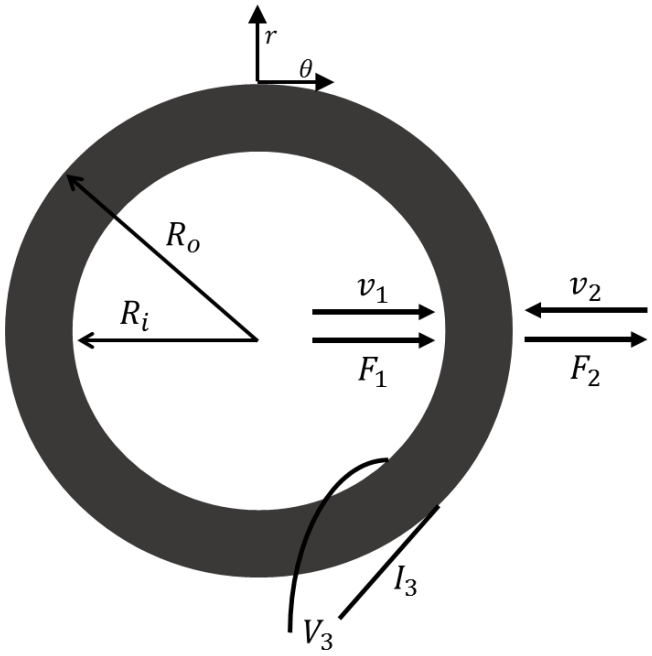

Figure 3.5: The annular piezoelectric transducer geometry as modeled by Liang.[4] The transducer is assumed to be infinite in axial length. The inner and outer surfaces are active and poling is in the radial direction.

3.2.2 Annular transducers

The annular piezoelectric transducer geometry is modeled using an impedance matrix formulation as outlined by Liang.[4] The formulation describes the electrical and mechanical behavior of an infinitely long, annular transducer as shown in Figure 3.5. The transducer is assumed to be polarized in the radial direction with the electrodes covering the inner and outer surfaces. Liang uses the same three-port structure as outlined by Auld but modifies the impedances for the annular geometry.[104]

The system of equations in Equation 3.4 is again solved by dividing the force across the mechanical ports by their respective velocities to eliminate the force terms in favor of mechanical impedances. The inner surface of the transducer is then taken to be loaded by the fluid cavity impedance ($Z_{m,cav}$) and the outer surface by the impedance of air ($Z_{m,air}$). When a sinusoid driving voltage V is specified, the only remaining terms are material properties of the transducer:

$$\begin{bmatrix} F_1 \\ F_2 \\ V \end{bmatrix} = \begin{bmatrix} z_{11} & z_{12} & z_{13} \\ z_{21} & z_{22} & z_{23} \\ z_{31} & z_{32} & z_{33} \end{bmatrix} \begin{bmatrix} v_1 \\ v_2 \\ I_3 \end{bmatrix} \tag{3.4}$$

$$z_{11} = \frac{2\pi\beta R_1}{j\omega}\left[\frac{c_{33}^D[J_{\nu-1}(\beta R_1)Y_\nu(\beta R_2) - J_\nu(\beta R_2)Y_{\nu-1}(\beta R_1)]}{J_\nu(\beta R_2)Y_\nu(\beta R_1) - J_\nu(\beta R_1)Y_\nu(\beta R_2)} - \frac{\nu c_{33}^D - c_{13}^D}{\beta R_1}\right] \tag{3.5}$$

$$z_{12} = z_{21} = -\frac{4c_{33}^D}{j\omega}\frac{1}{J_\nu(\beta R_2)Y_\nu(\beta R_1) - J_\nu(\beta R_1)Y_\nu(\beta R_2)} \tag{3.6}$$

$$z_{13} = z_{31} = -\frac{j}{\omega}\left[h_{33} + h_{31}\frac{Y_\nu(\beta R_2)b_1 - J_\nu(\beta R_2)b_2}{J_\nu(\beta R_2)Y_\nu(\beta R_1) - J_\nu(\beta R_1)Y_\nu(\beta R_2)}\right] \tag{3.7}$$

$$z_{22} = \frac{2\pi\beta R_2}{j\omega}\left[\frac{c_{33}^D[J_{\nu-1}(\beta R_2)Y_\nu(\beta R_1) - J_\nu(\beta R_1)Y_{\nu-1}(\beta R_2)]}{J_\nu(\beta R_2)Y_\nu(\beta R_1) - J_\nu(\beta R_1)Y_\nu(\beta R_2)} + \frac{\nu c_{33}^D - c_{13}^D}{\beta R_2}\right] \tag{3.8}$$

$$z_{23} = z_{32} = -\frac{j}{\omega}\left[h_{33} + h_{31}\frac{Y_\nu(\beta R_1)b_1 - J_\nu(\beta R_1)b_2}{J_\nu(\beta R_2)Y_\nu(\beta R_1) - J_\nu(\beta R_1)Y_\nu(\beta R_2)}\right] \tag{3.9}$$

$$z_{33} = -\frac{j}{\omega}\left[\frac{\ln(R_2/R_1)}{2\pi\epsilon_{33}^s}\right.$$

$$\left. - \frac{h_{31}^2}{4c_{33}^D}\left[\frac{[Y_\nu(\beta R_1)b_1 - J_\nu(\beta R_1)b_2][Y_\nu(\beta R_2)b_1 - J_\nu(\beta R_2)b_2]}{J_\nu(\beta R_2)Y_\nu(\beta R_1) - J_\nu(\beta R_1)Y_\nu(\beta R_2)}\right.\right. \tag{3.10}$$

$$\left.\left. + \int_{R_1}^{R_2}\frac{1}{r}\int_{\beta R_1}^{\beta r}\frac{J_\nu(\beta r)Y_\nu(\mu) - J_\nu(\mu)Y_\nu(\beta r)}{\mu}d\mu dr\right]\right]$$

where R_1 is the inner transducer radius, R_2 is the outer radius, and ν is the order of the Bessel functions given by $\sqrt{c_{11}^D/c_{33}^D}$. The elastic stiffness constants at constant displacement are c_{11}^D, c_{33}^D, and c_{13}^D in azimuthal, radial and off-diagonal azimuthal/radial cross directions respectively. Coefficients b_1 and b_2 are obtained through the following integrations:

$$b_1 = \int_{\beta R_1}^{\beta R_2} \frac{J_\nu(\mu)}{\mu} d\mu \tag{3.11}$$

$$b_2 = \int_{\beta R_1}^{\beta R_2} \frac{Y_\nu(\mu)}{\mu} d\mu \tag{3.12}$$

Due to the cylindrical geometry, the impedances are expressed in terms of Bessel functions of the first and second kinds. Mechanical and electrical losses can again be included by modifying the wavenumber and transmitting constant as in Equations 3.2 and 3.3. The system of equations given in the impedance matrix formulation can be solved directly for the velocity associated with the i nner surface of the transducer which is then applied as the boundary condition to the fluid cavity model. In addition, the electrical behavior of the transducer, such as its electrical impedance and energy loss, can be readily determined.

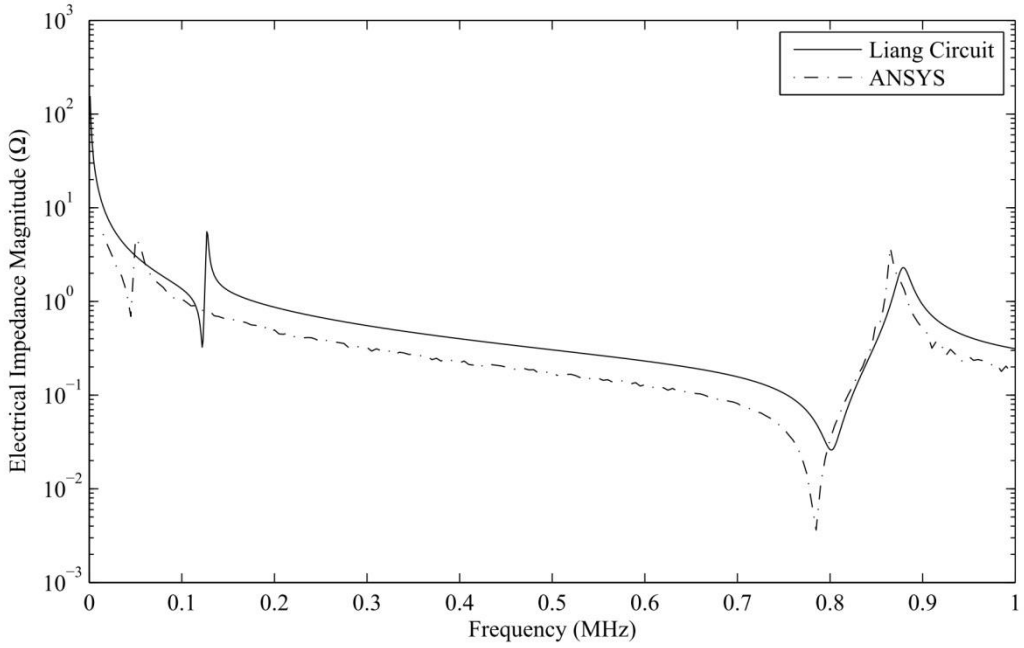

Figure 3.6: A comparison of the predicted electrical impedance magnitude for an annular transducer using both ANSYS and the Liang impedance matrix. The geometry is taken to have a 9 mm inner radius and a 11.54 mm outer radius. Material properties are taken as PZT5.

As the annular impedance matrix formulation is less well documented than its planar counterpart, a validation was conducted by comparing the response of a free transducer as predicted by the analytical model to an ANSYS Mechanical (ANSYS) model (Figure 3.6).[108] ANSYS is a commercially available, finite element software package designed to solve problems involving coupled physics which is able to simulate the behavior of piezoelectric transducers. Pre-programmed element types provide the basis for model construction and incorporating material behavior. The domain was comprised of a piezoelectric transducer (APC International PZT855) with Plane13 elements driven by 1V peak amplitude sinusoidal signal. Due to the assumption of infinite axial length, only thickness and hoop resonances are to be expected in the transducer response. The hoop mode is also commonly referred to as a "breathing" mode as the hoop moves radially outward uniformly about the centerline. As the transducer thickness is much less than the circumference, the thickness mode should be the higher frequency mode. The Liang formulation and ANSYS both predict a similar thickness resonant frequency near 850 kHz. However, the Liang impedance matrix predicts a hoop resonance at approximately twice the frequency of ANSYS. ANSYS predicts a hoop resonance closer to the analytical value given by McMahon:

$$f = \frac{1}{2\pi}\sqrt{\frac{c_{11}^{E}}{\rho_{trans}\bar{R}^2}} \tag{3.13}$$

with $\bar{R}$ being taken as the mean radius of the annulus.[109] This implies that the Liang formulation over predicts the stiffness of the transducer in the azimuthal direction. The discrepancy does not prevent the use of the Liang impedance matrix; however, it must be recognized that response of any component model driven by the annular transducer will

be higher in frequency as compared to physical devices. This is due to the higher frequency of the transducer hoop resonance in the Liang formulation and the over prediction of the amount of energy placed into the frequencies near the hoop resonance. The off-resonance difference in electrical impedance magnitude results from the lack of damping in the ANSYS model which lowers the overall impedance magnitude. Based on this analysis, the Liang impedance matrix can be utilized to model squeeze type transducers, recognizing the bias toward higher frequencies as a result of the discrepancy in the hoop resonance.

3.3 Development of the acoustic pipe models

The second component to be considered is the acoustic pipe. Two pipe models, one for pipes bounded by a wall and a second for pipes without a wall, are necessary to model wave propagation in the micromachined fluid ejectors under investigation. While pipes without confining walls have an established modeling methodology, the complexity of wave propagation in pipes with walls causes the development of an analytical model to be nontrivial. The governing equations must be simplified to be amenable to closed-form analytical solutions by retaining significant terms and neglecting terms small in magnitude based on ejector operating regimes. Moreover, the effect of the wall compliance on the pipe acoustic field must also be incorporated. The complexity of wave propagation in acoustic pipes motivates the development of a regime map to aid in determining applicability of the subsequently developed models in ejector operating regimes.

3.3.1 Development of the acoustic pipe without a wall model

Considering the case of acoustic pipe lacking a wall, the component can be modeled as a one-dimensional acoustic pipe with length l and radius R as given in Figure 3.7. The acoustic field is assumed to be uniform across the radius with propagation occurring only in the axial direction. The pipe acoustic field is composed of two harmonic propagating waves with complex amplitudes A and B, the values of which are determined by the boundary conditions at the left and right ends. The acoustic field can be represented with pressure and volume velocity of the form: [110]

$$P = Re\left\{\left(Ae^{-jkz} + Be^{jkz}\right)e^{j\omega t}\right\} \tag{3.14}$$

$$V_z = Re\left\{\frac{S}{\rho_0 c}\left(Ae^{-jkz} - Be^{jkz}\right)e^{j\omega t}\right\} \tag{3.15}$$

where k is the wavenumber, ω is the angular frequency, ρ_0 is the fluid density, c is the fluid speed of sound, S is the cross-sectional area, z is the spatial position along the pipe, and t is the time. The two imposed boundary conditions at each end must be either pressure, volume velocity, or volume impedance conditions. As the pipe is situated between two other components, a boundary condition must be applied at both ends of the domain to ensure proper coupling between domains. The coupling between domains will be discussed in further detail in Sections 3.5 and 3.6.

A result of the absence of constraining surfaces is that the only mechanism of energy loss within the subdomain is bulk attenuation. This can be included in the acoustic pipe through the use of a complex wavenumber, $\bar{k} = k - j\alpha_s$, where α_s is the classical attenuation coefficient expressed as $2\omega^2\mu/3\rho c^3$ for liquids, where μ is the fluid

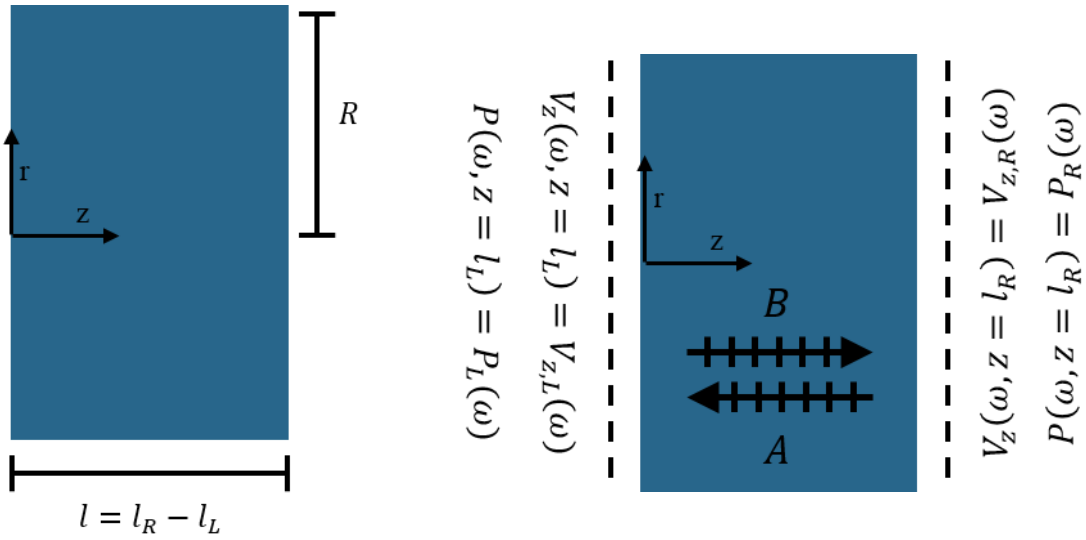

Figure 3.7: Left: Geometry of the acoustic pipe without a wall model. Right: The boundary conditions and components of the acoustic field within the acoustic pipe without a wall.

viscosity.[67]

3.3.2 Development of the acoustic pipe with a wall model

Dijksman derived a model for an axisymmetric, compliant tube confined by a wall and driven by a radial displacement.[72] The geometry, a schematic of which is shown in Figure 3.8, has a length l, radius R, and is surrounded by a wall of thickness h. The acoustic boundary layer is directly incorporated into the model by cross-sectionally averaging the pressure and density, assuming that only the velocities vary radially so as to accommodate the no-slip condition at the wall. This assumption constrains the model to one-dimensional acoustic behavior in which the wavelength is much greater than the tube diameter. The elasticity of the wall is accounted for through the introduction of spatial dispersion, resulting in a modified speed of sound that depends on fluid and wall mechanical properties.

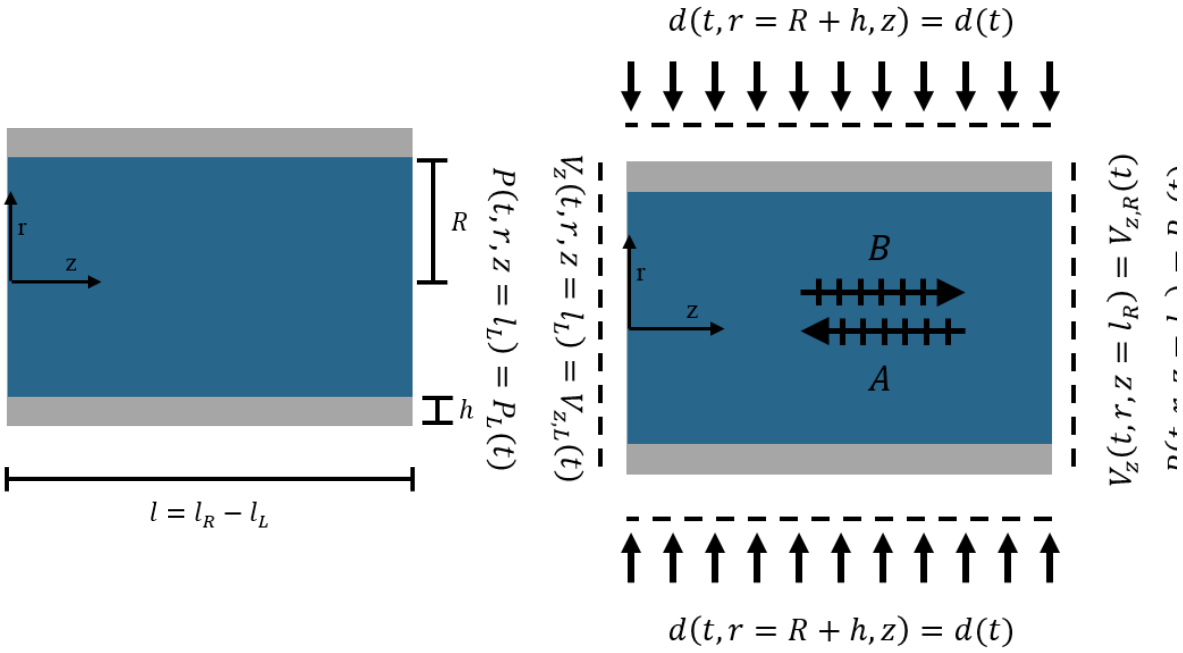

Figure 3.8: Left: Geometry of the acoustic pipe with a wall model. Right: The boundary conditions and components of the acoustic field within the acoustic pipe with a wall.

To begin the development of the model, one must confine analysis to Newtonian fluids in axisymmetric devices. Assuming that the radial length scale is much smaller than the wavelength and the radial velocity is much less than the axial velocity, one can neglect the radial component of momentum. These assumptions simplify the full three-dimensional formulation to a system governed by the continuity and axial momentum conservation equations:

$$\frac{\partial \rho}{\partial t} + \frac{1}{r}\frac{\partial}{\partial r}(r\rho v_r) + \frac{\partial}{\partial z}(\rho v_z) = 0 \tag{3.16}$$

$$\left(\frac{\partial \rho v_z}{\partial t} + v_r\frac{\partial \rho v_z}{\partial r} + v_z\frac{\partial \rho v_z}{\partial z}\right) = -\frac{\partial P}{\partial z} + \mu\left(\frac{1}{r}\frac{\partial}{\partial r}\left(r\frac{\partial v_z}{\partial r}\right) + \frac{\partial^2 v_z}{\partial z^2}\right) \tag{3.17}$$

with the following boundary and initial conditions for the pipe:

$v_r(t, r = R, z) = v_w$	No slip at the wall
$\frac{\partial v_z}{\partial r}(t, r = 0, z)$=0	Symmetry
$v_z\ (t, r = R, z) = 0$	No slip at the wall
$d(t, r = R, z) = d(t)$	Radial displacement imposed on exterior of the jacket
$P\ \ (t = 0, r, z) = 0$	Quiescent cavity
$\frac{\partial P}{\partial t^*}(t = 0, r, z) = 0$	Quiescent cavity
$P(t, r, z = l_L) = P_L(t)$	Pressure condition at the subdomain inlet
$P(t, r, z = l_R) = P_R(t)$	Pressure condition at the subdomain outlet

where d is the squeeze displacement on the outer surface of the surrounding jacket material, v_r is the radial velocity component, and v_z is the axial velocity component. The boundary conditions imposed at pipe inlet and outlet can be either a pressure, volume velocity, or volume impedance condition; for the purposes of developing the model a pressure condition can be assumed without loss of generality. One can then decompose the velocities, density, and pressure into mean values denoted by the zero subscript and deviations from the mean denoted by the prime superscript. As the flow rate from micromachined ejectors during ejection is small, one can assume that the mean velocity in the fluid cavity is approximately zero.[3] Further neglecting terms that are second order gives:

$$\frac{\partial \rho'}{\partial t} + \frac{1}{r}\frac{\partial}{\partial r}(r\rho_0 {v_r}') + \frac{\partial}{\partial z}(\rho_0 {v_z}') = 0 \tag{3.18}$$

$$\rho_0\left(\frac{\partial {v_z}'}{\partial t} + {v_r}'\frac{\partial {v_z}'}{\partial r} + {v_z}'\frac{\partial {v_z}'}{\partial z}\right) = -\frac{\partial P'}{\partial z} + \mu\left(\frac{1}{r}\frac{\partial}{\partial r}\left(r\frac{\partial {v_z}'}{\partial r}\right) + \frac{\partial^2 {v_z}'}{\partial z^2}\right) \tag{3.19}$$

Averaging all properties across the cross-section is done to obtain mean values, excepting the density and pressure which are assumed not to vary significantly across the cross-section such that they can be considered independent of r. This assumption holds

as along as the actuation wavelength remains much larger than the tube diameter. Both the radial and axial velocities are taken to be functions of r. The radial velocity can then be eliminated from the equations through application of the boundary conditions at the wall to yield:

$$\frac{\partial \rho'}{\partial t} + \frac{2\rho_0}{R}(v_r')|_R + \rho_0 \frac{\partial \bar{v_z}'}{\partial z} = 0 \tag{3.20}$$

$$\rho_0 \left(\frac{\partial \bar{v_z}'}{\partial t} + \frac{2\pi}{\pi R^2} \int_0^R \left(v_r' \frac{\partial v_z'}{\partial r} + v_z' \frac{\partial v_z'}{\partial z} \right) r dr \right) = -\frac{\partial P'}{\partial z} + \frac{2\mu}{R} \frac{\partial v_z'}{\partial r}|_R + \mu \frac{\partial^2 \overline{v_z'}}{\partial z^2} \tag{3.21}$$

where $\bar{v_z}$ is the cross-section averaged axial velocity. Further assuming that the advection is small compared to the inertia, one can eliminate the advective terms from the momentum equation. The assumption holds as long as:

$$v_z \omega_r \gg v_r v_z \left(\frac{\rho \omega_r}{\mu} \right)^{\frac{1}{2}} \qquad v_z \omega_r \gg \frac{v_z^2}{l_t} \tag{3.22}$$

$$\omega_r \gg \frac{\mu}{\rho_0 R^2} \qquad \omega_r \ll \frac{c}{w_0} \tag{3.23}$$

The remaining radial velocity term in Equation 3.20 is eliminated by relating the radial velocity imposed on the external surface of the tube surrounding the fluid cavity to the velocity on the interior surface of the tube using stress-strain relations for thin walled cylinders. Timescale analysis provides a means to validate the thin wall approximation. The three acoustic timescales can be defined based on the propagation time of acoustic perturbations within the fluid and tube material: the radial propagation time in the glass (t_g), the radial propagation time in the fluid cavity (t_r), and the axial propagation time in the fluid cavity (t_z). These can be defined mathematically as:

$$t_g = \frac{h}{c_g} \qquad t_r = \frac{R}{c_f} \qquad t_z = \frac{l_t}{c_f} \qquad 3.24$$

where R is the inner radius of the jacket material, l_t is the total fluid cavity length, c_g is the sound speed within the jacket material, and c_f is the fluid sound speed. The driving of the ejector will be governed by the fourth timescale, t_d , inversely proportional to the signal repeat rate ω_r. In general, one expects that the propagation time within the glass to be much less than either the radial or axial propagation times within the fluid cavity as $c_g > c_f$ and $h < R < l_t$. Furthermore, as propagation time in the glass is generally much less than the driving timescale, the displacement within the glass can be considered uniform as a function of space with the imposed displacement instantaneously applied from the jacket exterior to the jacket interior. The displacement and velocity imposed then by the transducer on the inner jacket surface are $d(t)$ and $\frac{\partial d}{\partial t}$, respectively.

Utilizing the thin-walled cylindrical stress-strain relationships, one can determine the response of the jacket material to the combination of the imposed displacement and the pressure field in the fluid cavity.[111] The thin walled approximation is permitted as long the wall thickness (h) is much less than the inner diameter ($2R$) of the cylinder. Figure 3.9 shows an axial representation of a loaded, thin walled cylinder.

One can express the average hoop stress and radial strain within the cylinder as:

$$\sigma = \frac{P\left(R + \frac{1}{2}h\right)}{h} \qquad 3.25 \qquad \epsilon = \frac{\Delta r}{R + \frac{1}{2}h} \qquad 3.26$$

with P as the pressure on the inner surface and Δr as the change in radial displacement due to the stress. As the wall is thin, uniform stress and strain are assumed across the

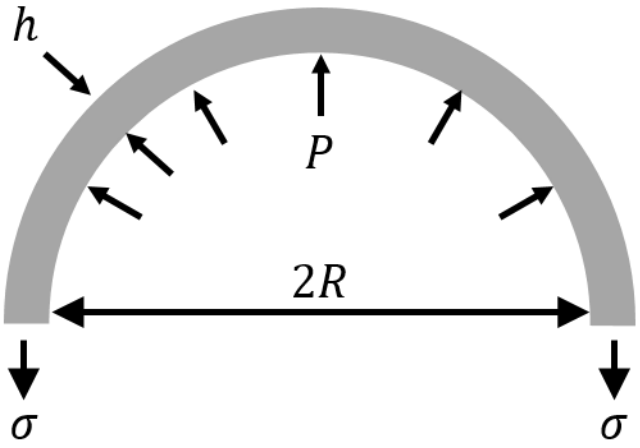

Figure 3.9: A representation of a thin cylinder of radius R and thickness h loaded on the interior with a pressure P. The cylinder has length L into the page. The stress and strain are assumed to be uniform due to the thinness of the wall.

shell which makes the mean tube radius the appropriate governing radius. Equating the stress to the strain using the Young's modulus (E) of the tube yields:

$$\sigma = E\epsilon \tag{3.27}$$

$$\Delta r = \frac{\left(R + \frac{1}{2}h\right)^2 P}{hE} \tag{3.28}$$

A time derivative of Equation 3.28 produces wall velocity due to the internal pressure field:

$$v_{r,P} = \frac{\left(R + \frac{1}{2}h\right)^2}{hE}\frac{\partial P}{\partial t} \tag{3.29}$$

Utilizing superposition, the total wall velocity is the sum of the imposed transducer velocity and the velocity resulting from the internal pressure field:

$$v_w = v_{r,T} + v_{r,P}$$

$$v_w = \frac{\partial d}{\partial t} + \frac{\left(R + \frac{1}{2}h\right)^2}{hE}\frac{\partial P}{\partial t} \tag{3.30}$$

The wall velocity can be substituted into Equation 3.20 as $v_r$evalutated at $r = R$ to give:

$$\frac{\partial \rho'}{\partial t} + \frac{2\rho_0}{R_i}\left(\frac{\partial d}{\partial t} + \frac{\left(R + \frac{1}{2}h\right)^2}{hE}\frac{\partial P}{\partial t}\right) + \rho_0 \frac{\partial \bar{v_z}'}{\partial z} = 0 \tag{3.31}$$

Through application of the chain rule and the definition of sound speed, a modified speed of sound ($\bar{c}$) can be introduced which accounts for elasticity and thickness of the jacket material:

$$\frac{\partial P'}{\partial t}\left(\frac{1}{c^2} + \frac{2\rho_0}{R}\frac{\left(R + \frac{1}{2}h\right)^2}{hE}\right) + \frac{2\rho_0}{R}\frac{\partial d}{\partial t} + \rho_0 \frac{\partial \bar{v_z}'}{\partial z} = 0 \tag{3.32}$$

$$\frac{1}{\bar{c}^2} = \frac{1}{c^2} + \frac{2\rho_0}{R}\frac{\left(R + \frac{1}{2}h\right)^2}{hE} \tag{3.33}$$

The modified speed of sound reflects the spatial dispersion caused by the changing physical properties of the jacket material along the axial length of the subdomain. The outlined simplifications produced a coupled system of differential equations for continuity and conservation of axial momentum given by:

$$\frac{1}{\bar{c}^2}\frac{\partial P'}{\partial t} + \frac{2\rho_0}{R}\frac{\partial d}{\partial t} + \rho_0 \frac{\partial \bar{v_z}'}{\partial z} = 0 \tag{3.34}$$

$$\rho_0 \frac{\partial \bar{v_z}'}{\partial t} = -\frac{\partial P'}{\partial z} + \frac{2\mu}{R}\frac{\partial v_z'}{\partial r}|_R + \mu \frac{\partial^2 \overline{v_z'}}{\partial z^2} \tag{3.35}$$

Differentiating Equation 3.34 by time, Equation 3.35 by z, and subtracting results in the system of equations as follows, dropping the prime notation for convenience:

$$\frac{1}{\bar{c}^2}\frac{\partial^2 P}{\partial t^2} + \frac{2\rho_0}{R}\frac{\partial^2 d}{\partial t^2} - \frac{\partial^2 P}{\partial z^2} + \frac{2\mu}{R}\frac{\partial}{\partial z}\left(\frac{\partial v_z}{\partial r}|_R\right) + \mu \frac{\partial^3 \bar{v_z}}{\partial z^3} = 0 \tag{3.36}$$

$$\rho_0 \frac{\partial v_z}{\partial t} = \frac{-\partial P}{\partial z} + \mu\left(\frac{1}{r}\frac{\partial}{\partial r}\left(r\frac{\partial v_z}{\partial r}\right) + \frac{\partial^2 v_z}{\partial z^2}\right) \tag{3.37}$$

Nondimensionalization is the first instance of deviation from the approach outlined by Dijksman.[72] In the present methodology, nondimensionalization is conducted to correctly reflect the scaling of the attenuation losses with frequency by the use of the acoustic wavelength as the axial length scale. Additionally, the resulting terms are written as common fluid mechanics nondimensional numbers to facilitate interpretation of ejector behavior. The utilized scales are:

$$P^* = \frac{P}{P_0} \qquad t^* = \omega_r t \qquad v_z^* = \frac{v_z}{\omega_r w_0} \qquad z^* = \frac{z\omega_r}{c} \qquad 3.38$$

$$r^* = r\left(\frac{\rho_0 \omega_r}{\mu}\right)^{\frac{1}{2}} \qquad d^* = \frac{d}{w_0}$$

where P_0 is the ambient pressure, ω_r is the repeat rate of the driving pulse in transient cases or the driving frequency in the single harmonic case, and w_0 is the maximum spectral density of the Fourier transform of the driving signal. Selection of the repeat rate as the temporal scale normalizes the time during an ejection cycle between zero and one. The maximum spectral density is utilized to normalize all imposed displacements between zero and one. The radial dimension scaled as the boundary layer thickness to expand the boundary layer. Defining the following nondimensional terms as:

$Eu = \frac{P_0}{\rho_0 w_0^2 \omega_r^2}$	Euler number	Ratio of the ambient pressure to the kinetic energy imposed at the transducer surface, defining the extent of energy transfer to the fluid cavity from the transducer
$Re = \frac{\omega_r w_0 \rho_0 R}{\mu}$	Particle Speed Reynolds number	Ratio of fluid inertia to viscous effects on the radial length scale, defining the importance of the radial component of the viscous stress
$Ma = \frac{\omega_r w_0}{c}$	Mach number	Ratio of driving velocity to the speed of sound, defining the importance of compressibility effects

$R_a = \frac{w_0}{R}$	Displacement ratio	Ratio of the driving displacement amplitude to the radius of the fluid cavity, defining the importance of the imposed radial displacement
$R_c = \frac{\bar{c}}{c}$	Dispersion ratio	Ratio of the modified fluid speed of sound resulting from wall compliance to the true fluid speed of sound, defining the importance of spatial dispersion
$Re^* = \frac{ReR_a}{Ma^2} = \frac{c^2\rho_0}{\mu\omega_r}$	Sound Speed Reynolds number	Ratio of fluid inertia to viscous effects on the wavelength length scale, defining the importance of axial component of the viscous stress

the governing equations become:

$$\frac{\partial^2 P^*}{\partial t^{*2}} - R_c^2\frac{\partial^2 P^*}{\partial z^{*2}} + \frac{2R_aR_c^2}{EuMa^2}\frac{\partial^2 d^*}{\partial t^{*2}} + \frac{2R_c}{EuMa}\left(\frac{R_a}{Re}\right)^{\frac{1}{2}}\frac{\partial}{\partial z^*}\left(\frac{\partial v_z^*}{\partial r^*}|_{R^*}\right) + \frac{R_c^2 Ma}{EuRe^2}\frac{\partial}{\partial z^*}\left(\int_0^{R^*}\frac{\partial^2 v_z^*}{\partial z^{*2}}r^* dr^*\right) = 0 \tag{3.39}$$

$$\frac{\partial v_z^*}{\partial t^*} = -EuMa\frac{\partial P^*}{\partial z^*} + \frac{1}{r^*}\frac{\partial}{\partial r^*}\left(r^*\frac{\partial v_z^*}{\partial r^*}\right) + \frac{Ma^2}{ReR_a}\frac{\partial^2 v_z^*}{\partial z^{*2}} \tag{3.40}$$

where R^* is the radius of the pipe nondimensionalized by the acoustic boundary layer thickness.

Nondimensionalization in this manner is advantageous as it produces five groups of dimensionless numbers that govern device behavior. In order from left to right, the magnitude coefficients of Equation 3.39 can be taken as showing the relative importance of inertia, the axial pressure gradient, the radial driving component, radial component of the viscous stress, and axial component of the viscous stress. As the inertial term remains important regardless of the magnitude of the other terms, its coefficient is set to one by dividing the equation by the appropriate scales. Unfortunately, an analytical solution of

the governing equations in the present form retaining all terms is not possible. However, by examining the magnitude of viscous stress and spatial pressure gradient nondimensional groups as a function the particle and sound speed Reynolds numbers, as is done in detail in Section 3.3.3, one can make informed simplifications to the governing equations based on the regimes of ejector operation where each of the viscous loss mechanisms is dominant. This allows the development of simplified models which capture the physics relevant to ejector operation but are limited to a region of device operation. If one confines the analysis to when the radial component of the viscous stress is dominant, that is boundary layer losses are more important than the bulk attenuation losses, one can eliminate the z-component of the viscous stress. The inertial, spatial, and radial driving terms are also retained as the magnitude of the terms is comparable to or larger than the boundary layer term.

$$\frac{\partial^2 P^*}{\partial t^{*2}} - R_c^2 \frac{\partial^2 P^*}{\partial z^{*2}} + \frac{2R_a R_c^2}{EuMa^2} \frac{\partial^2 d^*}{\partial t^{*2}} + \frac{2R_c}{EuMa} \left(\frac{R_a}{Re}\right)^{\frac{1}{2}} \frac{\partial}{\partial z^*} \left(\frac{\partial v_z^*}{\partial r^*}|_{R^*}\right) = 0 \tag{3.41}$$

$$\frac{\partial v_z^*}{\partial t^*} = -EuMa \frac{\partial P^*}{\partial z^*} + \frac{1}{r^*} \frac{\partial}{\partial r^*} \left(r^* \frac{\partial v_z^*}{\partial r^*}\right) \tag{3.42}$$

The system of differential equations are simplified in such a way as to have a closed form analytical solution, which is subject to the following boundary and initial conditions:

$P^*\left(t^*, z^* = \frac{\mathrm{l_L}\omega_r}{c}\right) = \mathrm{P}_1^*(t^*)$	Pressure condition at the subdomain inlet
$P^*\left(t^*, z^* = \frac{\mathrm{l_R}\omega_r}{c}\right) = \mathrm{P}_2^*(t^*)$	Pressure condition at the subdomain aperture
$\frac{\partial v_{z^*}}{\partial r^*}(t^*, r^* = 0, z^*)=0$	Symmetry
$v_z^*(t^*, z^*, r^* = R^*) = 0$	No slip at the wall

$$d^* = \frac{d(t)}{w_0}$$ Displacement imposed by the transducer on glass surface

$$P^*(t^* = 0, z^*) = 0$$ Quiescent cavity

$$\frac{\partial P^*}{\partial t^*}(t^* = 0, z^*) = 0$$ Quiescent cavity

To solve the system of equations given by Equations 3.41 and 3.42, a Fourier transform is taken and a separation of variables solution is sought in the following form:

$$P^* = Re\{\Psi(z)e^{jt^*}\} \tag{3.43}$$

$$v_z^* = Re\left\{(\Phi(r) + j)EuMa\ \frac{d\Psi}{dz^*}e^{jt^*}\right\} \tag{3.44}$$

$$d^* = Re\{e^{jt^*}\} \tag{3.45}$$

where $Re\{\}$ indicates the real component of the term contained within the braces.

Substituting the proposed solution into Equation 3.42 yields the differential equation governing Φ:

$$r^{*2}\frac{d^2\Phi}{dr^{*2}} + r^*\frac{d\Phi}{dr} - j\Phi r^{*2} = 0 \tag{3.46}$$

$$\Phi = A[ber_0(r^*) + jbei_0(r^*)] + B[\ker_0(r^*) + jkei_0(r^*)] \tag{3.47}$$

the solutions of which are Kelvin functions of the zeroth order.[112] The coefficients A and B must be determined by recasting the radial boundary conditions on v_z to conditions on Φ:

$$\frac{\partial v_{z^*}}{\partial r^*}(t^*, r^* = 0, z^*) = 0 \qquad \frac{d\Phi}{dr^*}(r^* = 0) = 0 \tag{3.48}$$

$$v_z^*(r^* = R^*) = 0 \qquad 0 = \Phi(R^*) + j \qquad \Phi(R^*) = -j \tag{3.49}$$

$$\Phi(r^*) = -\frac{ber_0(r^*) + jbei_0(r^*)}{bei_0(R^*) - jber_0(R^*)} \tag{3.50}$$

Applying the radial boundary conditions to Φ causes only the Kelvin function of the first kind to be retained. Substituting Equation 3.50 into Equation 3.44 gives an expression for the axial velocity in terms of r^*, which can be differentiated, evaluated at R^*, and substituted into Equation 3.41 to obtain Ψ.

$$v_z^* = Re\left\{\left(-\frac{ber_0(r^*)+jbei_0(r^*)}{bei_0(R^*)-jber_0(R^*)}+j\right)EuMa\frac{d\Psi}{dz^*}e^{jt^*}\right\} \tag{3.51}$$

$$\frac{\partial v_z^*}{\partial r} = Re\left\{\left(-\frac{ber_0{}'(r^*)+jbei_0{}'(r^*)}{bei_0(R^*)-jber_0(R^*)}\right)EuMa\frac{d\Psi}{dz^*}e^{jt^*}\right\} \tag{3.52}$$

$$\frac{\partial v_z^*}{\partial r}|_{R^*} = Re\left\{\left(-\frac{ber_0{}'(R^*)+jbei_0{}'(R^*)}{bei_0(R^*)-jber_0(R^*)}\right)EuMa\frac{d\Psi}{dz^*}e^{jt^*}\right\} \tag{3.53}$$

$$\begin{aligned}&\frac{\partial^2}{\partial t^{*2}}\left(\Psi e^{jt^*}\right)-R_c^2\frac{\partial^2}{\partial z^{*2}}\left(\Psi e^{jt^*}\right)+\frac{2R_aR_c^2}{EuMa^2}\frac{\partial^2}{\partial t^{*2}}\left(e^{jt^*}\right)\\&+\frac{2R_c}{EuMa}\left(\frac{R_a}{Re}\right)^{\frac{1}{2}}\frac{\partial}{\partial z^*}\left(\left(-\frac{ber_0{}'(R^*)+jbei_0{}'(R^*)}{bei_0(R^*)-jber_0(R^*)}\right)EuMa\frac{d\Psi}{dz^*}e^{jt^*}\right)=0\end{aligned} \tag{3.54}$$

$$\Psi+\left[R_c^2+2R_c\left(\frac{R_a}{Re}\right)^{\frac{1}{2}}\left(\frac{ber_0{}'(R^*)+jbei_0{}'(R^*)}{bei_0(R^*)-jber_0(R^*)}\right)\right]\frac{d^2\Psi}{dz^{*2}}+\frac{2R_aR_c^2}{EuMa^2}=0 \tag{3.55}$$

Defining ϵ as:

$$\epsilon = R_c^2+2R_c\left(\frac{R_a}{Re}\right)^{\frac{1}{2}}\left(\frac{ber_0{}'(R^*)+jbei_0{}'(R^*)}{bei_0(R^*)-jber_0(R^*)}\right) \tag{3.56}$$

Equation 3.55 can be written more compactly as:

$$\epsilon\frac{d^2\Psi}{dz^{*2}}+\Psi+\frac{2R_aR_c^2}{EuMa^2}=0 \tag{3.57}$$

A solution for Ψ can be determined using the method of undetermined coefficients, assuming a form of the solution of:

$$\Psi = Ae^{-jmz^*}+Be^{jmz^*}+C \tag{3.58}$$

which yields the following expression for Ψ:

$$\Psi = Ae^{-j\frac{1}{\sqrt{\epsilon}}z^*} + Be^{j\frac{1}{\sqrt{\epsilon}}z^*} - \frac{2R_aR_c^2}{EuMa^2} \tag{3.59}$$

Ψ can be substituted into Equations 3.43 and 3.44 to obtain expressions for the axial particle velocity and the acoustic pressure.

$$v_z^* = Re\left\{EuMa\left(-\frac{ber_0(r^*) + jbei_0(r^*)}{bei_0(R^*) - jber_0(R^*)} + j\right)\left(\frac{-j}{\sqrt{\epsilon}}Ae^{-j\frac{1}{\sqrt{\epsilon}}z^*} + j\frac{1}{\sqrt{\epsilon}}Be^{j\frac{1}{\sqrt{\epsilon}}z^*}\right)e^{jt^*}\right\} \tag{3.60}$$

$$P^* = Re\left\{\left(Ae^{-j\frac{1}{\sqrt{\epsilon}}z^*} + Be^{j\frac{1}{\sqrt{\epsilon}}z^*} - \frac{2R_aR_c^2}{EuMa^2}\right)e^{jt^*}\right\} \tag{3.61}$$

The two unknown complex amplitude coefficients A and B must be determined by the boundary conditions on the inlet and exit of each element, giving a system of algebraic equations for the velocity and pressure that represent the acoustic field in the horn. As the Fourier transform of the governing equations was taken during the course of model development, the Fourier transform of the boundary conditions must also be taken:

$$P^*\left(t^*, z^* = \frac{l_L\omega_r}{c}\right) = \widehat{P_1^*}e^{jt^*} \tag{3.62}$$

$$P^*\left(t^*, z^* = \frac{l_R\omega_r}{c}\right) = \widehat{P_2^*}e^{jt^*}$$

The hat notation indicates the spectral density of the boundary condition. An expression for the volume velocity can be obtained by integrating Equation 3.60 over the cross section:

$$V_z^* = Re\left\{2\pi EuMae^{jt^*}\left(-j\frac{1}{\sqrt{\epsilon}}Ae^{-j\frac{1}{\sqrt{\epsilon}}z^*} + j\frac{1}{\sqrt{\epsilon}}Be^{j\frac{1}{\sqrt{\epsilon}}z^*}\right)\int_0^{R^*}\left(-\frac{ber_0(r^*)+jbei_0(r^*)}{bei_0(R^*)-jber_0(R^*)}+j\right)r^*dr^*\right\} \quad 3.63$$

For acoustic pipes without squeeze type actuation, the squeeze driving term in Equation 3.61 ($2R_aR_c^2/EuMa^2$) is set to zero.

3.3.3 Applicability of the pipe models in various ejector regimes

The appropriate pipe model for ejector operational regimes can be obtained by comparing the groups of nondimensional numbers developed for the walled acoustic pipe model that govern the radial component of the viscous shear stress, the axial component of the viscous shear stress, and the spatial pressure gradient. Comparing the magnitude of these terms produces the regime map as shown in Figure 3.10, given in terms of the particle velocity Reynolds number ($Re = \omega_r w_0 \rho_0 R/\mu$) and the sound speed Reynolds number ($Re^* = c^2\rho_0/\mu\omega_r$). These two Reynolds numbers utilize different characteristic velocities and length scales (radius and wavelength respectively) to account for the difference in scaling associated with radial and axial viscous losses.

Examining Figure 3.10 more closely, line A is produced by balancing the radial and axial components of viscous stress while retaining the spatial pressure gradient in the axial direction. This produces the transition between where each viscous stress component dominates ejector behavior; above the line the radial component dominates and below it the axial component dominates. Line B in the upper left is produced by balancing the spatial pressure gradient against the radial component of the viscous stress, yielding the transition between propagating and lumped element behavior in the radial direction. Lumped element behavior occurs when the magnitude of the viscous stress

becomes much larger than the spatial gradient; as a consequence, the fluid has minimal spatial variation in the pressure over the associated length scale and moves as a rigid body. Line C in the lower right balances the spatial pressure gradient against the axial component of the viscous stress, giving the transition to lumped element behavior in the axial direction.

A scaling analysis of ejectors thus reveals four unique regions of pipe behavior: a propagating wave region where radial viscous losses due to the boundary layer dominate, a propagating wave region where the axial viscous losses due to bulk attenuation dominate, a lumped element region in the axial direction, and a lumped element region in the radial direction. As all terms necessary to model the lumped element behavior of acoustic pipes are captured in the models for the propagating operating regions, specific

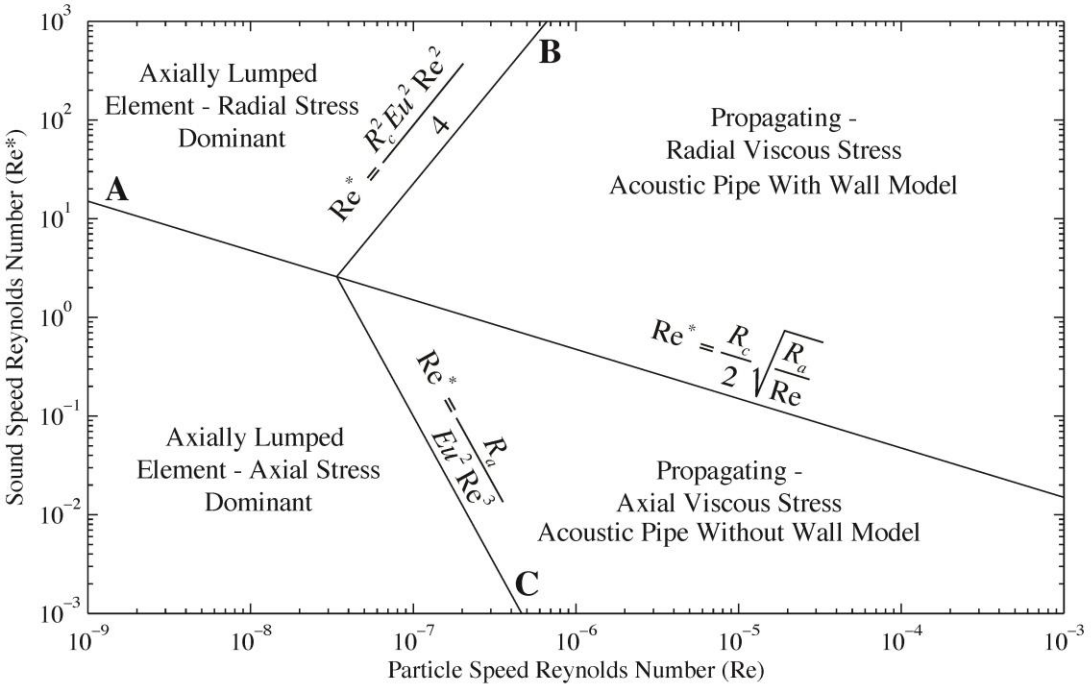

Figure 3.10: A regime map for the operation of acoustic pipes based on the dimensionless parameter groups produced during model formulation. Four operating regions exist from balancing the radial component of the viscous stress, the axial component of the viscous stress, and spatial pressure gradient.

focus on the lumped element regions is unnecessary. The previously developed pipe models capture both the region where the axial component of the viscous stress dominates through bulk attenuation in the model for an acoustic pipe without a wall and the region when the radial component of the viscous stress dominates through boundary layer losses in the model for an acoustic pipe with a wall. By calculating the particle speed and sound speed Reynolds numbers for a working fluid, the regime map can be used to select the appropriate model to capture the dominant source of viscous dissipation in the pipe. In general, acoustic pipes without walls will only have bulk attenuation as a source of viscous dissipation. In acoustic pipes with walls, viscous dissipation by boundary layer losses will be several orders of magnitude larger than bulk attenuation losses in most working fluids. However, for very high viscosity working fluids (>10Pas) or high operating frequencies, the dominant source of viscous dissipation can transition to bulk attenuation requiring the use of the acoustic pipe without a wall model even in the presence of a confining wall.

3.4 Derivation of the horn models

The third component to be considered is the acoustic horn which comprises the region of the ejectors with a changing cross-sectional area. Mirroring model development of acoustic pipes, multiple horn models are sought in order to capture the dominant sources of viscous dissipation while permitting an arbitrary horn shape. Horn models are constructed by first allowing the shape of the horn to vary continuously as a function of axial position within the horn and second by treating the change in area as a series of small, discretized area changes in an acoustic pipe. The result is three models, two of which capture bulk attenuation and one for boundary layer losses, which can be utilized for modeling the acoustic field in horn components.

3.4.1 Continuous variation in horn shape through the Webster Wave Equation

The change in horn cross-sectional area can be modeled as a continuous function of position using the Webster Wave Equation (WWE). The WWE predicts the acoustic field in a horn by relating the change in cross-sectional area to a change in acoustic field amplitude for one-dimensional waves.[113] Such an analysis yields the acoustic field within the horn to first order accuracy. [114, 115] Due to its simplicity, the WWE is commonly utilized as a means to predict amplitude changes in acoustic horns.[77, 83] Derivation of the acoustic field for a conical horn, given in Figure 3.11, follows; by utilizing the same procedure the WWE can be readily extended to horns of differing profiles.

The WWE is obtained by combining the continuity and conservation of axial momentum equations to form a wave equation, during which the advection and both viscous stress terms are neglected and a change in cross-section along the domain is permitted. This results in:

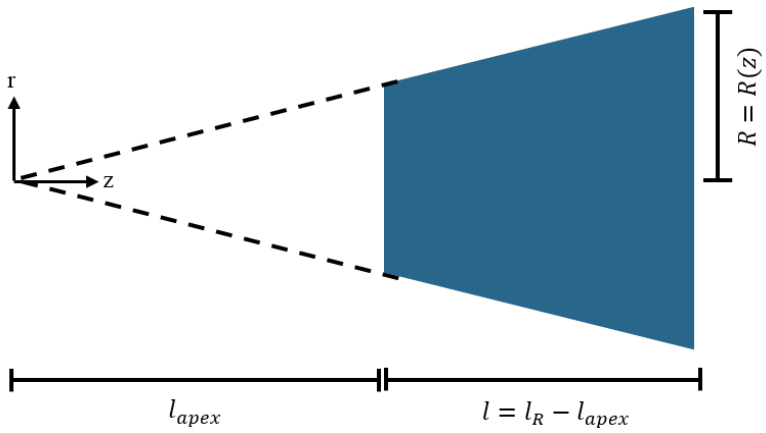

Figure 3.11: Geometry of a conical horn modeled with the WWE.

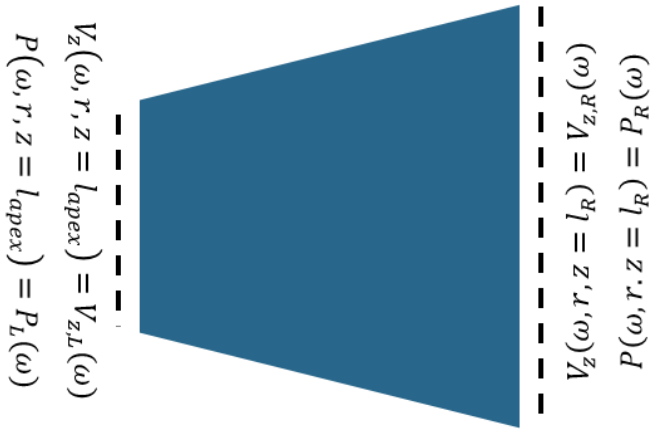

Figure 3.12: The boundary conditions and components of the conical horn modeled with the WWE.

$$\ddot{\phi} - c^2 \frac{\partial \phi}{\partial z} \frac{\partial}{\partial z}(lnS) - c^2 \frac{\partial^2 \phi}{\partial z^2} = 0 \tag{3.64}$$

$$S = S_0 z^2 \tag{3.65}$$

where Φ is the velocity potential, c is the speed of sound, and S is the change in cross-section expressed as a sole function of z, the spatial position in the horn.[77] The apex of the horn is taken to be the origin of the coordinate system. The resulting differential equation is solved using the method of unknown coefficients and d'Alembert two-wave decomposition, producing an algebraic equation for the velocity potential:

$$\phi = \frac{A}{z} e^{j(\omega t - kz)} + \frac{B}{z} e^{j(\omega t + kz)} \tag{3.66}$$

where A and B are the complex amplitude coefficients. Taking a time and space derivative of the velocity potential results in the pressure and volume velocity of the wave within the horn respectively:

$$P = -\frac{j\omega\rho A}{z} e^{j(\omega t - kz)} - \frac{j\omega\rho B}{z} e^{j(\omega t + kz)} \tag{3.67}$$

$$V_z = -\frac{S(1 + jkz)A}{z^2} e^{j(\omega t - kz)} - \frac{S(1 - jkz)B}{z^2} e^{j(\omega t + kz)} \tag{3.68}$$

The unknown coefficients are determined using the boundary conditions at the horn inlet and aperture. The boundary conditions imposed at pipe inlet and outlet can be either a pressure, volume velocity, or volume impedance condition. The effect of the axial component of the viscous stress, namely bulk attenuation, is added into the horn model by the use of a complex wavenumber and the attenuation coefficient. The result is an analytical horn model based on a simplified one-dimensional treatment of the geometry which includes bulk attenuation losses but lacks any wall compliance.

While the WWE is useful in that it gives an exact solution for wave propagation in a domain of changing cross-sectional area, the method is limited by the geometries that can be solved analytically. In general, a horn has four parameters of interest – an inlet radius, an outlet radius, a length, and a radius profile between the inlet and outlet radii – each of which is independently specified. The WWE approach utilizes a two parameter shape profile – an initial area constant and a flare constant – which is insufficient to specify four independent parameters outside of a conical geometry. One cannot for example maintain fixed inlet, outlet radii, and length for a changing flare constant using other WWE area functions. This limitation requires the use of the discretized pipe approach for non-conical geometries.

3.4.2 Discretization of the acoustic pipe models

To overcome the geometric limitations of the WWE approach, horns can be modeled as a discretized acoustic pipe. The length over which the horn radius changes is divided into elements, with each element having a different cross-sectional area as shown in Figure 3.13. The number of elements is set so that the variation in the acoustic amplitude from element entrance to exit is linear and so that the change in area between

adjacent elements is small. The volume velocity and pressure are matched at the interface between elements to form a continuous acoustic pipe with varying cross-sectional area.

Utilizing Figure 3.13 as a reference, the matching of pressure and volume velocity at the interface between elements can in general be expressed as:

$$P_1(\omega, z = l_1)|_{l_1^-} = P_2(\omega, z = l_1)|_{l_1^+} \tag{3.69}$$

$$V_{z,1}(\omega, z = l_1)\big|_{l_1^-} = V_{z,2}(\omega, z = l_1)\big|_{l_1^+} \tag{3.70}$$

The "-" subscript denotes evaluation of the acoustic field for the element on the left of side of the interface while the "+" subscript denotes the element on the right side. The form of Equations 3.69 and 3.70 will be dependent on whether the model for an acoustic pipe with or without a wall is utilized. If scaling shows that bulk attenuation is dominant and the pipe model without a wall is utilized, Equations 3.69 and 3.70 become:

$$\left(Ae^{-jkl_1} + Be^{jkl_1}\right)\big|_{l_1^-} = \left(Ce^{-jkl_1} + De^{jkl_1}\right)\big|_{l_1^+} \tag{3.71}$$

$$S\left(Ae^{-jkl_1} - Be^{jkl_1}\right)\big|_{l_1^-} = S\left(Ce^{-jkl_1} - De^{jkl_1}\right)\big|_{l_1^+} \tag{3.72}$$

where amplitude coefficients (A,B,C,D) and area S will in general have different values on each side of the interface. If scaling shows that boundary layer losses are dominant and the pipe model with a wall must be utilized, Equations 3.69 and 3.70 become the following:

$$\left(Ae^{-j\frac{1}{\sqrt{\epsilon}}\frac{\omega_r l_1}{c}} + Be^{j\frac{1}{\sqrt{\epsilon}}\frac{\omega_r l_1}{c}} - \frac{2R_a R_c^2}{EuMa^2}\right)\Bigg|_{l_1^-} = \left(Ce^{-j\frac{1}{\sqrt{\epsilon}}\frac{\omega_r l_1}{c}} + De^{j\frac{1}{\sqrt{\epsilon}}\frac{\omega_r l_1}{c}} - \frac{2R_a R_c^2}{EuMa^2}\right)\Bigg|_{l_1^+} \tag{3.73}$$

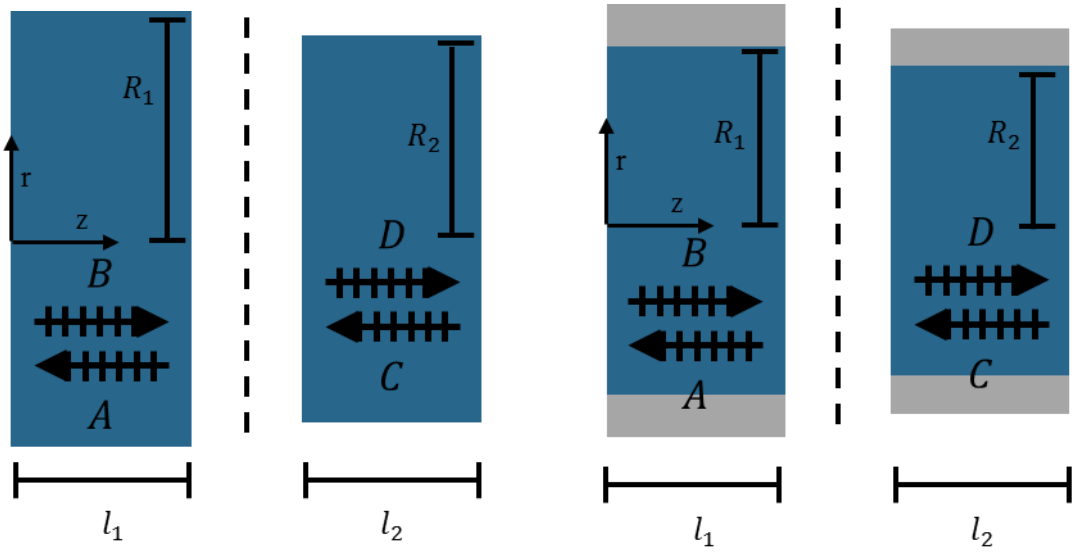

Figure 3.13: Left: Diagram of the discretization of the acoustic pipe without a wall model. Right: Diagram of the discretization of the acoustic pipe with a wall model. Elements in both models are coupled together by matching pressure and volume velocity at the interface between elements.

$$R^2 Ma\left(-j\frac{1}{\sqrt{\epsilon}}Ae^{-j\frac{1}{\sqrt{\epsilon}}\frac{\omega_r l_1}{c}} + j\frac{1}{\sqrt{\epsilon}}Be^{j\frac{1}{\sqrt{\epsilon}}\frac{\omega_r l_1}{c}}\right)$$

$$\int_0^{R^*}\left(-\frac{ber_0(r^*)+jbei_0(r^*)}{bei_0(R^*)-jber_0(R^*)}+j\right)r^*dr^*\Big|_{l_1^-} =$$

$$R^2 Ma\left(-j\frac{1}{\sqrt{\epsilon}}Ce^{-j\frac{1}{\sqrt{\epsilon}}\frac{\omega_r l_1}{c}} + j\frac{1}{\sqrt{\epsilon}}De^{j\frac{1}{\sqrt{\epsilon}}\frac{\omega_r l_1}{c}}\right) \quad 3.74$$

$$\int_0^{R^*}\left(-\frac{ber_0(r^*)+jbei_0(r^*)}{bei_0(R^*)-jber_0(R^*)}+j\right)r^*dr^*\Big|_{l_1^+}$$

By repeating the above coupling between successive discretized pipe elements, a change in cross-sectional area can be modeled. Moreover, as no restrictions have been placed on the way the area changes besides a requiring area changes be small between any two adjacent elements, arbitrary shapes can be accommodated.

3.5 Development of an electro-mechanical model for horn-based ultrasonic atomizers

The structure of the horn-based ultrasonic atomizer cell was previously shown to be composed of three components (Figure 3.3): a planar piezoelectric transducer, an acoustic pipe without a wall, and a horn section. With the development of the component models done in the preceding sections, the appropriate component models must now be selected and joined together via boundary conditions to form a complete electromechanical atomizer model of the ejector. Figure 3.14 describes the atomizer model components and the boundary conditions that are used for coupling them. The planar piezoelectric transducer (A) is modeled with the Mason impedance matrix, and the fluid reservoir (B) is modeled as an acoustic pipe without a wall. As acoustic boundary layer losses will dominate bulk attenuation losses for the majority of working fluids due to low bulk attenuation coefficients and the comparatively low frequencies under consideration, the acoustic horn (C) is modeled as a discretized acoustic pipe with a wall. However, as the WWE with no boundary layer losses is a commonly employed methodology for modeling wall bounded acoustic horns, a second model is also developed where component C is taken as a conical WWE section for the purposes of comparison.

Considering first the atomizer model utilizing the discretized acoustic pipe with a wall model for the horn component (also referred to as the modified Dijksman model for clarity), the boundary condition at the aperture of the acoustic horn is assumed to be a pressure release condition, given by:

$$P_0\left(Ae^{-j\frac{1}{\sqrt{\epsilon}}\frac{\omega_r(l_{res}+l_{horn})}{c}}+Be^{j\frac{1}{\sqrt{\epsilon}}\frac{\omega_r(l_{res}+l_{horn})}{c}}\right)\Big|_{(l_{res}+l_{horn})^-}=0 \qquad 3.75$$

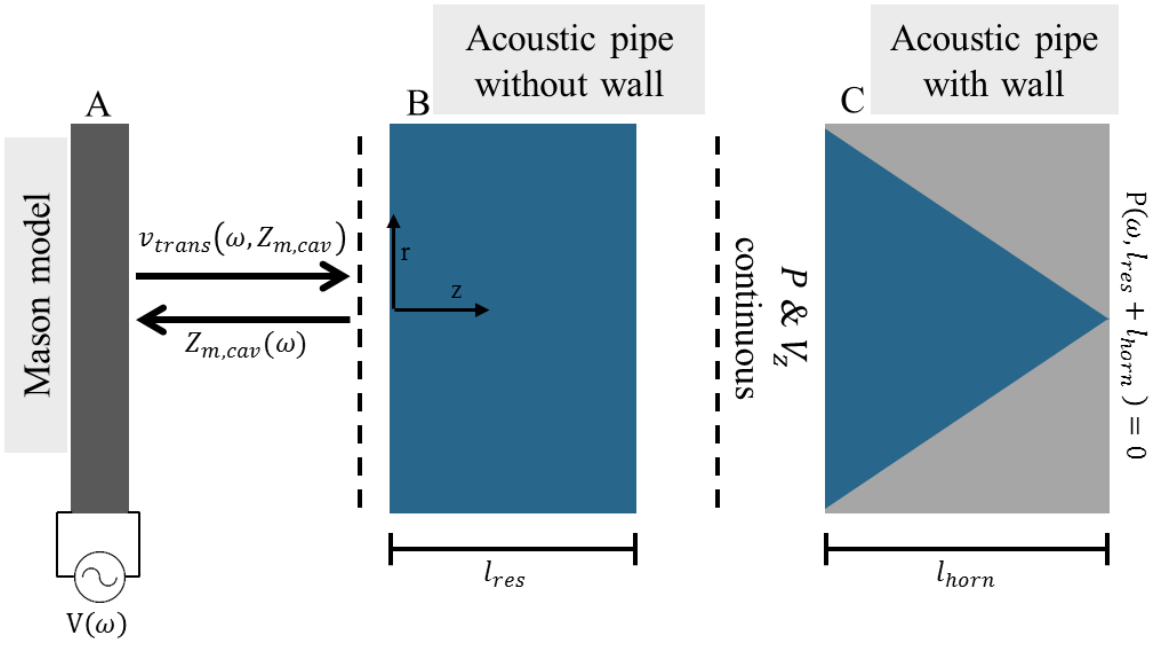

Figure 3.14: A schematic diagram of the ultrasonic atomizer based on the acoustic horn structure and its decomposition into the components used to develop the analytical acoustic models of the atomizer.

The components are coupled by enforcing continuity of pressure and volume velocity at their interfaces. At the interface between components B and C, the coupling condition is given by:

$$\left(Ae^{-jkl_{res}} + Be^{jkl_{res}}\right)\Big|_{l_{res}^-} = P_0\left(Ce^{-j\frac{1}{\sqrt{\epsilon}}\frac{\omega_r l_{res}}{c}} + De^{j\frac{1}{\sqrt{\epsilon}}\frac{\omega_r l_{res}}{c}}\right)\Bigg|_{l_{res}^+} \tag{3.76}$$

$$S\left(Ae^{-jkl_{res}} - Be^{jkl_{res}}\right)\Big|_{l_{res}^-} =$$

$$EuMa(\omega_r w_0 \pi R^2)Ma\left(-j\frac{1}{\sqrt{\epsilon}}Ce^{-j\frac{1}{\sqrt{\epsilon}}\frac{\omega_r l_{res}}{c}} + j\frac{1}{\sqrt{\epsilon}}De^{j\frac{1}{\sqrt{\epsilon}}\frac{\omega_r l_{res}}{c}}\right) \tag{3.77}$$

$$\int_0^{R^*}\left(-\frac{ber_0(r^*) + jbei_0(r^*)}{bei_0(R^*) - jber_0(R^*)} + j\right)r^* dr^*\Bigg|_{l_{res}^+}$$

where Equation 3.76 is the for pressure and Equation 3.77 is for the volume velocity. Coupling the components results in a single fluid cavity with a continuous acoustic field.

The coupling between components A and B again enforces continuity of pressure and volume velocity, formulated in terms of the fluid cavity mechanical impedance. The fluid cavity mechanical impedance is determined by first applying an arbitrary velocity condition at the reservoir inlet surface assuming a perfectly rigid driver. The acoustic pressure within the fluid cavity is then calculated, yielding the pressure at the driving surface corresponding to the arbitrarily imposed velocity. The ratio of these quantities is the cavity impedance which is used as the load on the transducer. The Mason impedance matrix is then used to calculate the velocity at the driving surface based on the cavity acoustic impedance, the properties of the transducer, and the applied voltage. The calculated velocity is then reapplied to the driving surface to obtain an accurate acoustic field for the ejector when driven by the transducer. At the fluid cavity inlet/transducer surface, the coupling condition can be expressed as:

$$Sv_{trans} = S(A - B)|_{0^+} \tag{3.78}$$

$$Z_{m,load}(\omega) = Z_{m,cav}(\omega) \tag{3.79}$$

with Equation 3.78 being continuity of volume velocity and Equation 3.79 being the impedance matching condition. The following conditions are associated with the piezoelectric transducer:

$$V(\omega) = V_{applied}(\omega) \tag{3.80}$$

$$Z_{m,load}(\omega) = Z_{m,cav}(\omega) \tag{3.81}$$

where $V_{applied}$is the voltage applied to the transducer.

The model applying the WWE for the acoustic horn differs only in the form of the equations at the aperture pressure release condition:

$$Ae^{-jkl_{apex}} + Be^{jkl_{apex}}\big|_{l_{apex}{}^-} = 0 \tag{3.82}$$

and similarly at the interface between components B and C:

$$\left(Ae^{-jkl_{res}} + Be^{jkl_{res}}\right)\big|_{l_{res}{}^-} =$$

$$= \left(-\frac{j\omega\rho C}{l_{horn} + l_{apex}} \mathrm{e}^{-\mathrm{j}k(l_{horn}+l_{apex})} \right. \tag{3.83}$$

$$\left. -\frac{j\omega\rho D}{l_{horn} + l_{apex}} \mathrm{e}^{\mathrm{j}k(l_{horn}+l_{apex})} \right)\Bigg|_{l_{res}{}^+}$$

$$S\left(Ae^{-jkl_{res}} - Be^{jkl_{res}}\right)\big|_{l_{res}{}^-}$$

$$= \left(-\frac{S\left(1 + jk\left(l_{horn} + l_{apex}\right)\right)C}{\left(l_{horn} + l_{apex}\right)^2} \mathrm{e}^{-\mathrm{j}k(l_{horn}+l_{apex})} \right. \tag{3.84}$$

$$\left. -\frac{S\left(1 - jk\left(l_{horn} + l_{apex}\right)\right)D}{\left(l_{horn} + l_{apex}\right)^2} \mathrm{e}^{\mathrm{j}k(l_{horn}+l_{apex})} \right)\Bigg|_{l_{res}{}^+}$$

The position of the interface for the WWE horn has been modified to account for the change of the coordinate system for the horn, locating the origin at the horn apex rather than the entrance to the fluid reservoir. The transducer, fluid reservoir, and solution methodology parallel those of the modified Dijksman model.

3.5.1 Model validation

The ability of the atomizer models to accurately capture the acoustics of horn-based ultrasonic atomization was tested by comparing model predictions to finite element based simulations implemented in ANSYS.[116] ANSYS is able to simulate the wave propagation in the fluid cavity as well as the behavior of the piezoelectric transducer in a single coupled computational domain. ANSYS has been previously shown to capture ultrasonic atomizer operation with a high degree of accuracy.[3] The fluid cavity

resonance frequencies, electrical input impedance of the piezoelectric transducer, and acoustic field characteristics are compared against ANSYS to determine if the analytical models accurately predict atomizer behavior.

ANSYS simulations were limited to a single, two-dimensional axisymmetric cell as shown in Figure 3.14. The domain is comprised of a 1.5mm thick piezoelectric transducer (APC International 855 material) with Plane13 elements driven by 10V peak AC signal. The fluid cavity is implemented as Fluid79 elements. Fluid79 is a secondary acoustic fluid element that incorporates bulk attenuation loss but does not accurately model the acoustic boundary layer. Element shape is constrained to rectangular with two displacement degrees of freedom requiring fine discretization of any sloped surfaces to minimize numerical error. The horn is treated as acoustically lossless silicon having a Young's Modulus of 150 GPa, a Poisson's ratio of 0.21, and a density of 2330 kg/m^3 with Plane183 as the element type. The fluid reservoir was taken to be 2.1mm in height, coupled to 0.5mm horn with a 725 micrometer entrance and 50 micron aperture diameter which is a typical device geometry used in experiments.[3, 59] The exterior boundary of the computational domain is subjected to the symmetry boundary condition, recognizing that this condition only approximates the condition in an array of multiple cells. Further details regarding the ANSYS simulation can be found in Appendix B. These parameters are replicated as closely as possible in the analytical models.

Table 3.1 compares fluid cavity resonance frequencies between the analytical models and ANSYS for water. Fluid cavity resonance was defined as the frequency which corresponded to the peak pressure gradient a nozzle radius away from the aperture, generally consistent with the short circuit resonance frequency of the piezoelectric

Table 3.1: A comparison of the fluid cavity resonant frequencies predicted by the modified Dijksman, WWE, and ANSYS models for water as the working fluid.

Mode number	Modified Dijksman	WWE		ANSYS	
	Frequency (kHz)	Frequency (kHz)	Error (%)	Frequency (kHz)	Error (%)
0	62	72	16.1	60	3.3
1	333	340	2.1	338	1.5
2	647	654	1.1	656	1.4
3	958	966	0.8	965	0.7

transducer. Agreement between the modified Dijksman and ANSYS models across all resonant modes is generally good with error at or less than 1.5%. The large error at the zeroth order mode is due to the behavior of the Fluid79 element at low frequencies; below 100kHz, the element begins to incorrectly account for fluid mass and, at sufficiently low frequencies, produces large numerical error manifest as a discontinuous acoustic field between numerical elements. The WWE model shows a much greater discrepancy at the zeroth order mode as compared to the constrained horn model; this results from the difference in the fluid cavity impedance caused by the lack of spatial dispersion introduced by the wall compliance which is ignored in the WWE model.

The electrical behavior of the transducer can be determined by examining the electric input impedance as given in Figure 3.15. The electrical impedance was calculated by imposing a constant voltage across the transducer and sweeping the frequency from 100 kHz to 1 MHz. All the models agree closely across the frequency spectrum with the main discrepancies occurring near the fluid cavity resonances. Both the WWE and ANSYS models show a slight frequency offset from the modified Dijksman model as well as a difference in the predicted magnitude. While the shift in fluid cavity

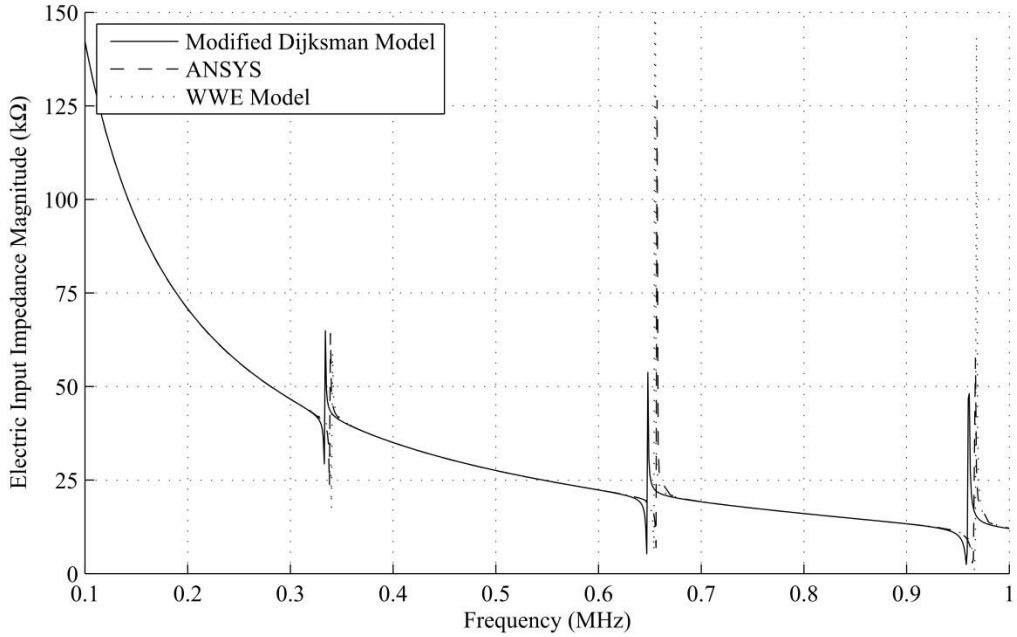

Figure 3.15: The magnitude of the electrical input impedance as predicted by the modified Dijksman, WWE, and ANSYS models with water as the working fluid.

resonance is determined by the boundary layer viscous loss mechanism and wall compliance incorporated only into the modified Dijksman model, the difference in the magnitude of the electrical input impedance results from the sensitivity of the model near the fluid cavity resonances to the transducer behavior. The models each predict similar fluid cavity mechanical impedances but, due to the difference in the operating frequency, the transducer response varies significantly. The shift in the fluid cavity resonance frequency is thus accentuated and produces the difference in the electrical impedance amplitude.

Predictive capabilities of the constrained horn model were investigated by plotting the pressure amplitude along the centerline of the atomizer, shown in Figure 3.16 for 500 kHz in water as a function of distance from the transducer surface. At this frequency, the predicted electrical impedance magnitudes of the models coincide, and the pressure field of the analytical models and ANSYS closely agree. As the considered frequency moves

toward one of the fluid cavity resonances, the magnitude of the electrical impedance begins to differ and the pressure field has less agreement. Figure 3.17 shows this for first order fluid cavity resonance of water. To reduce the effect of sampling frequencies at differing resonance qualities, the resonant frequency for each model was determined to the nearest Hertz. At the first order cavity resonance, the modified Dijksman model underestimates the ANSYS prediced amplitude by a factor of two. This discrepancy results in part from the difference in the quality factor at the sampled frequency for each model, with the ANSYS model sampling a point with a greater quality factor than the modified Dijksman model. The transducer in the ANSYS model therefore transfers more energy to the fluid cavity than the modified Dijksman model, producing a higher pressure amplitude. The discrepancy also results in part from ANSYS lacking the dominant source of viscous dissipation through the acoustic boundary layer. The amplitude of the ANSYS acoustic field will therefore always overstate the amplitude of the modified Dijksman model all else being equal. While the matching of quality factors issue can be partly eliminated by increasing the sampling resolution near the fluid cavity resonances, the computational time associated with the ANSYS model prohibits increasing the frequency resolution indefinitely. Understanding that a discrepancy may occur near the fluid cavity resonances for low viscosity liquids is necessary for application of the modified Dijksman model to such working fluids.

As the viscosity of the working fluid is increased, the effect of the quality factor variation on the pressure field is lessened due to the viscous damping in the device. Figure 3.18 shows the predicted electrical input impedance for glycerol as a working fluid. The additional viscous damping in the system reduces the quality factor of the fluid

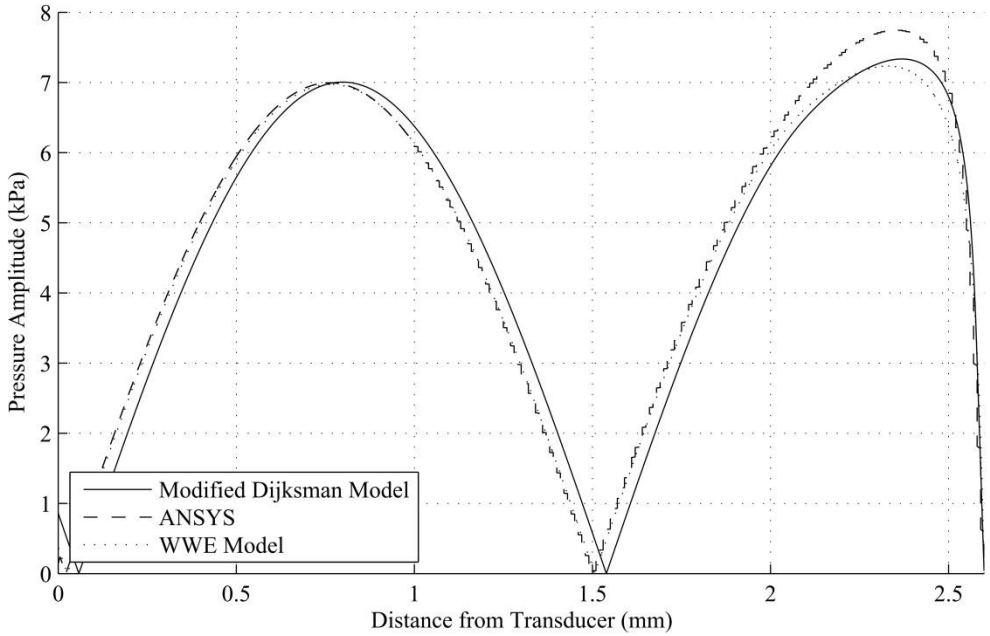

Figure 3.16: A comparison of the pressure amplitude along the atomizer axis as predicted by the modified Dijksman, WWE, and ANSYS models for 500kHz in water as a function of the distance from the transducer surface. The amplitude of the voltage signal applied to the transducer was 10V.

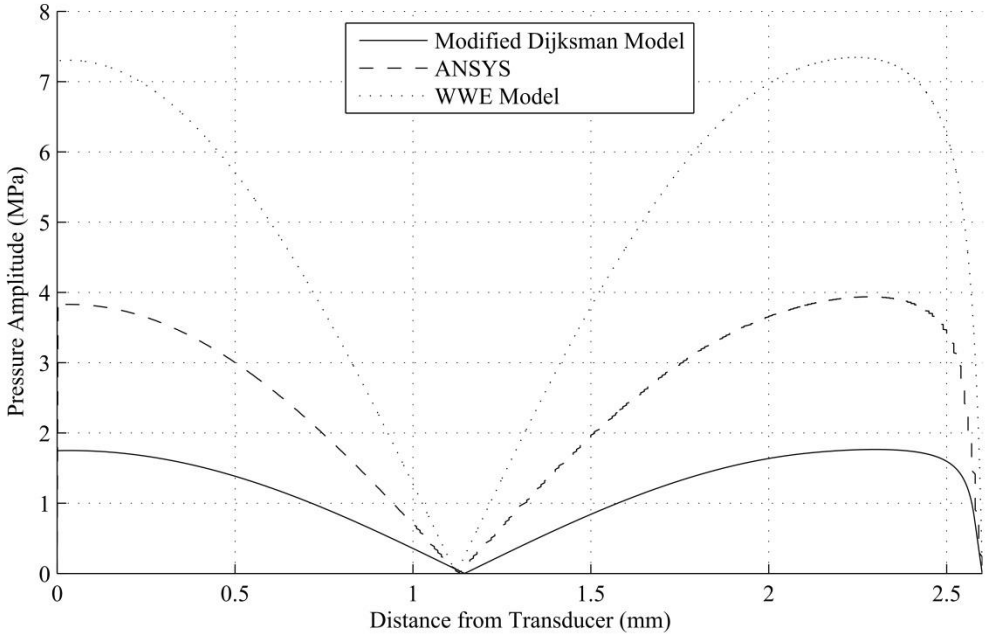

Figure 3.17: A comparison of the pressure amplitude along the atomizer axis as predicted by the modified Dijksman, WWE, and ANSYS models for the first order cavity resonance mode in water as a function of the distance from the transducer surface. The amplitude of the voltage signal applied to the transducer was 10V. The frequencies for each model are as given in Table 3.1.

cavity resonances for the modified Dijksman and ANSYS models while that of the WWE model continues to remain relatively large. The reduction in the quality factor translates into better agreement in the pressure field as seen in Figure 3.19 for glycerol at the first order cavity resonance. While a small difference in the fluid cavity resonance frequency exists, the predicted pressure field of the modified Dijksman and ANSYS models agree closely. Moreover, the modified Dijksman model predicts the ANSYS distribution with much better accuracy than the WWE model. While part of the disagreement between analytical models is undoubtedly related to the difference in dimensionality and the inclusion of acoustic boundary layer losses, the combination of the wall compliance (captured by ANSYS) and radial viscous losses (not captured by ANSYS) clearly dominate the behavior of the atomizer and must be included in any analytical model. Furthermore, the pressure gradient magnitude at the horn aperture, which is a critical parameter for fluid ejection, is not very accurately determined by ANSYS due to finite discretization of the acoustic field near the nozzle. In contrast, the modified Dijksman model provides a consistent and continuous pressure variation to calculate this quantity. The modified Dijksman model therefore provides a new tool for understanding the effect of geometry, working fluid, and transducer properties on the acoustic field of horn-based ultrasonic atomizers when the radial component of the viscous stress is of greater magnitude than the axial component, thereby precluding the use of the WWE modeling framework.

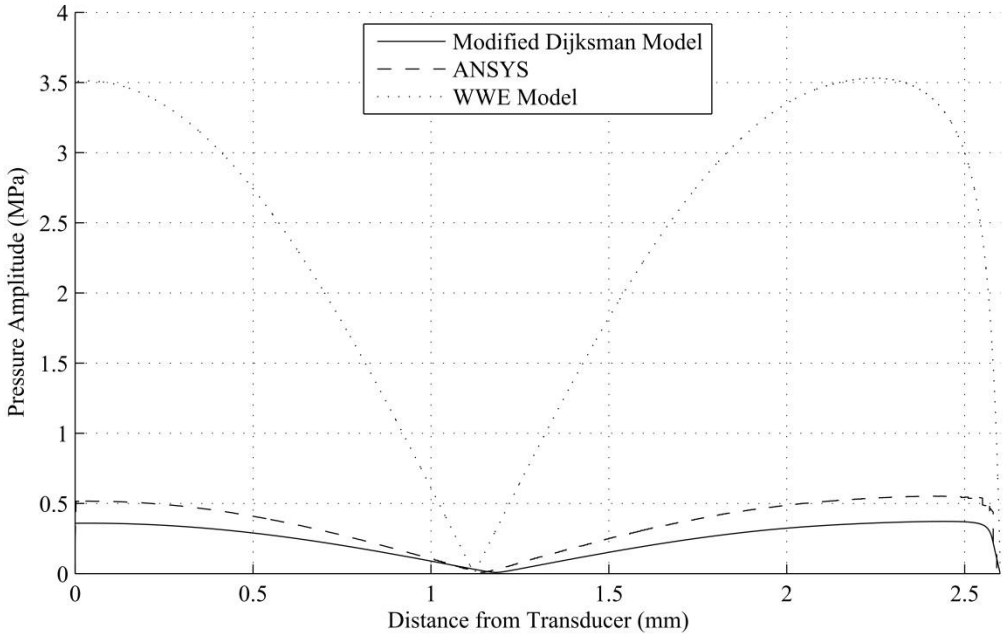

Figure 3.18: The magnitude of the electrical input impedance as predicted by the modified Dijksman, WWE, and ANSYS models with glycerol as the working fluid.

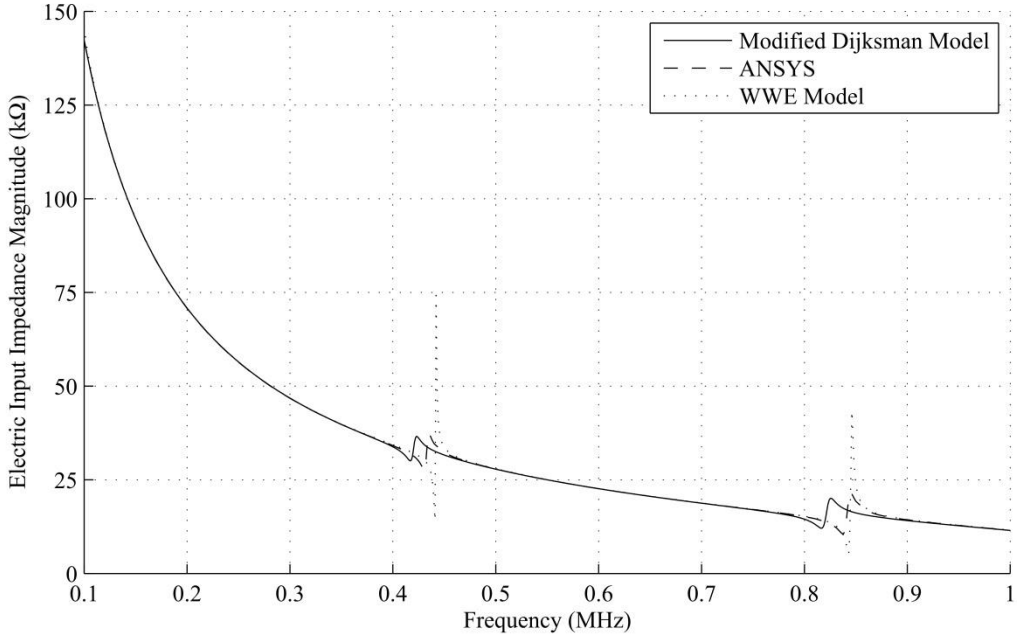

Figure 3.19: A comparison of the pressure amplitude along the atomizer axis as predicted by the modified Dijksman, WWE, and ANSYS models for the first order cavity resonance mode in glycerol as a function of the distance from the transducer surface. The amplitude of the voltage signal applied to the transducer was 10V.

3.6 Development of an electro-mechanical model for squeeze type inkjets

The structure of the squeeze ejector was previously shown to be comprised of five components (Figure 3.4): an annular piezoelectric transducer, an acoustic pipe with a confining wall, a driven acoustic pipe with a confining wall, and a horn section. Using the component models developed in previous sections, the appropriate models must now be selected and coupled together via boundary conditions to form a complete electromechanical squeeze ejector model. Figure 3.20 describes the squeeze ejector model components and the boundary conditions used to couple them. The annular piezoelectric transducer (A) is modeled with the Liang impedance matrix, tube sections B and D are modeled as an acoustic pipe with a wall, and tube section C is modeled as an acoustic pipe with a wall surrounded by the annular piezoelectric transducer in component A. The acoustic horn (E) is modeled as a discretized acoustic pipe with a wall.

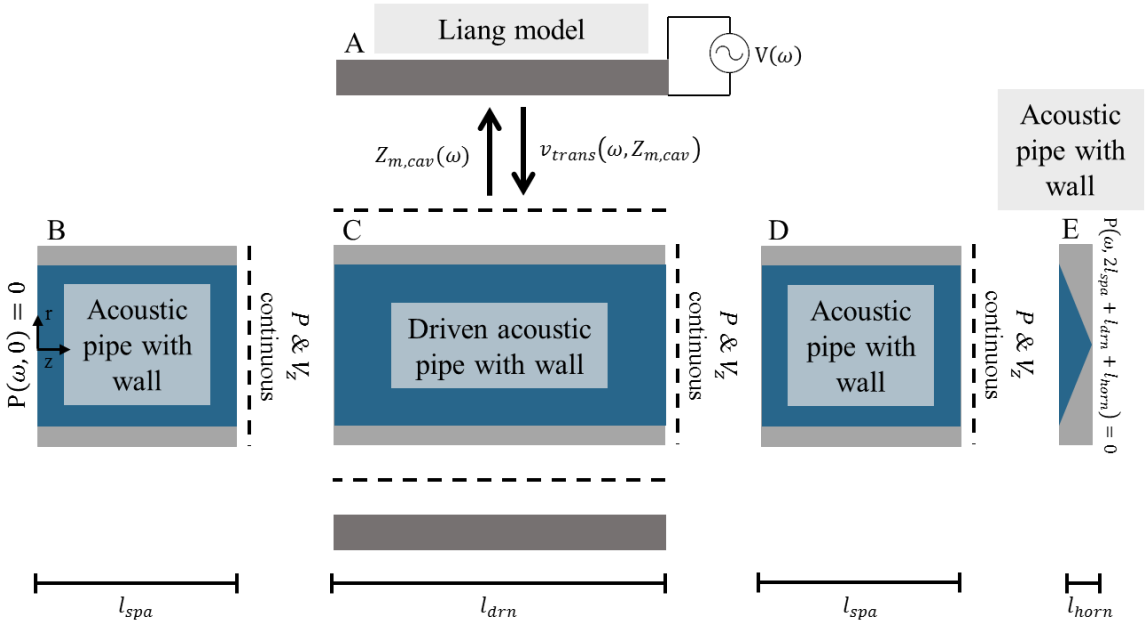

Figure 3.20: A decomposition of the squeeze ejector into the basic components utilized for developing an analytical model.

At the aperture of the acoustic horn, a pressure release condition is assumed given by:

$$P_0\left(Ae^{-j\frac{1}{\sqrt{\epsilon}}\frac{\omega_r(2l_{spa}+l_{drn}+l_{horn})}{c}}+Be^{j\frac{1}{\sqrt{\epsilon}}\frac{\omega_r(2l_{spa}+l_{drn}+l_{horn})}{c}}\right)\Big|_{(2l_{spa}+l_{drn}+l_{horn})^-} \quad 3.85$$

$$= 0$$

Similarly, inlet of component B is also taken as a pressure release with the acoustic pressure set to zero:

$$0 = P_0(A_+ + B_+)|_{0^+} \quad 3.86$$

The mean pressure imposed by the fluid reservoir at the left side of component B is assumed to be uniform over the extent of the ejector and thus has no effect on the acoustic analysis. The interfaces between components are coupled by enforcing continuity of pressure and volume velocity at their interfaces. At the interface between components B and C, the coupling condition is given by:

$$P_0\left(Ae^{-j\frac{1}{\sqrt{\epsilon}}\frac{\omega_r l_{spa}}{c}}+Be^{j\frac{1}{\sqrt{\epsilon}}\frac{\omega_r l_{spa}}{c}}\right)\Big|_{l_{spa}^-}$$

$$= P_0\left(Ce^{-j\frac{1}{\sqrt{\epsilon}}\frac{\omega_r l_{spa}}{c}}+De^{j\frac{1}{\sqrt{\epsilon}}\frac{\omega_r l_{spa}}{c}}-\frac{2R_aR_c^2}{EuMa^2}\right)\Big|_{l_{spa}^+} \quad 3.87$$

$$EuMa(\omega_r w_0 \pi R^2)Ma\left(-j\frac{1}{\sqrt{\epsilon}}Ae^{-j\frac{1}{\sqrt{\epsilon}}\frac{\omega_r l_{spa}}{c}}+j\frac{1}{\sqrt{\epsilon}}Be^{j\frac{1}{\sqrt{\epsilon}}\frac{\omega_r l_{spa}}{c}}\right)$$

$$\int_0^{R^*}\left(-\frac{ber_0(r^*)+jbei_0(r^*)}{bei_0(R^*)-jber_0(R^*)}+j\right)r^*dr^*\Big|_{l_{spa}^-} \quad 3.88$$

$$= EuMa(\omega_r w_0 \pi R^2)Ma\left(-j\frac{1}{\sqrt{\epsilon}}Ce^{-j\frac{1}{\sqrt{\epsilon}}\frac{\omega_r l_{spa}}{c}}+j\frac{1}{\sqrt{\epsilon}}De^{j\frac{1}{\sqrt{\epsilon}}\frac{\omega_r l_{spa}}{c}}\right)$$

$$\int_0^{R^*}\left(-\frac{ber_0(r^*)+jbei_0(r^*)}{bei_0(R^*)-jber_0(R^*)}+j\right)r^*dr^*\Big|_{l_{spa}{}^+}$$

with Equation 3.87 being the condition on the pressure and Equation 3.88 being the condition on volume velocity. As component C is driven with a squeeze displacement, the driving term must be retained in Equation 3.87. Similar coupling conditions can be written between components C and D:

$$P_0\left(Ae^{-j\frac{1}{\sqrt{\epsilon}}\frac{\omega_r(l_{spa}+l_{drn})}{c}}+Be^{j\frac{1}{\sqrt{\epsilon}}\frac{\omega_r(l_{spa}+l_{drn})}{c}}-\frac{2R_aR_c^2}{EuMa^2}\right)\Big|_{(l_{spa}+l_{drn})^-}$$
$$=P_0\left(Ce^{-j\frac{1}{\sqrt{\epsilon}}\frac{\omega_r(l_{spa}+l_{drn})}{c}}+De^{j\frac{1}{\sqrt{\epsilon}}\frac{\omega_r(l_{spa}+l_{drn})}{c}}\right)\Big|_{(l_{spa}+l_{drn})^+} \quad 3.89$$

$$EuMa(\omega_r w_0\pi R^2)Ma\left(-j\frac{1}{\sqrt{\epsilon}}Ae^{-j\frac{1}{\sqrt{\epsilon}}\frac{\omega_r(l_{spa}+l_{drn})}{c}}+j\frac{1}{\sqrt{\epsilon}}Be^{j\frac{1}{\sqrt{\epsilon}}\frac{\omega_r(l_{spa}+l_{drn})}{c}}\right)$$
$$\int_0^{R^*}\left(-\frac{ber_0(r^*)+jbei_0(r^*)}{bei_0(R^*)-jber_0(R^*)}+j\right)r^*dr^*\Big|_{(l_{spa}+l_{drn})^-}= \quad 3.90$$
$$EuMa(\omega_r w_0\pi R^2)Ma\left(-j\frac{1}{\sqrt{\epsilon}}Ce^{-j\frac{1}{\sqrt{\epsilon}}\frac{\omega_r(l_{spa}+l_{drn})}{c}}+j\frac{1}{\sqrt{\epsilon}}De^{j\frac{1}{\sqrt{\epsilon}}\frac{\omega_r(l_{spa}+l_{drn})}{c}}\right)$$
$$\int_0^{R^*}\left(-\frac{ber_0(r^*)+jbei_0(r^*)}{bei_0(R^*)-jber_0(R^*)}+j\right)r^*dr^*\Big|_{(l_{spa}+l_{drn})^+}$$

as well as between D and E:

$$P_0\left(Ae^{-j\frac{1}{\sqrt{\epsilon}}\frac{\omega_r(2l_{spa}+l_{drn})}{c}}+Be^{j\frac{1}{\sqrt{\epsilon}}\frac{\omega_r(2l_{spa}+l_{drn})}{c}}\right)\Big|_{(2l_{spa}+l_{drn})^-}$$
$$=P_0\left(Ce^{-j\frac{1}{\sqrt{\epsilon}}\frac{\omega_r(2l_{spa}+l_{drn})}{c}}+De^{j\frac{1}{\sqrt{\epsilon}}\frac{\omega_r(2l_{spa}+l_{drn})}{c}}\right)\Big|_{(2l_{spa}+l_{drn})^+} \quad 3.91$$

$$EuMa(\omega_r w_0 \pi R^2)Ma\left(-j\frac{1}{\sqrt{\epsilon}}Ae^{-j\frac{1}{\sqrt{\epsilon}}\frac{\omega_r(2l_{spa}+l_{drn})}{c}}+j\frac{1}{\sqrt{\epsilon}}Be^{j\frac{1}{\sqrt{\epsilon}}\frac{\omega_r(2l_{spa}+l_{drn})}{c}}\right)$$

$$\int_0^{R^*}\left(-\frac{ber_0(r^*)+jbei_0(r^*)}{bei_0(R^*)-jber_0(R^*)}+j\right)r^*dr^*\Big|_{(2l_{spa}+l_{drn})^-}=$$

$$EuMa(\omega_r w_0 \pi R^2)Ma\left(-j\frac{1}{\sqrt{\epsilon}}Ce^{-j\frac{1}{\sqrt{\epsilon}}\frac{\omega_r(2l_{spa}+l_{drn})}{c}}+j\frac{1}{\sqrt{\epsilon}}De^{j\frac{1}{\sqrt{\epsilon}}\frac{\omega_r(2l_{spa}+l_{drn})}{c}}\right) \quad 3.92$$

$$\int_0^{R^*}\left(-\frac{ber_0(r^*)+jbei_0(r^*)}{bei_0(R^*)-jber_0(R^*)}+j\right)r^*dr^*\Big|_{(2l_{spa}+l_{drn})^+}$$

Coupling the components results in a single fluid cavity with a continuous acoustic field.

The coupling between components A and C again enforces continuity of pressure and volume velocity, formulated in terms of the fluid cavity mechanical impedance. The fluid cavity mechanical impedance is determined by first applying an arbitrary velocity condition on the exterior tube surface assuming a perfectly rigid driver. The acoustic pressure within the fluid cavity is then calculated, yielding the pressure at the interior wall surface corresponding to the arbitrarily imposed velocity. The mean pressure and radial particle velocity are calculated at the interface of the fluid cavity and glass wall by averaging Equations 3.61 and 3.30 along the length of component C. The ratio of these quantities is the cavity impedance which is used as the load on the transducer as the stress and strain are assumed to be uniform across the tube wall. The Liang impedance matrix is then used to calculate the velocity and pressure at the inner transducer surface based on the fluid cavity acoustic impedance, the properties of the transducer, and the applied voltage. The calculated velocity is then reapplied as the driving velocity to obtain an accurate acoustic field for the ejector when driven by the transducer. At the interface between the glass tube and transducer, the coupling condition can be expressed as:

$$v_{trans}(\omega) = \frac{dd}{dt}(\omega) \quad 3.93$$

$$Z_{m,load}(\omega) = Z_{m,cav}(\omega) \quad 3.94$$

with Equation 3.93 being continuity of volume velocity and Equation 3.94 being the impedance matching condition. The following conditions are associated with the piezoelectric transducer:

$$V(\omega) = V_{applied}(\omega) \quad 3.95$$

$$Z_{m,load}(\omega) = Z_{m,cav}(\omega) \quad 3.96$$

where $V_{applied}$ is the voltage applied to the transducer.

3.6.1 Model validation

The ability of the analytical model to accurately capture the acoustics of squeeze type ejectors was evaluated by comparing model predictions to finite element based simulations implemented in ANSYS.[116] ANSYS is able to simulate the wave propagation in the fluid cavity as well as the behavior of the piezoelectric transducer in a single coupled computational domain. ANSYS simulations were limited to the axisymmetric domain as shown in Figure 3.20. The domain is comprised of a 100 μm thick piezoelectric transducer (APC International 855) with Plane13 elements driven by 1V peak AC signal. The fluid cavity is implemented as lossless Fluid29 elements. The glass is treated as a material having a Young's Modulus of 150 GPa, a Poisson's ratio of 0.21, and a density of 2500 kg/m^3 with Plane183 as the element type. The fluid reservoir was taken to be 500 μm in diameter a 1.5 mm in length, composed of a 1 mm central driving section with a 250 μm undriven section on each end so as to minimize the size of the computational domain while maintaining realistic dimensions of physical ejectors.

The exterior boundaries of the fluid cavity were taken as pressure release with stress free conditions on the remainder of the ejector exterior. Further details regarding the ANSYS simulation can be found in Appendix B. These parameters are replicated as closely as possible in the analytical model.

Figures 3.21 through 3.22 give the predicted pressure and velocity amplitudes on the interior surface of the glass tube for the squeeze ejector and ANSYS models. In general, the pressure predicted by the models agree to within a factor of two. The same holds for the velocity except for the lowest investigated frequency at 10 kHz. At this frequency, the ejector model predicts a constant axial velocity due to the long wavelength in the fluid cavity while ANSYS predicts a distribution with a significant amplitude reduction near the ends of the driven segment. This discrepancy is a product of the assumptions built into the models. The ejector model coupled with the Liang impedance matrix formulation assumes that the transducer is axially infinite, meaning axial motion is not permitted in either the transducer or the glass. In the ANSYS model, the piezoelectric transducer has a finite length which introduces an axial response to the transducer. The amount of axial deformation predicted by ANSYS at the ends of the transducer is particularly significant as the transducer looks less one-dimensional as compared to the transducer center. Moreover, the introduction of axial resonances can significantly alter the transducer behavior as compared to the Liang formulation, particularly at low frequencies where axial resonances will be dominant. Understanding that a discrepancy may occur at low operating frequencies due to the geometric differences between models is necessary for application of the model to squeeze type ejectors.

In addition to the geometric considerations given to the squeeze type ejector utilized by Bogy and Talke, a key reason for its selection as the basis of the squeeze type model was the availability of experimental data for validation.[2] Bogy and Talke measured the deformation of the meniscus for the squeeze type ejector pictured in Figure 3.24 at the ejector aperture as a function of time for various ejector lengths, data for which is reproduced in Figure 3.25. Confirmation of the modeling methodology is possible by comparing the displacement at the ejector aperture predicted by the squeeze ejector model to the experimental data. However, the comparison is complicated by the fact that no data regarding the transducer thickness is reported in reference [2] and ejector diameters are not stated other than at the aperture. Selection of the unknown ejector parameters was informed by currently available components and tuned such that the model reproduced the experimental results.

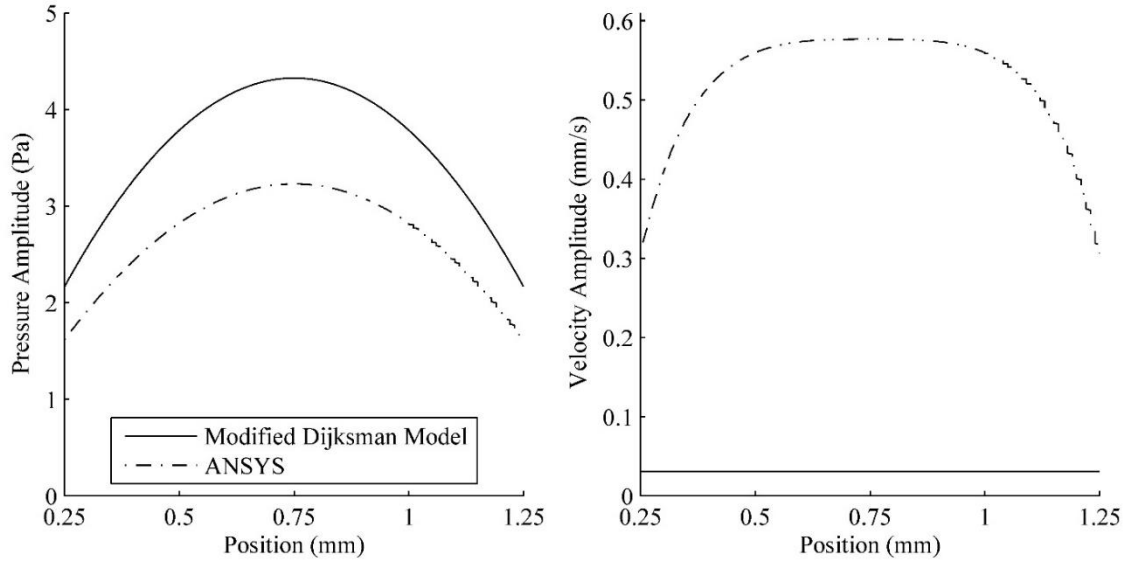

Figure 3.21: Comparison of the predicted pressure and axial velocity magnitudes on the inner glass tube surface of the squeeze ejector model when driving the piezoelectric transducer with sinusoidal 1V amplitude voltage signal at 10kHz. Glycol was utilized as the working fluid.

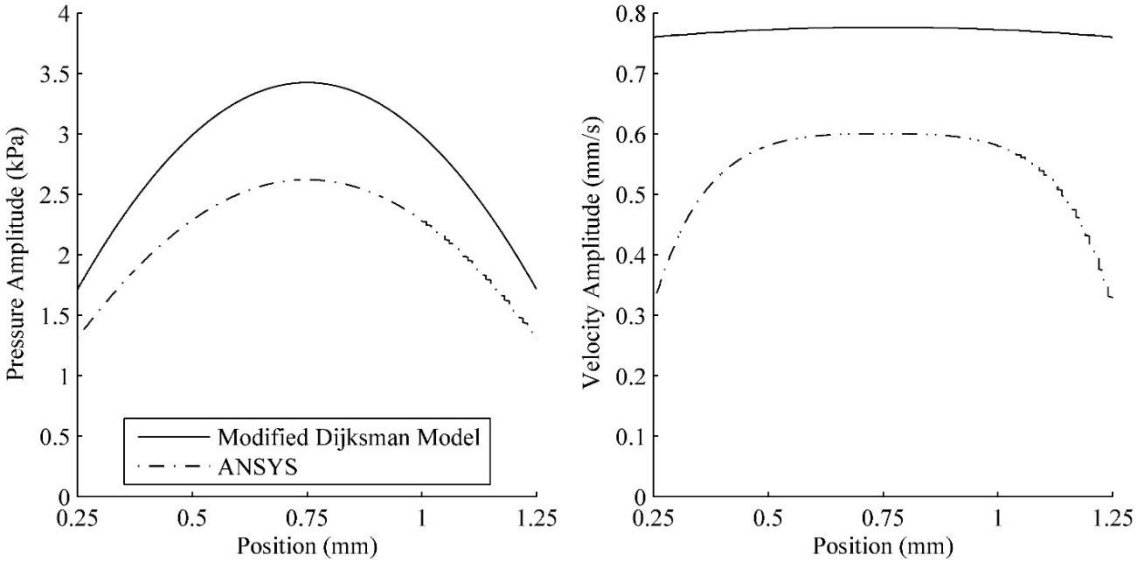

Figure 3.22: Comparison of the predicted pressure and axial velocity magnitudes on the inner glass tube surface of the squeeze ejector model when driving the piezoelectric transducer with sinusoidal 1V amplitude voltage signal at 250kHz. Glycol was utilized as the working fluid.

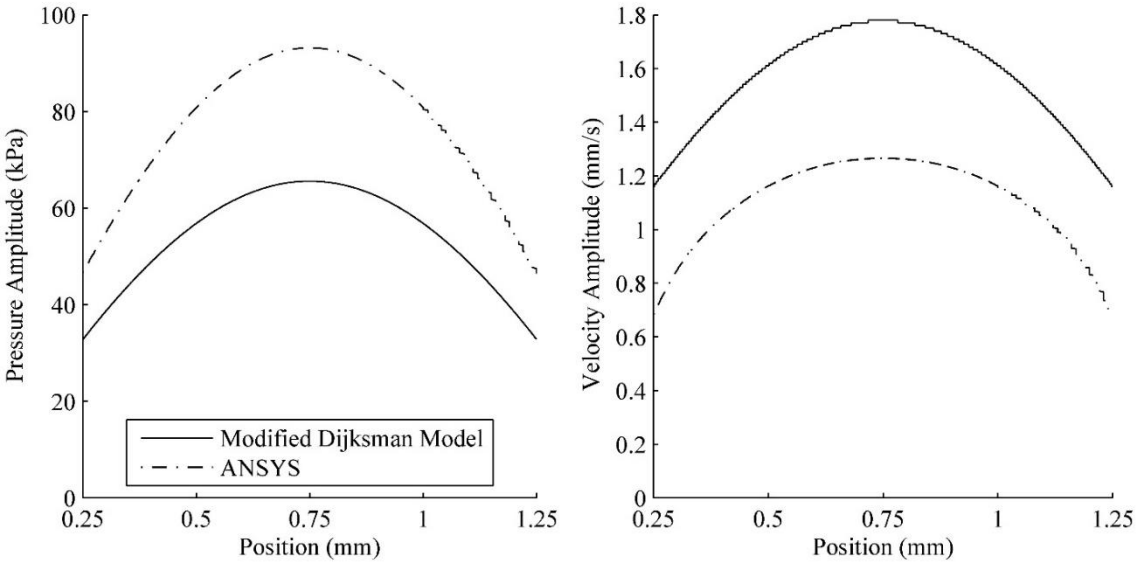

Figure 3.23: Comparison of the predicted pressure and axial velocity magnitudes on the inner glass tube surface of the squeeze ejector model when driving the piezoelectric transducer with sinusoidal 1V amplitude voltage signal at 500kHz. Glycol was utilized as the working fluid.

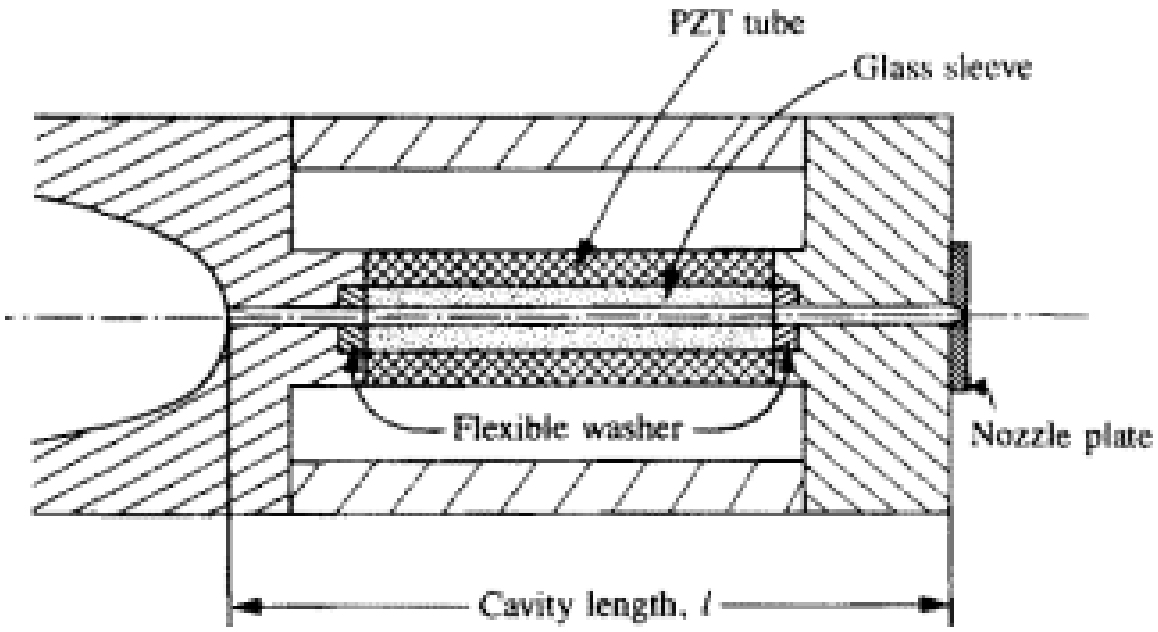

Figure 3.24: The squeeze ejector geometry as investigated by Bogy and Talke.[2] The device consists of a glass tube surrounded by an annular piezoelectric transducer connected to undriven tube segments on either side. The tube opens to the environment through a nozzle plate on the right and to a large fluid reservoir on the left.

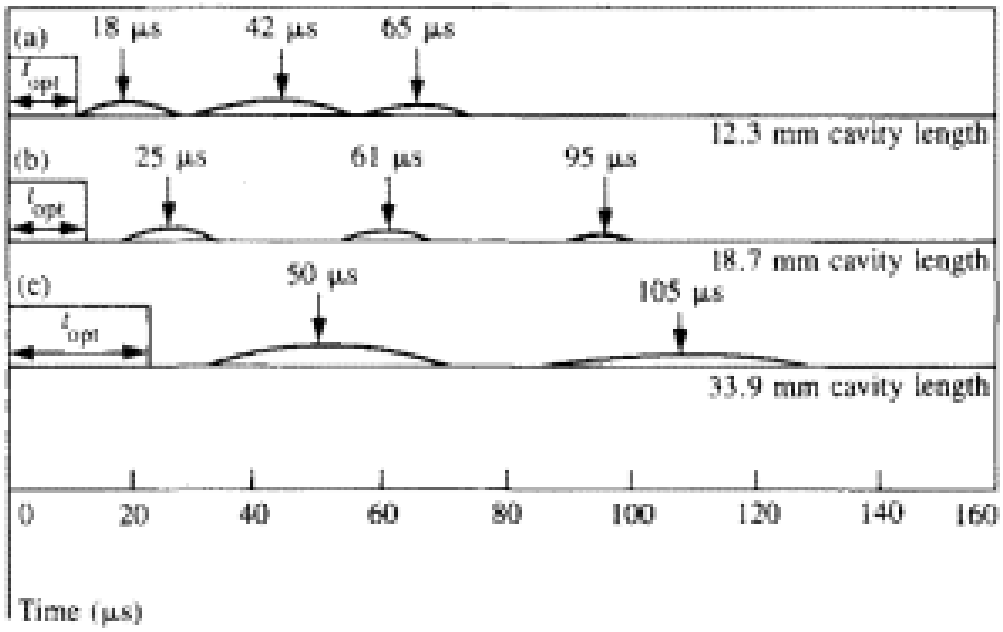

Figure 3.25: Meniscus displacement at the ejector aperture as measured by Bogy and Talk for squeeze ejectors of various lengths. The duration of driving pulse for each geometry is indicated at the left[2]

Table 3.2: The driving pulse parameters used by Bogy and Talke for squeeze type ejectors of varying lengths.[2]

Ejector Total Length (mm)	Transducer Length (mm)	Time on Peak (μm)	Peak Voltage (V)
12.3		8.2	12.7
18.7		11.8	8.5
33.9		22.4	4.5

Figure 3.26 shows the prediction of the squeeze model for the three geometries and driving conditions given by Bogy and Talke. The values not explicitly specified in reference [2] were taken to be an inner tube diameter of 1 mm, an outer tube diameter of 2 mm, and a transducer outer diameter of 3 mm. These dimensions are feasible when considering small tubes. The spacer length was taken as 3mm with a horn length of 100 μm. The time-dependent meniscus displacement was calculated by imposing a time-dependent voltage signal on the transducer analogous in shape to the square pulse voltage applied by Bogy and Talke. Both the time on peak and the peak voltage of the signal were adjusted to be equivalent to the values used experimentally for each ejector length which are provided in Table 3.2. The Fourier transform of the applied voltage was then taken assuming a repeat rate of 1000 Hz, and the squeeze model solved for each frequency component up to 300 kHz. Additional frequencies above 300 kHz were not necessary to obtain a converged solution. The meniscus displacement was calculated by taking the inverse Fourier transform of the velocity at the element nearest to the aperture which was subsequently integrated to obtain the displacement as a function of time. As Figure 3.26 demonstrates, the squeeze model resolves the first peak in the meniscus displacement particularly well. In subsequent peaks, the error between the experimental and model prediction grows due to two main effects. First, as the Liang impedance

matrix formulation used for the transducer predicts a hoop resonance higher in frequency than that of actual devices, the transducer stimulates the higher frequencies of the fluid cavity associated with shorter wavelengths. The increased amplitude of the higher frequency components in the fluid cavity response directly yields a reduction in the period between peaks in the meniscus displacement as the mean wavelength is shorter in the fluid cavity. Secondly, as the transducer becomes a larger fraction of the ejector length, the change in the wall elasticity due to the presence of the transducer becomes more important to wave propagation in the fluid cavity, a factor which is currently neglected as only the glass elasticity is considered. Despite these effects, the first several

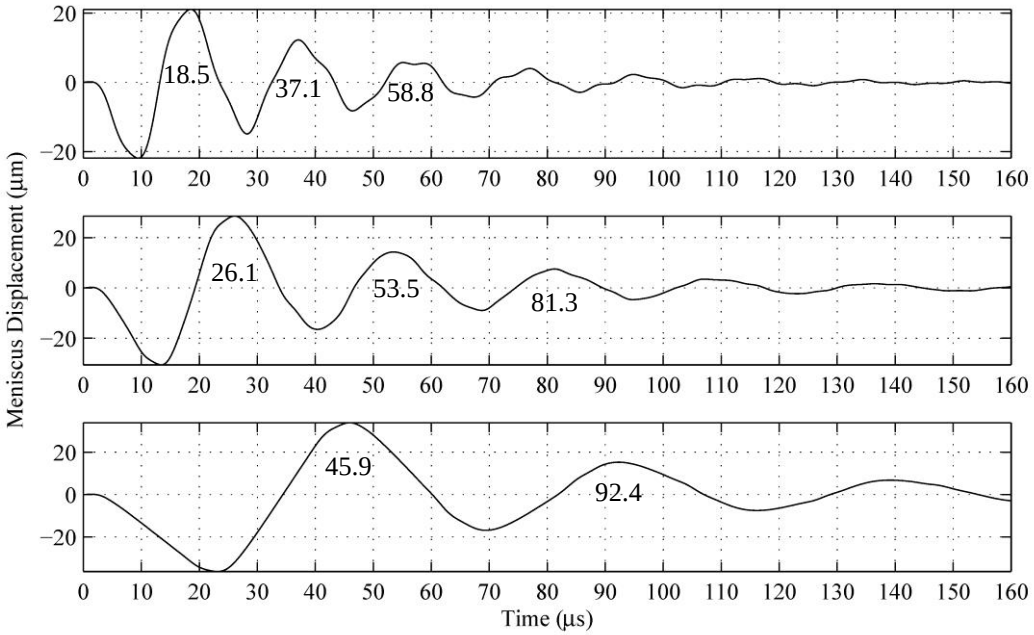

Figure 3.26: Model result corresponding to the conditions of the Bogy and Talke experiment which measured meniscus displacement in various ejector operating configurations. The tube inner diameter was taken to be 1 mm with an outer diameter of 2 mm. The transducer outer diameter was taken as 3 mm. The time in μm at which the first several peaks occur is indicated.

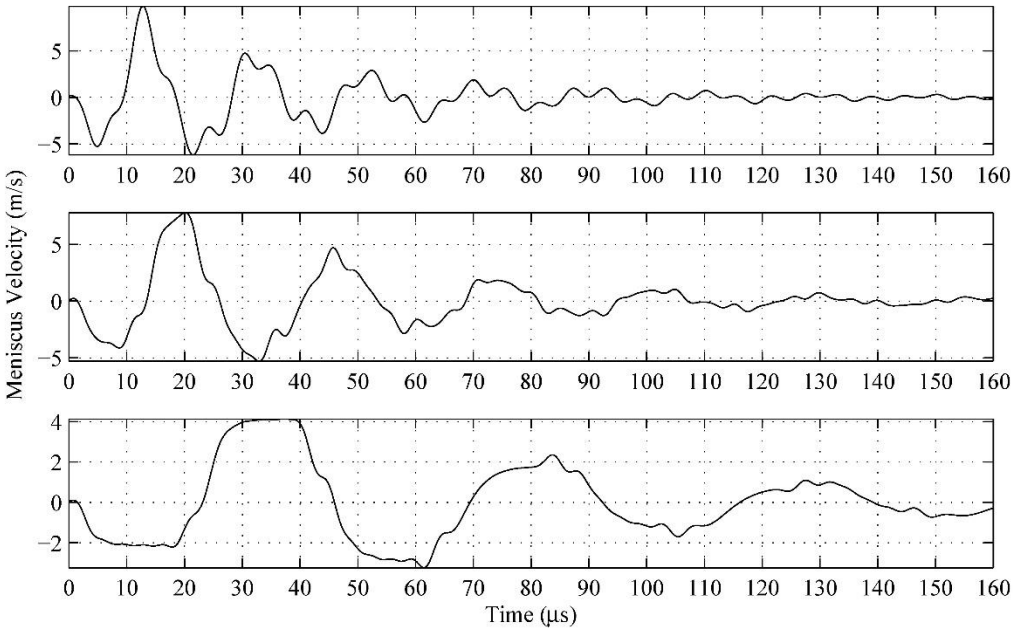

Figure 3.27: Model results corresponding to the conditions of the Bogy and Talke experiment for the meniscus velocity using squeeze ejector model. The tube inner diameter was taken to be 1 mm with an outer diameter of 2 mm. The transducer outer diameter was taken as 3 mm. The ejector ends are assumed to be pressure release conditions.

peaks which are of most interest in terms of fluid ejection are well predicted by the analytical squeeze ejector model.

The second aspect investigated by Bogy and Talke was the velocity of the ejected fluid droplet. The voltage on the transducer was increased until the droplet velocity attained 3.5 m/s, corresponding to 12.7 V in the 12.3 mm geometry and 4.5 V in the 33.9 mm geometry respectively. The necessary voltage for the 18.7 mm geometry is not reported in reference [2] and is assumed to be 8.5 V, approximately half the difference in voltage between the larger and smaller fluid cavity lengths. In general, the velocity of the ejected droplet should correspond to the acoustic velocity of the fluid at the ejector aperture. This provides a means to determine if the squeeze ejector model accurately predicts the amplitude of the acoustic field. The velocity at the ejector aperture is given in Figure 3.27. The squeeze model over predicts the maximum velocity at the aperture

but remains below the maximum experimental values recorded by Bogy and Talke. This gives confidence that the squeeze ejector model accurately models the physics governing squeeze type ejectors. The model therefore provides a new tool for understanding the effect of geometry, working fluid, and transducer properties on the acoustic field in the squeeze type fluid ejector.

3.7 Concluding remarks on model development

A coupled electro-mechanical modeling approach was developed which yielded closed-form analytical solutions that accurately capture the electrical and mechanical properties for a broad class of fluid ejectors, specifically horn-based ultrasonic atomizers and squeeze type devices. The modeling strategy divided an ejector into components, modeled each component individually, and then coupled the component models to establish a complete ejector model. Impedance matrix formulations were developed and validated for planar and annular piezoelectric transducers. Modeling the fluid acoustic pipes was facilitated by simplifications to the governing acoustic equations through an understanding of the dominant loss mechanisms. This allowed the formulation of two different models which jointly cover a broad range of atomizer operation in terms of operation frequency and working fluid viscosity: the acoustic pipe with a wall model for the regime in which the losses due to the radial component of the viscous stress in the acoustic boundary layer are the dominant loss mechanism and the acoustic pipe without a wall model for the regime in which the losses due to the axial component of the viscous stress are the dominant loss mechanism. By examining the nondimensional groups that govern atomizer behavior using scaling analysis, the bounds on the applicability of each model were established by comparing the magnitudes of the viscous stress components and the spatial pressure gradient. Modeling the change in the ejector cross-sectional area

within the horn was accomplished through the WWE and discretizing the acoustic pipe into sections with changing area.

The fluid cavity resonances, electric input impedance, and the axial pressure distribution for the horn-based ultrasonic atomizer model were compared to ANSYS finite-element simulations to confirm that the modified Dijksman model accurately predicts atomizer behavior within its applicable regime. The fluid cavity resonance frequencies agree with ANSYS to a small margin of error. The electric input impedance was shown to agree between the analytical and ANSYS models, as was the acoustic field along the device centerline, particularly for fluids with high viscosities. Discrepancies in the acoustic field were attributable to the transducer response and the difference in modeled viscous dissipation mechanisms. The modified Dijksman model emerged as a valid and computationally efficient analytical tool for horn based ultrasonic atomizers operating with high viscosity fluids.

The acoustic field predicted by the squeeze ejector model was compared to both ANSYS simulations and experimental data to confirm that the model accurately predicts ejector behavior. The coupling between the fluid cavity and transducer agree with ANSYS simulations when sufficiently far from the hoop resonance in operating frequency. The acoustic field of the model was also shown to agree with that present in an experimentally characterized device, both in terms of the propagation characteristics of the cavity as well as the amplitude of the acoustic field.

CHAPTER 4: OPTIMIZATION OF HORN-BASED ULTRASONIC ATOMIZER GEOMETRY

The ejection of viscous liquids is investigated and a design methodology for horn-based ultrasonic atomizers is developed through comprehensive analytical electro-mechanical acoustic modeling of device operation. A coupled electromechanical model, shown in the previous chapter to predict the acoustic field and viscous loss mechanisms in ultrasonic fluid ejectors, is applied to determine the atomizer geometry and operating parameters that maximize the pressure gradient magnitude for working fluids of various viscosities. The maximum pressure gradient magnitude is then compared to the required pressure gradient derived by hydrodynamics scaling to predict fluid ejectability as a function of the fluid viscosity.

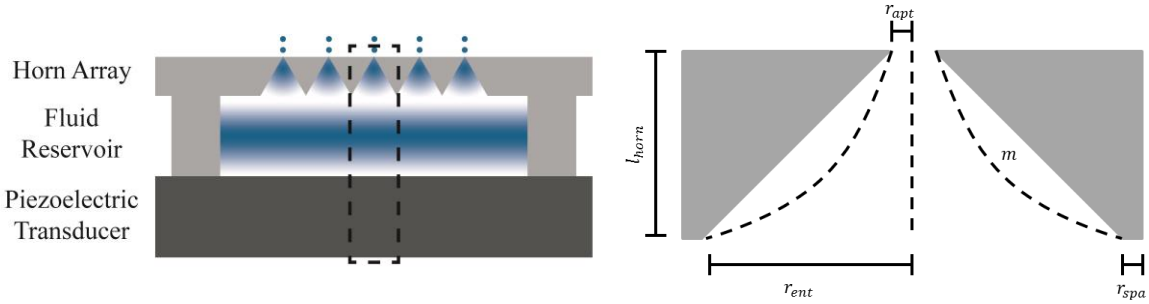

Figure 4.1: Left: A schematic of the ultrasonic atomizer based on an array of acoustic horn structures. The cell under consideration is defined by the dashed lines. Right: A magnified view of atomizer unit cell horn geometry. The horn has a fixed aperture radius, r_{apt}=25 µm, and horn entrance radius, r_{ent} = 387.5 µm. The entrance flat region, r_{spa}, is set equal to the aperture radius. The horn length, h_{horn} and flare constant m are varying parameters of the horn model.

4.1 Performance of current horn-based ultrasonic atomizers

Optimization of horn-based ultrasonic atomizer performance first requires characterization of commonly utilized geometries in order to establish a baseline for later device modifications. An atomizer geometry was selected which consists of a 2.1 mm fluid reservoir, a 500 µm horn, and a 1.5 mm transducer for this purpose. The conical

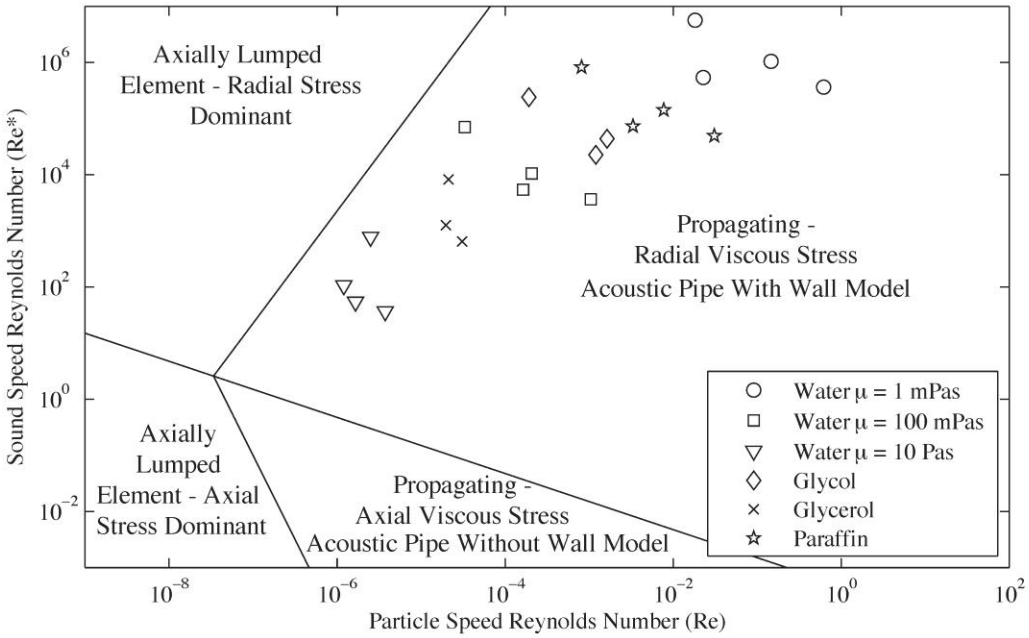

Figure 4.2: The regime map for horn-based ultrasonic atomizer operating with common working fluids. The considered fluids fall into the region where the discretized acoustic pipe with wall model applies for the horn. The multiple points for each considered fluid represent all fluid cavity resonant modes occurring below 1MHz.

horn has an entrance diameter of 775 µm, an aperture diameter of 50 µm, and an initial wall thickness (r_{spa}) of 25 µm. A schematic of the horn is provided in Figure 4.1. The appropriate atomizer model for this geometry can be determined by plotting the sound speed and particle speed Reynolds numbers for the fluid cavity resonance modes below 1 MHz in several working fluids. As is shown in Figure 4.2, for all considered fluids atomizer operation falls into the regime captured by the modified Dijksman model. The model should therefore capture the dominant sources of viscous dissipation present in physical devices and scale correctly with the physical device response.

Atomizer characterization was conducted by examining the pressure gradient magnitude at horn aperture as a function of working fluid viscosity for the fluid cavity modes below 1 MHz, given in Figure 4.3 for a transducer driven by a 1 V sinusoidal signal. To isolate the influence of working fluid viscosity on the horn acoustic field, an

artificial working fluid is introduced with a fixed density and sound speed equal to those of water and only changing the fluid viscosity. The pressure gradient magnitude was determined by sampling the acoustic pressure an aperture radius back from the horn aperture and dividing by the aperture radius as this is the length scale relevant to fluid ejection from the aperture. Fluid cavity resonances were defined as the frequencies at which a maximum in the pressure gradient occurred that is not attributable to a transducer resonance. The dependence of the generated pressure gradients on the fluid cavity resonance mode is most evident in low viscosity working fluids. At low working fluid viscosities, the pressure gradient amplitude near the horn aperture can be increased with the use of higher order fluid cavity resonance modes. The increase in the pressure gradient is most significant when shifting from the zeroth to the first mode and subsequently decreases with increasing cavity mode, implying a decreasing return from increasing the fluid cavity resonance frequency used for atomization as viscous dissipation increases.

When working fluids with viscosities greater than that of water are considered, the effect of the fluid cavity resonant mode on the atomizer pressure gradient is reduced. For working fluid viscosities on the order of 1 Pas, the first, second, and third order fluid cavity resonances collapse to a similar pressure gradient amplitude. This behavior is intuitive as the increased pressure amplitude from the larger displacement imposed by the transducer is offset by the greater viscous dissipation present at the higher order fluid cavity resonances. Interestingly, the model predicts a local maximum in the pressure gradient amplitude occurring near 5 Pas as a result of the standing wave pattern in the nozzle. The atomizer response thus displays two kinds of behavior based on the viscosity

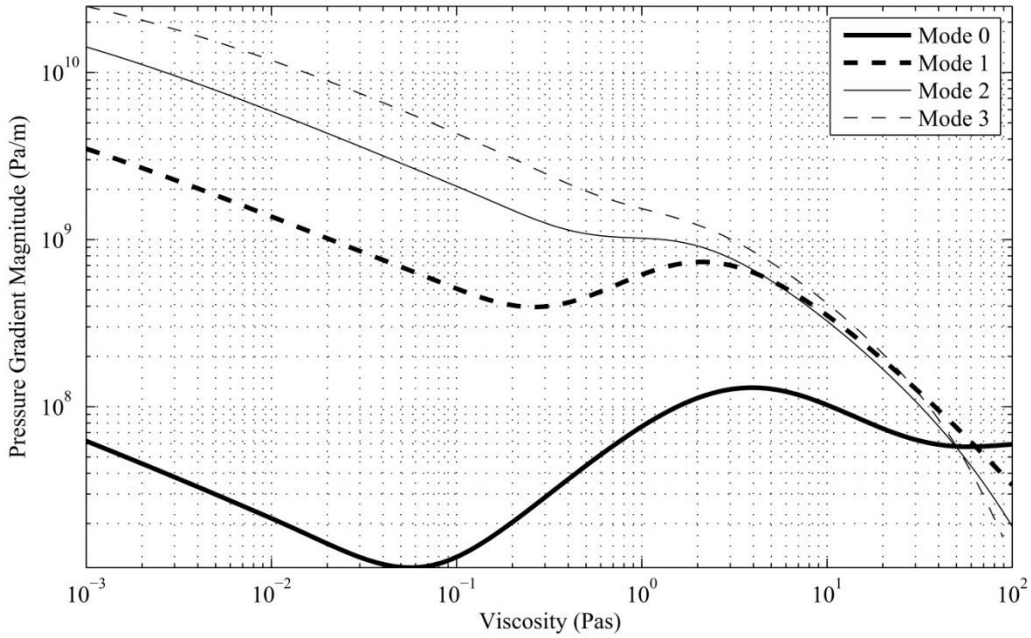

Figure 4.3: Variation in the predicted pressure gradient at the horn aperture for each fluid cavity resonance as a function of viscosity when driven by a sinusoidal voltage input of 1V. The sound speed and density of the working fluid are taken to be equal to those of water. The fluid cavity resonant frequencies are adjusted to account for their change as a function of working fluid viscosity.

of the working fluid. In the low viscosity case, the greatest pressure gradient occurs at high order fluid cavity resonant modes as viscous dissipation remains insignificant even at high frequencies. In the high viscosity case, the maximum pressure gradient is largely independent of the fluid cavity resonant mode until the zeroth mode becomes favored at the largest viscosities. Viscous dissipation increases by such an extent at higher order cavity modes that the third order fluid cavity resonance is damped completely from the fluid cavity response above 95 Pas.

It is assumed that the pressure gradient at the horn aperture must achieve a frequency independent value of the pressure gradient, called the pressure gradient threshold which depends on the fluid viscosity, for ejection to take place from an atomizer. The atomizer model can be applied to predict if the ejection of a working fluid is possible by determining if the maximum pressure gradient created by the atomizer is

greater than a specified pressure gradient threshold. Atomizer configurations which yield a pressure gradient below the pressure gradient threshold can be eliminated as unviable. To estimate the pressure gradient thresholds for fluids of various viscosities, a scaling approach is utilized. Numerical simulations and comparison with experiments for water atomization by Meacham and coworkers, showed successful ejection with pressure gradients on the order of 10^{10} Pa/m.[1] Taking this as the order of magnitude for the pressure gradient required to achieve fluid ejection at that (water) viscosity, one can develop a relationship for the pressure gradient threshold as function of the fluid viscosity by balancing the driving pressure gradient against the viscous stress and assuming a quasi-steady liquid flow rate from the ejector, $\nabla P \propto \nabla P_{ref}\ (\mu/\mu_{ref})$. One therefore expects the pressure gradient required for fluid ejection to increase linearly with increasing viscosity as the ejection resisting shear stresses at the fluid cavity aperture grow. By substituting in the pressure gradient threshold for water as the reference fluid, one can obtain an order of magnitude estimate for the pressure gradient threshold of any other fluid.

Table 4.1: Maximum values of the pressure gradient generated by the atomizer as a function of the working fluid viscosity and fluid cavity resonance mode. The examined geometry consisted of a 2.1 mm fluid reservoir, a 500 μm horn, and 1.5 mm transducer driven at its dielectric breakdown voltage.

Working Fluid Viscosity (Pas)	Maximum Pressure Gradient Magnitude (GPa/m)				Pressure Gradient Threshold (GPa/m)	Fluid Ejection
	Mode 0	Mode 1	Mode 2	Mode 3		
0.001	18.5	1047.9	4264.6	7389.8	10	Yes
0.01	7.2	337.8	1486.0	3144.4	100	Yes
0.1	3.7	148.5	606.4	1240.8	1000	Yes
1	10.2	94.5	206.0	358.7	10,000	No
10	30.6	105.4	97.9	127.2	100,000	No

The displacement amplitude imposed on the fluid cavity by the transducer provides the upper bound on the atomizer pressure gradient magnitude at a given operating frequency. The maximum pressure gradient magnitude for a given transducer thickness occurs at the upper limit on the voltage allowed across the transducer given by the dielectric breakdown voltage. Typical piezoelectric transducers are limited to voltages resulting in an electric field on the order of 5 V/mil (1.97×10^5 V/m).[116] The maximum pressure gradient as a function of working fluid viscosity and fluid cavity resonances for the 1.5 mm transducer of APC International 855 is given in Table 4.1 along with the pressure gradient threshold. For the 1 mPas viscosity, any fluid cavity resonance produces a sufficiently large pressure gradient to yield fluid ejection. However, for 100 mPas, only the third order fluid cavity resonance yields a sufficient pressure gradient for fluid ejection. The 10 Pas working fluid shows no viable fluid cavity resonances. Increased working fluid viscosity simultaneously reduces the maximum pressure gradient magnitude able to be generated in the horn-based ultrasonic atomizer while requiring an increased pressure gradient threshold to overcome the greater shear stresses present at the horn aperture. The question thus becomes whether all potential atomizer configurations exhibit a similar limitation.

4.2 Geometric optimization of horn-based ultrasonic atomizers

Fluid ejection from horn-based ultrasonic atomizers is governed by the pressure gradient magnitude at the horn aperture produced by the atomizer fluid cavity acoustic field. As the viscosity of the working fluid is increased, a greater pressure gradient is required at the horn aperture to overcome the larger viscous shear stresses resisting ejection. Maximization of the pressure gradient to eject high viscosity working fluids necessitates consideration of each of the three main components of the atomizer: the

horn, the fluid reservoir, and the piezoelectric transducer. The maximum atomizer pressure gradient can then be compared to the pressure gradient required to eject a working fluid, i.e. the pressure gradient threshold, to determine the ability of a working fluid to eject with horn-based ultrasonic atomization.

The examined horn-based ultrasonic atomizer horn geometries are guided by the actual devices created by Meacham et al.[3] To facilitate the comparison among the atomizer configurations, the entrance and aperture radii of the silicon horn are fixed as given in Figure 4.1. The piezoelectric transducer material also remains fixed as APC International 855 with a varying thickness and quality factor.[116]

4.2.1 The effect of horn shape on the generated pressure gradient

The acoustic horn increases the pressure gradient magnitude at the atomizer aperture by concentrating volume velocity from a larger cross-sectional area at the horn entrance to a smaller cross-sectional area at the horn aperture. For a fixed horn length, the two geometric parameters which determine the acoustic response of the horn section are the magnitude and rate of the area reduction across the horn. The magnitude of the reduction in area, given by the diameter ratio ($R_d = r_{ent}/r_{apt}$) between the entrance and aperture, determines by how much the volume velocity in concentrated across the horn while the horn profile determines how rate at which the contraction in area occurs. Both these parameters influence the acoustic boundary layer loss which is the dominant source of dissipation in the fluid cavity. It is therefore desirable to select a horn geometry which maximizes the concentration of volume velocity while minimizing the boundary layer losses to yield a large pressure gradient.

The effect of the horn diameter ratio on the pressure gradient magnitude is shown in Figure 4.4 as a function of frequency for silicon horns 0.5 and 2.5 mm in length with 1mPas and 10Pas working fluid viscosities. The artificial working fluid is again utilized with sound speed and density equal to water to isolate the effect of changing working fluid viscosity. The aperture diameter was also maintained at 25 μm and the entrance diameter increased to obtain changing R_d. A R_d of one corresponds to a straight acoustic pipe with larger R_d indicating a greater reduction in area across the conical horn. The upper limit on the considered diameter ratio is established by two limits on the entrance diameter: the first being numerical in the ability to evaluate the modified Dijksman horn model and the second being a physical constraint on the assumptions underlying the development of the analytical model. Considering first the numerical limitation, during model formulation the pipe radius is scaled by the acoustic boundary layer thickness ($r^* = r(\rho_0\omega_r/\mu)^{\frac{1}{2}}$) to produce a non-dimensional radius. As the pipe radius and operating frequency become large or the viscosity becomes small, the nondimensional radius becomes large. For large nondimensional radii, the Kelvin functions which govern the radial dependence of the axial particle velocity cannot be numerically evaluated. In the 1 mPas case, the maximum pipe radius that can be considered for a 1 MHz operating frequency prior to the Kelvin functions becoming numerically undefined is 390 μm corresponding to $R_d = 15.6$. As the viscosity of the working fluid is increased, the nondimensional radius becomes smaller which permits larger pipe radii to be considered. For these cases, the maximum entrance radius is established through the assumption of a one dimensional acoustic field in the axial direction during model formulation. For this assumption to hold, the pipe radius must be less than half of an acoustic wavelength:

$$R_{max} = \frac{\lambda}{2} = \frac{c}{2f}$$

Above this value, the acoustic field in the horn becomes two dimensional and cannot be captured by the developed analytical model.

As the horn diameter ratio is increased, the pressure gradient magnitude generated in the horn section grows. This is a result of the greater volume velocity which is imposed at the horn entrance with the constant amplitude driving driving condition which is subsequently concentrated to the same aperture area. While an increase in pressure gradient magnitude occurs across all considered geometries, the effect is most significant in high viscosity working fluids for long horns as seen in the 10 Pas working fluid and the 2.5 mm horn. For the $R_d = 1$ case corresponding to the straight acoustic pipe, the pressure gradient magnitude declines rapidly with operating frequency as viscous dissipation becomes large. For the $R_d = 30$ case, while viscous dissipation effects are again large at high operating frequencies, the volume velocity imposed at the entrance of the horn is sufficiently large that a meaningfully large acoustic field amplitude remains after propagation to the horn aperture. In both low and high viscosity working fluids, the maximum pressure gradient magnitude is generated in the horn when the largest diameter ratio is utilized that maintains a one-dimensional axial acoustic field in the horn.

When the maximum diameter ratio is utilized across the horn, the only remaining parameter for a fixed length horn is the horn flare. Horn flare governs the rate at which the reduction in cross-sectional area occurs as well as the contact surface area between the horn and the working fluid. To determine an optimal horn flare, the horn component model was applied to horns of varying flare, resulting in Figure 4.5 which examines pressure gradient as a function of frequency for silicon horns 0.5 and 2.5 millimeters in

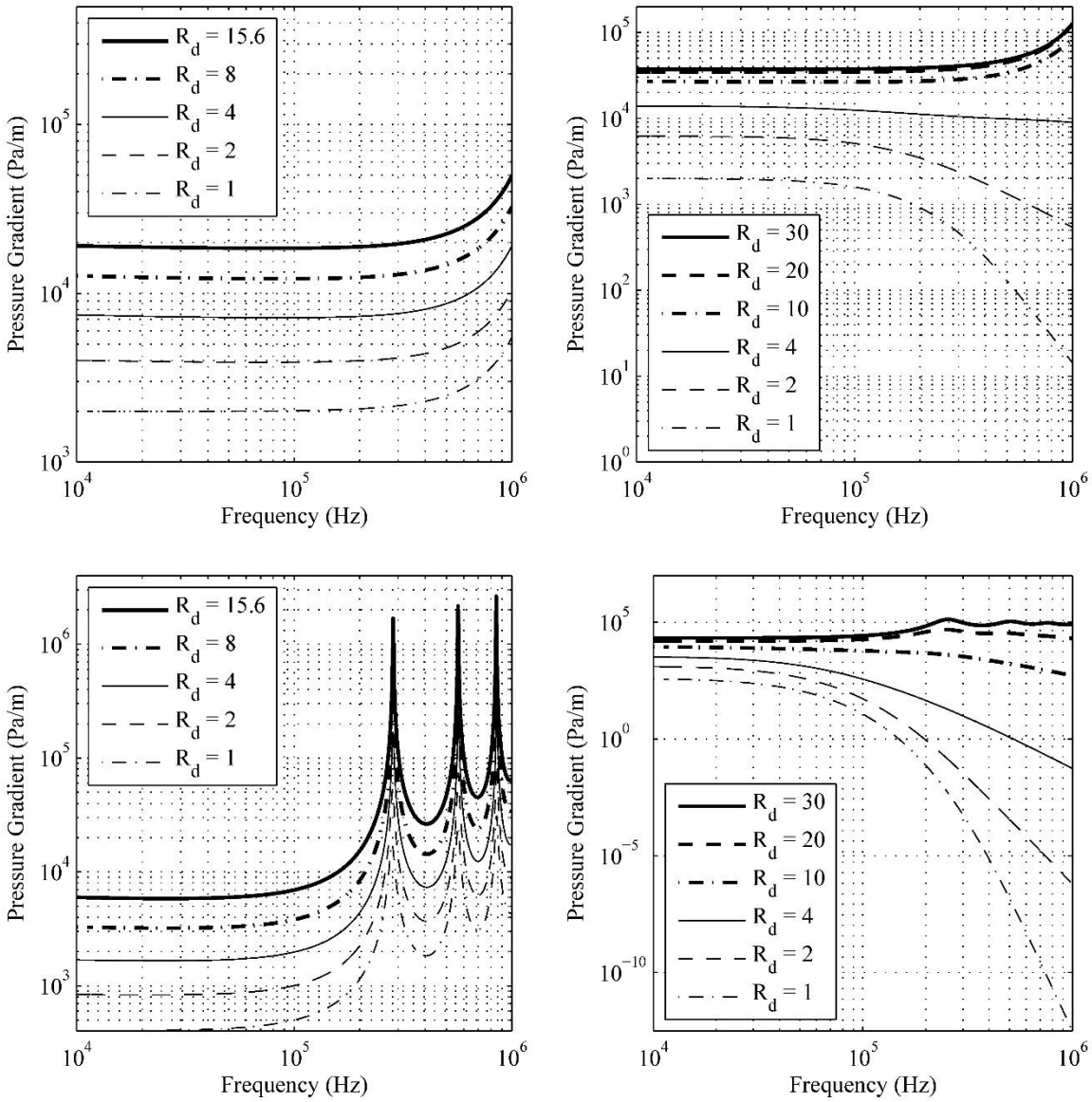

Figure 4.4: Pressure gradient magnitude in the horn as a function of frequency and diameter reduction when driven by sinusoidal pressure input of 1 Pa. The horn aperture diameter is 50 μm with a varying entrance diameter. The sound speed and density of the working fluid are taken to be equal to those of water. Top left: 500 μm horn with 1 mPas working fluid viscosity. Top right: 500 μm horn with 10 Pas working fluid viscosity. Bottom left: 2500 μm horn with 1mPas working fluid viscosity. Bottom right: 2500 μm horn with 10 Pas working fluid viscosity.

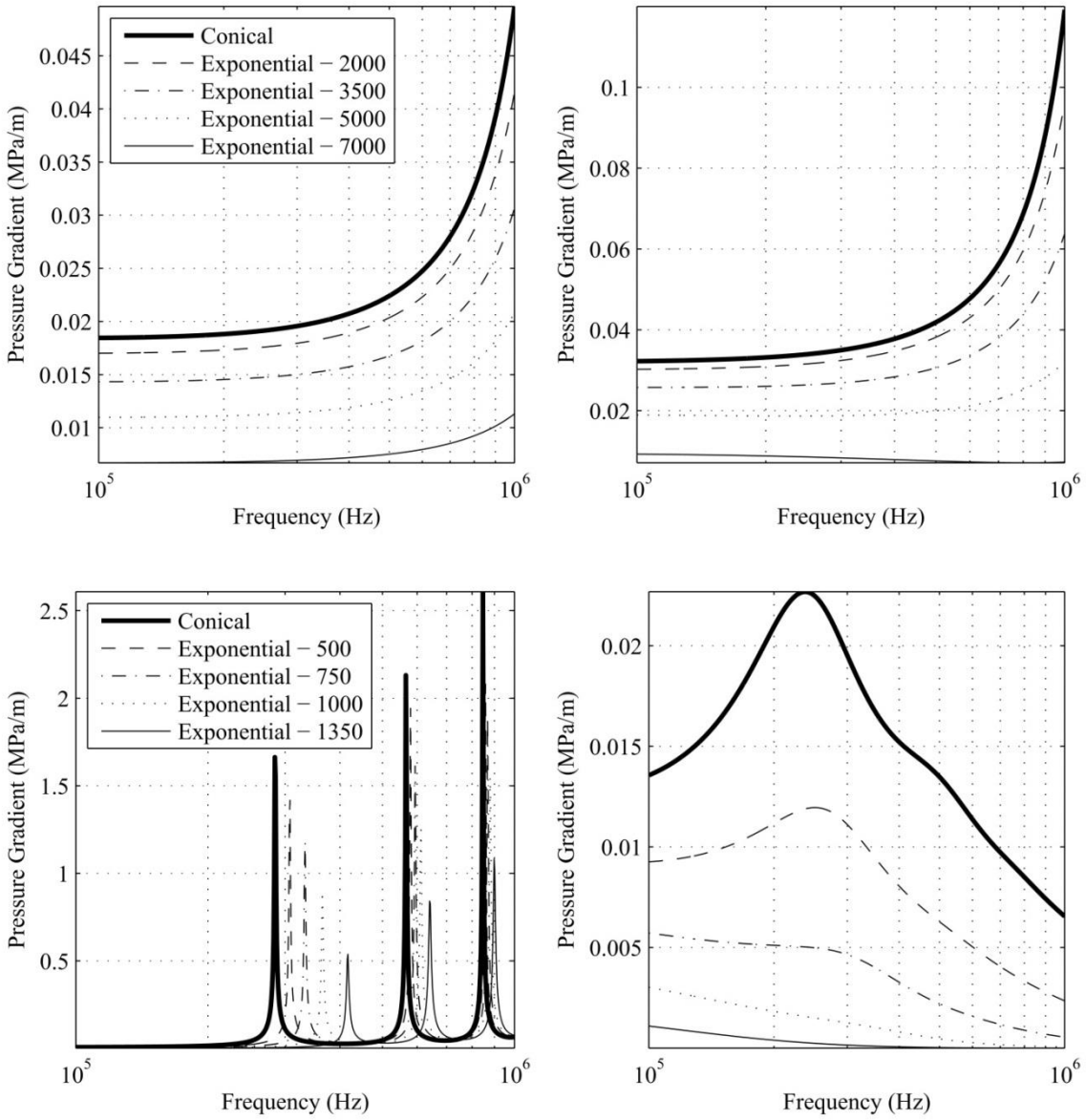

Figure 4.5: Pressure gradient magnitude in the horn as a function of frequency and horn flare when driven by sinusoidal pressure input of 1 Pa. The horn entrance is 775 micrometers with an aperture diameter of 50 micrometers. The sound speed and density of the working fluid are taken to be equal to those of water. The legend values next to the exponential are the flare constant of the horn, with higher numbers indicating greater flare. Top left: 500 μm horn with 1 mPas working fluid viscosity. Top right: 500 μm horn with 10 Pas working fluid viscosity. Bottom left: 2500 μm horn with 1mPas working fluid viscosity. Bottom right: 2500 μm horn with 10 Pas working fluid viscosity.

length at a fixed entrance to aperture diameter ratio. Figure 4.5 again utilizes the artificial working fluid with viscosities of 1 mPas and 10 Pas. The conical horn consistently results in the largest pressure gradient across working fluid viscosities and horn resonance modes as it minimizes the surface area that generates a boundary layer. As one expects these results to be independent of horn length, the following analyses are confined to conical horn profiles with a fixed diameter ratio. Selection of a horn length, which also determines the magnitude of the acoustic boundary layer losses for a given horn profile, is dependent on reservoir length and is therefore considered in the subsequent section.

4.2.2 The effect of horn and reservoir length on the generated pressure gradient

The horn and fluid reservoir, in their combined length and fraction of the combined length, determine the fluid cavity resonance modes available for fluid ejection as well as magnitude and mechanism of the dissipated acoustic power. The importance of the fluid cavity resonant mode utilized for operation can be seen in Figure 4.6 where acoustic behavior of a fixed geometry fluid cavity is evaluated when driven by a constant amplitude sinusoidal inlet velocity condition at the first six fluid cavity resonance modes. The pressure gradient magnitude at the horn aperture initially increases with the fluid cavity resonance mode, reaches a maximum at the fourth order mode, and subsequently declines. The increase with resonance mode is the combined effect of a greater fluid cavity acoustic impedance yielding a larger pressure amplitude within the cavity and the shifting of the final pressure antinode closer to the horn aperture due to the fluid cavity mode shape. Beyond the fourth order fluid cavity resonance, the decline in the fluid cavity acoustic impedance and the growth in the acoustic energy dissipation, which scales

with a square root of the frequency, together result in a decreased atomizer pressure gradient. This behavior demonstrates the sensitivity of atomizer performance to the selected fluid cavity configuration and operating parameters for a given working fluid.

Systematic variation of the fluid cavity geometry and operating frequency provides a means to determine an optimal atomizer configuration for a given working fluid. Figures 4.6 through 4.8 illustrate the interplay among the horn length, reservoir length, and operating frequency that maximizes the atomizer pressure gradient magnitude for the artificial test fluids with viscosity of 1 mPas, 100 mPas, and 10 Pas, respectively. The figures were generated by the exhaustive comparison of various combinations of horn lengths, reservoir lengths, and operating frequencies with the atomizer model for a fixed velocity condition at the fluid cavity inlet.

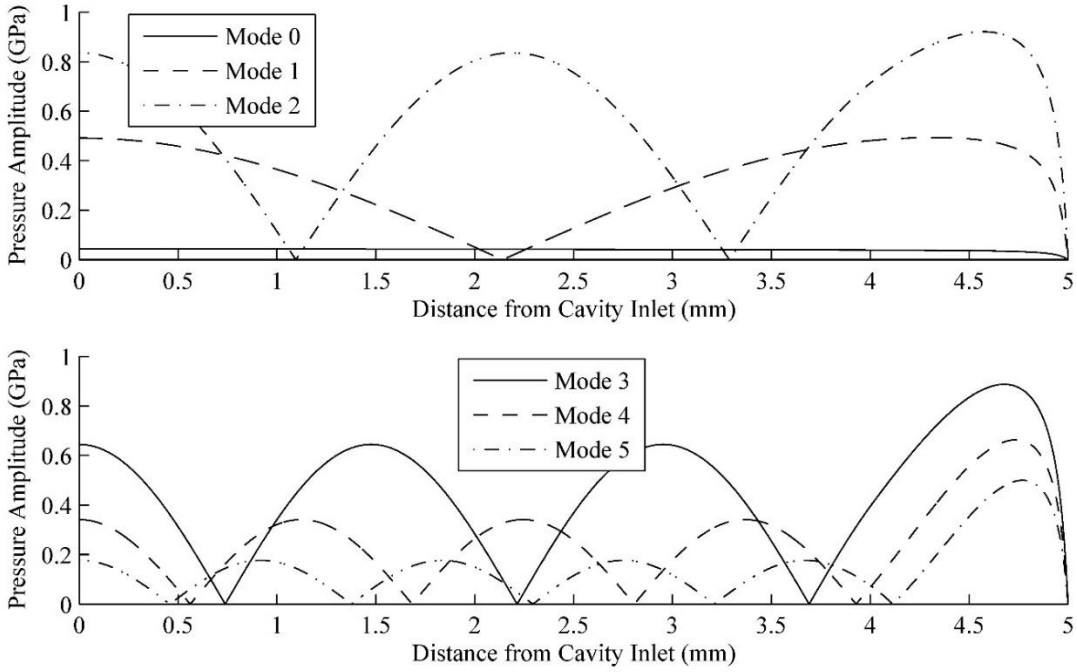

Figure 4.6: Pressure amplitude in the atomizer fluid cavity as a function of distance from the cavity inlet for the first six cavity resonance modes in the artificial test fluid with 1 mPas viscosity when driven by a constant amplitude (1 m/s) sinusoidal velocity inlet condition.

The fluid cavity filled with the low viscosity working fluid (Figure 4.7) yields the largest pressure gradient magnitudes when driven at one of the fluid cavity resonant modes. Operation at fluid cavity resonances is beneficial as the fluid cavity amplifies the pressure imposed at the fluid cavity inlet and, due to the low viscosity, little acoustic energy dissipation occurs at the high operating frequencies associated with the high fluid cavity resonant modes. Interestingly, while all fluid cavity resonant modes result in pressure amplification, the largest pressure gradient magnitude is seen at the first order fluid cavity resonance. Near the first order fluid cavity resonance, the fluid cavity acoustic impedance is comparatively large which implies that an increased inlet pressure amplitude provides more benefit than the anti-node shifting towards the cavity aperture that occurs at high operating frequencies. However, the configuration with the optimum pressure gradient magnitude is not concurrent with the configuration with the largest fluid cavity impedance. This indicates that small changes to the fluid cavity geometry and operating frequency affecting the fluid cavity mode shape and viscous dissipation can be influential on the pressure gradient magnitude resulting from a given fluid cavity inlet condition. The linkage between the reservoir length, horn length, and the operating frequency is manifested as resonant bands in the maps, Figures 4.6 through 4.8, wherein the pressure gradient is large. Each of these bands corresponds to the same cavity resonant mode, such that with an increase in the reservoir or horn length the operating frequency proportionally decreases.

In contrast, the largest pressure gradient magnitudes for high viscosity fluids (Figure 4.9) are generated far below the fluid cavity resonance frequencies due to the strong dependence of acoustic energy dissipation on operating frequency and working

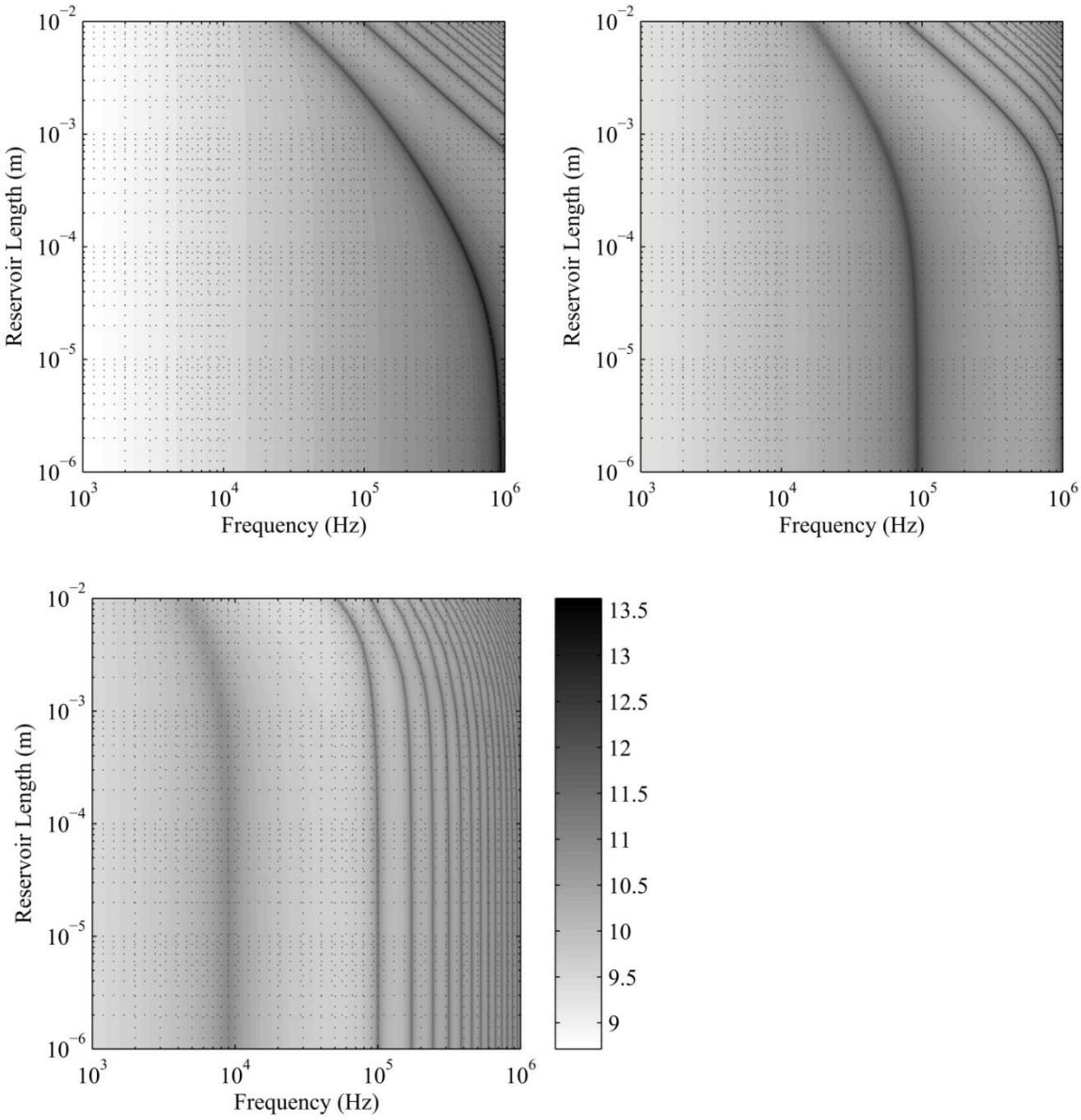

Figure 4.7: Representative maps of the pressure gradient magnitude (log_{10}(Pa/m)) at the fluid cavity aperture for the artificial working fluid with 1mPas viscosity as a function of reservoir length and operating frequency. Top left: Horn length is 0.1 mm. Top right: Horn length is 1 mm. Bottom left: Horn length is 10 mm. The global maximum (not shown) occurs for a 258 µm horn and 649 µm reservoir operating at 1MHz, corresponding to the first order cavity resonance.

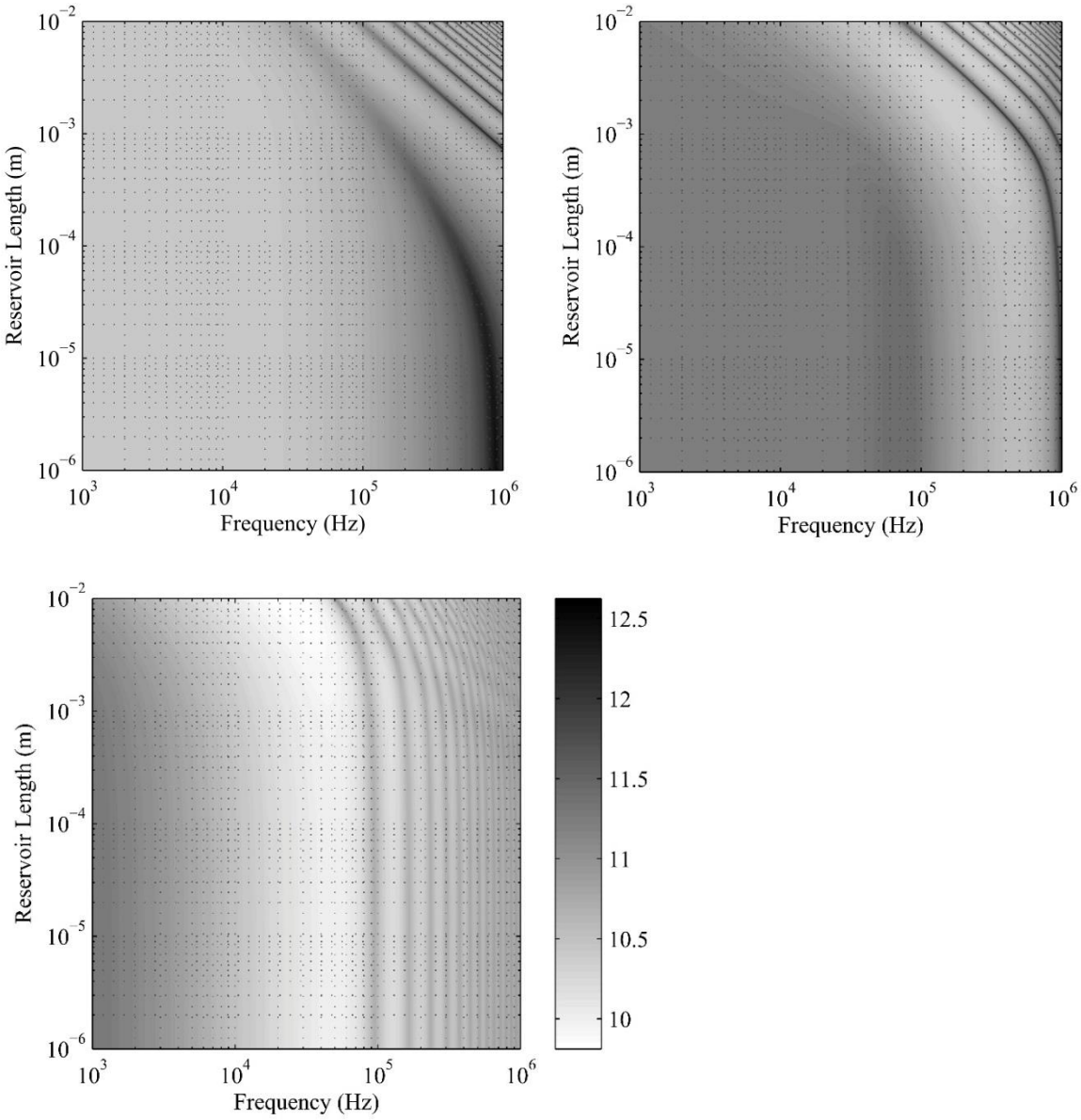

Figure 4.8: Representative maps of the pressure gradient magnitude (log_{10}(Pa/m)) at the fluid cavity aperture for the artificial working fluid with 100mPas viscosity as a function of reservoir length and operating frequency. Top left: Horn length is 0.1 mm. Top right: Horn length is 1 mm. Bottom left: Horn length is 10 mm. The global maximum (not shown) occurs for a 271 µm horn and 642 µm reservoir operating at 1MHz, corresponding to the first order cavity resonance.

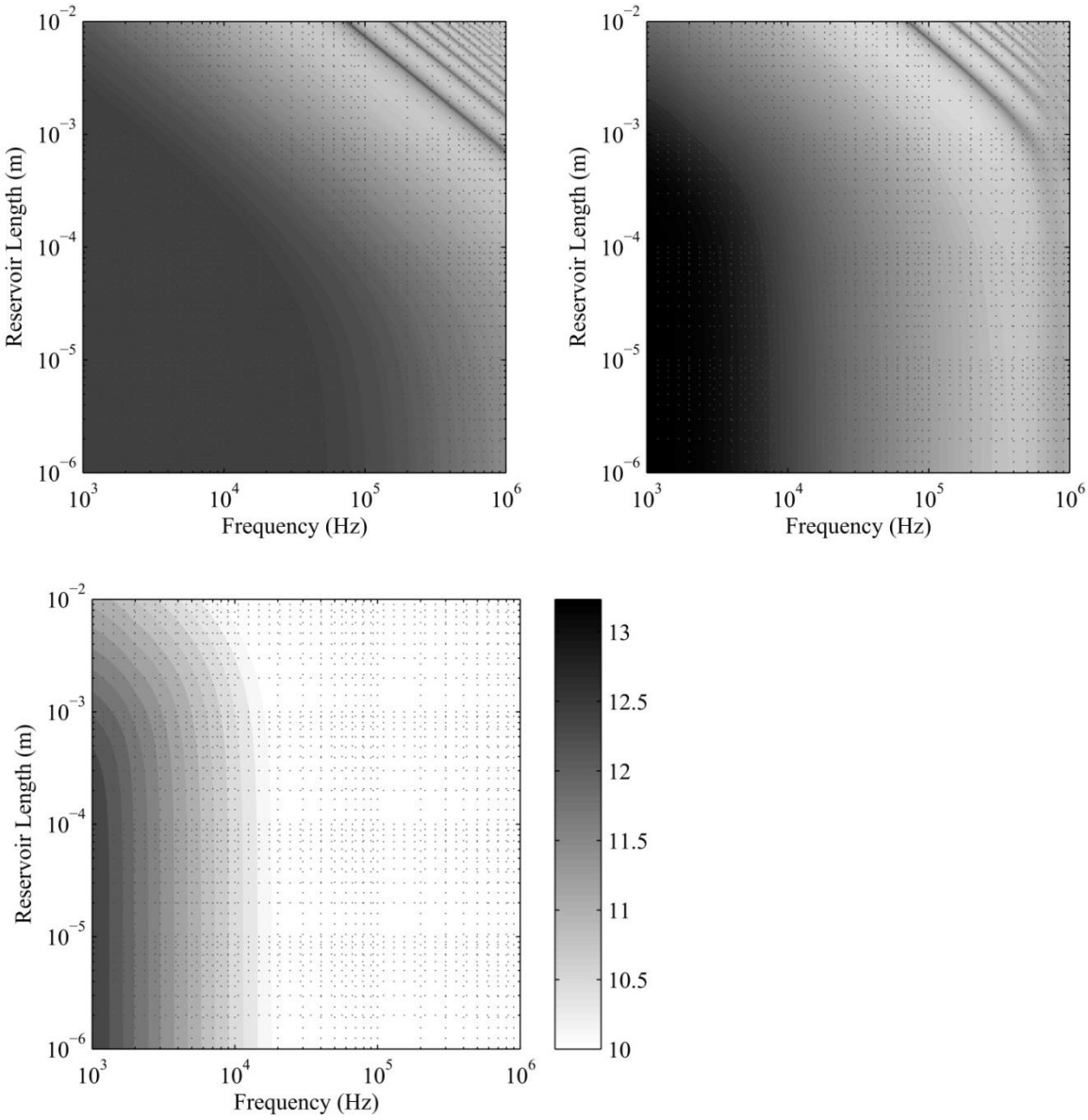

Figure 4.9: Representative maps of the pressure gradient magnitude (log_{10}(Pa/m)) at the fluid cavity aperture for the artificial working fluid with 10 Pas viscosity as a function of reservoir length and operating frequency. Top left: Horn length is 0.1 mm. Top right: Horn length is 1 mm. Bottom left: Horn length is 10 mm. The global maximum (not shown) occurs for a 1.47 mm horn and 1 µm reservoir operating at 1 kHz.

fluid viscosity. At large working fluid viscosities, any increase in operating frequency causes significant dissipation of the wave energy, primarily in the acoustic boundary layer where energy losses scale with the square root of the operating frequency. The degree to which acoustic power dissipation dictates the fluid cavity response is most evident in considering high frequency operation and configurations with long horns in which the fluid cavity resonances are completely damped. Minimization of the acoustic power losses consequently forces the operating frequency to be as low as possible which prohibits operating at a fluid cavity resonance for any meaningful size of the fluid reservoir/horn. It is also of interest to note that the unexpectedly long horn, and not the reservoir, appears to yield the highest pressure gradient for atomization of high viscosity fluids. As the acoustic power loss the reservoir where bulk attenuation dominates is several orders of magnitude less than the acoustic boundary layer loss that dominates within the horn, one would expect an optimal configuration with a short horn and a long reservoir. However, the optimal configuration with a short reservoir and long horn has a much greater impedance as compared to configurations with longer reservoirs/shorter horn, which produces a large pressure amplitude at the fluid cavity inlet that ultimately yields a larger pressure gradient despite the losses in the horn boundary layer.

The 100 mPas working fluid given in Figure 4.8 exhibits behavior between the low and high viscosity cases. At this viscosity, viscous dissipation has increased such that it is no longer negligible as in the 1 mPas case but not by such as extent as to eliminate the benefits of operation at the fluid cavity resonances as in the 10 Pas case. While the fluid cavity resonances still yield the largest pressure gradient magnitude, frequencies below 100 kHz show an improved pressure gradient over the 1 mPas case.

Moreover, the 100 mPas working fluid ceases to exhibit a clear zeroth order fluid cavity resonance for some horn lengths. The low frequency, large pressure gradient region expands to encompass all frequencies less than 100 kHz. Improved performance in this region is governed by the same phenomena as in the 10 Pas seconds case, minimization of the viscous energy dissipation and a high fluid cavity inlet impedance. The 100 mPas working fluid marks the transition viscosity between an atomizer response governed by lossless behavior and one governed by viscous dissipation.

4.2.3 The effect of transducer thickness on the generated pressure gradient

The piezoelectric transducer drives the atomizer by imposing a time dependent displacement at the fluid cavity inlet. Because the electromechanical response of the piezoelectric transducer is not independent of but coupled to the acoustics of the fluid cavity, the overall behavior of the atomizer cannot be predicted based on either the fluid cavity or piezoelectric transducer alone. In general, the displacement generated by the transducer is a function of the fluid cavity inlet acoustic impedance, the operating frequency, and the transducer physical properties. The transducer properties which impact atomizer operation most significantly are the transducer thickness and its resonance quality factor.

The effect of transducer thickness on atomizer performance can be seen in Figure 4.10 which plots the pressure gradient magnitude as a function of transducer thicknesses for a sinusoidal voltage input of 1V with the 1mPas and 10Pas viscosity artificial working fluids and a fixed fluid cavity configuration. The short circuit transducer resonances create maxima in the pressure gradient magnitude when they become comparable in frequency to the fluid cavity resonances. At such frequencies, the large displacements

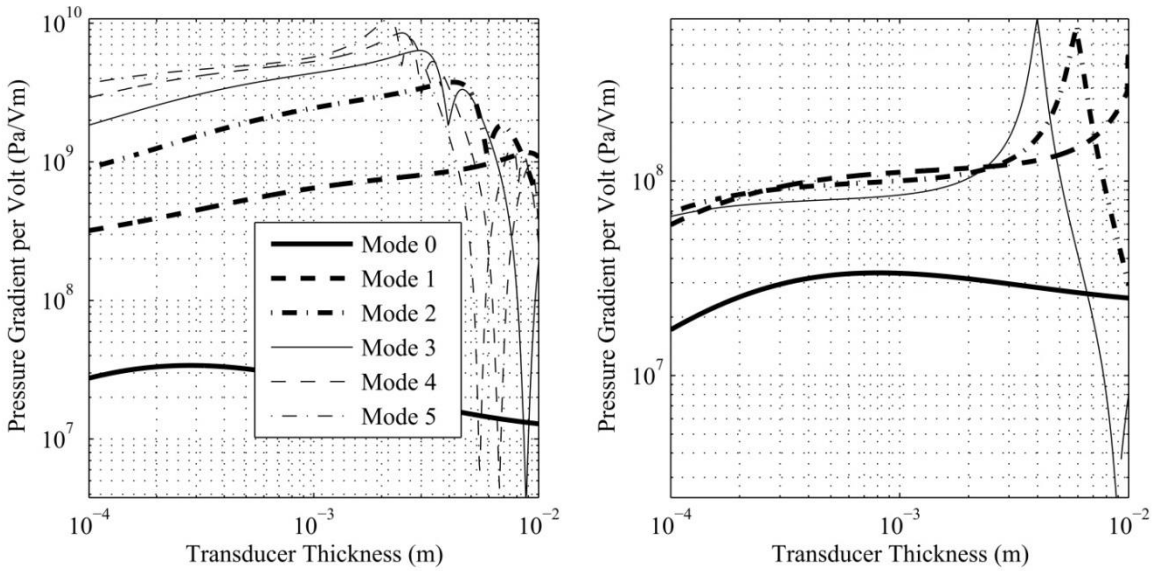

Figure 4.10: Variation in the pressure gradient magnitude at the horn aperture for each fluid cavity resonant mode as a function of transducer thickness when driven with a sinusoidal voltage input of 1V and a transducer quality factor of 60. The horn is 1mm with a 4mm reservoir. The sound speed and density of the working fluid are taken to be equal to those of water. Left: Low viscosity (1mPas) fluids yield the highest pressure gradient at the highest 5th cavity mode using a thinner transducer. Right: Higher viscosity (10Pas) fluids favor transducers that yield large displacements per applied volt at a given fluid cavity resonance. The absolute value is also an order of magnitude lower than that for the low viscosity fluid.

generated by the transducer are further amplified by the fluid cavity to result in high pressure gradient magnitudes. The greatest pressure gradient magnitudes are associated with the first order transducer short circuit resonance which generates the largest transducer displacements; subsequent transducer short circuit resonances also yield the local pressure gradient maxima but of a lesser magnitude. Maximization of the pressure gradient magnitude therefore calls for a selection of a transducer thickness such that its first order short circuit resonance is located near the optimal frequency mode of a fluid cavity that yields the highest pressure gradient at the horn aperture for a given viscosity fluid.

The resonance quality factor of the piezoelectric transducer plays as significant role as the transducer thickness in determining atomizer performance. Figure 4.11 plots

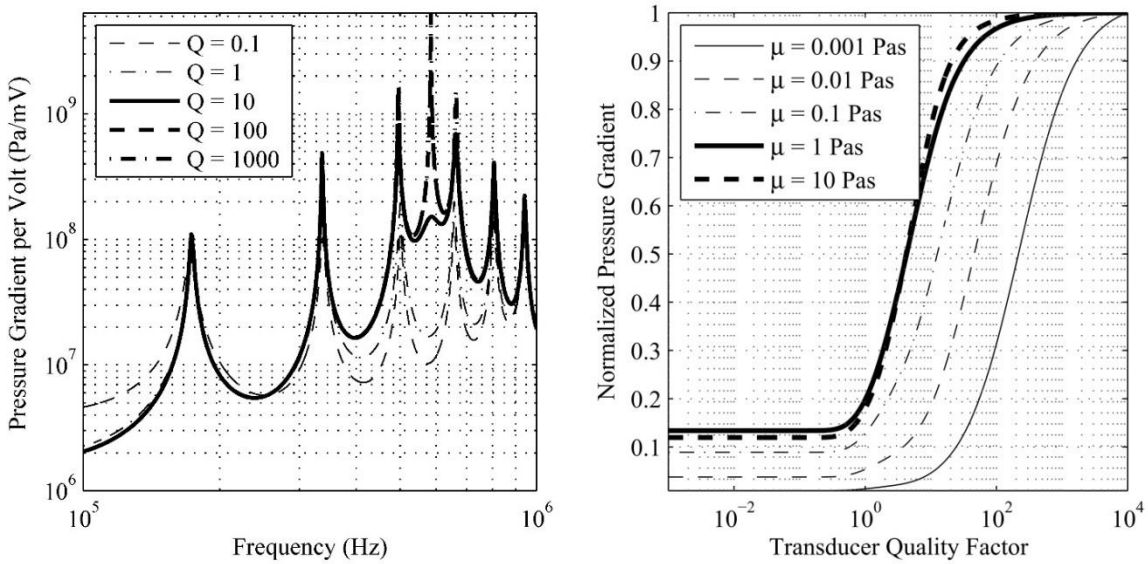

Figure 4.11: Left: Pressure gradient magnitude as a function of the resonance quality factor of the piezoelectric transducer when driven with 3.4mm transducer and a sinusoidal voltage input of 1V. The horn is 1mm with a 4mm reservoir. The sound speed and density of the working fluid are taken to be equal to those of water with a 100mPas viscosity. Right: Pressure gradient magnitude at the first order transducer short circuit resonance as a function of the transducer resonance quality factor for various working fluid viscosities. The horn is 1mm with a 4mm reservoir. The sound speed and density of the working fluid are taken to be equal to those of water.

the pressure gradient in the artificial working fluid with 100mPas viscosity as a function of frequency for varying transducer quality factors and a fixed fluid cavity configuration. The maximum pressure gradient magnitude is set by the atomizer component with the largest quality factor. At low transducer quality factors, the fluid cavity resonant modes with high quality factor dominate the atomizer response, causing the maximum pressure gradient magnitude to occur at a fluid cavity resonance. As the quality factor of the transducer increases and becomes comparable to that of the fluid cavity modes, a new local maximum is produced based on the transducer short circuit resonance that is largely independent on the fluid cavity behavior. At very large transducer quality factors, the transducer quality factor completely dominates the atomizer response and the pressure gradient magnitude generated by the first order transducer short circuit resonance

outperforms the fluid cavity resonances. When the piezoelectric transducer is coupled to the fluid cavity, the quality factor of the fluid cavity convolves with that of the transducer to yield the overall quality of the atomizer; whichever quality factor is larger dominates the behavior of the atomizer with influence of the cavity mode shapes in frequency domain.

The extent to which the transducer quality factor influences atomizer operation and the transition from fluid cavity to transducer dominance is a function of the working fluid viscosity. Figure 4.10 utilizes the same transducer quality for fluids of differing viscosities and produces distinctly different fluid cavity responses. Whereas the low viscosity case shows multiple distinct local maxima as a function of the fluid cavity resonance mode, the high viscosity case produces only a single maximum across the fluid cavity resonance modes. For low viscosity working fluids, the quality factor of the fluid cavity resonances is sufficiently large to remain relevant to the atomizer response even when a transducer with a high quality factor is used. For fluids of high viscosity, viscous losses have damped the wave propagation in cavities to such an extent that the transducer quality factor is much larger than the fluid cavity quality factor, causing the atomizer response to be a function of the piezoelectric transducer alone, in essence behaving as transducer driven liquid pump rather than a resonant acoustic device. Figure 4.11 shows how working fluid viscosity influences the behavior of the atomizer, plotting the pressure gradient at the transducer resonance as a function of the transducer quality factor for fluids of increasing viscosity normalized by the maximum value of the gradient for each fluid viscosity. Each curve represents how quickly with respect to an increase of its quality factor the piezoelectric transducer becomes the dominant component of the

atomizer for fluids of various viscosities. For high viscosity working fluids, a piezoelectric transducer of any meaningful quality factor is dominant over the entire frequency spectrum, whereas in low viscosity fluids the transducer only becomes a significant factor at very high transducer quality factors and cavity resonances exert the dominant influence on the atomizer performance.

This understanding of the coupled transducer-cavity electromechanical-acoustic behavior allows one to formulate a set of simple guidelines for optimal design of horn-based ultrasonic atomizers, in particular accounting for the viscosity of the working fluid to be atomized. Atomizer performance with low viscosity working fluids can be optimized by selecting the fluid cavity geometry such that it operates at one of its fluid cavity resonances and also exhibits large acoustic input impedance. A high quality factor transducer is then selected with a first order short circuit transducer resonance near the fluid cavity resonance. Taken together, the combined effect of the high quality factor fluid cavity resonance and the high quality factor transducer short circuit resonance generate the largest pressure gradients. Atomizer performance with high viscosity working fluids is a sole function of the transducer characteristics. The generated pressure gradient is maximized by selecting a piezoelectric transducer with a high resonance quality factor and short circuit transducer resonance at the operating frequency of interest. Atomizer operation would ideally occur at as low of frequency as possible to minimize the acoustic power loss in the cavity. In this manner using the developed model for horn-based ultrasonic atomizers, an optimum atomizer can be constructed for any given working fluid to maximize the pressure gradient at the horn aperture and thereby promote fluid ejection to the greatest possible extent.

4.3 Application of the ejection threshold to determine fluid ejectability

Maximization of the generated pressure gradient magnitude does not in itself guarantee the ejection of a working fluid by horn-based ultrasonic atomization. The pressure gradient magnitude must attain a value in excess of the pressure gradient threshold for fluid ejection to take place. As done for the initial geometry, the maximum generated pressure gradient magnitude when driven at the dielectric breakdown voltage can be compared to the pressure gradient threshold for atomizer configurations more broadly. Due to linearity of the problem, scaling the pressure gradient produced for 1V input to the transducer by the maximum voltage for each transducer thickness directly gives the maximum pressure gradient that can ever be achieved for each transducer thickness. Figure 4.12 gives the maximum pressure gradient magnitude at the breakdown voltage as a function of transducer thickness for the artificial test fluids with 1mPas and 10Pas viscosities and a fixed fluid cavity configuration. These viscosities correspond to ejection thresholds of 10^{10} and 10^{14} Pa/m. For 1mPas viscosity, almost any fluid cavity resonance produces a sufficiently large pressure gradient for fluid ejection. The 10 Pas test fluid shows no viable fluid cavity resonances for fluid ejection in the examined atomizer configuration.

When the fluid cavity geometry is allowed to vary, this same trend is found to hold across all the fluid cavity geometries - that is that most atomizer configurations are capable of ejecting low viscosity fluids at multiple cavity resonant modes but none are capable of producing a sufficient pressure gradient to eject liquids with viscosities greater than 1 Pas. Table 4.2 provides the maximum generated pressure gradient magnitude as a function of viscosity in the artificial working fluid when the atomizer geometry is allowed to vary as well as the associated pressure gradient threshold. The highest

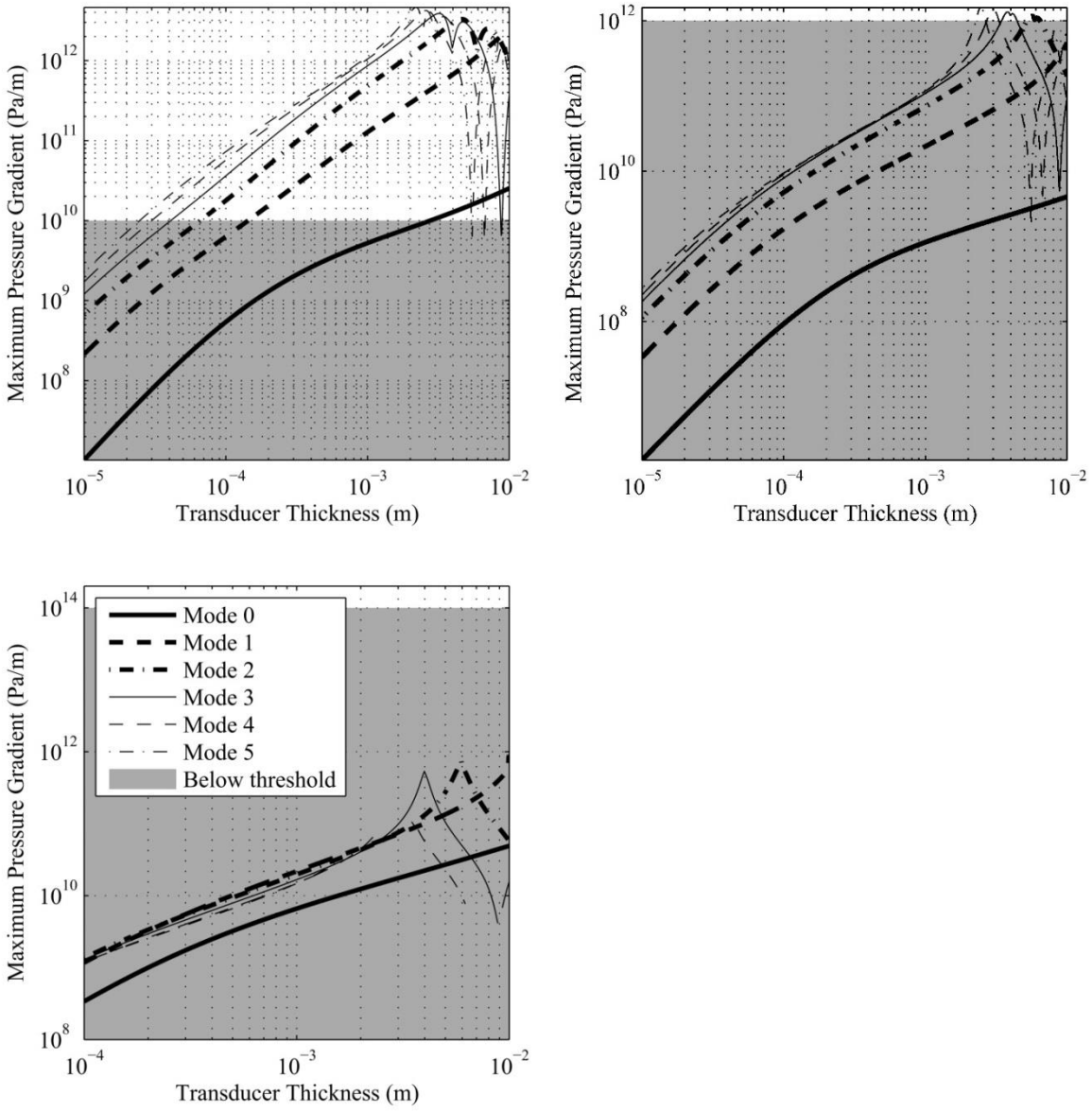

Figure 4.12: Variation in the pressure gradient magnitude at the horn aperture for each fluid cavity resonance as a function of transducer thickness when driven by a voltage signal limited by the transducer dielectric breakdown field threshold. The pressure gradient threshold for each viscosity is shown in gray, with configurations in white zone capable of producing a sufficient pressure gradient for fluid ejection. The horn is 1mm with a 4mm reservoir. The sound speed and density of the working fluid are taken to be equal to those of water. Top left: Working fluid viscosity is equal to 1mPas. Top right: Working fluid viscosity is equal to 100mPas. Bottom left: Working fluid viscosity is equal to 10Pas.

Table 4.2: The maximum pressure gradient magnitude produced by a horn-based ultrasonic atomizer for increasing viscosity in the artificial working fluid. The atomizer geometry was allowed to vary in order to generate the largest pressure gradient possible when the fluid cavity was driven at the dielectric breakdown voltage of the coupled transducer.

Working Fluid Viscosity (Pas)	Horn Length (μm)	Reservoir Length (μm)	Transducer Thickness (mm)	Frequency (kHz)	Maximum Pressure Gradient (GPa/m)	Pressure Gradient Threshold (GPa/m)	Ejection
0.001	230	653	1.493	997	8300	10	Yes
0.01	235	641	1.645	998	4943	100	Yes
0.1	264	607	1.788	1000	2829	1000	Yes
1	310	547	1.889	997	1723	10,000	No
10	235	105	1000	217	2648	100,000	No

working fluid viscosity for which the pressure gradient threshold is exceeded is 100 mPas. This indicates that there is a fundamental limit on ejectability as function of fluid viscosity that can be realized by the exploiting horn-based ultrasonic atomization beyond which alternative atomization approaches need to be explored. Specifically, this analysis suggests that working fluids with viscosities on the order of 100mPas present the upper limit of fluids able to be ejected by the horn-based ultrasonic atomizers.

When multiple atomizer configurations are identified that produce a maximum pressure gradient above the pressure gradient threshold, the efficiency with which the pressure gradient is generated should be considered when selecting a configuration for a physical device. The efficiency of the atomizer can be judged by the pressure gradient produced per unit of electric power input to the piezoelectric transducer. This metric is important to the atomizer operation as only a small fraction of the power input to the transducer is transferred to the ejected fluid; the remainder is dissipated as heat by the transducer and the acoustic field which heats the working fluid.[62] Fluid heating could

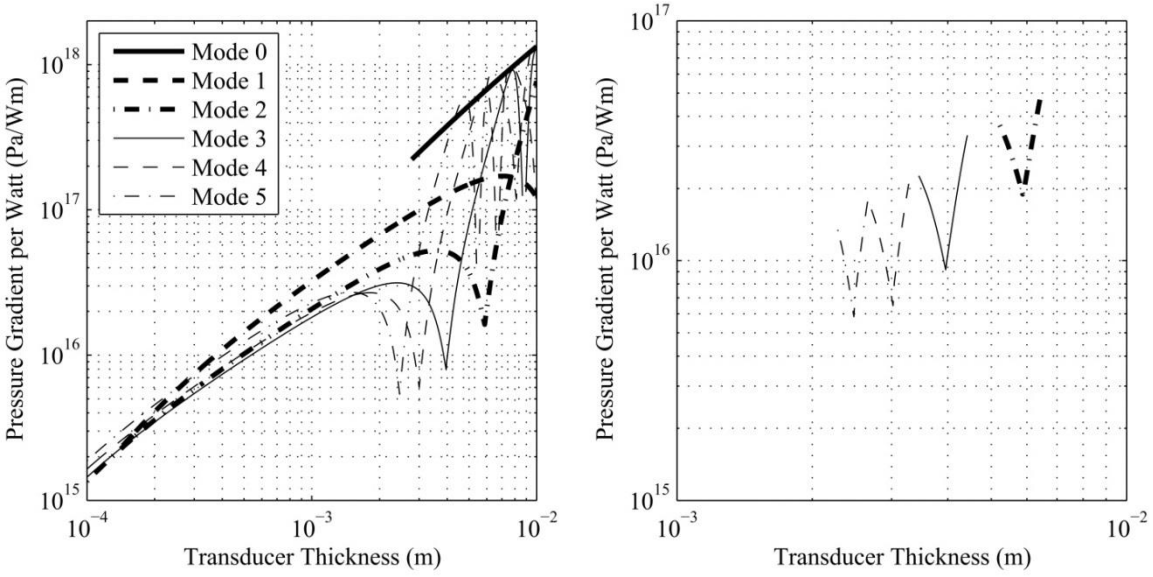

Figure 4.13: Variation in the pressure gradient magnitude per watt of input power to the transducer for each fluid cavity resonance as a function of transducer thickness. The sound speed and density of the working fluid are taken to be equal to those of water. The transducer area corresponds to the area of an individual atomizer cell. Left: Working fluid viscosity is equal to 1mPas. Right: Working fluid viscosity is equal to 100mPas.

result in degradation of the thermally sensitive polymers or premature curing of the working fluid.

Figure 4.13 gives the pressure gradient per watt of electric input power for the maximum gradient configurations in the artificial working fluid for 1mPas and 100mPas viscosities. In general, low order fluid cavity resonance modes tend to have the most efficient ejection; however, when a transducer short circuit resonance frequency becomes comparable to a fluid cavity resonance frequency, power consumption increases in the transducer resulting in a drop in atomizer efficiency. This results in transducer thicknesses where higher order fluid cavity modes yield more efficient ejection than lower modes, making the selection of an atomizer configuration nontrivial. Additionally, while the zeroth order fluid cavity mode efficiently produces pressure gradients, physical devices using piezoelectric transducers of reasonable thickness have difficulty accessing

the zeroth order fluid cavity mode due to its low frequency in spite of the model prediction. Feasible fluid cavity modes for ejection are thus confined to the first order and above. One can utilize the atomizer model to develop curves as in Figure 4.13 to select a configuration that meets the pressure gradient threshold in the most efficient manner.

Following a similar approach, it is possible to determine the ejectability of any working fluid as well as to determine an optimal atomizer configuration for its ejection. Although only an order of magnitude estimate, the ability to determine configurations that will eject working fluids of various viscosities is a powerful tool for optimizing both the design and operation of horn-based ultrasonic atomizers within the domain of the model applicability.

4.4 The ejectability of physical fluids

Characterization of the acoustic behavior of horn-based ultrasonic atomizers has thus far been limited to an artificial test fluid to isolate the effect of viscosity on fluid ejectability; here, the model is applied to two common liquids to determine their ejectability. Table 4.3 shows the atomizer configurations that yield the largest pressure gradient in glycol (30 mPas) and glycerol (1.4 Pas) following an exhaustive search of

Table 4.3: Configurations yielding the largest pressure gradient magnitude at the horn aperture for various working fluids when the piezoelectric transducer is driven by a voltage signal limited by its dielectric breakdown field.

Working Fluid	Horn Length (μm)	Reservoir Length (μm)	Transducer Thickness (mm)	Frequency (kHz)	Maximum Pressure Gradient (GPa/m)	Pressure Gradient Threshold (GPa/m)	Ejection
Glycol	245.6	707.8	1.691	1000	4115	3000	Yes
Glycerol	310.8	699.1	1.863	1000	1980	14000	No

various combinations of fluid cavity geometries and feasible transducer thicknesses. The pressure gradient thresholds were taken as 3×10^{12} Pa/m and 1.4×10^{14} Pa/m, respectively, based on the previously established scaling arguments. While the model predicts multiple atomizer configurations that are capable of ejecting glycol, no atomizer configuration yields a pressure gradient magnitude sufficient for glycerol ejection. This stands in contrast to the experimental work of Meacham et al. and Margolin which demonstrated the ability to eject glycerol with horn-based ultrasonic atomization.[28, 62] While the exact cause of the discrepancy between the ejectability predicted by the analytical model and that seen in physical devices is unknown, it is expected that the inconsistency could result from two different mechanisms: a reduction in the pressure gradient threshold compared to the scaling analysis or a reduction of the working fluid viscosity through heating.

The pressure gradient threshold obtained through scaling analysis, while useful in establishing an estimate of fluid ejectability, is limited by the assumptions inherent to a scaling analysis approach and the current understanding of the fluid mechanics that occur at the horn aperture. Scaling analysis provides an order of magnitude estimate of the pressure gradient threshold required for fluid ejection, meaning values are accurate only to the nearest power of ten. This produces a large uncertainty around the true ejection pressure gradient threshold for a given fluid as the true ejection threshold could be within a power of ten larger or smaller than the scaling analysis predicts, assuming that the fundamental mechanisms of fluid ejection remain consistent with increasing viscosity such that the scaling arguments remain valid. For very low (1 mPas) or very high viscosity working fluids (>10 Pas), the uncertainty in the pressure gradient threshold is

less important as several orders of magnitude separate the generated pressure gradient magnitude from the pressure gradient threshold. However, in medium viscosity working fluids (100 mPas - 1 Pas), this order of magnitude uncertainty in the pressure gradient threshold becomes significant in determining the ejectability of a working fluid. A pressure gradient threshold with greater accuracy is required to be able to say with more confidence that a given working fluid can or cannot be ejected based on the produced pressure gradient alone.

An additional limitation with the scaling analysis approach for the pressure gradient threshold lies in the assumption of a similar fluid mechanics regime at the horn aperture. In low viscosity working fluids, the fluid mechanics regimes at the horn aperture have been well documented by Meacham et al., being governed by the relative magnitude of the Strouhal number ($St = fr_{apt}/v_z$) and the Weber number ($We = \rho_0 v_z^2 r_{apt}/\sigma$).[59] For different values of the nondimensional groups, the atomizer can transition from a drop-on-demand to jetting ejection regimes. This alters the shear stresses present at the horn aperture and, in turn, modifies the pressure gradient threshold required for fluid ejection. While the fluid mechanics at the aperture have been characterized for low viscosity fluids, a similar characterization has not been conducted for medium and high viscosity working fluids. An increased working fluid viscosity could significantly alter the ejection characteristics at the aperture, potentially lowering the pressure gradient threshold. The utilized scaling analysis assumes that both St and We remained constant and that increasing viscosity does not influence the fluid mechanics behavior. While the former is a reasonable assumption based on the similarity in physical properties between water and glycerol, the latter assumption must be explored

further to determine if a reduction in the pressure gradient threshold occurs due to changing fluid mechanics underlying the ejection of medium and high viscosity working fluids. This would require additional research beyond the scope of the present work to develop a fundamental understanding of the fluid mechanics that occur at the aperture.

The second mechanism which would permit the ejection of high viscosity working fluids, either in combination with the revisions to the pressure gradient threshold or on its own, is heating of the working fluid to reduce the working fluid viscosity. When operating at a fluid cavity resonance, a large mechanical power in the acoustic field and electrical power in piezoelectric transducer is dissipated. If a significant fraction of the thermal energy remains in the working fluid, the working fluid temperature will increase. The viscosity of most working fluids declines with increasing temperature. Energy dissipation during operation could therefore result in a working fluid which, while not initially ejectable at room temperature due to high working fluid viscosity, becomes ejectable after a period of time due to rising working fluid temperature and lowering working fluid viscosity. During their experiments with horn-based ultrasonic atomizers, both Meacham et al. and Margolin recorded significant temperature increases during operation.[28, 62] However, neither rigorously recorded if fluid ejection preceded working fluid heating or if working fluid heating was a precondition to fluid ejection. The extent of working fluid heating expected during atomizer operation with high viscosity working fluids is subsequently examined in more detail.

4.5 The importance of heating effects to device operation

Horn-based ultrasonic atomizers are sensitive to the amount of heat produced during device operation through the reduction in the working fluid viscosity that occurs as the working fluid increases in temperature. The lowering of the working fluid

viscosity reduces both the viscous dissipation in the fluid cavity and the pressure gradient threshold. The former increases the acoustic pressure gradient magnitude generated by the atomizer while the later decreases the pressure gradient magnitude that must be obtained for fluid ejection to occur. The sensitivity of atomizer operation to working fluid heating depends on the how strong the viscosity of a working fluid is as a function of temperature. Taking glycerol as an example, a temperature increase of just 15 degrees from 20° C to 35° C is sufficient to reduce the viscosity of glycerol from 1.4 Pas to 0.4 Pas.[117] With a reduction in viscosity of this extent, the maximum predicted pressure gradient generated by the ultrasonic atomizer is within the order of magnitude estimate of the pressure gradient threshold which would indicate that fluid could be ejected.

The strength of the dependence of working fluid viscosity on temperature can be captured through the nondimensional Nahme number which compares the rate viscosity decrease due to viscous shear stress heat to the rate of viscosity increase due to heat conduction from the working fluid, given as:

$$Na = \frac{\alpha_T v_z^2 \mu}{k_{cond}} \tag{4.1}$$

where k_{cond} is the thermal conductivity of the working fluid, v_z is taken to be the characteristic velocity of fluid ejection(fr_{apt}), and α_T is a fitting parameter with units of inverse Kelvin which gives the rate at which the working fluid viscosity changes with temperature.[118] The α_T parameter can be found by experimentally measuring the change in viscosity as a function of temperature and fitting an exponential function to the data:

$$\mu = \mu_0 e^{-\alpha_T (T - T_0)} \tag{4.2}$$

where μ_0 and T_0 are the viscosity and temperature at a reference condition. Nahme numbers much less than one indicate that the working fluid viscosity is insensitive to changes in working fluid temperature due to the combination of heat being conducted efficiently from the liquid and a limited dependence of working fluid viscosity on temperature. Nahme numbers much greater than one indicate that the working fluid viscosity is sensitive to change in working fluid temperature due to high shear stresses or a strong temperature dependence of the working fluid viscosity.

Figure 4.14 plots the Nahme number for various glycerol/water mixtures of increasing viscosity. Viscosity, α_T, and thermal conductivity values used in generating the figure are given in Table 4.4 and are referenced to 20 ºC. In both water and the 40% glycerol working fluids, Na is small due to the magnitude of μ and working fluid heating alters the viscosity little. However, beginning with the 60% glycerol mixture, μ is sufficiently large that Na begins to exceed one indicating that changes to the working fluid viscosity will become important as the working fluid temperature increases. Pure glycerol shows the most significant temperature dependence with Nahme values greater than one across all operating frequencies of interest. One therefore expects, particularly in pure glycerol, that small changes in operating temperature will result in large changes to the viscosity of the working fluid which will, in turn, have a significant impact on atomizer operation and fluid ejectability.

As the reduction in working fluid viscosity due to increased temperature is expected to be significant, an estimate of the rate of temperature increase in the working fluid is required to understand the magnitude of the heating effects. There are two main sources of energy dissipation in the operating device: mechanical losses in the acoustic

field and electrical resistance losses in the piezoelectric transducer. The dissipated power and the temperature increase associated with each dissipation mechanism can be determined through scaling analysis to obtain an order of magnitude estimate for the change in working fluid viscosity expected during device operation.

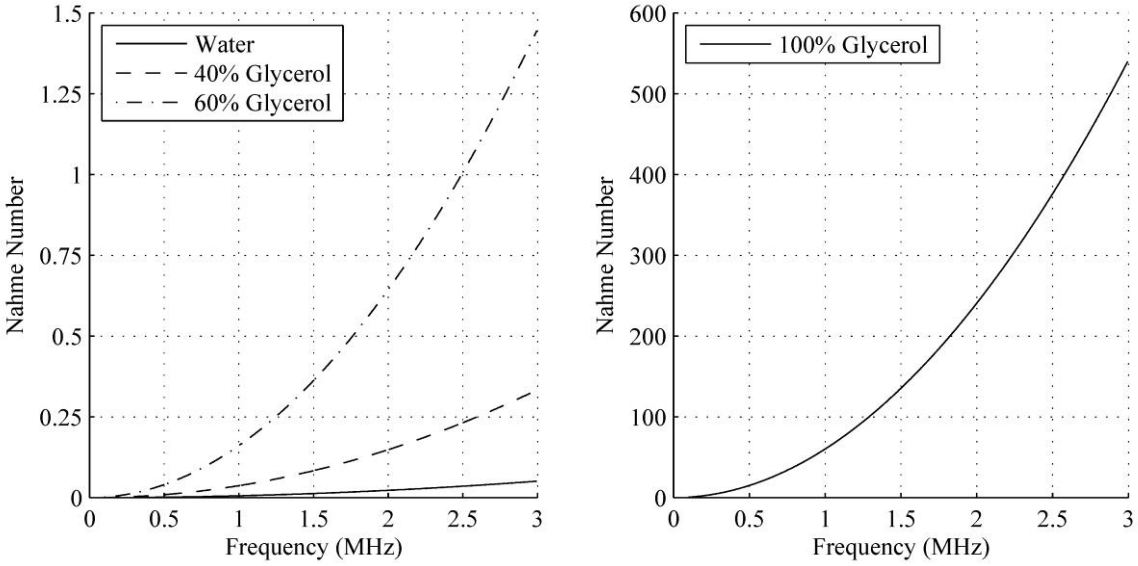

Figure 4.14: The Nahme number predicted for glycerol/water mixtures as a function of operating frequency.

Table 4.4: Physical data used to calculate the Namhe number for working fluid of increasing glycerol percentage by mass.[117, 119] A linear interpolation was utilized to obtain unavailable property values for mixtures between pure water and pure glycerol.

Glycerol percentage	α_t 1/K	Thermal conductivity W/mK	Viscosity mPas
0%	0.021	0.578	1
40%	0.029	0.448	3.7
60%	0.036	0.381	10.8
100%	0.078	0.285	1410

4.5.1 Heating due to power dissipation in the acoustic field

Power in the acoustic field is maximum at the fluid cavity/transducer interface and declines with propagation distance as energy is transferred into viscous dissipation, kinetic energy of the ejected fluid, and motion of the confining wall. Of these three loss mechanisms, only viscous dissipation in the fluid cavity contributes significantly to fluid heating through bulk attenuation and boundary layer shear stresses. As energy loss due to bulk attenuation is several orders of magnitude less than that due to the acoustic boundary layer, the principal dissipation mechanism can be taken as the radial component of the shear stress in the acoustic horn. Moreover, as the overall magnitude of the viscous energy dissipation is small, an increased temperature is only expected in the aperture region where the radial component of the shear stress is largest.

The extent of the localized increase in temperature and resulting reduction in working fluid viscosity can be determined through the use of scaling analysis. Considering the radial component of the viscous stress which is dominant in the aperture region, the viscous heat generation per unit volume is given as:

$$w_{diss} = \mu \left[\frac{\partial v_z}{\partial r}\right]^2 \tag{4.3}$$

The characteristic velocity in the aperture region is proportional to the operating frequency multiplied by the aperture radius. Substituting and simplifying yields a volumetric energy dissipation at the aperture of the following form:

$$w_{diss} \propto \mu \frac{\left(f r_{apt}\right)^2}{r_{apt}^2} = \mu f^2 \tag{4.4}$$

The large shear stresses occur over a volume proportional to the area of the aperture with an axial length scale also proportional to the aperture radius:

$$V \sim \left(\pi r_{apt}^2\right) r_{apt} = \pi r_{apt}^3 \tag{4.5}$$

The total power dissipation in the aperture region is thus proportional to:

$$W_{diss} \propto \pi \mu f^2 r_{apt}^3 \tag{4.6}$$

The dominant mechanism of heat dissipation in the aperture region is governed by the two timescales associated with the thermal diffusivity and fluid advection. The thermal diffusivity timescale (t_{diff}) is associated with the time required for the heat generated in the aperture region to be conducted to the surrounding environment. The advective timescale (t_{adv}) is associated with the fluid leaving the aperture region due to ejection:

$$t_{diff} \propto \frac{L^2}{\alpha} = \frac{r_{apt}^2 \rho_0 c_p}{k_{cond}} \tag{4.7}$$

$$t_{adv} \propto \frac{L}{v_z} = \frac{r_{apt}}{r_{apt} f} = \frac{1}{f} \tag{4.8}$$

where c_p is the specific heat at constant pressure. Two thermal regimes exist based on the relative magnitude of the two timescales.

Considering the case where $t_{diff} \ll t_{adv}$, heat is generated in the aperture region and has sufficient time to conduct axially to produce a uniform temperature. All the produced heat goes into increasing the internal energy of the fluid in the aperture region. Assuming a uniform temperature in the aperture region, the change in internal energy can be expressed as:

$$\frac{dU}{dt} = m_{apt} c_v \frac{dT}{dt} \tag{4.9}$$

where U is internal energy, c_v is the specific heat at constant volume, and T is temperature. Taking the volume as Equation 4.5, the change in internal energy becomes:

$$\frac{dU}{dt} = \pi \rho_0 r_{apt}^3 c_v \frac{dT}{dt} \tag{4.10}$$

In the aperture region, the governing timescale is the operating frequency. This allows the change in temperature as a function of time to be approximated as:

$$\frac{dT}{dt} \propto \Delta T f \tag{4.11}$$

Substituting Equation 4.11 into Equation 4.10 and taking the increase in internal energy to be proportional to the energy dissipated in the aperture region (Equation 4.6), one can calculate the expected increase in temperature:

$$\Delta T \propto \frac{\mu f}{\rho_0 c_v} \tag{4.12}$$

Considering the case where $t_{diff} \gg t_{adv}$, fluid advection occurs much more rapidly than axial thermal conduction in the aperture region. Heating in the aperture region can be modeled as flow through pipe with a constant radial temperature and volumetric heat generation, given as:

$$\dot{m} c_p \frac{dT}{dz} = A w_{diss} \tag{4.13}$$

where $\dot{m}$ is the mass flow rate, c_p is the heat capacity at constant pressure, and A is the cross-sectional area. The mass flow rate in the aperture region can be taken to be proportional to the axial velocity and the cross-sectional area:

$$\dot{m} \sim \rho_0 A v_z \tag{4.14}$$

The axial velocity can be approximated as the characteristic ejection velocity $f r_{apt}$ and substituting for the area gives:

$$\dot{m} \sim \pi \rho_0 f r_{apt}^3 \tag{4.15}$$

The axial temperature derivative can be approximated as the change in temperature over an axial length scale proportional to the aperture radius:

$$\frac{dT}{dz} \propto \frac{\Delta T}{r_{apt}} \tag{4.16}$$

Substituting Equations 4.16 and 4.15 into Equation 4.13 as well as Equation 4.4 for the volumetric heat generation gives an estimate for the expected change in temperature:

$$\Delta T \propto \frac{\mu f}{\pi \rho_0 c_p} \tag{4.17}$$

This expression is a closely resembles Equation 4.12 for the expected temperature increase with c_p substituted for c_v. This follows physical intuition as all dissipated energy remains stored in the working fluid producing the maximum temperature increase. In general, this would be an upper value to the expected temperature increase as heat conduction would also transfer heat into the walls surrounding the working fluid.

Of the two thermal regimes at the aperture, the advective timescale is expected to be much smaller than the diffusivity timescale, meaning the fluid advection regime will occur for the majority of operating conditions. Operating at 1 MHz with water as a working fluid results in $t_{adv} = 1 \times 10^{-6}$ with $t_{diff} = 5 \times 10^{-3}$. As the thermal conductivity of other working fluids will in general be less than water, the fluid advection regime will continue to be dominant as the thermal diffusivity timescale will increase. Table 4.5 gives the order of magnitude estimate for the local temperature increase at the aperture at 1 MHz as a function of working fluid viscosity, assuming a constant density and heat capacity equivalent to water. The temperature increase per ejection cycle predicted at the aperture due to viscous dissipation is small and increases as a function of the working fluid viscosity.

Viscous heating at the aperture occurs rapidly upon the start of atomizer operation and is cumulative if ejection does not occur. Mechanical energy in the acoustic field is transported to the aperture and dissipated by the local shear stresses at the timescale:

$$t_{mech} = \frac{L}{c} \tag{4.18}$$

where L is the total ejector length. The transport timescale is on the order of 10^{-6} s in typical device geometries with most working fluids. As t_{mech} is quite small in absolute terms, heating due to mechanical dissipation can be assumed to be immediate upon atomizer startup. A limitation of the present analysis is the assumption that the working fluid will be advected via ejection with each ejection cycle. If ejection does not advect the working fluid from the aperture region, the predicted fluid heating would accumulate and increase temperature beyond the predicted value. The increase in working fluid temperature could become large and result in a significant reduction of the working fluid viscosity were fluid not to leave the aperture region for several ejection cycles. The extent to which liquid fails to advect from the aperture region, particularly at atomizer startup, remains an area which requires further analysis beyond the scope of the present work.

4.5.2 Heating due to power dissipation in the piezoelectric transducer

The second heating mechanism in the fluid cavity is the dissipation of electric energy in the piezoelectric transducer. The electric power dissipated in the transducer can be directly calculated from the transducer electrical impedance and the applied voltage:

Table 4.5: Local temperature increase at the horn aperture due to viscous shear stresses as a function of working fluid viscosity.

Working fluid viscosity mPas	Temperature increase K
1	$2x10^{-4}$
10	$2x10^{-3}$
100	$2x10^{-2}$
1000	$2x10^{-1}$
10,000	$2x10^{0}$

$$\dot{W}_{diss} = Re\left\{\frac{V_{rms}^2}{Z_e}\right\} \tag{4.19}$$

$$Z_e = R + jX \tag{4.20}$$

$$\dot{W}_{diss} = \frac{V_{rms}^2 R}{R^2 + X^2} \tag{4.21}$$

Heat generated in the transducer is dissipated to both the working fluid and the air on either side of the transducer. In general, as the thermal conductivity of the working fluid is larger than air, one would expect that heat preferentially is transferred into the working fluid. Taking the limiting case where all the thermal energy generated by the transducer is transferred to the fluid cavity, one must calculate the time rate of change in the internal energy of the working fluid to determine the time rate of change in temperature of the atomizer cell with the addition of thermal energy. The time rate of change in internal energy is given by:

$$\frac{dU}{dt} = mc_V \frac{dT}{dt} \tag{4.22}$$

where m is the mass of the working fluid in an atomizer cell. The mass of the working fluid in the atomizer cell is given by the volume of the fluid in the fluid reservoir and the volume of the fluid in the horn section, multiplied by the fluid density:

$$m = \rho_0(V_{res} + V_{horn}) \tag{4.23}$$

The volume of the fluid in the reservoir can be treated as a cylinder with length equal to the length of the reservoir and a radius equal to the horn entrance area:

$$V_{res} = \pi r_{ent}^2 l_{res} \tag{4.24}$$

The volume of fluid in the horn can be treated as a conical frustum with length equal to the horn length and with large and small diameters given by the entrance and aperture diameters respectively:[120]

$$V_{horn} = \frac{1}{3}\pi l_{horn}(r_{ent}^2 + r_{ent}r_{apt} + r_{apt}^2) \tag{4.25}$$

The form of the change in internal energy can be found by substituting in for the mass of the liquid:

$$\frac{dU}{dt} = \pi\rho\left[r_{ent}^2 l_{res} + \frac{1}{3} l_{horn}(r_{ent}^2 + r_{ent}r_{apt} + r_{apt}^2)\right] c_V \frac{dT}{dt} \tag{4.26}$$

One can then balance the dissipated power against the change in internal energy to arrive at an expected rate of temperature increase due to the dissipation of electric power alone:

$$\dot{W}_{diss} \propto \frac{dU}{dt} \tag{4.27}$$

$$\frac{dT}{dt} \propto \frac{V_{rms}^2 R}{R^2 + X^2} \frac{1}{\rho\pi\left[r_{ent}^2 l_{res} + \frac{1}{3} l_{horn}(r_{ent}^2 + r_{ent}r_{apt} + r_{apt}^2)\right] c_v} \tag{4.28}$$

Taking 40 V_{rms} as the maximum voltage applied to the transducer during experimental operation, one can plot the expected increase in temperature for

glycerol/water mixtures as a function of operating frequency as is done in Figure 4.15.[62] The predicted temperature increase using this lumped thermal model is large when operating at fluid cavity resonances. However, the transport of thermal energy from electrical dissipation occurs much more slowly than the transport and dissipation of mechanical energy in the working fluid. The transport of thermal energy from the transducer where the electrical energy is dissipated to the fluid cavity aperture where viscosity reduction is of interest occurs over the timescale t_{therm}, given by:

$$t_{therm} \propto \frac{L^2}{\alpha} \tag{4.29}$$

where L is again the total ejector length from the transducer surface to the ejector aperture. The transport timescale is on the order of 10 s in typical device geometries with most working fluids. An extended period of time is thus required for the fluid at the aperture to have an initial temperature increase from the dissipation of electrical energy. Furthermore, several multiples of t_{therm} would be necessary before the temperature at the aperture would become significantly elevated. Figure 4.15 must be interpreted in the context of this extended thermal transport time; while the transducer dissipates sufficient energy to greatly increase the working fluid temperature, the temperature increase would significantly lag operation of the atomizer and require long times to obtain the uniform values predicted by the lumped thermal model. Electrical dissipation in the transducer would therefore not contribute significantly to heating of the working fluid at the aperture during atomizer startup. The atomizer would need to run for an extended period of time before heat from the transducer would become important and a viscosity reduction could be achieved. After the device is powered off having been operated, heating of the working fluid would continue as the heat from the transducer would still be conducted

into the working fluid. An extended time would be required between operating sessions in order to ensure the fluid cavity returns to ambient temperature.

4.5.3 Comments on experimental results presented in literature

In actual devices, the combined effect of mechanical power dissipation in the acoustic field and electric power dissipation in the transducer act to increase the temperature of the fluid cavity. Either heating mechanism is sufficient to yield a significant increase in temperature and a reduction in working fluid viscosity provided long operating times and no fluid ejection. However, if the reduction of working fluid viscosity through heating is the enabling mechanism for the ejection of high viscosity working fluids, working fluid heating must be shown to precede fluid ejection during atomizer operation on the timescales of mechanical and electrical energy dissipation.

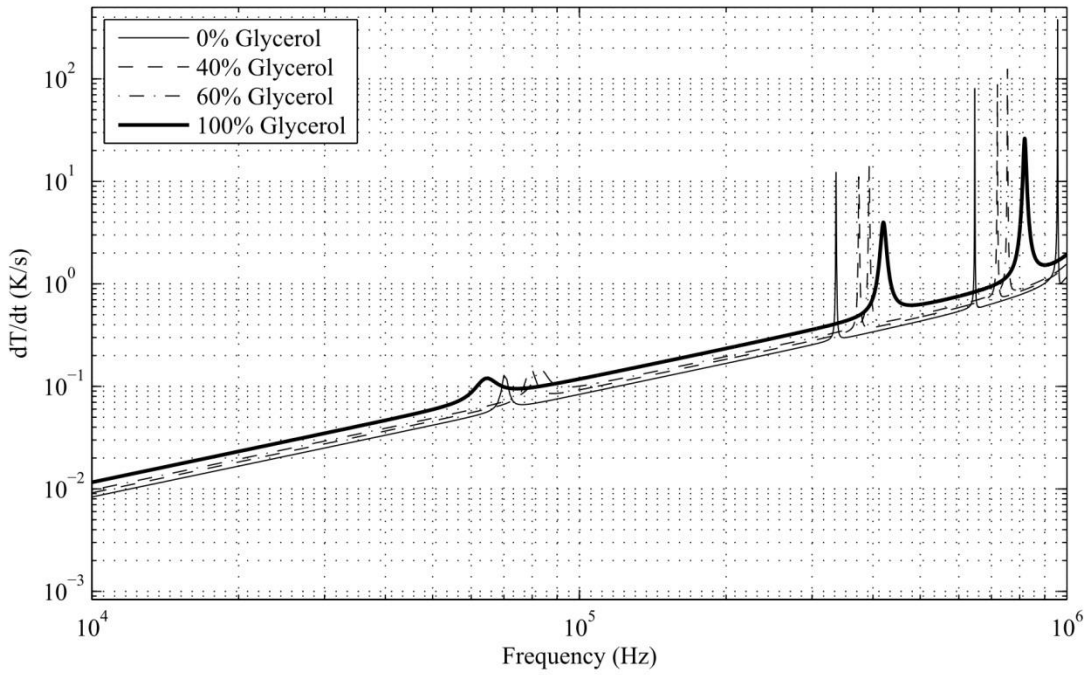

Figure 4.15: Time rate of temperature increase in glycerol/water mixtures due to electric power dissipation as obtained through scaling analysis. The considered atomizer geometry was a 2.1mm reservoir with a 0.5mm horn. The transducer thickness was taken to be 1.5mm.

Understanding the order of events during atomizer operation necessitates an examination of the experiments conducted with the device.

Considerable heating of the working fluid during atomizer operation is supported by the experimental work of Meacham et al. and Margolin, both which recorded operating temperatures and experimental observations for working fluids of various viscosities.[28, 62] Meacham et al. operated the atomizer in two regimes for glycerol/water mixtures, a pulsed regime and a continuous regime. In the pulsed regime, the atomizer was driven with a burst of pulses ($10 < n < 200$) occurring at a repeat rate ($f_{dc} = 500$ Hz) to minimize the operating time of the device while maintaining fluid ejection. The atomizer was active for between approximately five and ten seconds with a net powered time of approximately one second. Table 4.6 reproduces the operating temperature measured at the back port of the transducer in contact with air for the considered working fluids. Meacham et al. a records an elevated operating temperature of 45 °C during the ejection of 100% glycerol. Had a similar increase in temperature occurred in the fluid cavity, the viscosity of 100% glycerol would be reduced from 1.4 Pas to 326 mPas. While the magnitude of the transducer temperature implies that the temperature of the working fluid is also likely elevated, Meacham et al. made no direct measurements of the working fluid to confirm its temperature. Moreover, as fluid ejection likely began at an elevated working fluid temperature, no definitive statements can be made as to whether fluid ejection or heating occurred first during atomizer operation. In the continuous operation extending over 70 s, Meacham reports that the measured temperature rose as high as 50 °C for glycerol which would reduce the working

fluid viscosity to 150 mPas. A reduction in the number of driving pulses was necessary to prevent the temperature from exceeding this value.

Margolin also investigated the ejection of various medium to high viscosity working fluids with horn-based ultrasonic atomization. In contrast to Meacham et al. who measured temperature on the back port of the piezoelectric transducer, Margolin made temperature measurements at the surface of the silicon horn array. This is more representative of the fluid temperature as measurements are not influenced by the high transducer temperatures due to electrical dissipation. In her experiments with glycerol/water mixtures, Margolin also recorded an increase in atomizer temperature, growing as high as 90 °C in continuous operation. At this operating temperature, the viscosity of the highest

Table 4.6: Experimental operating temperatures as reported by Meacham et al. for pulsed operation trials with glycerol/water mixtures.[28]

Glycerol percentage	Operating temperature ºC	Operating viscosity mPas	Nominal viscosity @ 20 ºC mPas
65%	30	10	15
85%	30	59	109
	30	59	
90%	30	112	219
	30	112	
92%	32	131	310
	36	101	
96%	40	143	624
	40	143	
100%	45	201	1410
	38	326	

percentage glycerol mixture is greatly reduced from 625 mPas to 17 mPas. A similar behavior is reported in polyethelene glycol with temperatures increasing from 20 °C to 66 °C with a corresponding viscosity decrease from 500 mPas to 150 mPas. While this work again validates the expectation that the viscosity of the working fluid is greatly reduced during device operation, it does not provide an answer as to whether viscosity reduction through heating is a prerequisite for the ejection in high viscosity working fluids. However, Margolin also remarks that ejection of polyethelene glycol was not immediate with the powering on of the atomizer. Several seconds of atomizer operation were necessary prior to the start of ejection, during which time polyethelene glycol bubbled from the aperture. While this is indicative of the need to reduce the viscosity through heating for ejection to be possible, it is not a sufficient basis by itself to generalize the conclusion across high viscosity working fluids.

The large increase in working fluid temperature predicted by the scaling analysis for extended operation times is supported by the experimental work with horn-based ultrasonic atomizers. The importance of heating effects to the ejection of high viscosity working fluids is also circumstantially supported by the lag between powering the atomizer and the start of fluid ejection noted by Margolin, potentially indicative that power is being dissipated in the device and stored to induce the required working fluid heating. However, this limited information is only sufficient to speculate that heating is the mechanism which permits the ejection of high viscosity fluids but is not sufficient to outright support the heating mechanism hypothesis. The mechanism which enables the ejection of high viscosity fluids with horn-based ultrasonic atomizers remains an

unanswered question. Additional research is necessary to examine both the fluid heating and pressure gradient threshold mechanisms to close the discrepancy between the analytical model and experimental results, such as experimental measurements of the working fluid temperature at the aperture as a function of operating time or a more detailed examination of the fluid mechanics at the fluid cavity aperture that govern fluid ejection.

4.6 The transition to nonlinear device operation

Nonlinear acoustic operation of horn-based ultrasonic atomizers would occur when the acoustic field amplitude generated by the atomizer becomes large enough to influence wave propagation within the fluid cavity. A determination as to whether the atomizer has a nonlinear acoustic response can be made by examining the Goldberg number and shock distance.[121] These parameters quantify nonlinearity in terms of the waveform steepening that results from the variation in acoustic impedance over a wavelength at large amplitudes. The Goldberg number (Go), given in Equation 4.30, compares the rate of waveform steepening due to large acoustic amplitudes to the rate of waveform flattening due to energy dissipation:

$$Go = \frac{\beta \mathrm{Mak}}{\alpha_s} \tag{4.30}$$

where Ma is the Mach number, k is the wave number, β is the coefficient of nonlinearity in liquids given by $\beta = 1 + B/2A$, and α_s is the classical attenuation coefficient. B/A is measured quantity which relates the first and second derivatives of pressure with respect to density for a given medium. As Go becomes large, the waveform steepens faster than attenuation can dissipate energy from high amplitude wave crests leading to shock formation. Conversely, as Go becomes small, attenuation rapidly dissipates energy from

the wave crests thereby delaying shock development. By calculating Go for the maximum Ma seen in the atomizer, the likelihood of a nonlinear atomizer response can be established.

Figure 4.16 plots Go as a function of Ma for three physical fluids at the optimal driving configuration, with the Go number predicted by the atomizer model indicated for each fluid. The nonlinearity and attenuation parameters utilized for the analysis are given in Table 4.7. Previous work by Khelladi indicates that significant nonlinear effects can develop for a Go as low as 55 in water for free space propagation.[122] The large values of Go predicted by the model for all three fluids suggest that significant waveform steepening would be present in the fluid cavity. However, the Go values given in Figure 4.16 represent an upper limit as bulk attenuation is utilized which is known to underpredict the losses in the fluid cavity by several orders of magnitude due to the greater extent of boundary layer dissipation. It is therefore expected that the true Go of the fluid cavity to be much smaller than the calculated value. Even with this reduction, the Go would still remain large which would indicate that nonlinear effects are important at the limiting cases of atomizer operation at the transducer dielectric breakdown voltage.

Table 4.7: Parameters utilized for the nonlinearity analysis. B/A ratios are those given by Hamilton and Blackstock.[121] The maximum velocity for each fluid is the velocity at the aperture when each fluid is driven by its optimal atomizer configuration.

Working Fluid	B/A	Classical Attenuation Coefficient (α/f^2)	Maximum Velocity (m/s)
Water	5.0	8.12×10^{-15}	500
Glycol	9.7	1.56×10^{-13}	213
Glycerol	9.0	4.13×10^{-12}	61

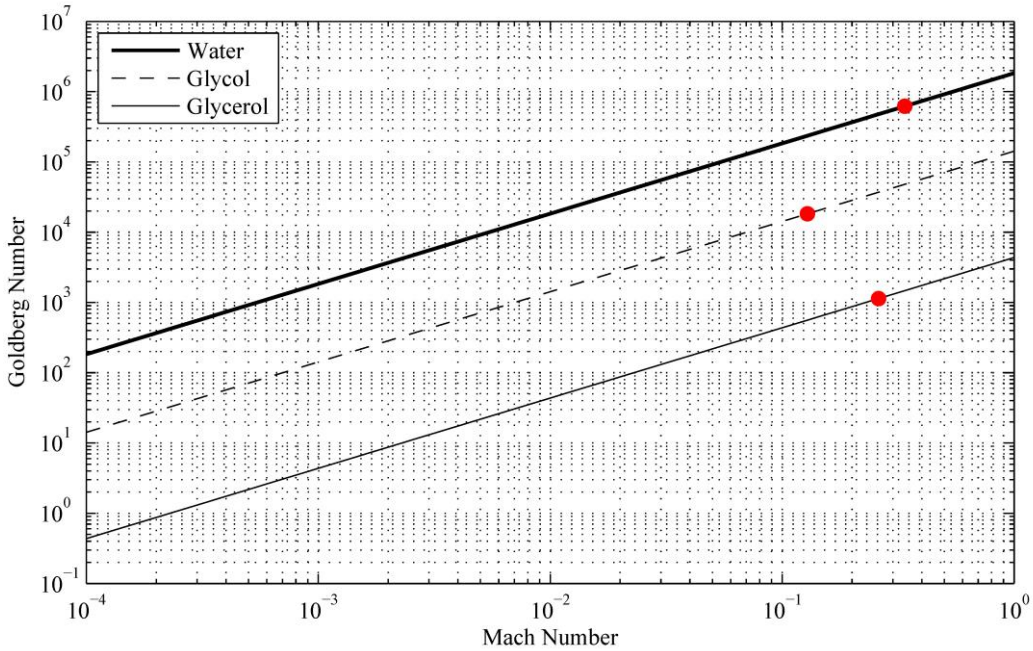

Figure 4.16: Goldberg number as a function of Mach number for various working fluids at their optimal driving configuration. The maximum value predicted by the atomizer model is indicated by the dot. The utilized physical properties are given in Table 4.7 and the frequency corresponds to the optimal driving frequency of each fluid.

The second parameter to examine when determining the importance of nonlinear effects is the shock distance. The shock distance is the minimum distance from the source where the first shock could form in the acoustic field. If the maximum extent of the considered domain in much less than the shock distance, the acoustic field can be considered linear as nonlinear effects have not had sufficient propagation distance to develop. Hamilton and Blackstock derived an expression for shock distance given by Equation 4.31:

$$x_{rt} = \frac{(c + \beta v)^2}{\beta f'} \tag{4.31}$$

where v is the maximum particle velocity amplitude and f' is the derivative of the source velocity forcing function. This expression can be cast as a function of Ma first by factoring the sound speed factor from the numerator:

$$x_{rt} = \frac{c^2(1+\beta Ma)^2}{\beta f'} \tag{4.32}$$

Next, assuming that the source is driven harmonically, f' can be related to f which yields:

$$f' = |j\omega f| = \omega f \tag{4.33}$$

$$x_{rt} = \frac{c^2(1+\beta Ma)^2}{\omega \beta f} \tag{4.34}$$

Finally, a relationship between f and v must be developed to eliminate dependence on the source velocity. In the linear regime, the velocity amplitude at the atomizer aperture scales directly with the velocity imposed by the source transducer:

$$f = \delta v \tag{4.35}$$

where the unknown constant δ can be determined by relating f and v for a given driving configuration. This assumption is sufficient to obtain an estimate of the shock distance, given by Equation 4.36 as a function of the Ma number at the fluid cavity aperture.

$$x_{rt} = \frac{\delta c(1+\beta Ma)^2}{\omega \beta Ma} \tag{4.36}$$

Figure 4.17 plots the shock distance as a function of Ma at the fluid cavity aperture in three physical fluids for the optimal driving configuration, with the shock distance predicted by the atomizer model indicated for each. The calculated shock distance for each fluid is more than an order of magnitude greater than the fluid cavity length associated with the optimal driving configurations. This implies that the fluid cavity is sufficiently small as to minimize nonlinear effects over the propagation domain. While elevated Go would indicate that nonlinear effects are likely to be present at the largest driving voltages, the small propagation distance with respect to the shock distance

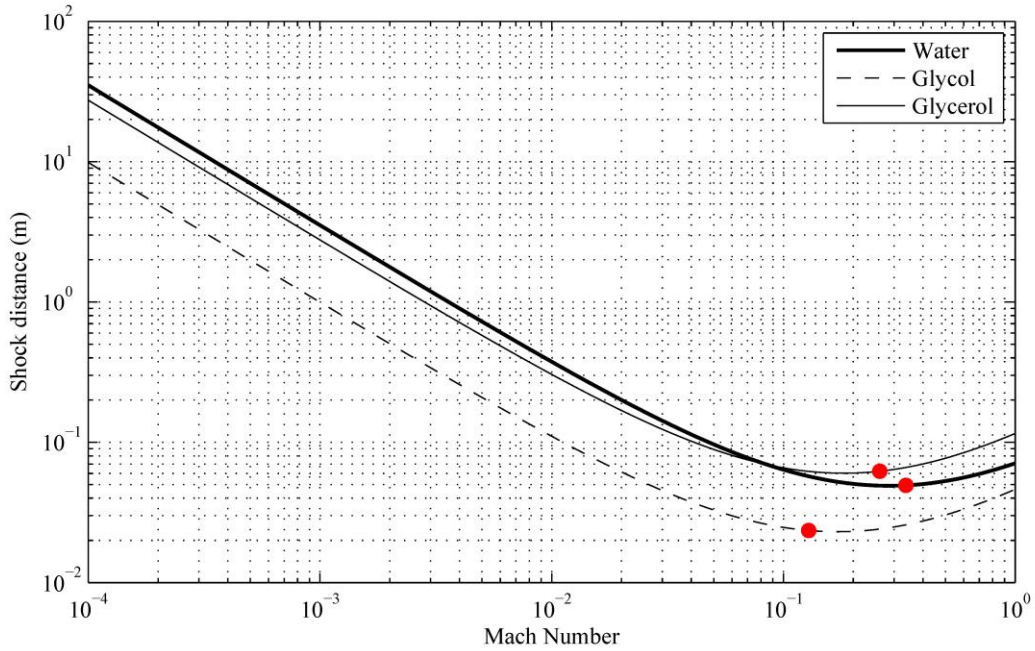

Figure 4.17: Shock distance as a function of Mach number for various working fluids at their optimal driving configuration. The maximum value predicted by the atomizer model is indicated by the dot. The utilized physical properties are given in Table 4.7 and the frequency corresponds to the optimal driving frequency for each fluid.

presents a minimal opportunity for nonlinear effects to accumulate and for the acoustic field to deviate significantly from the linear prediction. The linear prediction of the atomizer model therefore remains a valid representation of physical atomizer behavior.

4.7 Concluding remarks on fluid ejectability

A coupled electro-mechanical model was applied to understand the behavior of and develop design guidelines for the ejection of high viscosity fluids by horn-based ultrasonic atomizers. Each component of the atomizer - the horn, reservoir, and transducer - was examined for its impact on the pressure gradient magnitude produced by the atomizer. The analysis of horn flare showed that the maximum pressure gradient is achieved by the use of a conical profile which minimizes the horn surface area and associated acoustic boundary layer losses. The horn and fluid reservoir lengths were shown to affect the pressure gradient by defining the extent of the acoustic power

dissipation and the frequencies of the fluid cavity resonant modes. Finally, the piezoelectric transducer was shown to impact the response of the atomizer through both its short circuit resonance frequency and its mechanical resonance quality factor. By comparing the maximum pressure gradient magnitude produced by the optimal atomizer configuration against an estimated pressure gradient threshold value required for ejectability, it was shown that working fluids with viscosities on the order of 100 mPas are approaching the limits of ejection capabilities of horn-based ultrasonic atomization devices. Application of the model to assess the ejectability of physical working fluids indicates a discrepancy between the predictive capabilities of the analytical model and experimental measurements. Further research is required to clarify the source of the discrepancy, most likely due to either viscosity reduction through heating of the working fluid or a lack of understanding of the fluid mechanics governing the pressure gradient threshold.

A simple design methodology emerged from the performed analysis for selecting an atomizer configuration as a function of working fluid viscosity. For low viscosity working fluids, a fluid cavity length should first be selected that permits operation at a fluid cavity resonance. A high quality factor transducer should then be selected with a first order short circuit resonance frequency near to the fluid cavity resonance frequency as the high displacements generated by the transducer will be amplified by the fluid cavity. For high viscosity fluids in which the transducer dominates the atomizer response, selection of a high quality factor transducer is most important, preferably with a low frequency short circuit resonance to minimize acoustic losses if a particular operation frequency is not required for the application of interest. A fluid cavity configuration with

a high fluid cavity inlet acoustic impedance occurring at a frequency near the short circuit transducer resonance should then be selected to establish a large pressure amplitude at the fluid cavity inlet.

CHAPTER 5: EXPLORATION OF ALTERNATIVE HORN-BASED ULTRASONIC ATOMIZER DESIGNS

Modifications to the design of horn-based ultrasonic atomizers are examined in an effort to increase the maximum pressure gradient magnitude generated by the device and permit the ejection of higher viscosity working fluids. The previously developed models of the ejector components are utilized to formulate electro-mechanical models of several atomizer designs which have potential to simultaneously minimize the viscous dissipation in the fluid cavity and maximize the amplitude of the acoustic field. The performance of the proposed designs is evaluated with various working fluids and against the standard, unaltered horn-based ultrasonic atomizer.

5.1 Alternative horn-based ultrasonic atomizer designs

Alternative designs to the standard horn-based ultrasonic atomizer given in Chapters 3 and 4 are of interest to increase the maximum pressure gradient magnitude generated by the atomizer so as to exceed the pressure gradient threshold and permit ejection in high viscosity working fluids. Optimization of the standard atomizer geometry in Chapter 4 showed that the acoustic response of the atomizer with high viscosity working fluids is limited by the viscous dissipation occurring in the acoustic boundary layer. Moreover, for highly viscous working fluids, a large acoustic impedance at the fluid cavity inlet is necessary to establish a high amplitude acoustic field to overcome viscous dissipation as the wave propagates to the fluid cavity aperture. Alterative atomizer designs are sought which both reduce the viscous dissipation in the fluid cavity as well as increase the amplitude of the acoustic field.

Minimization of viscous dissipation occurring in the fluid cavity can be accomplished with low operating frequencies or by changing the propagation media within the fluid cavity to a less viscous liquid. As low frequency operation was shown not to be optimal due to the low velocities imposed on the fluid cavity by the transducer, substitution of the propagation media becomes the viable means by which viscous dissipation can be reduced. The high viscosity working fluid targeted for fluid ejection can be confined to the region of the fluid cavity nearest the aperture; the remainder of the fluid cavity can be filled with a low viscosity working fluid which is used as a low loss medium for acoustic wave propagation. The two fluids are kept separate by a thin membrane which, due to its thinness as compared to the wavelength, is acoustically transparent. By means of the impermeable membrane, the working fluid viscosity throughout the majority of the fluid cavity can be significantly reduced. This, by extension, minimizes viscous dissipation and retains a larger fraction of the energy imposed by the transducer in the acoustic field.

The second means to increase atomizer performance is by imposing a larger driving amplitude at the inlet of the fluid cavity. With a sufficiently large amplitude imposed at the fluid cavity inlet, a large amplitude wave can be maintained near the horn aperture where ejection occurs in spite of the viscous dissipation as the wave propagates to the fluid cavity aperture. The boundary condition at the interface between the fluid cavity and the transducer surface is continuity of volume velocity, or the particle velocity at the transducer surface multiplied by the transducer area. The maximum particle velocity imposed by the piezoelectric transducer is limited by the dielectric breakdown voltage. However, a greater volume velocity can be generated by increasing the

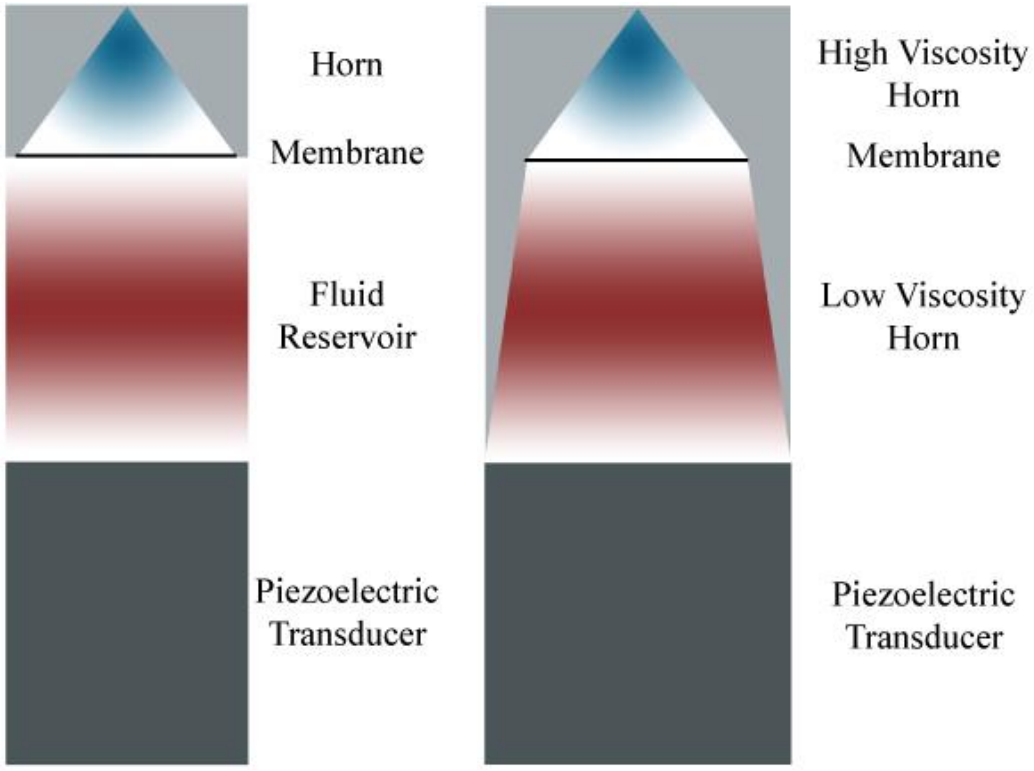

Figure 5.1: Alternative horn-based ultrasonic atomizer designs aiming to increase the maximum generated pressure gradient. The blue fluid indicates the high viscosity working fluid with the red fluid indicating the low viscosity working fluid. Left: The high viscosity horn is coupled to a low viscosity reservoir. The two fluids are separated by a thin membrane. Right: The high viscosity horn is coupled to a low viscosity horn. The two fluids are separated by a thin membrane.

transducer surface area with a second acoustic horn to concentrate the volume velocity to the entrance of the first horn. The greater transducer area combined with the second acoustic horn achieves a greater imposed volume velocity at the entrance of the fluid cavity without damaging the transducer. Furthermore, the secondary horn can utilize the low viscosity working fluid as previously outlined to minimize the losses due to the acoustic boundary layer.

Application of these concepts gives two potential design modifications to the baseline horn-based ultrasonic atomizer, both shown in Figure 5.1. The first design considers an acoustic horn with a high viscosity working fluid, joined to a reservoir with a low viscosity working fluid, and separated by an acoustically transparent membrane.

The second design considers the case where an acoustic horn with a high viscosity working fluid is joined to a second acoustic horn with a low viscosity working fluid, again separated by an acoustically transparent membrane. The subsequent sections develop an analytical model for each of the proposed designs using the previously developed modeling components. The maximum pressure gradient magnitude generated by each design is then compared to the baseline design of the same device loaded in all domains with the high viscosity working fluid only and also to the standard horn-based ultrasonic atomizer configuration of similar horn dimensions as analyzed in the previous chapters.

5.2 Modification of the horn-based ultrasonic atomizer with a low viscosity fluid reservoir

A horn-based ultrasonic atomizer model was developed to investigate a fluid cavity consisting of two media – a low viscosity fluid in the reservoir and a high viscosity fluid in the horn – separated by a thin, acoustically transparent membrane. Development of the model was motivated by the reduction in bulk attenuation resulting from the substitution of a lower viscosity propagation medium in the reservoir region. The formulation of the low viscosity fluid reservoir model will be detailed utilizing the modeling components outlined in Chapter 3. The low viscosity fluid reservoir model will subsequently be applied to various working fluid combinations to determine if such an atomizer configuration can increase maximum pressure gradient magnitude generated by horn-based ultrasonic atomizers.

5.2.1 Development of the low viscosity reservoir model

The structure of the horn-based ultrasonic atomizer with a low viscosity working fluid in the reservoir is equivalent to that of the previously developed atomizer, being

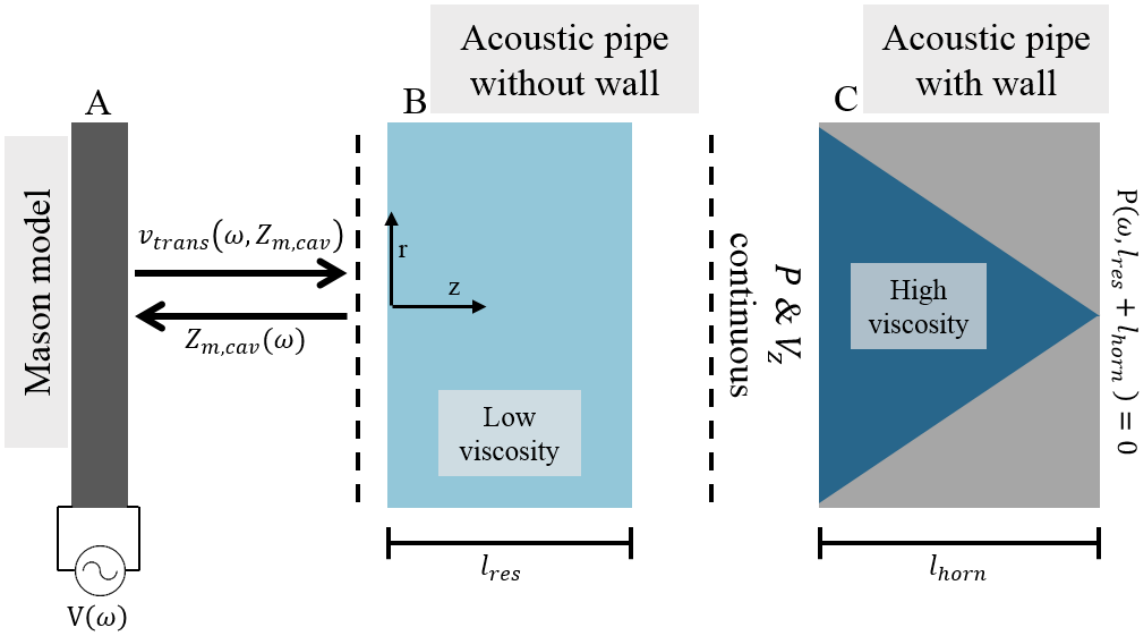

Figure 5.2: A schematic diagram of the ultrasonic atomizer utilizing both a low and high viscosity fluid as propagation media. The model is decomposed into the individual components and the boundary conditions are shown. The low viscosity fluid is utilized in the reservoir with the high viscosity fluid in the horn.

composed of three components: a planar piezoelectric transducer, an acoustic pipe without a wall, and a horn section. Figure 5.2 describes the components of the low viscosity reservoir atomizer model and the boundary conditions that join them. The planar piezoelectric transducer (A) is modeled with the Mason impedance matrix, and the fluid reservoir (B) is modeled as an acoustic pipe without a wall. The acoustic horn (C) is again modeled as a discretized acoustic pipe with a wall. The principal difference in the present model is the usage of two different sets of fluid properties, the first set for the reservoir and the second for the horn, rather than a single set of properties throughout the entire fluid cavity.

At the aperture of the acoustic horn a pressure release condition is assumed given by:

$$P_0\left(Ae^{-j\frac{1}{\sqrt{\epsilon}}\frac{\omega_r(l_{res}+l_{horn})}{c_{horn}}} + Be^{j\frac{1}{\sqrt{\epsilon}}\frac{\omega_r(l_{res}+l_{horn})}{c_{horn}}}\right)\Bigg|_{(l_{res}+l_{horn})^-} = 0 \qquad 5.1$$

The components are coupled by enforcing continuity of pressure and volume velocity at their interfaces. However, the difference in fluid properties and thus the mismatch of acoustic impedances must be accounted for between the models by applying the fluid properties on either side of the interface. At the interface between components B and C, the coupling condition is given by:

$$\left(Ae^{-jk_{res}l_{res}} + Be^{jk_{res}l_{res}}\right)\Big|_{l_{res}^{-}} = P_0\left(Ce^{-j\frac{1}{\sqrt{\epsilon}}\frac{\omega_r l_{res}}{c_{horn}}} + De^{j\frac{1}{\sqrt{\epsilon}}\frac{\omega_r l_{res}}{c_{horn}}}\right)\Bigg|_{l_{res}^{+}} \quad 5.2$$

$$S\left(Ae^{-jk_{res}l_{res}} - Be^{jk_{res}l_{res}}\right)\Big|_{l_{res}^{-}}$$

$$= EuMa(\omega_r w_0 \pi R^2)Ma\left(-j\frac{1}{\sqrt{\epsilon}}Ce^{-j\frac{1}{\sqrt{\epsilon}}\frac{\omega_r l_{res}}{c_{horn}}} + j\frac{1}{\sqrt{\epsilon}}De^{j\frac{1}{\sqrt{\epsilon}}\frac{\omega_r l_{res}}{c_{horn}}}\right) \quad 5.3$$

$$\int_0^{R^*}\left(-\frac{ber_0(r^*) + jbei_0(r^*)}{bei_0(R^*) - jber_0(R^*)} + j\right)r^* dr^*\Bigg|_{l_{res}^{+}}$$

where Equation 5.2 is the for pressure and Equation 5.3 is for the volume velocity. Terms denoted by the subscript *res* indicate fluid properties evaluated in the fluid reservoir while terms denoted by the subscript *horn* indicate fluid properties valuated in the horn. Coupling of component models via the boundary conditions results in a single fluid cavity model. It should be noted that as the speed of sound and density are different across the interface of components B and C, the acoustic field properties (pressure and velocity) will exhibit a discontinuity in slope at the interface.

The coupling between the transducer (A) and the acoustic pipe without walls (B) again enforces continuity of pressure and volume velocity, formulated in terms of the fluid cavity mechanical impedance, and follows the procedure for the atomizer model outlined in Section 3.5. The boundary conditions at the transducer/fluid cavity interface are similar as well, however the calculated fluid cavity acoustic impedance is now a

function of the combined response of the acoustic horn with the high viscosity working fluid and the fluid reservoir with the low viscosity working fluid. At the fluid cavity inlet/transducer surface, the coupling condition can be expressed as:

$$Sv_{trans} = S(A - B)|_{0^+} \quad 5.4$$

$$Z_{m,load}(\omega) = Z_{m,cav}(\omega) \quad 5.5$$

with Equation 5.4 being continuity of volume velocity and Equation 5.5 being the impedance matching condition. The following conditions are associated with the piezoelectric transducer:

$$V(\omega) = V_{applied}(\omega) \quad 5.6$$

$$Z_{m,load}(\omega) = Z_{m,cav}(\omega) \quad 5.7$$

where $V_{applied}$is the voltage applied to the transducer.

5.2.2 Application of the low viscosity reservoir model

The potential for a low viscosity working fluid in the atomizer reservoir to increase the generated pressure gradient magnitude was evaluated by imposing both a specified frequency independent, sinusoidal velocity input and a more realistic condition of a piezoelectric transducer as the driving conditions at the fluid cavity inlet. The velocity condition is utilized to characterize the behavior of the standalone fluid cavity without the electromechanical response of the transducer. This permits a direct comparison of the dual fluid model to the single fluid, baseline atomizer model when driven by the same amplitude acoustic field.

Figure 5.3 gives the pressure gradient magnitude at the horn aperture as a function of frequency for two artificial working fluid combinations and water/glycerol. All fluid combinations were driven with a sinusoidal velocity signal of 1 m/s amplitude applied at

the fluid cavity inlet. Use of the artificial working fluid isolates the effect of working fluid viscosity by maintaining a fixed density and sound speed equal to those of water and only changing the fluid viscosity. The high viscosity artificial working fluids were taken to be 10 Pas and 1 Pas with the reservoir working fluid viscosity as 1 mPas. The 10 Pas working fluid case demonstrates a factor of two improvement in the generated pressure gradient magnitude from using the low viscosity working fluid in the reservoir as compared to the case when both the reservoir and the horn are filled with a high viscosity fluid. The increased pressure gradient occurs only at the fluid cavity resonances below 600 kHz; above 600 kHz the use of the low viscosity fluid cavity reservoir becomes beneficial off the fluid cavity resonances as well. When the working fluid viscosity in the horn component is reduced from 10 Pas to 1 Pas, the difference between the dual fluid and the uniformly high viscosity fluid cavity becomes negligible.

While atomizer performance can be improved using two working fluids, the dual working fluid configuration is not expected to increase the generated pressure gradient magnitude such that the pressure gradient threshold can be attained in working fluids of high viscosity. Moreover, the enhancement of atomizer performance with dual working fluids will be limited across all potential geometries. Substitution of the low viscosity working fluid in the atomizer reservoir is a means to minimize viscous dissipation in the fluid cavity. However, the main source of viscous dissipation is the acoustic boundary layer in the horn component. Substitution of a low viscosity working fluid in the reservoir component reduces the bulk attenuation which is initially several orders of magnitude smaller than the boundary layer losses in the horn component. Substituting a

lower viscosity fluid in the reservoir region does reduce viscous dissipation but the effect of doing so is marginal as viscous dissipation primarily occurs in the horn.

For combinations of physical fluids (e.g., water and glycerol), the use of a low viscosity working fluid (water) in the reservoir has a marginal impact on atomizer performance. Despite the large disparity in working fluid viscosity, the water/glycerol combination in Figure 5.3 generates similar pressure gradient magnitudes as compared to the glycerol/glycerol filled fluid cavity. Since the viscous losses in the horn component are similar for both fluid combinations, one expects that the greater bulk attenuation of glycerol in the fluid reservoir should yield a lesser pressure gradient magnitude. However, due to its greater density and speed of sound, the glycerol filled fluid cavity has a larger acoustic impedance at the fluid cavity entrance producing a larger pressure amplitude (Figure 5.3). The larger pressure amplitude at the fluid cavity entrance offsets the increased bulk attenuation in the fluid reservoir, yielding a similar pressure gradient magnitude at the horn aperture. The effect of the acoustic impedance at the fluid cavity entrance on the pressure gradient magnitude can be seen in Figure 5.4. For a glycerol filled cavity, the density of the fluid in the reservoir component was reduced until approximating water with all other parameters held fixed. As the density of the working fluid in the reservoir decreases, the acoustic impedance at the fluid cavity inlet declines leading to a reduction in the pressure gradient magnitude. The larger density and speed of sound in high viscosity working fluids increase the fluid cavity inlet acoustic impedance which offsets the effects of greater bulk attenuation, ultimately producing a

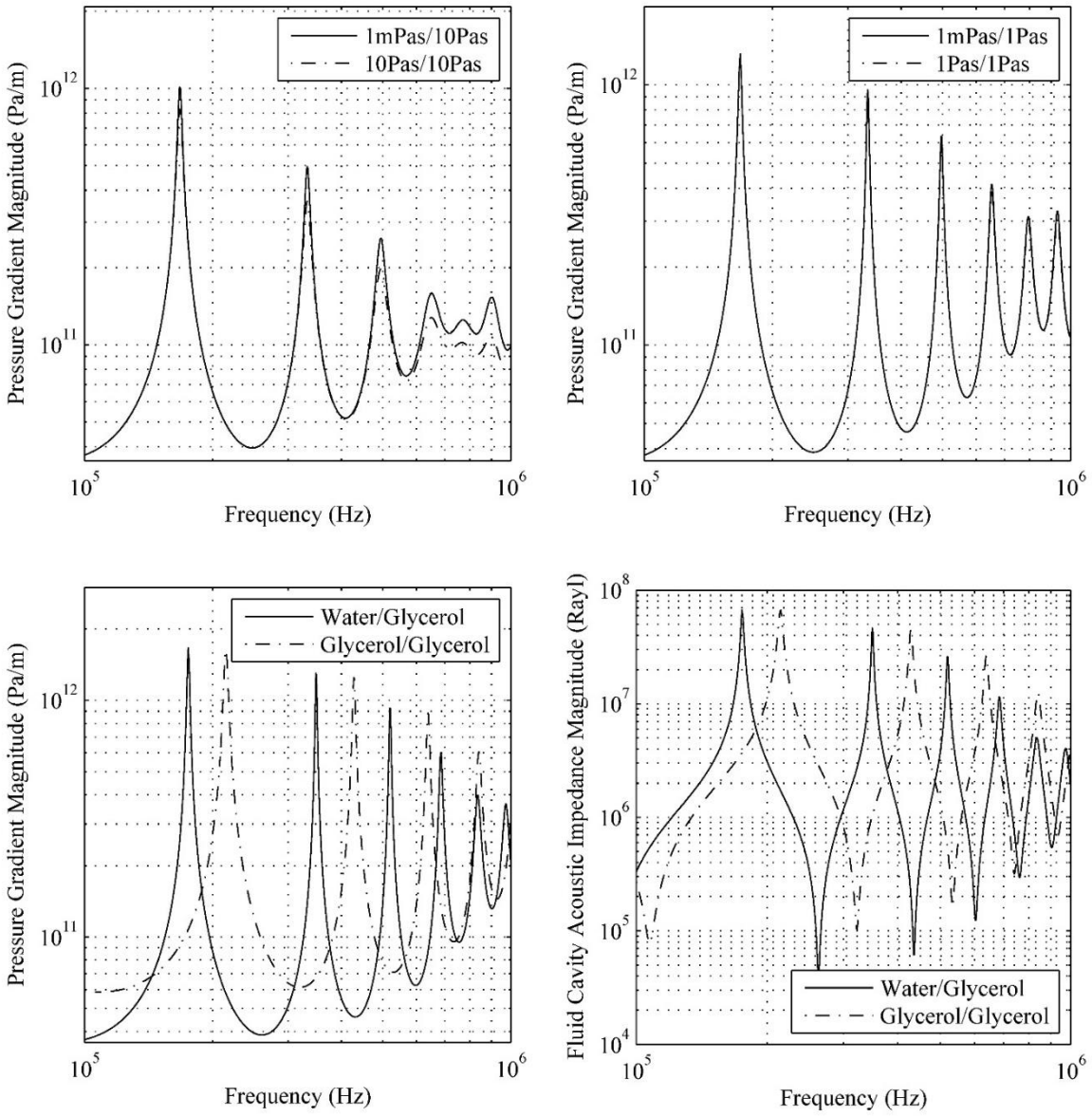

Figure 5.3: The acoustic response of the dual fluid horn-based ultrasonic atomizer when driven by a constant velocity boundary condition of 1 m/s at the fluid cavity inlet for various working fluid combinations. The horn is 1mm with a 4mm reservoir. Upper left: The working fluid is the artificial test fluid with 10 Pas high viscosity in the horn and 1 mPas low viscosity in the reservoir. Upper right: The working fluid is the artificial test fluid with 1 Pas high viscosity in the horn and 1 mPas low viscosity in the reservoir. Lower left: The working fluid is glycerol for the high viscosity in the horn and water for the low viscosity fluid in the reservoir. Lower right: The magnitude of the fluid cavity inlet acoustic impedance as predicted by the model for the water/glycerol and glycerol/glycerol working fluid combinations.

similar pressure gradient magnitude at the horn aperture as the low viscosity reservoir case.

The effect of the fluid cavity entrance acoustic impedance on the generated pressure gradient is accentuated when the behavior of the piezoelectric transducer is considered, given in Figure 5.5 for a 1.5 mm transducer thickness. Cases with the artificial working fluid continue to predict better performance in the low viscosity/high viscosity model as there is no change in sound speed or density to alter the fluid cavity acoustic impedance placed on the transducer. For the physical (actual) fluid combination, the glycerol filled cavity consistently produces a larger pressure gradient magnitude than the mixed water/glycerol case. While part of the increased pressure gradient magnitude in the glycerol only case is attributable to the shift in the fluid cavity resonances toward the transducer resonance which increases the velocity imposed by the transducer, fluid cavity resonances that occur at a similar frequency still show better performance in the glycerol only filled cavity due to the larger fluid cavity acoustic impedance. To determine if any transducer thickness would result in better performance in for the dual working fluid cavity, the transducer thickness was swept and the pressure gradient magnitude determined as a function of fluid cavity resonance mode, given in Figure 5.6. While some transducer thicknesses do yield a pressure gradient magnitude for the dual fluid cavity in excess of that for the high viscosity at certain fluid cavity resonance modes, in general no improvement in atomizer performance is seen as a function of transducer thickness. The difference in the pressure gradient magnitude at a transducer thickness is attributable to the change in the fluid cavity resonance frequencies caused by the different speed of sounds in the glycerol only and water/glycerol fluid cavities. This

remains insufficient for any meaningful increase in the upper limit of the working fluid viscosities able to be ejected by horn-based ultrasonic atomization.

5.3 Modification of the horn-based ultrasonic atomizer with a second acoustic horn

A horn-based ultrasonic atomizer model was developed to investigate a fluid cavity consisting of two acoustic horns – the first filled with a low viscosity fluid and the second filled with a high viscosity fluid targeted for ejection – separated by a thin, acoustically transparent membrane. Development of the model was motivated by the reduction in bulk attenuation resulting from the substitution of a lower viscosity propagation medium in the fluid cavity as well as the increase in volume velocity resulting from the larger cavity inlet entrance diameter. This section details the formulation of the double horn model for horn-based ultrasonic atomizers utilizing the modeling components outlined in Chapter 3. The double horn model will subsequently

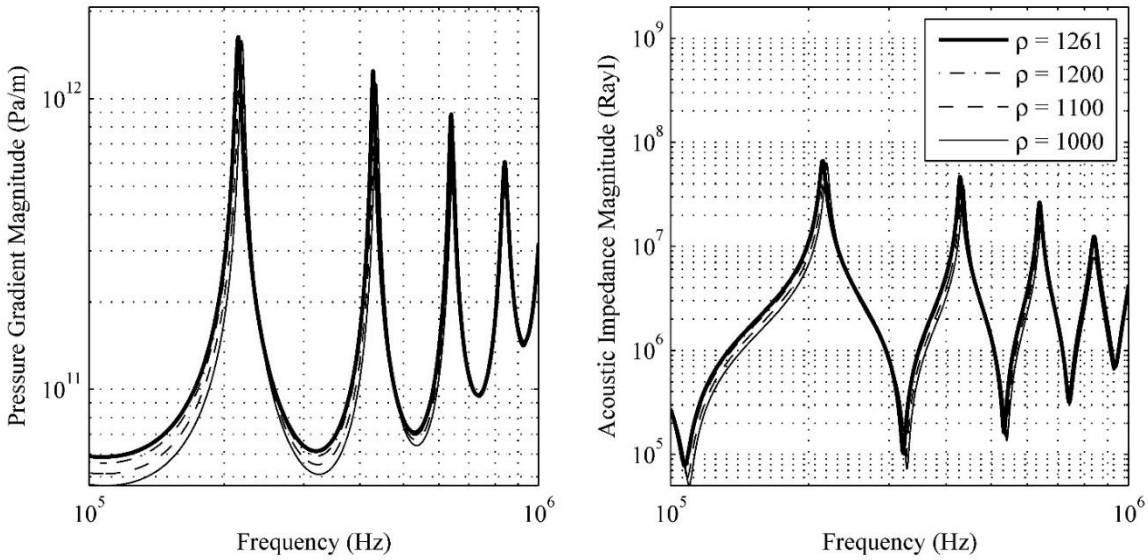

Figure 5.4: Variation in the predicted pressure gradient magnitude and fluid cavity inlet impedance with the density of the working fluid in the low viscosity reservoir for glycerol. The driving condition is a 1 m/s velocity at the fluid cavity inlet. The horn is 1mm with a 4mm reservoir. All fluid properties, including the working fluid density in the high viscosity reservoir, remain fixed and the density in the reservoir region artificially reduced to that of water.

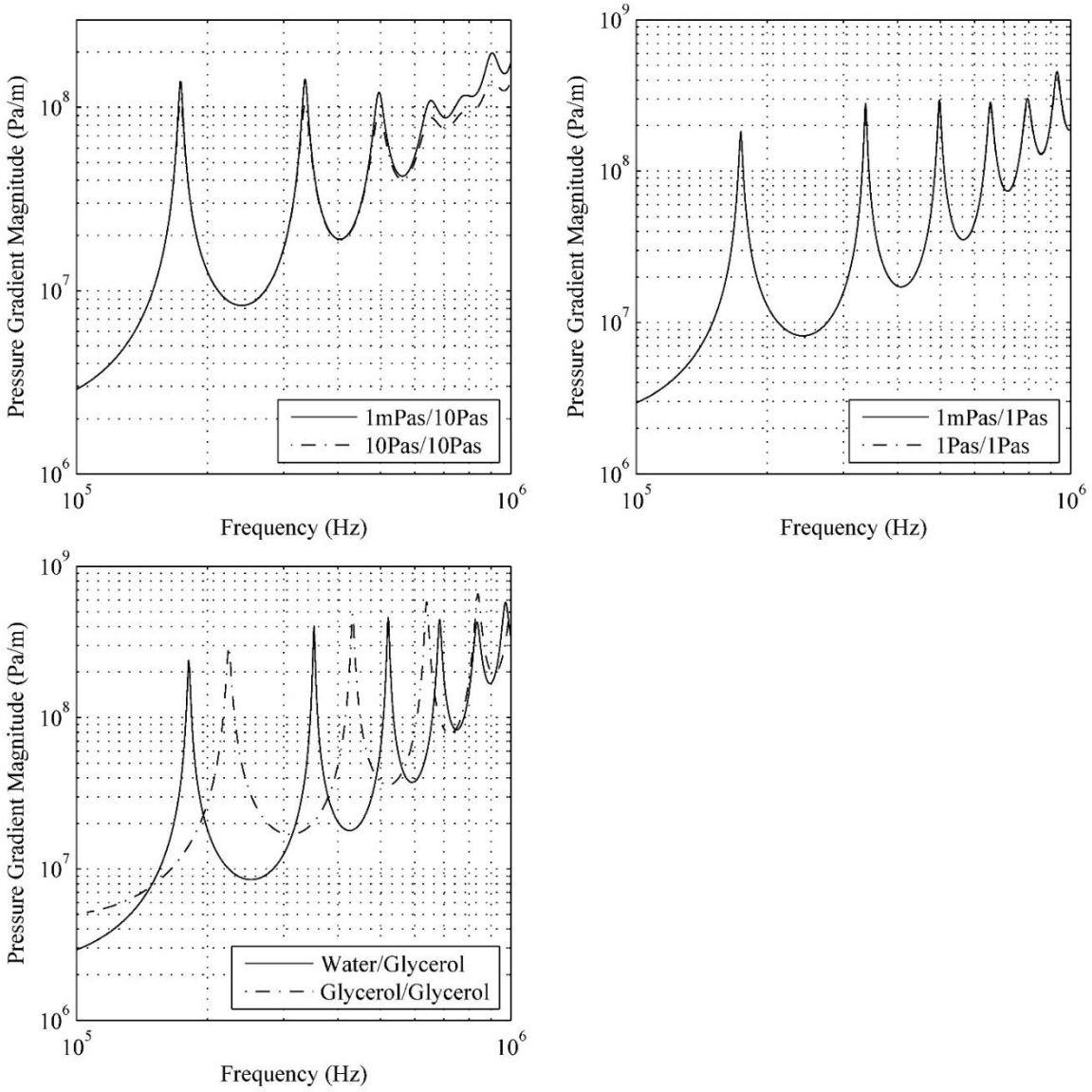

Figure 5.5: The acoustic response of the dual fluid horn-based ultrasonic atomizer when driven by a 1.5mm piezoelectric transducer for various working fluid combinations. The horn is 1mm with a 4mm reservoir. Upper left: The working fluid is the artificial test fluid with 10 Pas high viscosity and 1 mPas low viscosity. Upper right: The working fluid is the artificial test fluid with 1 Pas high viscosity and 1 mPas low viscosity. Lower left: The working fluid is glycerol for the high viscosity and water for the low viscosity fluid.

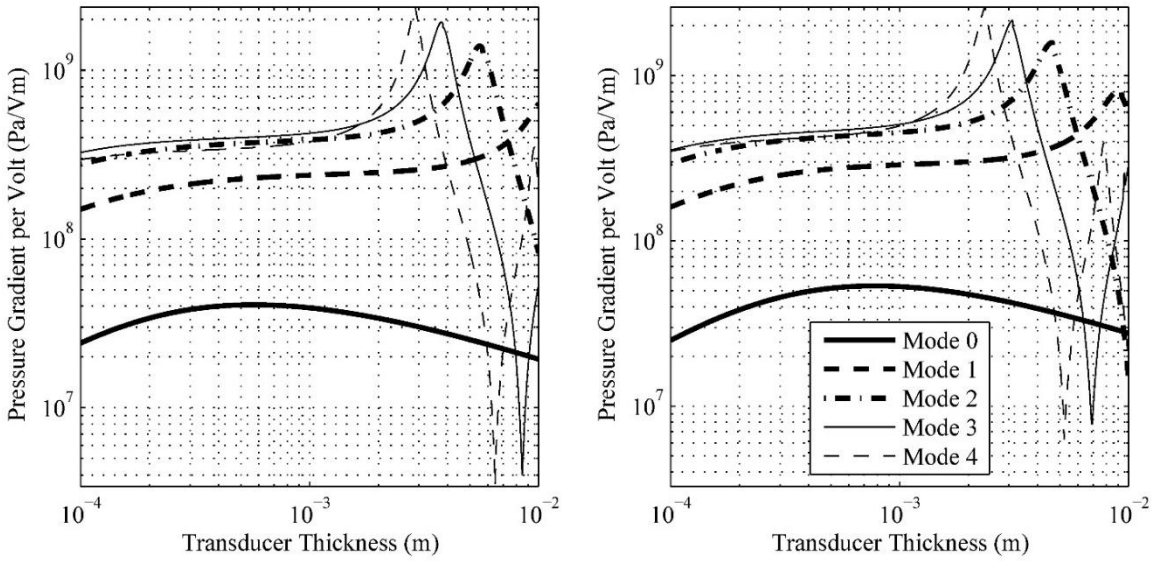

Figure 5.6: The acoustic response of the dual fluid horn-based ultrasonic atomizer when driven by a piezoelectric transducers of varying thicknesses driven by a 1V amplitude, sinusoidal signal. The horn is 1mm with a 4mm reservoir. Left: The working fluid is glycerol for the high viscosity and water for the low viscosity fluid. Right: The working fluid throughout the entire cavity is glycerol.

be applied to various working fluid combinations to determine if such an atomizer configuration can increase maximum pressure gradient magnitude generated by horn-based ultrasonic atomizers.

5.2.1 Development of the double acoustic horn model

The structure of a horn-based ultrasonic atomizer cell with two acoustic horns can be divided into three component sections as seen in Figure 5.7: a planar piezoelectric transducer, an acoustic horn with a low viscosity working fluid, and an acoustic horn with a high viscosity working fluid. As walls are present in both acoustic horn components, the discretized acoustic pipe with a wall would be the appropriate model for wave propagation in the horns as it includes the dominant source of viscous dissipation due the acoustic boundary layer. However, while the acoustic pipe with a wall model can be utilized for the high viscosity working fluid horn component, limitations of the model prevent its application to the horn with the low viscosity working fluid. In spite of this

limitation, the low viscosity working fluid horn can still be well approximated by the discretized acoustic pipe without a wall model given relatively small acoustic boundary layer losses and spatial dispersion.

The inability to numerically evaluate the radial dependence of the axial particle velocity prevents the application of the acoustic pipe with a wall model to the low viscosity working fluid horn. The radial dependence of the axial particle velocity, reproduced in Equation 5.8 for convenience, employs Kelvin functions to account for the radial variation in the axial particle velocity in order to match the no-slip boundary condition at the wall.

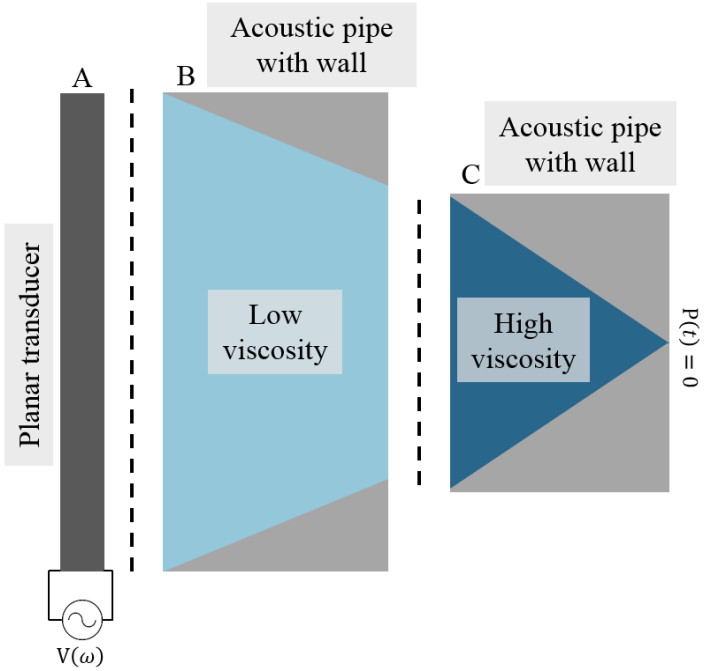

Figure 5.7: A schematic of a horn-based ultrasonic atomizer with dual acoustic horns, highlighting its constitutive components. The device can be modeled as an individual planar piezoelectric transducer and two acoustic pipes with wall components utilizing different working fluid properties in each.

$$v_z^* = Re\left\{EuMa\left(-\frac{ber_0(r^*)+jbei_0(r^*)}{bei_0(R^*)-jber_0(R^*)}+j\right)\left(\frac{-j}{\sqrt{\epsilon}}Ae^{-j\frac{1}{\sqrt{\epsilon}}z^*}\right.\right.$$
$$\left.\left.+j\frac{1}{\sqrt{\epsilon}}Be^{j\frac{1}{\sqrt{\epsilon}}z^*}\right)e^{jt^*}\right\} \quad 5.8$$

A characteristic of the Kelvin functions is that for large argument values the functions go to infinity. In the context of the acoustic pipe with a wall model, the argument of the Kelvin functions is the nondimensional radius of the acoustic pipe which is the radius of the pipe scaled by $\sqrt{\rho\omega_r/\mu}$. As ω_r or R becomes large and μ becomes small, the nondimensional pipe radius becomes large such that the Kelvin functions cannot be numerically evaluated. The second acoustic horn with the low viscosity working fluid exceeds the numerical capability to evaluate the Kelvin functions in water at 1 MHz. As such, the discretized acoustic pipe with a wall model cannot be utilized for the low viscosity horn component.

The acoustic pipe without a wall can be reasonably substituted in the horn with the low viscosity working fluid due to limited viscous dissipation and spatial dispersion expected in the component. The choice between the acoustic pipe model with or without a wall is determined by comparing the sound speed and particle speed Reynolds numbers in the context of the model regime map given in Section 3.3.3. Table 5.1 gives the predicted values for each Reynolds number based on the entrance and exit radii of the low viscosity horn, using the maximum velocity predicted to occur in a horn-based ultrasonic atomizer filled completely with water. The sound speed and particle speed Reynolds numbers are both much greater than one throughout the entirety of the horn, indicating that inertial effects are dominant over both types of viscous dissipation mechanisms and that the combined losses from both viscous dissipation mechanisms will

be small. This allows substitution of the acoustic pipe without a wall model as the viscous dissipation predicted in the fluid cavity will not be significantly altered.

The spatial dispersion present in the fluid cavity due to the compliance of the wall must also be considered. Spatial dispersion is accounted for in the acoustic pipe with a wall model through a modified speed of sound which includes the wall elasticity and thickness, reproduced in Equation 5.9 for convenience:

$$\frac{1}{\bar{c}^2} = \frac{1}{c^2} + \frac{2\rho_0}{R}\frac{\left(R + \frac{1}{2}h\right)^2}{hE} \tag{5.9}$$

The inclusion of spatial dispersion in the acoustic pipe with wall model was previously shown to be necessary to accurately model the acoustic field in a standard horn-based ultrasonic atomizer. For the discretized acoustic pipe without a wall to be a reasonable approximation, there must be limited spatial dispersion within the fluid cavity. Table 5.1 gives the modified speed of sound at the entrance and exit of the low viscosity working fluid horn. The entrance radius is taken to be half the wavelength of water at 1 MHz with an initial wall thickness of 25 μm. Horns with a larger entrance radius cannot be considered as this would violate the assumption of a one-dimensional axial acoustic field. The exit radius was taken to be 362.5 μm, half the difference between the entrance radius

Table 5.1: Reynolds numbers and sound speeds at the entrance and exit of the low viscosity acoustic horn. A frequency of 1 Hz was assumed with a maximum velocity of 500 m/s. The inlet wall thickness was taken to be 25 μm with an exit thickness of 387.5 μm.

Location	Sound Speed Reynolds Number (Re^*)	Particle Speed Reynolds Number (Re)	Sound Speed (m/s)	Modified Speed of Sound (m/s)
Entrance	348,386	374,250	1481	1073
Exit	348,386	180,888	1481	1434

and fluid cavity aperture radius of 25 μm. At the exit of the horn, the modified speed of sound is close to the physical speed of sound. However, at the entrance of the horn, the modified speed of sound is significantly reduced due to the small wall thickness. The assumed small wall thickness at the horn entrance is characteristic of the horn in standard horn-based ultrasonic atomizers and permits the wall to have significant radial deformation. However, this need not be the case in the double horn model or physical devices which incorporate multiple acoustic horns. By increasing wall thickness to 50 μm, the speed of sound at the entrance of the horn can be increased to 1223 m/s, permitting the acoustic pipe without a wall to reasonably approximate the true behavior of the fluid cavity. This would increase the spacing between atomizer cells in physical devices but would otherwise not affect atomizer behavior.

The structure of the horn-based ultrasonic atomizer with a second, low viscosity working fluid acoustic horn can thus be modeled as three coupled components: a planar piezoelectric transducer (A), a discretized acoustic pipe without a wall for the low viscosity horn (B), and a discretized acoustic pipe with a wall for the high viscosity horn (C). Figure 5.8 describes the components of the double horn atomizer model and the boundary conditions that couple them. The double horn model must again utilize two sets of fluid properties, the first set for the low viscosity horn and the second for the high viscosity horn, rather than a single set of properties over the entire fluid cavity.

At the aperture of the high viscosity acoustic horn a pressure release condition is assumed, given by:

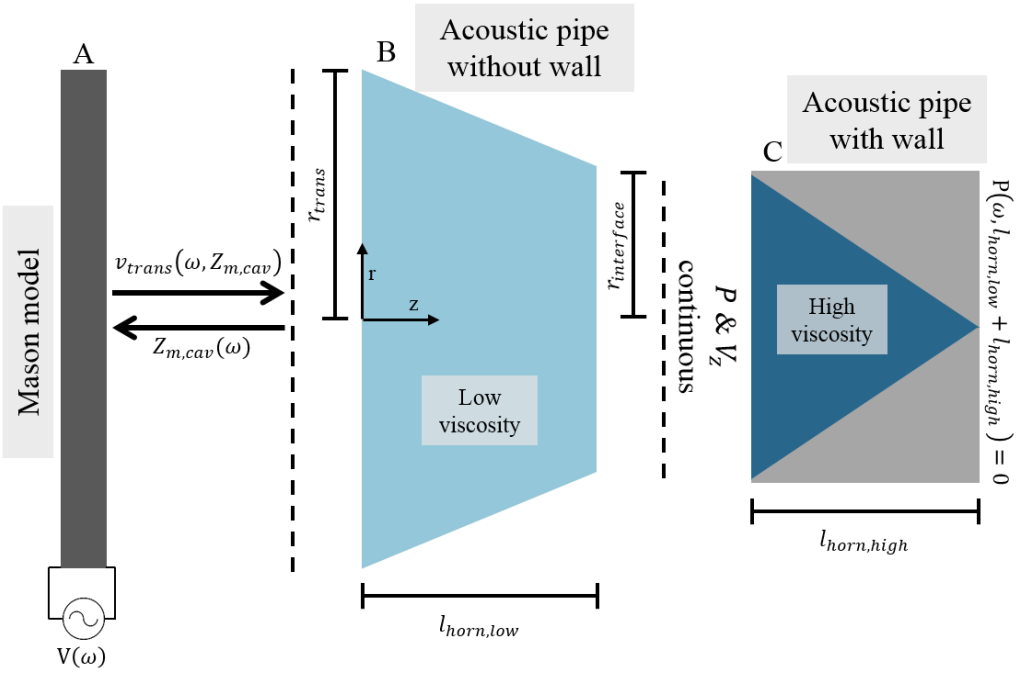

Figure 5.8: A schematic diagram of the ultrasonic atomizer utilizing dual acoustic horns with a low and high viscosity fluids as propagation media. The model is decomposed into the utilized components and the boundary conditions are shown. The low viscosity fluid is utilized in the first acoustic horn component with the high viscosity fluid in the second acoustic horn component.

$$P_0\left(Ae^{-j\frac{1}{\sqrt{\epsilon}}\frac{\omega_r(l_{horn,low}+l_{horn,high})}{c_{horn,high}}} + Be^{j\frac{1}{\sqrt{\epsilon}}\frac{\omega_r(l_{horn,low}+l_{horn,high})}{c_{horn,high}}}\right)\Bigg|_{(l_{horn,low}+l_{horn,high})^-} = 0 \quad 5.10$$

The components are coupled by enforcing continuity of pressure and volume velocity at their interfaces. However, the difference in fluid properties must again be accounted for between the models by applying the fluid properties on either side of the interface. At the interface between horn components B and C, the coupling condition is given by:

$$\left(Ae^{-jk_{horn,low}l_{horn,low}} + Be^{jk_{horn,low}l_{horn,low}}\right)\Big|_{l_{horn,low}^-} = P_0\left(Ce^{-j\frac{1}{\sqrt{\epsilon}}\frac{\omega_r l_{horn,low}}{c_{horn,high}}} + De^{j\frac{1}{\sqrt{\epsilon}}\frac{\omega_r l_{horn,low}}{c_{horn,high}}}\right)\Bigg|_{l_{horn,high}^+} \quad 5.11$$

$$S\left(Ae^{-jk_{horn,low}l_{horn,low}} - Be^{jk_{horn,low}l_{horn,low}}\right)\Big|_{l_{horn,low}^{-}} =$$

$$EuMa(\omega_r w_0 \pi R^2)Ma\left(-j\frac{1}{\sqrt{\epsilon}}Ce^{-j\frac{1}{\sqrt{\epsilon}}\frac{\omega_r l_{horn,low}}{c_{horn,high}}} + j\frac{1}{\sqrt{\epsilon}}De^{j\frac{1}{\sqrt{\epsilon}}\frac{\omega_r l_{horn,low}}{c_{horn,high}}}\right) \qquad 5.12$$

$$\int_0^{R^*}\left(-\frac{ber_0(r^*) + jbei_0(r^*)}{bei_0(R^*) - jber_0(R^*)} + j\right)r^* dr^*\Big|_{l_{horn,low}^{+}}$$

where Equation 5.11 is the for pressure and Equation 5.12 is for the volume velocity. Terms denoted by the subscript *low* indicate fluid properties evaluated in the low viscosity working fluid horn while terms denoted by the subscript *high* indicate fluid properties valuated in the high viscosity working fluid horn. It should be noted that as the speed of sound and density will be dissimilar across the interface of components B and C, the acoustic field parameters will exhibit a discontinuity in slope at the interface.

The coupling between components A and B again enforces continuity of pressure and volume velocity, formulated in terms of the fluid cavity mechanical impedance, and follows the procedure for the atomizer model outlined in Section 3.5. The boundary conditions at the transducer/fluid cavity interface are similar as well, however the calculated fluid cavity acoustic impedance is now a function of the combined response of the acoustic horns. At the fluid cavity inlet/transducer surface, the coupling condition can be expressed as:

$$Sv_{trans} = S(A - B)|_{0^+} \qquad 5.13$$

$$Z_{m,load}(\omega) = Z_{m,cav}(\omega) \qquad 5.14$$

with Equation 5.13 being continuity of volume velocity and Equation 5.14 being the impedance matching condition. The following conditions are associated with the piezoelectric transducer:

$$V(\omega) = V_{applied}(\omega) \quad 5.15$$

$$Z_{m,load}(\omega) = Z_{m,cav}(\omega) \quad 5.16$$

where $V_{applied}$is the voltage applied to the transducer.

5.2.2 Application of the secondary acoustic horn model

The potential for a dual acoustic horn atomizer to increase the generated pressure gradient magnitude was evaluated by imposing both a frequency independent, sinusoidal velocity signal and a piezoelectric transducer as the driving conditions at the fluid cavity inlet. The velocity condition is utilized to characterize the acoustic response of the standalone fluid cavity to decouple it from an impact of the frequency dependent electromechanical behavior of the transducer. This permits a direct comparison of the dual horn model to the single horn model when driven by the same amplitude acoustic field.

Figure 5.9 gives the pressure gradient magnitude at the fluid cavity aperture as a function of frequency for two artificial working fluid combinations and also for actual low and high viscosity fluids such as water/glycerol. In all cases the cavity was driven with a sinusoidal velocity condition of 1 m/s at the inlet to the low viscosity working fluid horn. The high viscosity artificial working fluids were again taken to be 10 Pas and 1 Pas with the reservoir working fluid viscosity as 1 mPas. The baseline performance of a standard, single horn fluid atomizer completely filled with the high viscosity working fluid throughout is also plotted for an equivalent reservoir length and entrance radius as the low viscosity horn. The standard atomizer with the high viscosity working fluid generates a larger pressure gradient magnitude than every fluid combination in the dual acoustic horn atomizer. This rather counterintuitive difference in performance results

from a greater fluid cavity inlet impedance, shown in Figure 5.9 for the water/glycerol combination. The larger acoustic impedance at the fluid cavity inlet, taken together with the constant velocity boundary condition, results in a greater pressure amplitude at the fluid cavity inlet. As the dissipation resulting from bulk attenuation is small regardless of working fluid viscosity, the higher amplitude wave propagates with little dissipation from inlet of the low viscosity horn to the interface with the high viscosity horn. As the viscous dissipation in the high viscosity horn is similar among all simulated cases, the configuration with the largest pressure amplitude at the horn interface, i.e. the horn with the largest fluid cavity inlet acoustic impedance, yields the largest press gradient magnitude.

The reduction in fluid cavity acoustic impedance for the dual horn models occurs as a result of two separate mechanisms. The first is analogous to that seen in the dual fluid, single horn atomizer model discussed in the preceding section. As the density and sound speed of the working fluid in contact with the transducer diminish, the acoustic impedance of the fluid cavity is reduced. The second mechanism is a function of the shape of the second, low viscosity fluid horn. Figure 5.10 plots the pressure gradient generated by the dual horn atomizer as a function of the diameter ratio across the low viscosity horn when driven by the constant velocity boundary condition; the overall diameter ratio across the fluid cavity remains fixed. For simplicity, glycerol was assumed to be the working fluid in both horns. As the low viscosity fluid-filled horn becomes more tapered, the pressure gradient magnitude is reduced due to a decline in the fluid cavity acoustic impedance. This difference in the fluid cavity acoustic impedance is purely a function of the shape of the low viscosity region; a similar reduction will be

present for any working fluid with any horn lengths. It is important to note that while the standard atomizer without a dual horn yields the largest acoustic impedance at the fluid cavity resonances, the dual horn atomizer has a larger acoustic impedance at low operating frequencies and thus outperforms the baseline atomizer.

The effect of the fluid cavity inlet acoustic impedance on the generated pressure gradient is again accentuated when the behavior of the piezoelectric transducer is considered, as shown in Figure 5.11 for a 1.5 mm transducer thickness. Above the zeroth order fluid cavity resonance, the standard atomizer outperforms the dual horn combinations by a factor of two in the pressure gradient magnitude. At the zeroth order fluid cavity resonance, this behavior is reversed with the dual horn configuration performing better than the standard atomizer by a similar factor. This difference in the predicted behavior is attributable to the fluid cavity acoustic impedance imposed on the transducer as the transducer generates a similar velocity for each fluid combination across models. As detailed for the velocity driven case, the configuration with the largest pressure amplitude at the fluid cavity inlet yields the largest pressure gradient at the fluid cavity aperture due to the small magnitude of bulk attenuation losses and the similarity of the boundary layer losses in the high viscosity acoustic horn.

While some fluid cavity resonances show an improvement with the dual horn configuration, the improvement in atomizer generated pressure gradient magnitude is small with the largest enhancement being a factor of two. Furthermore, above the zeroth

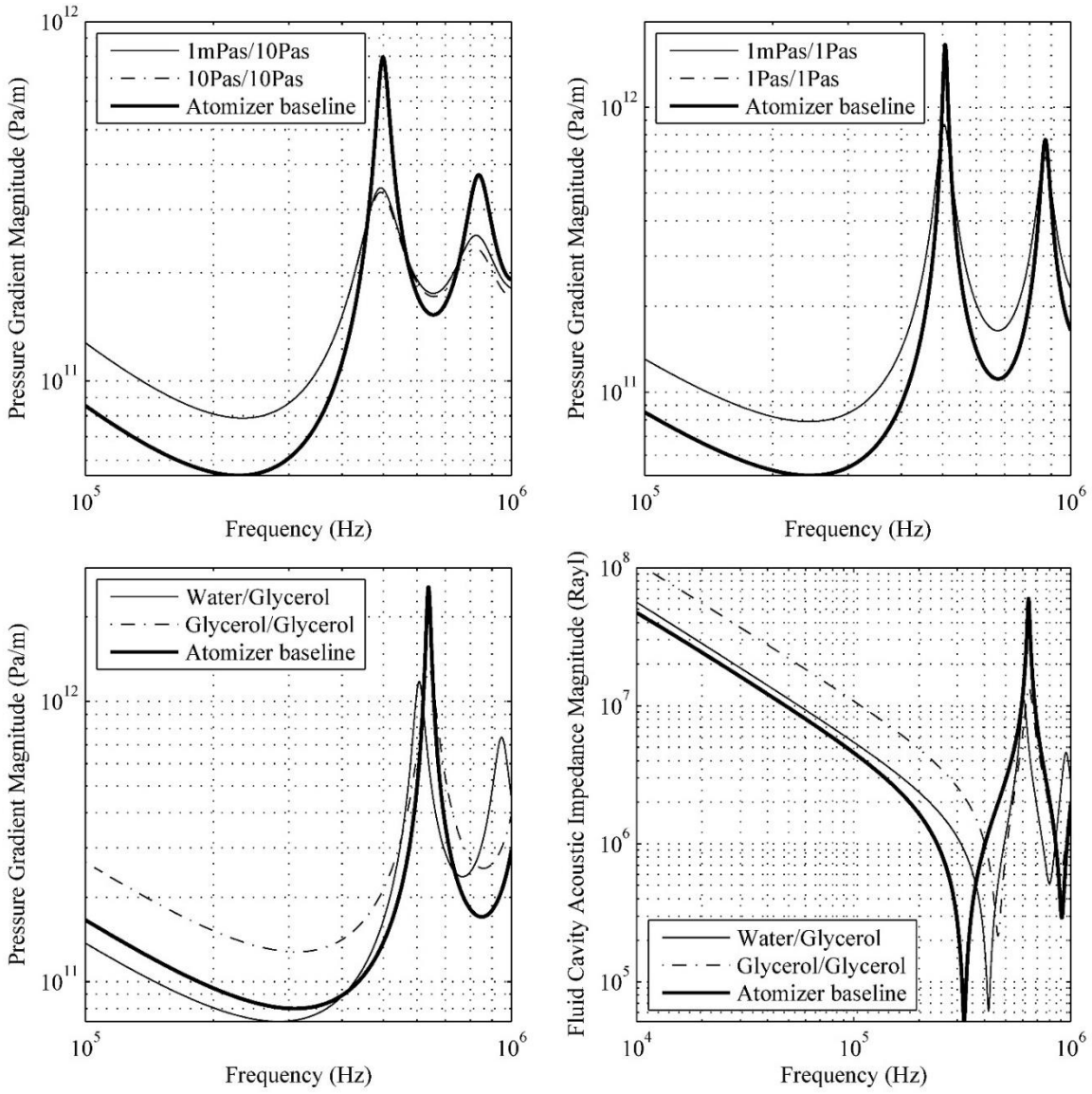

Figure 5.9: The acoustic response of the dual horn/dual fluid atomizer when driven by a constant amplitude of 1 m/s sinusoidal velocity boundary condition at the fluid cavity inlet for various working fluid combinations. The baseline atomizer refers to an atomizer without the second acoustic horn filled with the high viscosity working fluid throughout. Both the low and high viscosity fluid-filled horns are 1 mm in length. The fluid cavity entrance radius is 750 μm with a 362.6 μm interface radius and a 25 μm aperture radius. Upper left: The working fluids are the artificial test fluid with 10 Pas high viscosity and 1 mPas low viscosity. Upper right: The working fluids are the artificial test fluid with 1 Pas high viscosity and 1 mPas low viscosity. Lower left: The working fluids are glycerol for the high viscosity and water for the low viscosity fluid. Lower right: The magnitude of the fluid cavity inlet acoustic impedance as predicted by the model for the water/glycerol working fluid combinations.

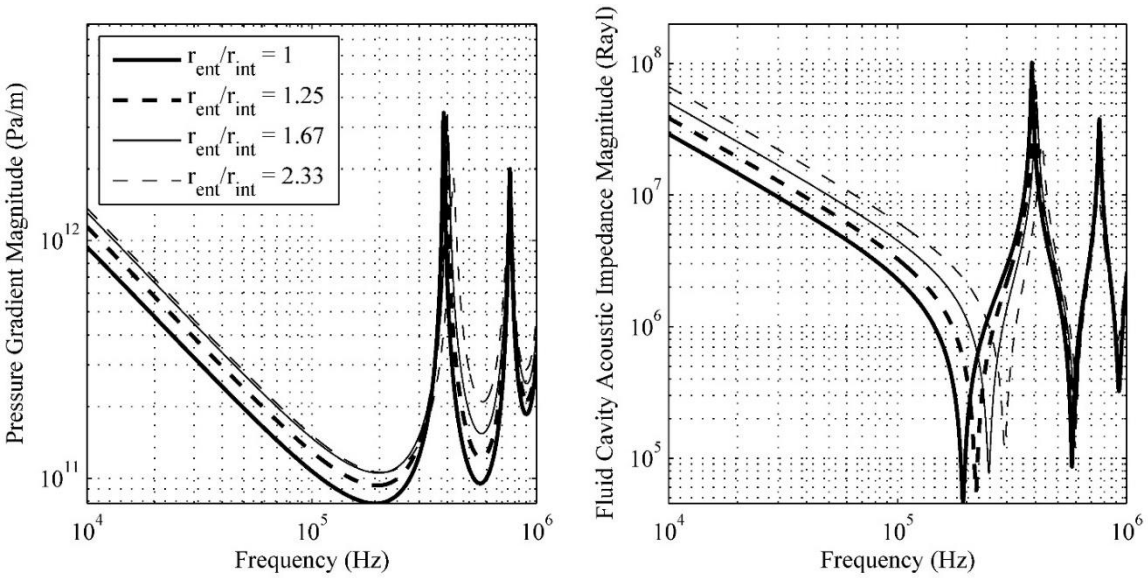

Figure 5.10: Variation in the predicted pressure gradient magnitude at the ejection apex and fluid cavity inlet impedance with the diameter ratio across the low viscosity horn for glycerol as the working fluid. The driving condition is a 1 m/s amplitude sinusoidal velocity signal at the fluid cavity inlet. The high viscosity horn is 1mm with a 2mm low viscosity horn. The diameter ratio across the fluid cavity is fixed with an entrance radius of 750 μm and an aperture radius of 25 μm.

order fluid cavity resonance, no performance benefit with the dual horn configuration is predicted. This result is expected to generalize across all dual horn geometries due to the strong dependence the fluid cavity acoustic impedance, which is the determining factor in the generated pressure gradient magnitude, on the shape of the low viscosity region. Additional performance gains in the dual acoustic horn atomizer may be possible with further increases to the entrance radius of the low viscosity horn; however a substantial increase in the atomizer base area quickly becomes impractical for implementation. The developed analytical framework is unable to quantify this potential given the violation of the one-dimensional acoustic field assumption with a large increase in the reservoir radius. The trends revealed by the analysis are however sufficient to conclude that only limited increase in atomizer performance due to the use of a dual horn configuration can be expected and it will remain insufficient for any meaningful increase in the upper limit

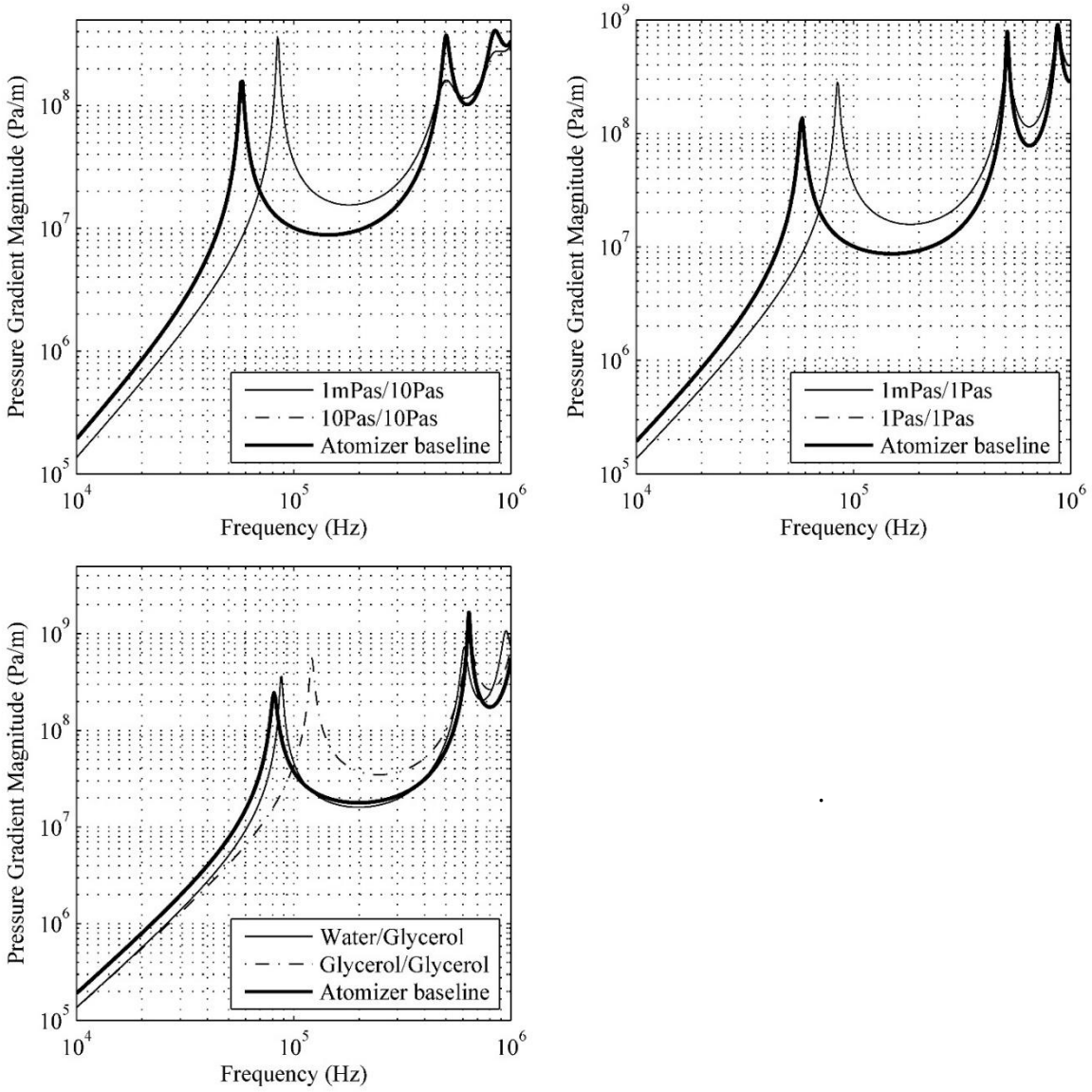

Figure 5.11: The acoustic response of the dual acoustic horn atomizer when driven by a 1.5mm piezoelectric transducer for various working fluid combinations. The baseline atomizer refers to an atomizer without the second acoustic horn filled with the high viscosity working fluid. Both the low and high viscosity horns are 1 mm in length. The fluid cavity entrance radius is 750 μm with a 362.6 μm interface radius and a 25 μm aperture radius. Upper left: The working fluids are the artificial test fluids with 10 Pas high viscosity and 1 mPas low viscosity. Upper right: The working fluids are the artificial test fluids with 1 Pas high viscosity and 1 mPas low viscosity. Lower left: The working fluids are glycerol for the high viscosity and water for the low viscosity fluid

of the working fluid viscosities able to be ejected by horn-based ultrasonic atomization.

5.4 Concluding remarks on ejector design alternatives

Potential design modifications to increase the maximum pressure gradient magnitude generated by horn-based ultrasonic atomizers were investigated through coupled electro-mechanical models. The first proposed design, consisting of a fluid reservoir filled with a low viscosity working fluid as a wave propagation medium and a horn filled with a high viscosity working fluid targeted for ejection separated by an acoustically thin membrane, showed no performance benefit when physical fluids (water and glycerol, respectively) are employed due to the reduction in the fluid cavity inlet acoustic impedance and thus the amplitude of the output pressure generated by the transducer. The second proposed design, consisting of a horn with a high viscosity working fluid coupled to a second horn with a low viscosity working fluid, showed similar performance limitations. The pressure amplitude imposed by the transducer on the fluid cavity was again limited by the reduction in the fluid cavity inlet acoustic impedance due to the lowering of the overall fluid cavity acoustic impedance as seen by the transducer; moreover, the pressure gradient magnitude generated by the atomizer was reduced as the entrance radius of the low viscosity horn was increased to concentrate a larger volume velocity. Application of the developed analytical models for the design modifications thus indicate that neither alternation would yield a meaningful increase in the maximum pressure gradient magnitude generated by the atomizer and would therefore not expected to increase the maximum working fluid viscosity able to be ejected by horn-based ultrasonic atomizers.

CHAPTER 6: CHARACTERIZATION OF SQUEEZE EJECTORS

The ejection of viscous liquids by squeeze type ejectors is investigated through comprehensive electro-mechanical analytical modeling of device operation. A coupled electro-mechanical model for squeeze ejectors, developed and validated in Chapter 3, is applied to understand the ejector acoustic response with working fluids of increasing viscosity. The maximum predicted pressure gradient magnitude produced by the ejector is then compared to the required pressure gradient threshold derived from hydrodynamic considerations to predict fluid ejectability as a function of the working fluid viscosity. Emphasis is placed on the configurations investigated by Bogy and Talke in an effort to characterize the acoustic response of realized devices.[2] Key geometric parameters – fluid cavity length, transducer length, capillary radius, and transducer thickness – are also investigated for their effect on the maximum pressure gradient magnitude created by the ejector.

6.1 Overview of squeeze type ejectors

The structure of the squeeze ejector under investigation mirrors that introduced in Section 3.1, a schematic of which is reproduced for convenience in Figure 6.1 with key dimensions indicated. The main portion of the ejector is composed of a cylindrical, fluid-filled glass capillary divided into four sections. The left and right capillary sections (B and D) are loaded by the working fluid on the interior with the atmosphere on the exterior. The center section (C), or "driven" section, is surrounded by an annular piezoelectric transducer which imposes a radial displacement on the glass capillary. The capillary is bounded on one end by a large fluid reservoir used to fill the capillary and the other end by a short nickel horn through which fluid is ejected.

The investigation of squeeze ejectors for use with high viscosity working fluids is motivated by the potential advantages of the squeeze geometry. First, as compared to horn-based ultrasonic atomizers, the squeeze geometry has a much increased transducer surface area in respect to the cross-sectional area of the fluid-filled capillary. This could allow the transducer to impart a larger volume velocity to the fluid cavity to achieve a higher amplitude acoustic field. Secondly, a reduction in fluid cavity resonance frequencies can be achieved due to the larger axial length. This permits the use of the amplification occurring at the fluid cavity resonances without incurring significant viscous dissipation which increases with higher frequency operation. The subsequent sections apply the squeeze ejector model developed in Chapter 3 to understand the operation of squeeze ejectors of various geometries with high viscosity working fluids.

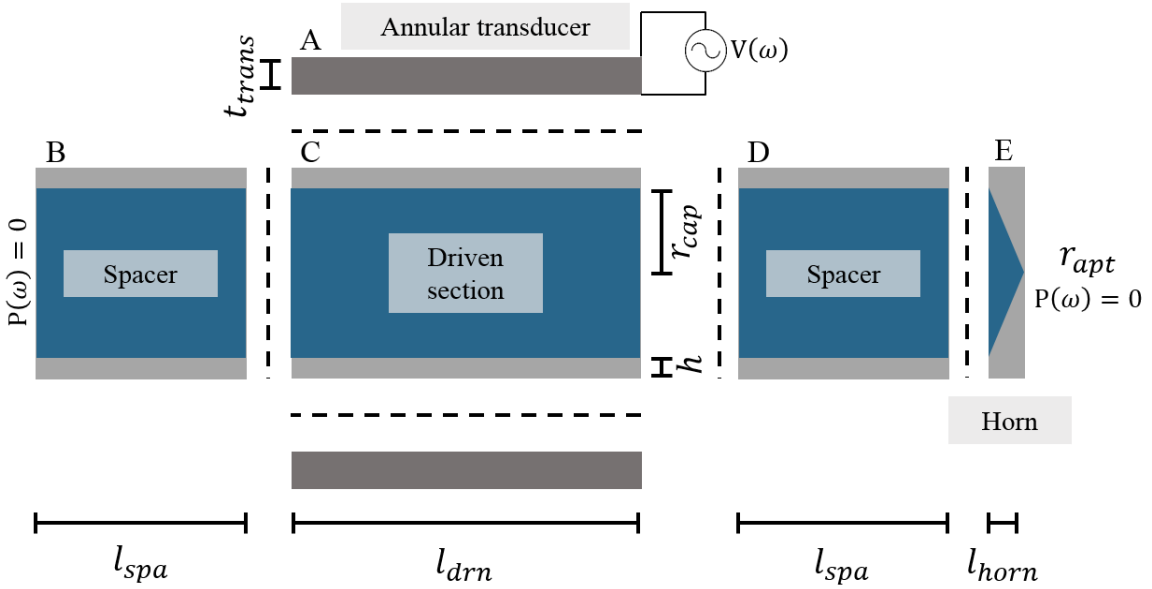

Figure 6.1: A schematic of a squeeze ejector with its constitutive components and dimensions identified. The device can be modeled as an individual annular piezoelectric transducer, acoustic pipes with a wall, a driven acoustic pipe with a wall, and a horn coupled together with the appropriate boundary conditions.

6.2 Bogy devices loaded with high viscosity working fluids

The ejector geometries experimentally studied by Bogy and Talke are investigated to understand the acoustics governing squeeze type ejectors and to establish the performance of practically realized devices with high viscosity working fluids.[2] Bogy and Talke characterized three different lengths of ejector with varying driven section (component C) lengths, given in Table 6.1. The left and right spacer sections (components B and D) are fixed at 3 mm in length. The spacer and driven sections have equal inner radius and wall thickness, both taken as 500 μm. The nickel horn is 125 μm in length and tapers from the tube radius to an aperture radius of 25 μm. The thickness of the transducer, which is assumed to be composed of APC International PZT855, is taken to be 500 μm. The squeeze ejector model with these geometric parameters was shown to accurately reproduce the measured acoustic response of realized ejectors as shown in Section 3.6.

Because the acoustic behavior of the fluid cavity is not independent of but coupled to the electro-mechanical response of the piezoelectric transducer, the overall behavior of the ejector cannot be predicted based on either the fluid cavity or the piezoelectric transducer alone. To separately examine the effect of the fluid cavity and the transducer on the pressure gradient magnitude generated by squeeze ejectors, a constant amplitude sinusoidal velocity condition and an annular piezoelectric transducer were both applied as the driving conditions at outer capillary surface of the driven section. The artificial working fluid is again utilized to isolate the effect of working fluid viscosity by maintaining a fixed density and sound speed; as the experimental ejectors were optimized for the speed of sound of glycol, the density and sound speed in the artificial working fluid are taken to equal to those of glycol and with an artificially

changing viscosity. This change to the artificial test fluid will not affect the generality of the analysis due to the similarity of physical properties between water and glycol and will only move the fluid cavity resonances higher in frequency.

The acoustic response of the standalone fluid cavity is strongly influenced by the fluid cavity resonances and the mode shape of the fluid cavity acoustic field. Figure 6.2 gives the predicted pressure gradient magnitude at the horn aperture of the 18.7 mm long ejector as a function operating frequency in the artificial working fluid when driven by a constant, sinusoidal velocity condition of 1 m/s at the glass surface. Figure 6.3 gives the mean (length averaged) acoustic impedance magnitude at the interior capillary surface in the driven section. At low operating frequencies sufficiently far from the first order fluid cavity resonance mode, the wavelength in the fluid cavity is long and the ejector operates as an acoustic pump with the displacement imposed at the capillary wall being directly transmitted to the horn aperture scaled inversely proportionally to the respective areas. The acoustic response of the fluid cavity at and above the first order fluid cavity resonance mode is governed by the number of quarter wavelengths present along the ejector axis. An even number of quarter wavelengths corresponds to multiples of a half wavelength fluid cavity resonance. In the ejector geometries examined by Bogy and

Table 6.1: Geometric properties utilized in the simulation of each of the geometries given by Bogy and Talke. [2]

Ejector Length (mm)	Driven Length (mm)	Driven Length Ratio	Capillary Inner Radius (μm)	Wall Thickness (μm)	Transducer Thickness (μm)
12.3	6.175	0.50	500	500	500
18.7	12.575	0.67	500	500	500
33.9	27.775	0.82	500	500	500

Talke, the half wavelength resonances also correspond to maxima in the pressure gradient magnitude generated by the ejector as the mode shape of the fluid cavity acoustic field induces strong coupling between the driven and spacer sections.

The mode shape of the fluid cavity acoustic field and location of the driven/spacer section interfaces dictate how strongly the driven section couples to the spacer sections. Put another way, the fluid cavity mode shape and the location of the driven/spacer section interfaces determine the effectiveness with which the driven section converts the imposed radial particle velocity into axial particle velocity. For a fixed length driven section and a constant imposed radial particle velocity, the same radial volume velocity is imposed on the driven section at every frequency. The effectiveness with which the imposed radial volume velocity is converted into axial volume velocity is governed by the mode shape within the driven section. A large axial particle velocity only leaves the driven section and enters the spacer sections when an antinode or a large amplitude point of the axial particle velocity mode shape occurs on the interface between sections. When this occurs, the driving term given in Equation 3.87 ($2R_aR_c^2/EuMa^2$) efficiently drives the mode shape and which produces a large amplitude acoustic field. In the 18.7 mm ejector geometry considered here, the length of the driven section is approximately an integer multiple of half wavelength shorter than the total cavity length at the fluid cavity resonances. This positions a large amplitude point of the velocity mode shape at the interfaces between the driven/spacer sections and creates a large amplitude acoustic field as shown in Figure 6.4 which plots the pressure and mean (cross-section averaged) particle velocity as a function of distance from the cavity inlet for the first two half wavelength resonances at 38 kHz and 77 kHz. The radial particle velocity imposed on

the glass capillary is effectively converted to axial particle velocity and a large axial particle velocity is imparted at both ends of the driven section of the fluid cavity into the spacer sections. Higher order fluid cavity resonances exhibit similar behavior, again positioning a large amplitude point of the mean particle velocity mode shape at the interface between the driven and spacer sections to create effective coupling between the components. This behavior can be generalized to understand when optimal coupling occurs between the driven and spacer sections. When the driven section is an integer number of half wavelengths less than the total ejector length, the fluid cavity resonances will position antinodes in the particle velocity at the driven/spacer section interfaces, producing an effective conversion of the imposed radial particle velocity to axial particle velocity.

By contrast, the minima in the pressure gradient magnitude correspond to an odd number of quarter wavelengths in the fluid cavity. At these operating frequencies, nodes in the mean axial particle velocity are positioned at the interfaces between the driven and spacer sections. This is shown in Figure 6.5 which plots the pressure and mean cross-sectional particle velocity as a function of distance from the fluid cavity inlet for the first two minima in the pressure gradient magnitude occurring at 69 kHz and 88 kHz. Only a small axial particle velocity is imparted at the exit of the driven section of the fluid cavity, creating a small amplitude acoustic field in the spacer sections. The driven surface area and radial volume velocity imposed at these anti-resonances are the same as those imposed for the resonances, showing the importance of the particle velocity mode shape to how effectively the radial input velocity is converted to axial particle velocity. It is interesting to note that some of the frequencies corresponding to an odd number of

quarter wavelengths in the fluid cavity do not produce as significant of reduction in the pressure gradient magnitude as other frequencies. This is due to the slight left/right asymmetry in the fluid cavity introduced by the horn. The mode shape associated with these frequencies does not have a node directly at the active/passive component interfaces but rather slightly askew which permits some energy to be transferred from the driven section of the capillary to the adjacent spacer components.

The effect of the mode shape on ejector performance is directly reflected in the mean (length averaged) fluid cavity acoustic impedance in the driven section. A large mean fluid cavity acoustic impedance is only produced when the imposed radial velocity results in a large amplitude acoustic pressure in the fluid. This only occurs when half wavelengths occur in the driven section as the driven section couples effectively with the spacer sections to produce a large amplitude acoustic field. The fluid cavity acoustic impedance is thus a direct proxy of the axial acoustic mode shape which accounts for how strongly the driven section couples to the spacer sections.

The effect of working fluid viscosity on the fluid cavity acoustic response is dependent on operating frequency. At low operating frequencies where the ejector behaves as an acoustic pump, the highest viscosity working fluid generates the largest pressure gradient magnitudes. A greater fluid cavity acoustic impedance occurs due to the fluid becoming more stiff at large viscosities and long wavelengths, yielding a larger pressure amplitude. The acoustic wave with an increased pressure amplitude is able to propagate through the spacer section to the nozzle aperture with minimal dissipation as boundary layer losses are small at low operating frequencies. When operating near the fluid cavity resonance frequencies, the predicted pressure gradient magnitudes decline as

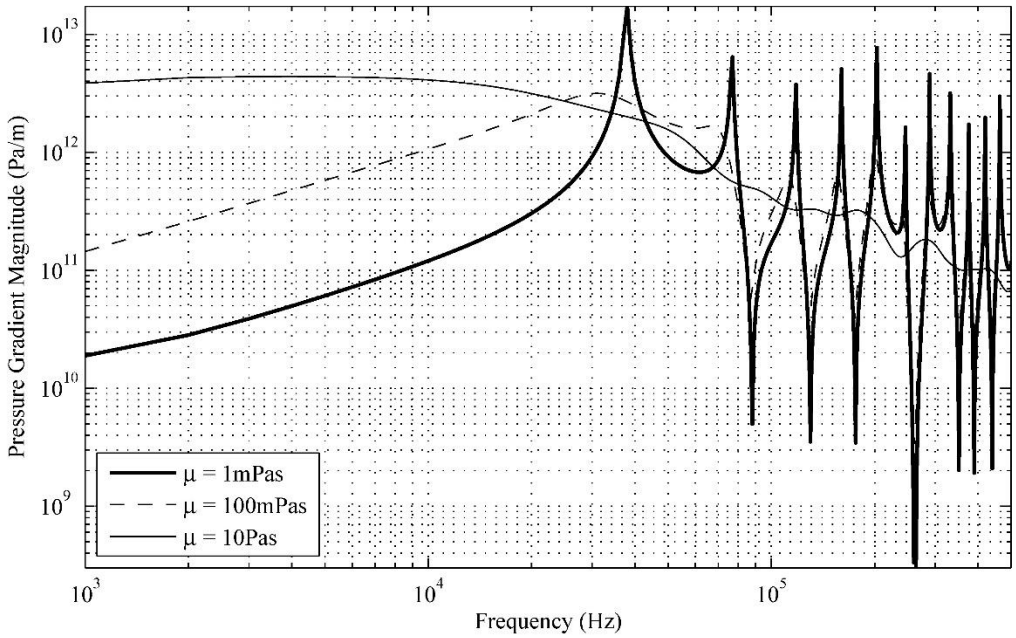

Figure 6.2: Variation in the pressure gradient magnitude at the ejector aperture as a function of frequency for artificial working fluids of increasing viscosity when driven by a constant amplitude (1 m/s) harmonic velocity signal on the capillary exterior. The sound speed and density of the working fluid are taken to be equal to those of glycol. The ejector length is 18.7 mm, composed of two 3 mm spacer sections, a 125 μm horn, and a 12.575 mm driven section.

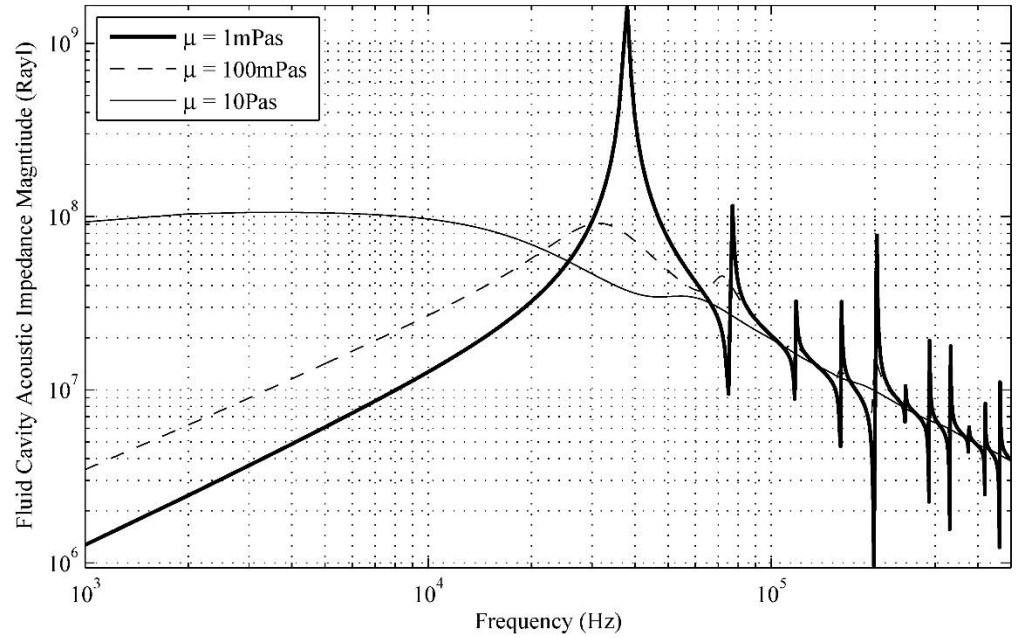

Figure 6.3: Variation in the mean (length averaged) acoustic impedance magnitude at the ejector driven section as a function of frequency for artificial working fluids of increasing viscosity. The sound speed and density of the working fluid are taken to be equal to those of glycol. The ejector length is 18.7 mm, composed of two 3 mm spacer sections, a 125 μm horn, and a 12.575 mm driven section.

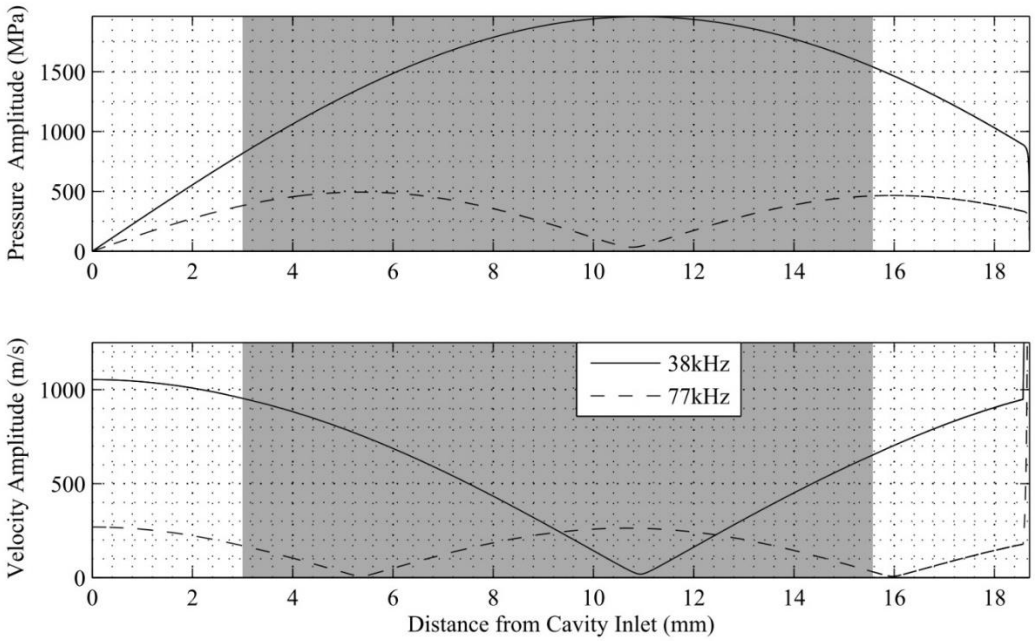

Figure 6.4: Pressure and mean particle velocity amplitude in the ejector fluid cavity as a function of distance from the cavity inlet for the first two fluid cavity resonance modes. The working fluid is taken to be the artificial test fluid with 1 mPas viscosity and is driven by a constant amplitude (1 m/s) sinusoidal velocity signal on the capillary exterior. The shaded area indicates the portion of the fluid cavity to which the driving condition is applied.

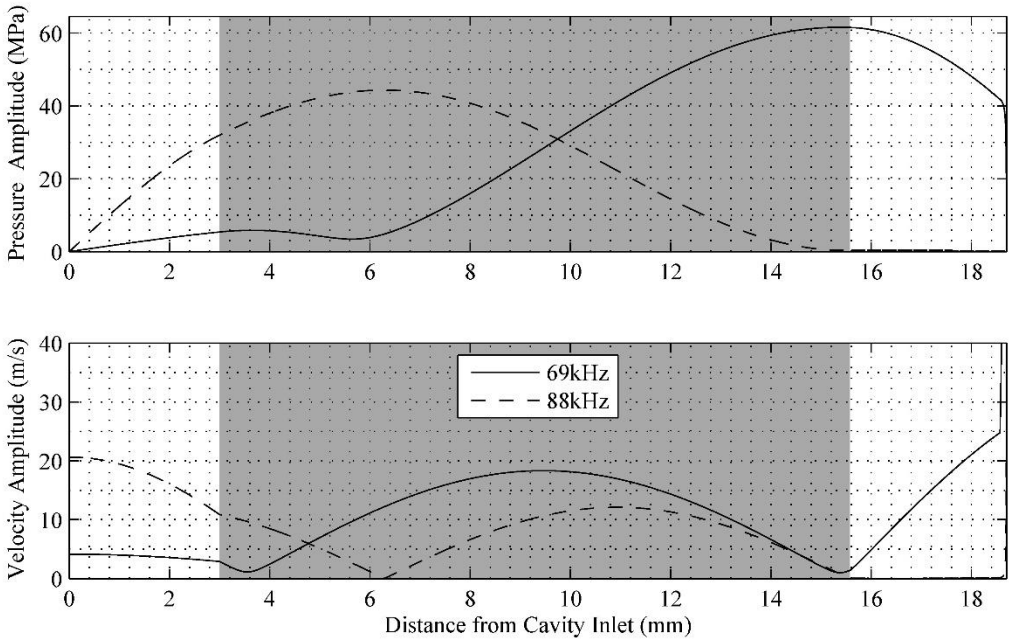

Figure 6.5: Pressure and mean particle velocity amplitude in the ejector fluid cavity as a function of distance from the cavity inlet for the first two minima in the pressure gradient magnitude. The working fluid is taken to be the artificial test fluid with 1 mPas viscosity and is driven by a constant amplitude (1 m/s) sinusoidal velocity signal on the capillary exterior. The shaded area indicates the portion of the fluid cavity to which the driving condition is applied.

a function of working fluid viscosity. This follows intuition as the quality factor of the fluid cavity resonances decreases with an increase in the viscous dissipation in the acoustic boundary layer. As working fluid viscosity is increased, the largest pressure gradient magnitude transitions from occurring at the first order fluid cavity resonance as in the 100 mPas working fluid to lower operating frequencies (5 kHz) as in the 10 Pas working fluid. The change in the optimal operating frequency is a function of the increase of viscous boundary layer dissipation with the square root of frequency.[74] Operation at the fluid cavity resonances with high viscosity working fluids incurs significant viscous dissipation in the acoustic field as compared to low frequency operation. The effect is analogous to that seen in horn-based ultrasonic atomizers where optimal ejection frequency was the lowest considered operating frequency.

To investigate the effect of the ejector total length in the physical ejector geometries examined by Bogy and Talke, the acoustic response of the 18.7 mm ejector is compared to that of the 12.3 mm long (Figure 6.6) and 33.9 mm long (Figure 6.7) ejectors. Changes to the ejector length affect the geometries considered by Bogy and Talke in two manners. First, the resonance frequencies of the fluid cavity are altered. This does not have a significant impact on ejector operation as the maximum pressure gradient magnitudes still occur at the half wavelength resonances of the fluid cavity where a large particle velocity is generated in the driven section. Behavior with high viscosity working fluids also is similar with largest pressure gradient magnitudes occurring at low operating frequencies. The second mechanism is the increased length of the driven section as shown in Table 6.1. Despite the 33.9 mm ejector having a much longer length with more surface area and boundary layer losses, the maximum pressure

gradient magnitude produced by the ejectors is comparable. The reason becomes clear by examining how imposed radial velocity in the driven section of the ejector is converted to axial particle velocity and the resulting effect on the pressure amplitude of the propagating acoustic waves. The only locations in the ejector where the driving constant term ($2R_aR_c^2/EuMa^2$) in the particle velocity does not cancel from the governing equations is at the interface of the driven and spacer sections. The interfaces between the driven and space sections of the ejector can thus be thought of as the acoustic sources for the ejector. As the spacer lengths are the same between ejectors, the viscous dissipation occurred through wave propagation from the driven/spacer interface is the same. Moreover, as a large amplitude point of the particle velocity mode shape occurs at the driven/spacer interface for each ejector, all the ejectors have a similar amplitude acoustic field produced by the driven section. The similar propagation distance and imposed acoustic amplitude create a similar pressure gradient magnitude, thus the longer length of the 33.9 mm device is thus irrelevant to the pressure gradient magnitude at the fluid cavity aperture.

When the acoustic response of the piezoelectric transducer is included with that of the fluid cavity, as done in Figure 6.8 for each of the ejectors lengths with a 500 μm transducer thickness, the achievable pressure gradient magnitude becomes more uniform across fluid cavity resonances. The interaction of the piezoelectric transducer with the fluid cavity is a function the mode shape of the acoustic field and the radial velocity imposed by the transducer. For a fluid cavity driven with a constant amplitude velocity input, the pressure gradient magnitude declined slowly with increasing fluid cavity resonance mode as the acoustic impedance declined and viscous dissipation grew. These

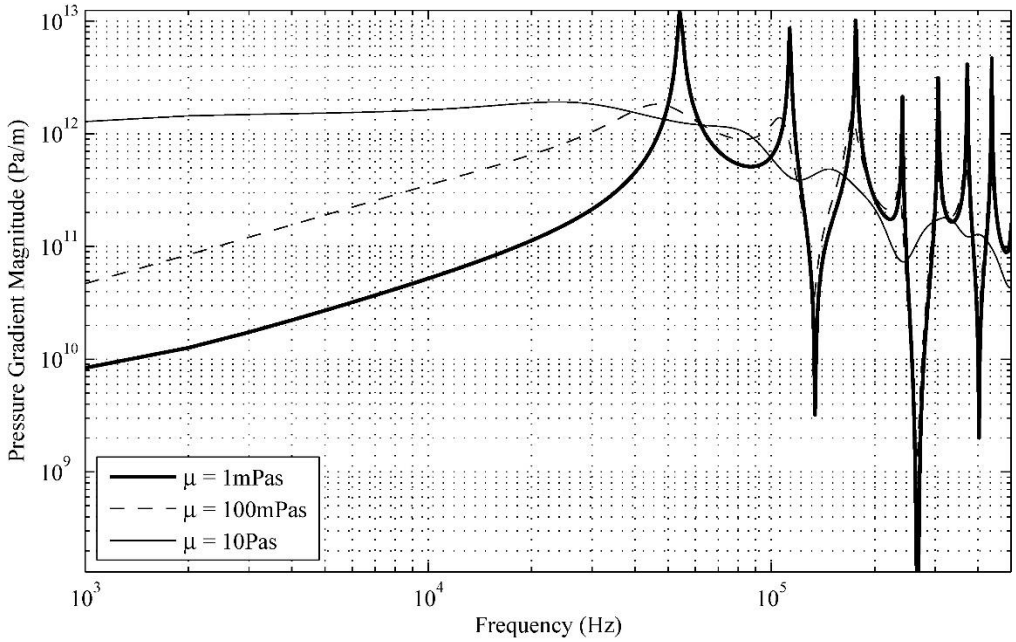

Figure 6.6: Variation in the pressure gradient magnitude at the ejector aperture as a function of frequency for artificial working fluids of increasing viscosity when driven by a constant amplitude (1 m/s) harmonic velocity signal on the capillary exterior. The sound speed and density of the working fluid are taken to be equal to those of glycol. The ejector length is 12.3 mm, composed of two 3 mm spacer sections, a 125 μm horn, and a 6.175 mm driven section

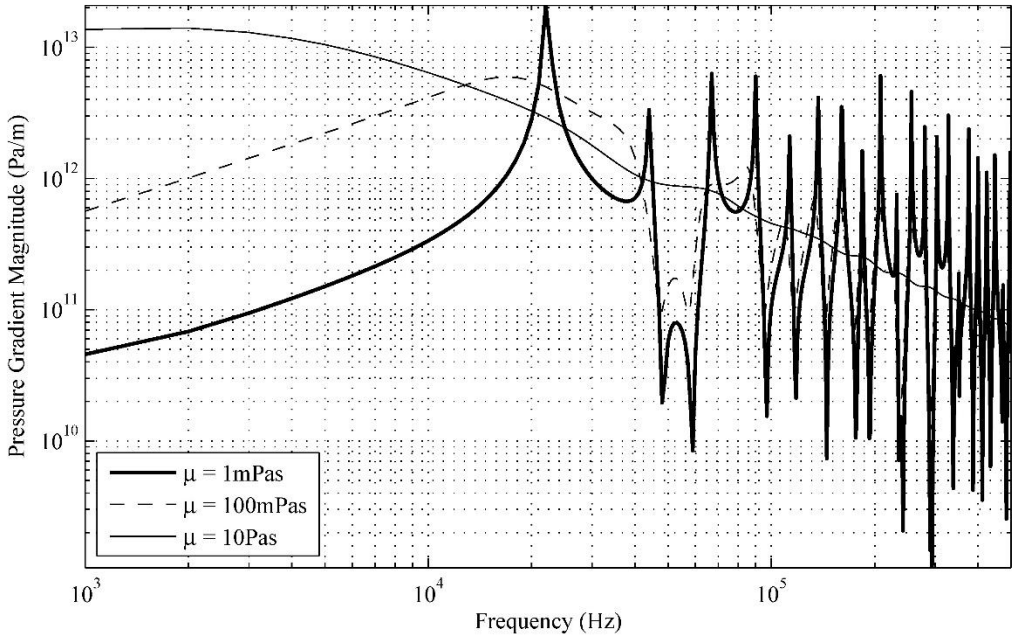

Figure 6.7: Variation in the pressure gradient magnitude at the ejector aperture as a function of frequency for artificial working fluids of increasing viscosity when driven by a constant amplitude (1 m/s) harmonic velocity signal on the capillary exterior. The sound speed and density of the working fluid are taken to be equal to those of glycol. The ejector length is 33.9 mm, composed of two 3 mm spacer sections, a 125 μm horn, and a 27.775 mm driven section

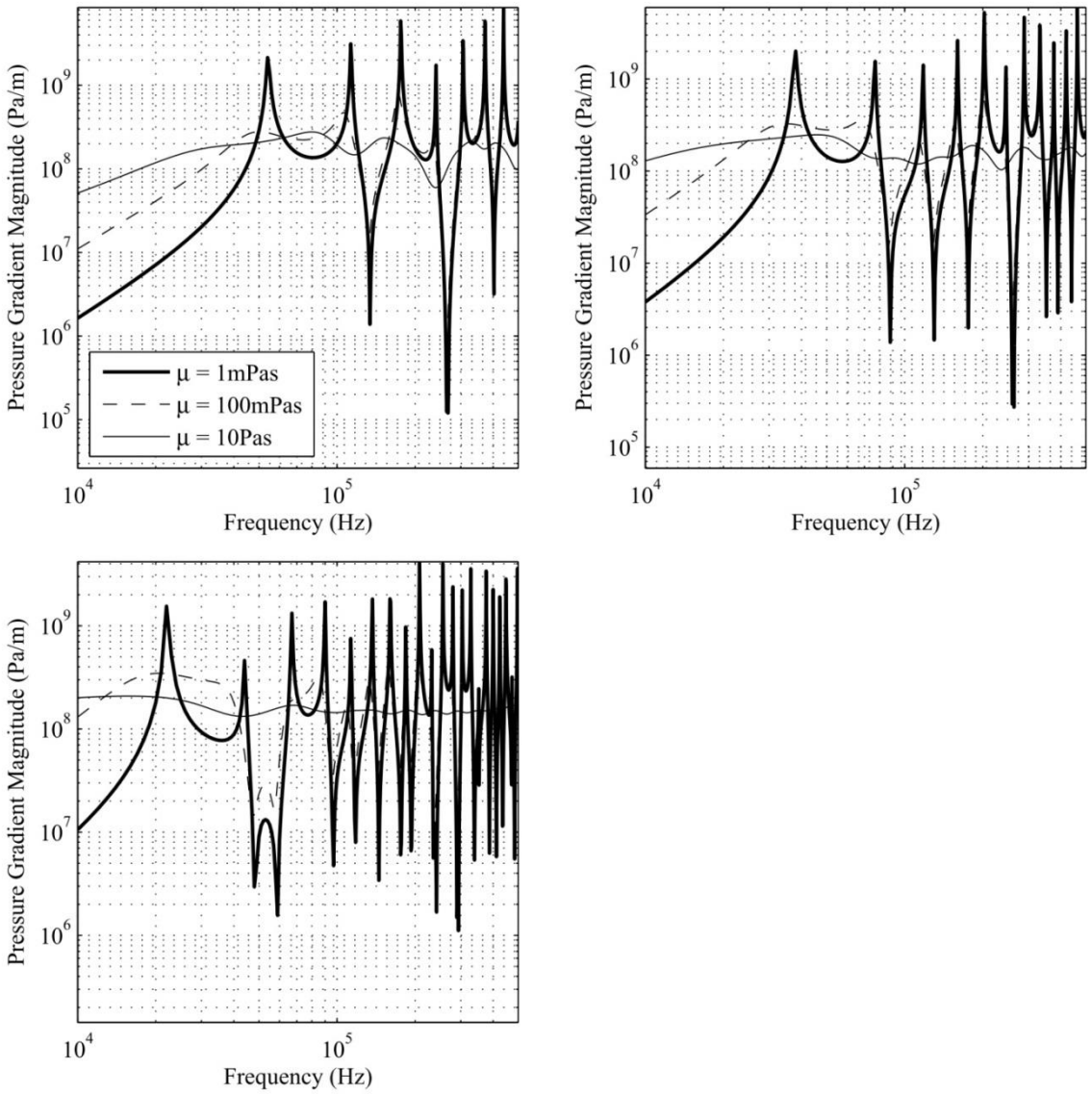

Figure 6.8: Variation in the pressure gradient magnitude at the ejector aperture as a function of frequency for artificial working fluids of increasing viscosity when driven by a 500 μm thick piezoelectric transducer with a sinusoidal input voltage of 1V. The sound speed and density of the working fluid are taken to be equal to those of glycol. Upper left: The ejector length is 12.3 mm, composed of two 3 mm spacer sections, a 125 μm horn, and a 6.175 mm driven section. Upper right: The ejector length is 18.7 mm, composed of two 3 mm spacer sections, a 125 μm horn, and a 12.575 mm driven section. Lower left: The ejector length is 33.9 mm, composed of two 3 mm spacer sections, a 125 μm horn, and a 27.775 mm driven section.

effects are offset in the transducer driven fluid cavity as the velocity imposed by the transducer grows as the operating frequency approaches the transducer thickness resonance. As the velocity imposed by the transducer grows linearly as a function of frequency much below the transducer thickness resonance, the variation in the predicted pressure gradient magnitude remains attributable to the response of the fluid cavity and the fluid cavity mode shape. The variation in the pressure gradient magnitude caused by the joint behavior of the fluid cavity and the piezoelectric transducer precludes the prediction of an optimal ejection configuration as the response of neither component is known prior to application of the analytical model.

As the viscosity of the working fluid is increased in the transducer driven ejector, the ejector response becomes still more uniform. For the 1 mPas artificial working fluid, the pressure gradient magnitude generated by the ejector is a strong function of operating frequency with the largest values occurring at the fluid cavity resonance modes. However, for the 10 Pas working fluid, most fluid cavity resonances are damped and the pressure gradient magnitude at low operating frequencies is the same order of magnitude as that occurring at high operating frequencies. This leveling of the response across the entire frequency spectrum occurs for high viscosity working fluids in part because the greater velocity imposed by the transducer at high operating frequencies approaching the transducer's resonance is offset by the greater viscous dissipation occurring at higher frequencies. Moreover, as the ejector becomes longer in length, the acoustic response of the fluid cavity with high viscosity working fluids becomes increasingly uniform as the resonance quality is reduced across a greater number of fluid cavity resonance modes.

To determine the ability of squeeze ejectors to eject working fluids of various viscosities, the maximum generated pressure gradient magnitude produced when the ejector is driven at the maximum (dielectric breakdown) voltage is compared to the pressure gradient threshold determined from a balance between the applied pressure gradient and viscous damping at the ejector nozzle apex. As the horn aperture radius is the same as in the previously examined horn-based ultrasonic atomizer and no fundamental change in the fluid mechanics governing fluid ejection is expected to exist between the device types, the pressure gradient thresholds as a function of working fluid viscosity developed in Chapter 4 can be applied. Due to linearity of the model, scaling the pressure gradient magnitude produced for 1V input to the transducer by the maximum voltage for each transducer thickness directly gives the maximum pressure gradient magnitude that can ever be achieved for each transducer thickness.

Tables 6.2 through 6.4 provide the maximum generated pressure gradient magnitude as a function of viscosity in the artificial working fluid for the ejector geometries studied by Bogy and Talke, as well as the associated pressure gradient threshold. Each ejector is assumed to be driven by transducer 500 μm in thickness. In all of the ejectors, irrespective of the fluid cavity length, the highest working fluid viscosity for which the pressure gradient threshold is exceeded is 1 mPas. This indicates that there is a fundamental limit on ejectability as function of fluid viscosity that can be realized by squeeze ejectors. While a larger driven surface area is present in squeeze devices as compared to horn-based ultrasonic atomizers, the conversion from the imposed radial velocity to axial velocity must account for the coupling between ejector sections. Greater viscous dissipation from the larger propagation length also overwhelms the benefits of

Table 6.2: The fluid cavity resonance frequencies and maximum pressure gradient magnitudes predicted in the squeeze ejector for artificial working fluids of increasing viscosity when driven by a 500 μm thick piezoelectric transducer at the dielectric breakdown voltage. The sound speed and density of the working fluid are taken to be equal to those of glycol. The ejector length is 12.3 mm, composed of two 3 mm spacer sections, a 125 μm horn, and a 6.175 mm driven section.

Working Fluid Viscosity (Pas)	Resonant Frequency (kHz)		
	Mode 1	Mode 2	Mode 3
0.001	54	113	176
0.01	53	112	175
0.1	50	106	172
1	32	95	162
10	80	152	330

Working Fluid Viscosity (Pas)	Maximum Pressure Gradient (GPa/m)			Pressure Gradient Threshold (GPa/m)	Fluid Ejection
	Mode 1	Mode 2	Mode 3		
0.001	211	307	579	10	Yes
0.01	68	109	220	100	Yes
0.1	27	46	78	1000	No
1	42	72	60	10,000	No
10	27	23	21	100,000	No

Table 6.3: The fluid cavity resonance frequencies and maximum pressure gradient magnitudes predicted in the squeeze ejector for artificial working fluids of increasing viscosity when driven by a 500 μm thick piezoelectric transducer at the dielectric breakdown voltage. The sound speed and density of the working fluid are taken to be equal to those of glycol. The ejector length is 18.7 mm, composed of two 3 mm spacer sections, a 125 μm horn, and a 12.575 mm driven section.

Working Fluid Viscosity (Pas)	Resonant Frequency (kHz)		
	Mode 1	Mode 2	Mode 3
0.001	38	77	118
0.01	37	76	117
0.1	35	68	113
1	21	61	104
10	46	90	140

Working Fluid Viscosity (Pas)	Maximum Pressure Gradient (GPa/m)			Pressure Gradient Threshold (GPa/m)	Fluid Ejection
	Mode 1	Mode 2	Mode 3		
0.001	198	153	139	10	Yes
0.01	67	58	52	100	No
0.1	32	35	22	1000	No
1	47	65	26	10,000	No
10	24	14	14	100,000	No

Table 6.4: The fluid cavity resonance frequencies and maximum pressure gradient magnitudes predicted in the squeeze ejector for artificial working fluids of increasing viscosity when driven by a 500 μm thick piezoelectric transducer at the dielectric breakdown voltage. The sound speed and density of the working fluid are taken to be equal to those of glycol. The ejector length is 33.9 mm, composed of two 3 mm spacer sections, a 125 μm horn, and a 27.775 mm driven section.

Working Fluid Viscosity (Pas)	Resonant Frequency (kHz)		
	Mode 1	Mode 2	Mode 3
0.001	22	44	67
0.01	22	43	66
0.1	21	85	109
1	12	32	75
10	16	68	134

Working Fluid Viscosity (Pas)	Maximum Pressure Gradient (GPa/m)			Pressure Gradient Threshold (GPa/m)	Fluid Ejection
	Mode 1	Mode 2	Mode 3		
0.001	152	45	130	10	Yes
0.01	50	19	39	100	No
0.1	34	32	16	1000	No
1	44	49	37	10,000	No
10	21	16	15	100,000	No

lowering the fluid cavity resonance frequencies to utilize the quality factor of the cavity. Collectively, these results indicate that the squeeze-type ejectors, as implemented by Bogy and Talke, are inferior in their ability to eject high viscosity fluids and fail to yield a sufficiently large pressure gradient magnitude for ejection of even moderately viscous fluids.

6.3 The effect of ejector and driving section lengths on the generated pressure gradient

The principal geometric parameters of squeeze type ejectors are examined to determine the potential for improving the maximum pressure gradient magnitude generated in the devices. The total ejector length, the driving length ratio (the fraction of the ejector total length which is driven by a transducer), and the transducer thickness are the geometric properties which impact ejector operation most significantly; the radius of the fluid cavity will also be considered but is less influential to the acoustic response of the ejector.

The ejector total length and the driving length ratio affect the ejector response primarily by determining the manner in which the piezoelectric transducer couples to the fluid cavity. The effect of ejector length on performance can be seen in Figures 6.9 and 6.10 which plot the pressure gradient magnitude as a function of ejector total length for the artificial test fluid. The ejector length was set by maintaining the driven and horn sections at a fixed length and increasing the spacer length. Figure 6.9 corresponds to a 5 mm transducer length and Figure 6.10 to a 15 mm transducer length, both driven with a sinusoidal input voltage of 1 V. Low working fluid viscosities exhibit a similar maximum pressure gradient magnitude above the first order fluid cavity resonance regardless of the ejector length as viscous dissipation is small for low viscosity working

fluids. In contrast, the pressure gradient magnitude produced at the first order fluid cavity resonance declines as a function of ejector length. As the ejector length grows, the mode shapes in the driven section are initially similar and yield similar velocities at the entrance to the spacer section. However, the longest spacer section significantly extends the wavelength at the first order fluid cavity resonance which places the interface of the driven/spacer sections at lower point on the particle velocity mode shape, reducing the coupling between sections. As the viscosity of the working fluid is increased, the similarity of mode shapes continues to produce comparable pressure gradient magnitudes for the smallest spacer lengths. However, the pressure gradient magnitude for the largest spacer length underperforms the shorter spacer lengths. The reduction in velocity entering the spacer sections combined with the greater viscous dissipation resulting from the longer spacer length yield a significantly reduced pressure wave amplitude at the horn aperture, resulting in a smaller pressure gradient. At low operating frequencies which minimize the acoustic boundary layer losses, the performance of the 10 mm spacer length ejector matches and exceeds that of the shorter spacers as the ejector transitions to operating as an acoustic pump taking advantage of the large fluid cavity impedance.

For the longer driven section length of 25 mm (Figure 6.10), the coupling effects between the fluid cavity and transducer are reduced. The driven section ratio becomes so large that the wavelength in the fluid cavity is not set by the spacer sections but rather by the length of the transducer. For small changes in the spacer length, similar large amplitude positions in the particle velocity mode shape fall on the interfaces between the driven/spacer sections. The largest impact of the variation in spacer length occurs at the longest considered spacer. For the 100 mPas working fluid, the ejector performance is

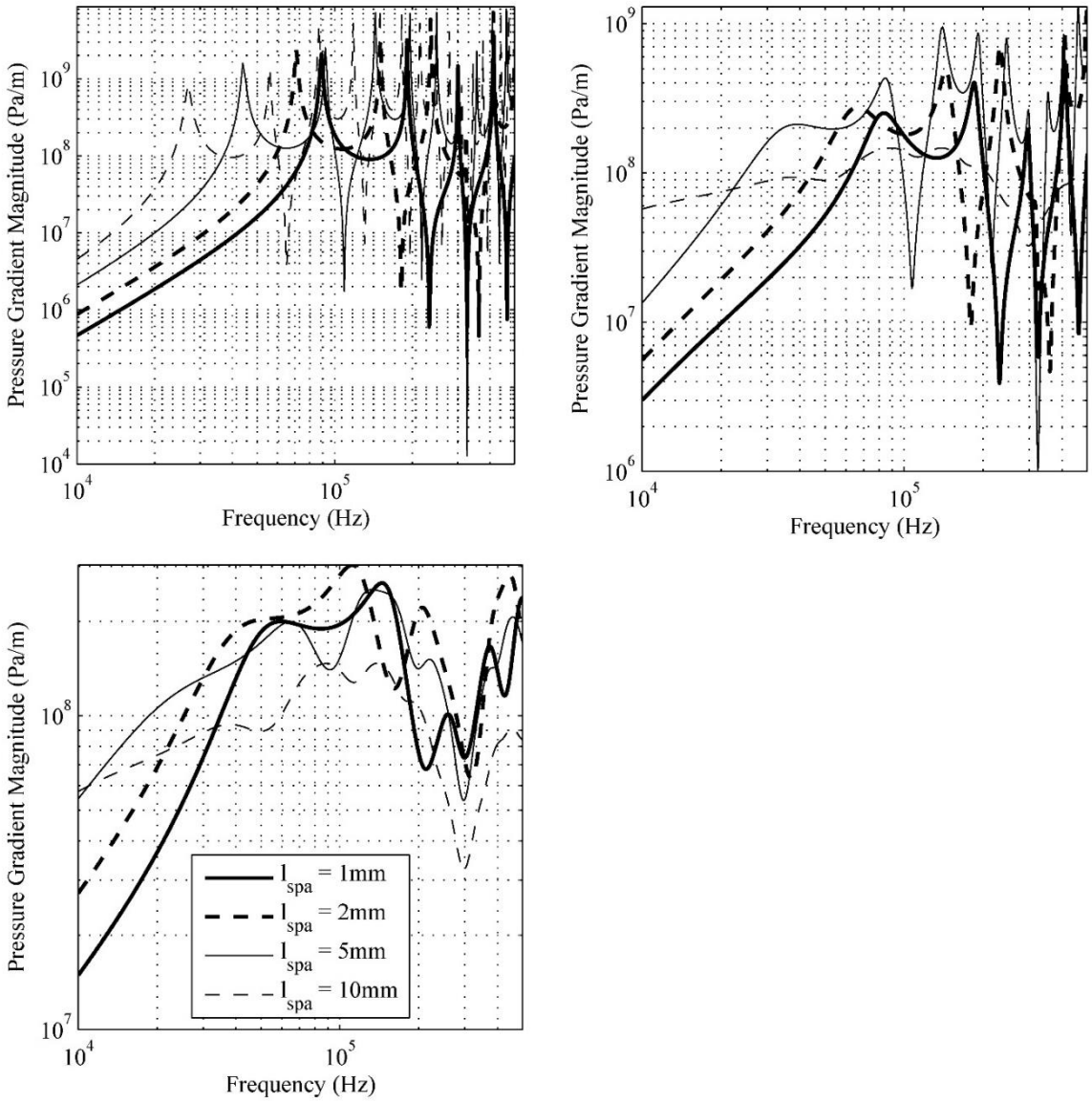

Figure 6.9: Variation in the pressure gradient magnitude at the ejector aperture as a function of frequency for artificial working fluids of increasing viscosity when driven by 5 mm long piezoelectric transducer with increasing spacer length. Each case was driven with a 500 μm transducer thickness and a 1V sinusoidal input voltage. The sound speed and density of the working fluid are taken to be equal to those of glycol. Upper left: Working fluid viscosity is equal to 1mPas. Upper right: Working fluid viscosity is equal to 100mPas. Lower left: Working fluid viscosity is equal to 10Pas.

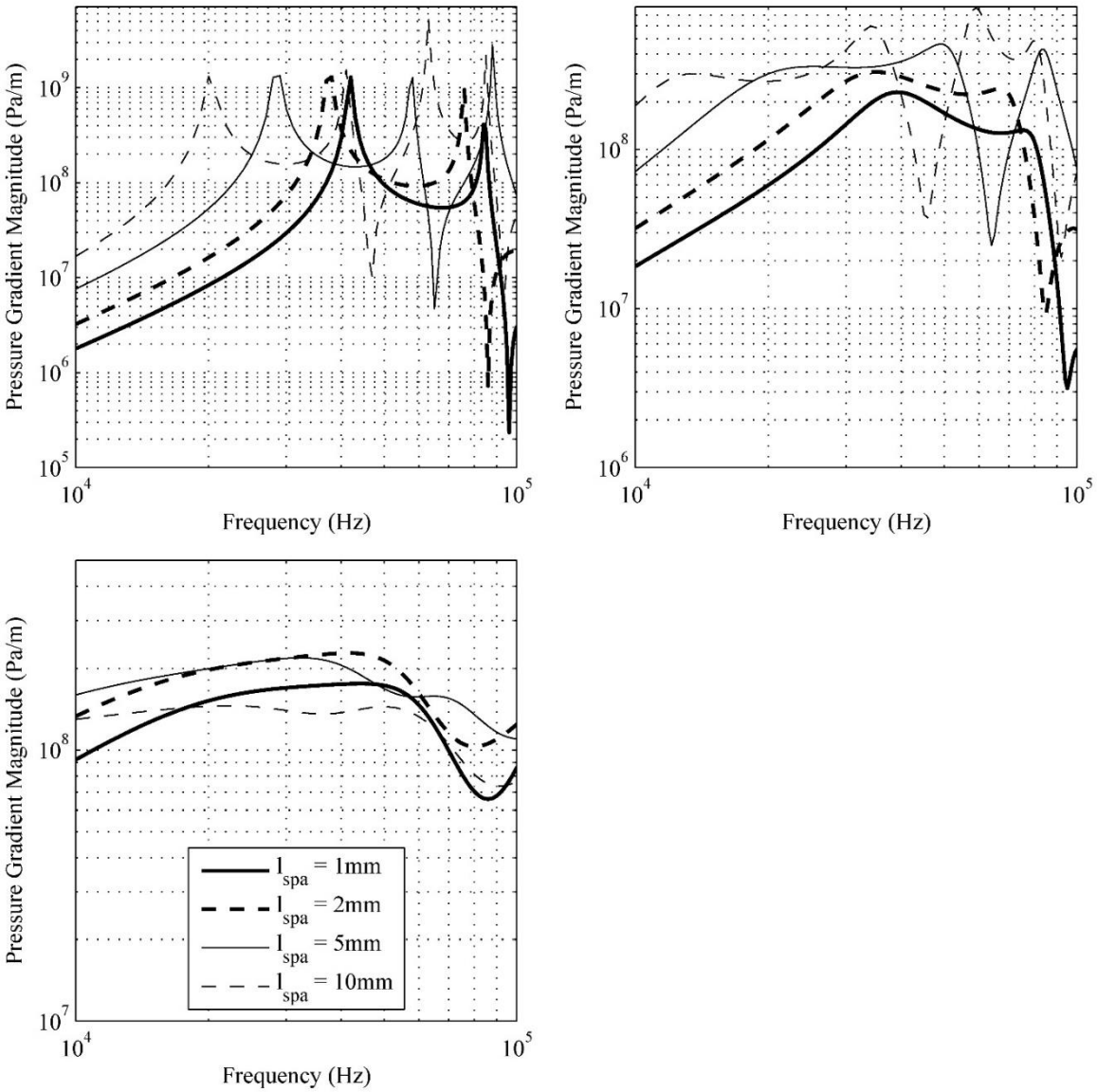

Figure 6.10: Variation in the pressure gradient magnitude at the ejector aperture as a function of frequency for artificial working fluids of increasing viscosity when driven by 15 mm long piezoelectric transducer with increasing spacer length. Each case was driven with a 500 μm transducer thickness and a 1V sinusoidal input voltage. The sound speed and density of the working fluid are taken to be equal to those of glycol. Upper left: Working fluid viscosity is equal to 1mPas. Upper right: Working fluid viscosity is equal to 100mPas. Lower left: Working fluid viscosity is equal to 10Pas.

improved with the 10 mm spacer length. The long spacer length lowers the fluid cavity resonances such that higher order fluid cavity resonance modes occur in the frequency range of interest. As higher order fluid cavity resonance modes have higher quality factors as compared to lower order resonance modes, they produce a larger amplitude acoustic field which offsets the large viscous dissipation occurring from the large ejector length. Moreover, the length of the driven section is approaches half of the total ejector length which was shown to be optimal for coupling between ejector components due to a half wavelength occurring in the driven section. However, as viscous dissipation is increased for fluids with 10 Pas viscosity, the performance of the longest spacer lengths again declines as viscous dissipation dominates the ejector acoustic response.

The dependence of ejector performance on the coupling between the driven and spacer sections can be seen in Figures 6.11 and 6.12 which plot the pressure gradient magnitude as a function of driven length ratio for a fixed total ejector length in the artificial test fluid. Fixed total ejector length is maintained by reducing the spacer length. Figure 6.11 corresponds to a 15 mm ejector length and Figure 6.12 to a 25 mm ejector length. As the total ejector length is maintained at a fixed value, the fluid cavity mode shapes are the same between driving conditions. Changes to the driven section length effect the extent of the mode shape within the driven portion of the capillary and, by extension, the fluid cavity acoustic impedance placed on the transducer. Also, as the transducer grows in length, the location of the interface between the driven and spacer sections occurs at varying positions along the mode shape in the fluid cavity. The resonances of the fluid cavity correspond to an integer number of half wavelengths along the extent of the fluid cavity; however, for optimal transducer coupling to occur between

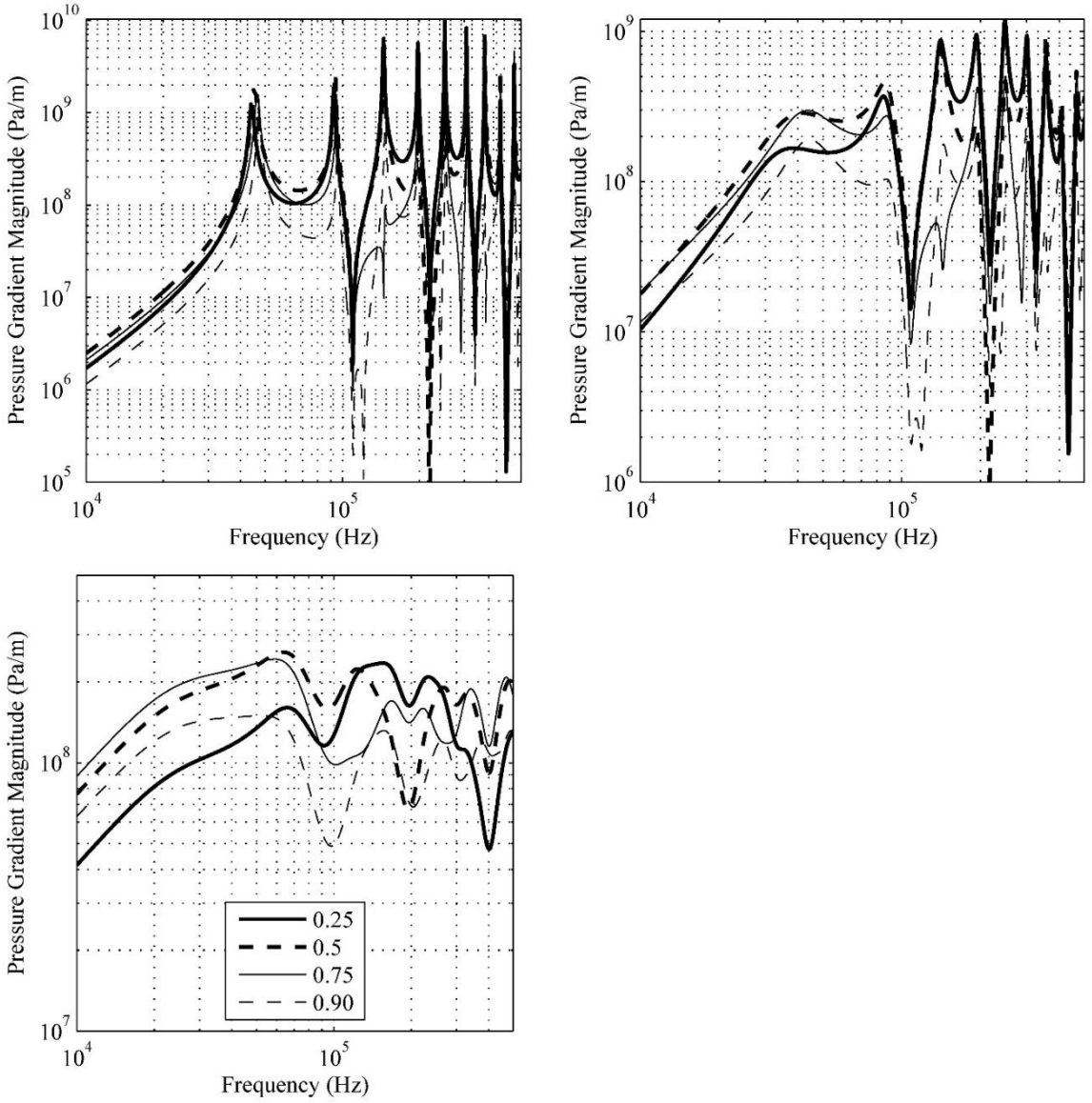

Figure 6.11: Variation in the pressure gradient magnitude at the ejector aperture as a function of frequency for artificial working fluids of increasing viscosity in a 15 mm ejector driven by transducers of various lengths. Each case was driven with a 500 μm transducer thickness and a 1V sinusoidal input voltage. The sound speed and density of the working fluid are taken to be equal to those of glycol. Upper left: Working fluid viscosity is equal to 1mPas. Upper right: Working fluid viscosity is equal to 100mPas. Lower left: Working fluid viscosity is equal to 10Pas.

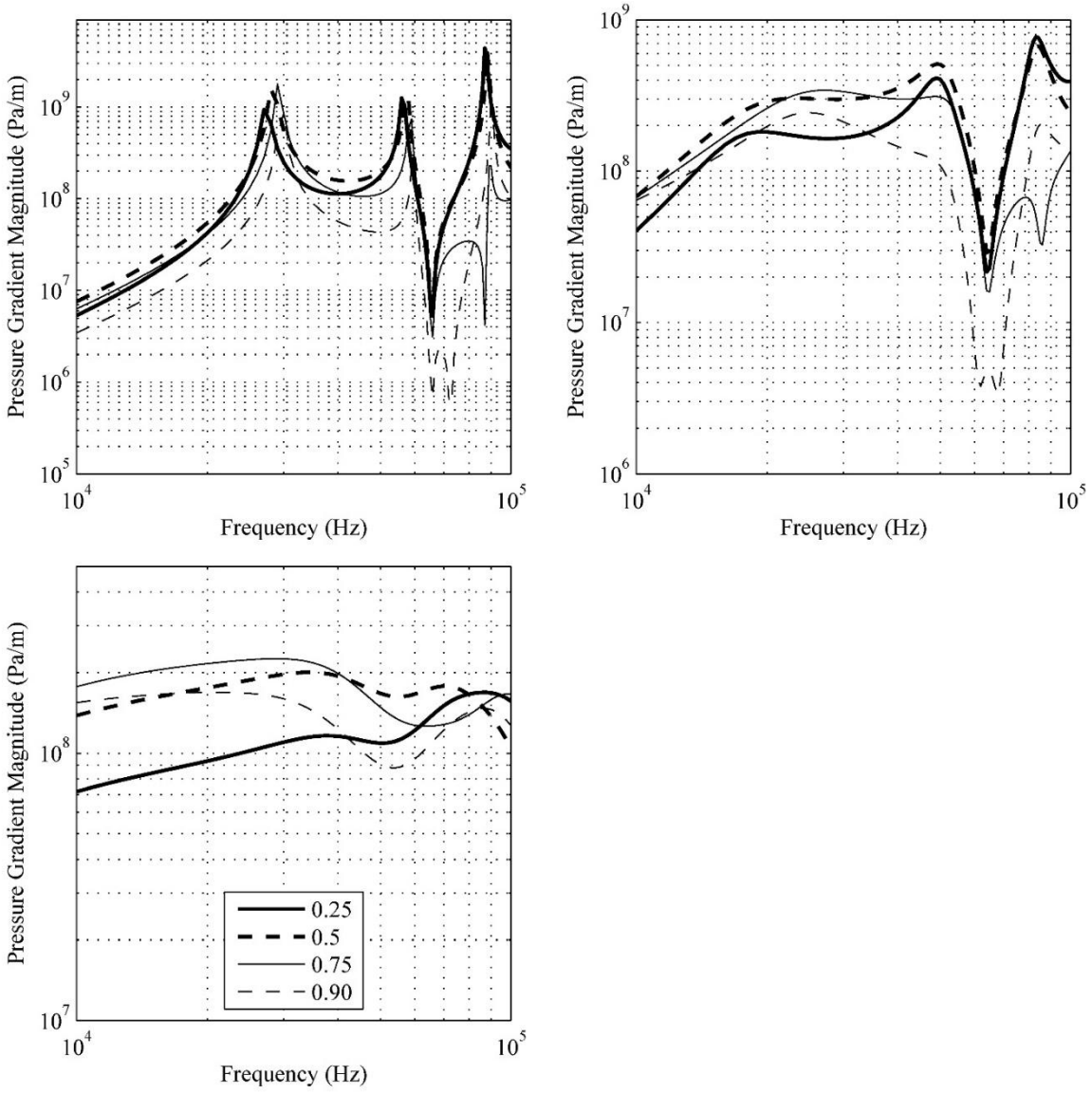

Figure 6.12: Variation in the pressure gradient magnitude at the ejector aperture as a function of frequency for artificial working fluids of increasing viscosity in a 25 mm ejector driven by transducers of various lengths. Each case was driven with a 500 μm transducer thickness and a 1V sinusoidal input voltage. The sound speed and density of the working fluid are taken to be equal to those of glycol. Upper left: Working fluid viscosity is equal to 1mPas. Upper right: Working fluid viscosity is equal to 100mPas. Lower left: Working fluid viscosity is equal to 10Pas.

the transducer and spacers an integer number of half wavelengths must also be confined in the driven section. At the first order fluid cavity resonance mode, the change in the amplitude of the particle velocity mode shape at the driven/spacer section interface is small for increasing driven section ratio since the wavelength is long as compared to the driven section length. The mean acoustic impedance loaded on the transducer for the transducer lengths is large as a pressure antinode occurs in the center of the ejector. However, when the driven section becomes long, it encompasses nearly the entire extent of the fluid cavity causing the mean acoustic impedance to decline as the low pressure regions near the pressure release conditions at the inlet/aperture are included in the mean acoustic impedance. This affect is particularly strong at the higher order fluid cavity resonances. Thus, as the transducer increases in length, the pressure amplitude produced by the transducer decreases. Despite the considered variation in the driven and spacer sections, no combination of the geometric parameters was shown which produced a significant increase in the pressure gradient magnitude generated by squeeze type ejectors.

6.4 The effect of ejector radius on the generated pressure gradient

The inner radius of the fluid ejector affects the viscous dissipation in the fluid cavity by defining the surface area over which the viscous boundary layer losses occur, as well as the spatial wave dispersion resulting from changes to the cross-sectional area of the capillary. For low and medium viscosity working fluids, changes to the capillary radius affect the acoustic response of the ejector little as shown in Figures 6.13 and 6.14 for a 12.3 mm and 18.7 mm ejector length, respectively. All dimensions other than the capillary inner radius are taken to be equal to the dimensions given by Bogy and Talke for each ejector length.[2] Increasing capillary radius for ejection of low and medium

viscosity working fluids improves the quality factor of the fluid cavity resonance modes to yield a larger pressure gradient magnitude at the nozzle apex without otherwise altering the behavior of the fluid cavity. For the high viscosity working fluid, the pressure gradient magnitude produced by the ejector initially increases with the capillary radius but plateaus beginning at the radius beyond 500 μm. This change in behavior as compared to the lower viscosity working fluids is a result of the increased rigidity of high viscosity fluids affecting the manner in which the fluid cavity responds to the pressure release condition at the horn aperture, as shown in Figure 6.15 for the 200 μm and 500 μm radius cases. For small capillaries, the area reduction between the capillary and the horn aperture is less which makes the transition from the fluid cavity to the horn more gradual with lesser impact of pressure release condition on the acoustic field in the horn. As the capillary radius is increased, the area reduction becomes more significant and the boundary condition at the end of the horn begins to appear more like a rigid condition (a solid wall) due to the drastic reduction in cross-sectional area. While large capillary radii do increase the pressure gradient magnitude produced by the fluid ejector for high viscosity fluids due to the appearance of a rigid boundary condition at the horn and therefore an increase in the total impedance of the fluid cavity, this improvement is not sufficient to result in a substantial increase to the maximum working fluid viscosity able to be ejected by squeeze type ejectors.

6.5 The effect of transducer thickness on the generated pressure gradient

The electro-mechanical response of squeeze fluid ejectors is determined by the interaction of the fluid cavity with the piezoelectric transducer. The displacement imposed on the fluid cavity by the driving piezoelectric transducer is in general a function of the fluid cavity acoustic impedance, the input voltage signal driving a transducer, and

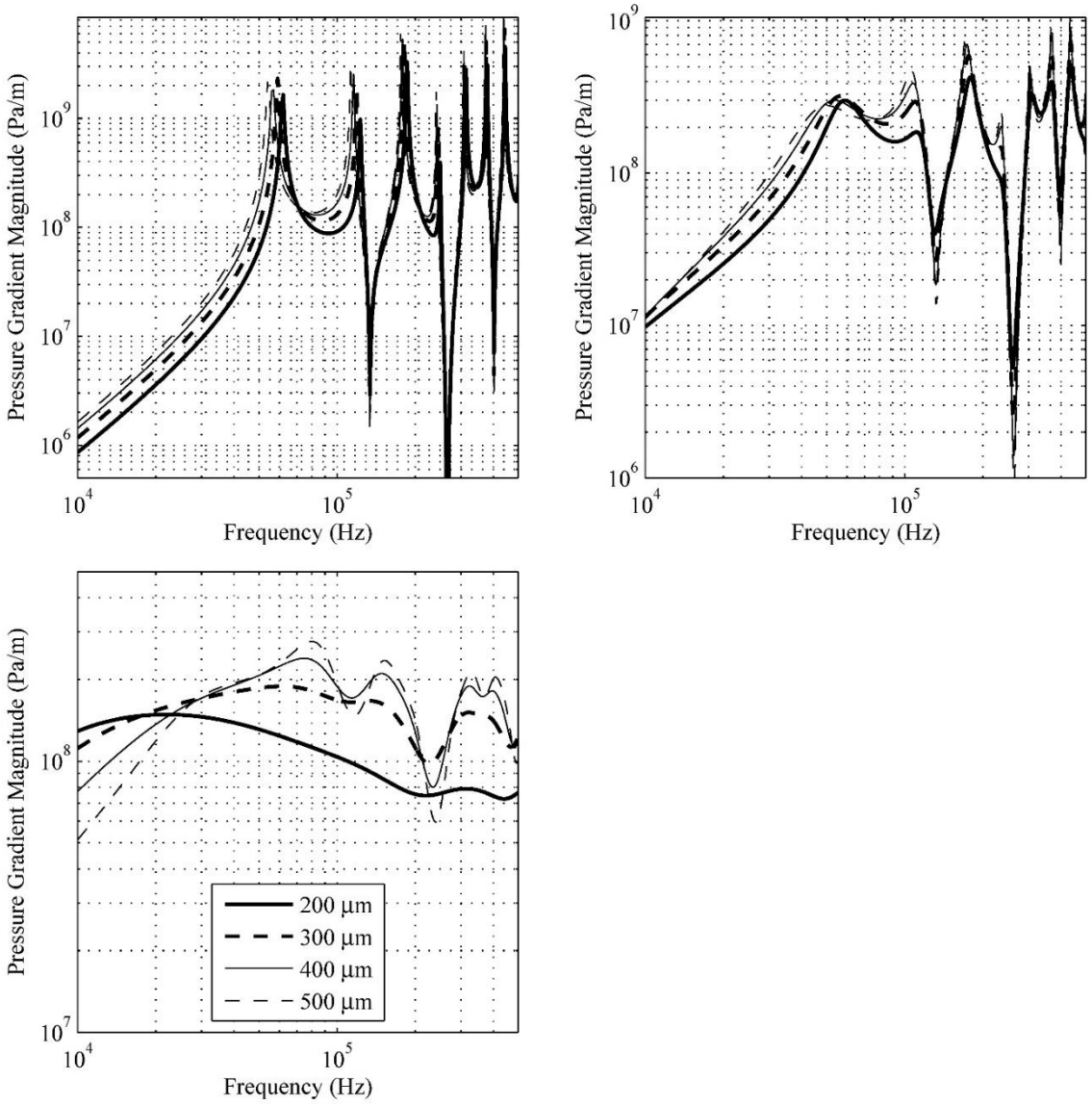

Figure 6.13: Variation in the pressure gradient magnitude at the ejector aperture as a function of frequency for artificial working fluids of increasing viscosity in a 12.3 mm ejector with increasing capillary inner radius. Each case was driven with a 500 μm transducer thickness and a 1V sinusoidal input voltage. The sound speed and density of the working fluid are taken to be equal to those of glycol. Upper left: Working fluid viscosity is equal to 1mPas. Upper right: Working fluid viscosity is equal to 100mPas. Lower left: Working fluid viscosity is equal to 10Pas.

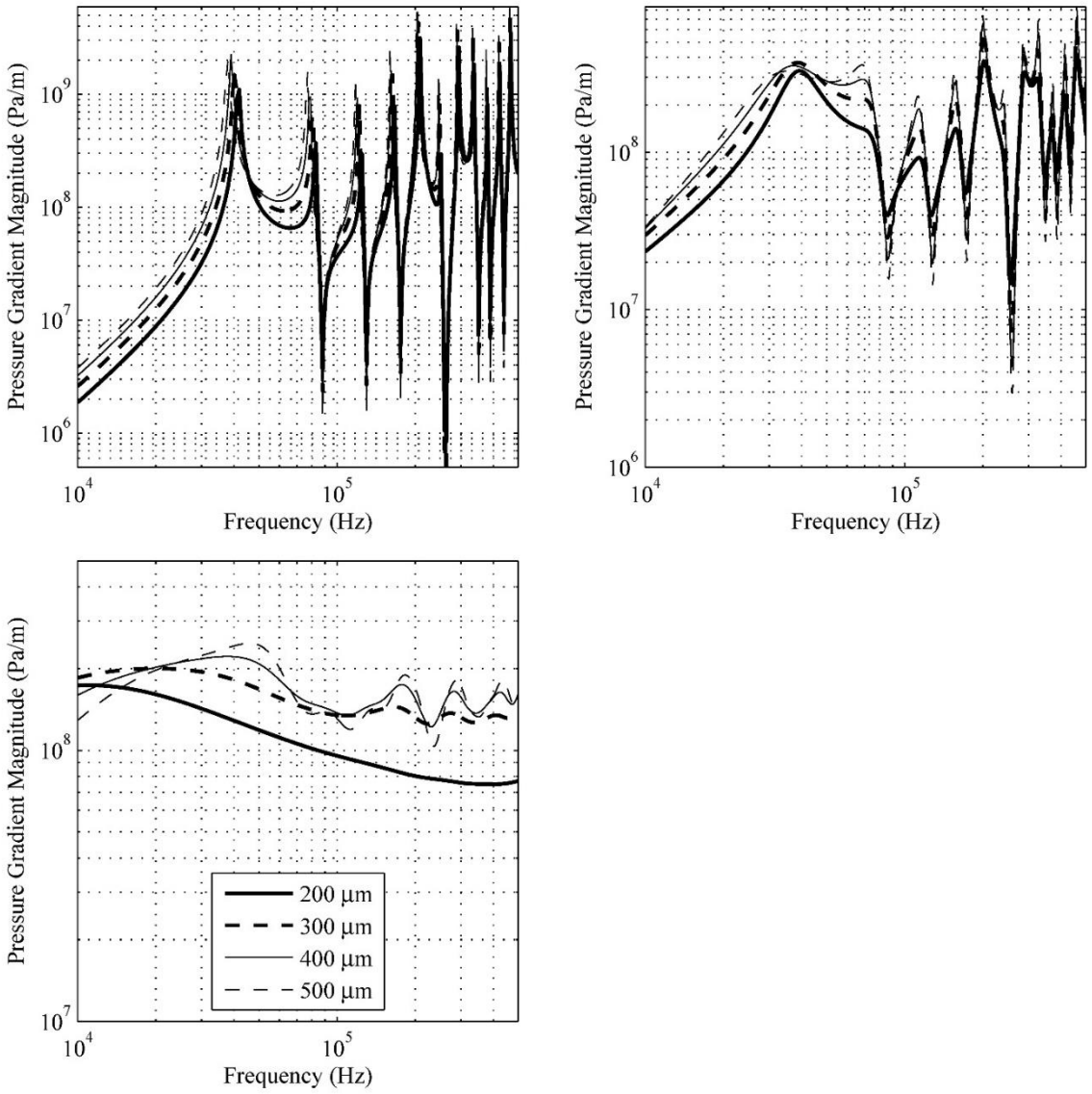

Figure 6.14: Variation in the pressure gradient magnitude at the ejector aperture as a function of frequency for artificial working fluids of increasing viscosity in a 18.7 mm ejector with increasing capillary inner radius. Each case was driven with a 500 µm transducer thickness and a 1V sinusoidal input voltage. The sound speed and density of the working fluid are taken to be equal to those of glycol. Upper left: Working fluid viscosity is equal to 1mPas. Upper right: Working fluid viscosity is equal to 100mPas. Lower left: Working fluid viscosity is equal to 10Pas.

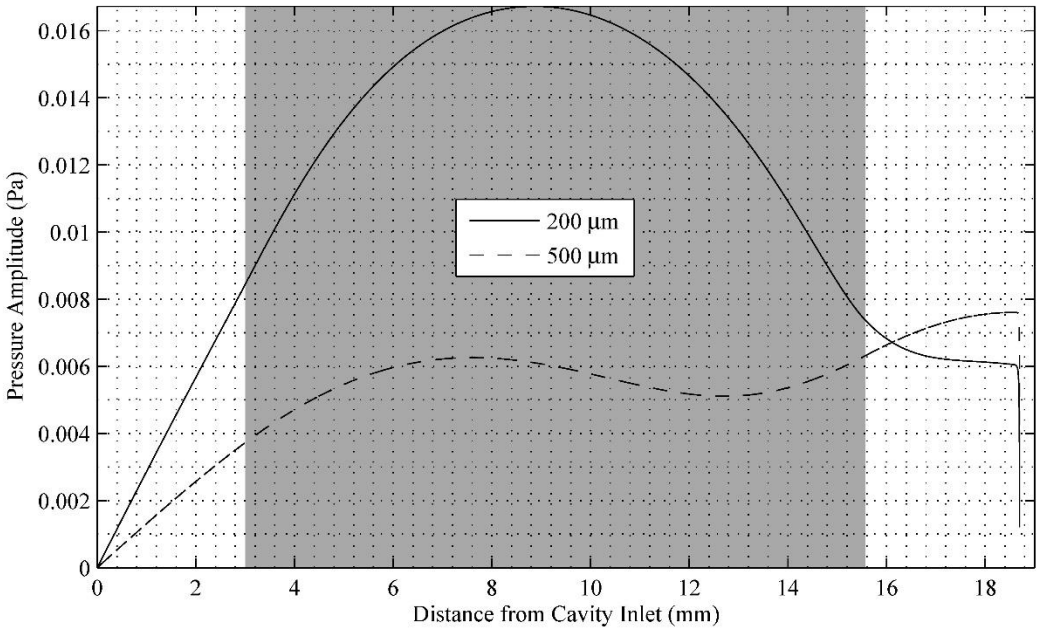

Figure 6.15: Pressure amplitude in the ejector fluid cavity as a function of distance from the cavity inlet for varying capillary radius at the first order fluid cavity resonance (80kHz). The working fluid is taken to be the artificial test fluid with 10 mPas viscosity and is driven by a 500 µm thick piezoelectric transducer. The shaded area indicates the portion of the fluid cavity to which the driving condition is applied.

the electromechanical properties of the transducer. For a fixed fluid cavity geometry and piezoelectric material, the only adjustable transducer parameter is the thickness.

To determine the effect of the piezoelectric transducer thickness on squeeze type ejectors, the transducer thickness was varied in the 12.3 mm geometry for the artificial working fluid with increasing viscosity as shown in Figure 6.16. Low viscosity working fluids can be ejected with almost any transducer thickness as the maximum pressure gradient generated by the ejector readily exceeds the ejection threshold obtained from scaling analysis. In contrast, the pressure gradient threshold for high viscosity fluids is several orders of magnitude larger than the maximum pressure gradient predicted by the model, indicating that the geometry presented by Bogy and Talke cannot eject working fluids of high viscosity. For working fluids with viscosities on the order of 100 mPas, fluid ejectability is determined by the thickness of the transducer. Thin transducers are

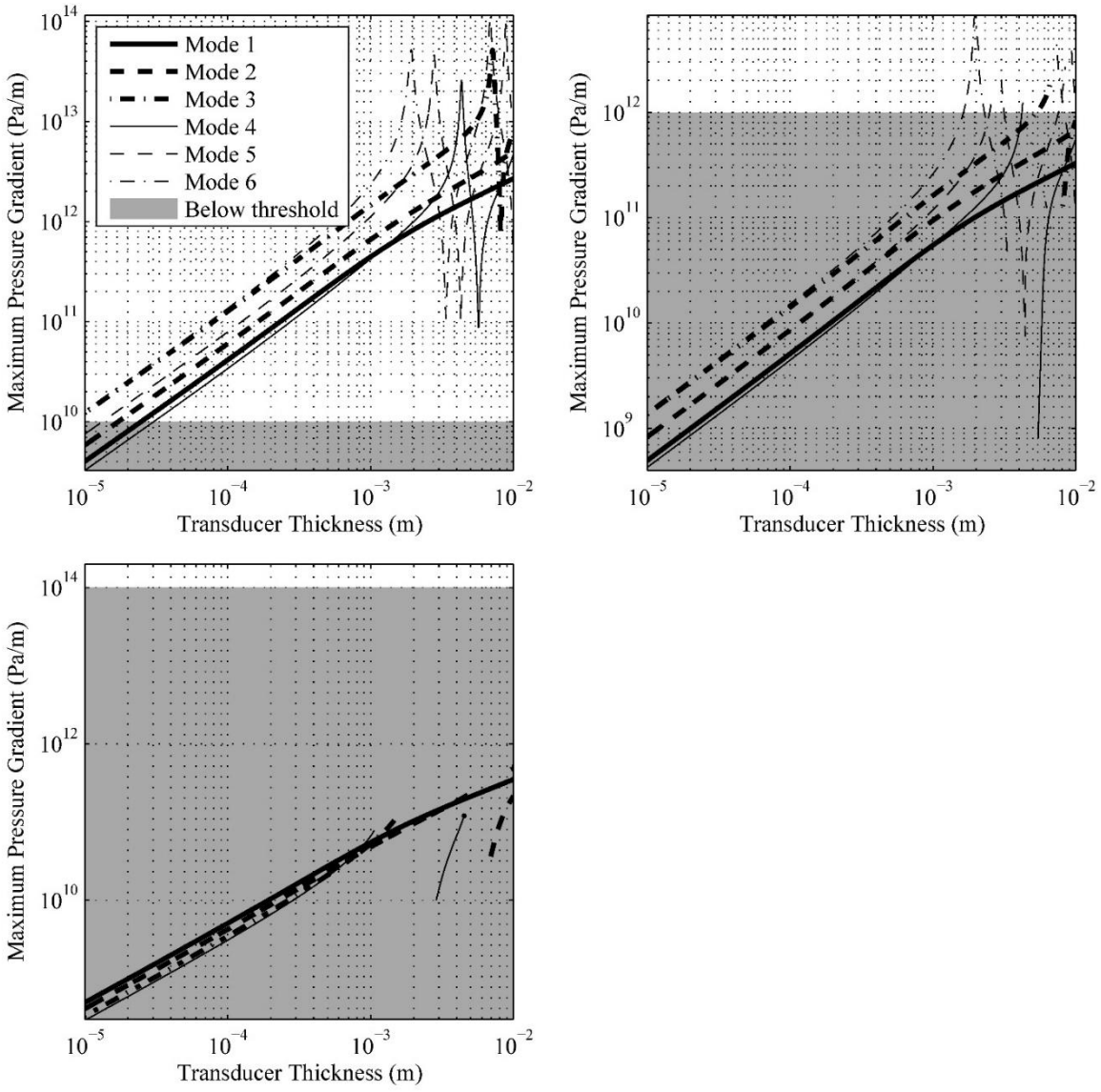

Figure 6.16: Variation in the pressure gradient magnitude at the horn aperture for each fluid cavity resonance as a function of transducer thickness when driven by a voltage signal limited by the transducer dielectric breakdown field. The pressure gradient threshold for each viscosity is shown in gray, with configurations in white zone capable of producing a sufficient pressure gradient for fluid ejection. The 12.3mm ejector geometry is utilized. The sound speed and density of the working fluid are taken to be equal to those of glycol. Top left: Working fluid viscosity is equal to 1mPas. Top right: Working fluid viscosity is equal to 100mPas. Bottom left: Working fluid viscosity is equal to 10Pas.

not able to impose a sufficiently large driving velocity on the fluid cavity to overcome the increased viscous dissipation and shear stresses at the nozzle aperture. For thick transducers, the fluid cavity resonance and transducer thickness resonance frequencies become comparable in magnitude. The large driving velocities imposed by the transducer are amplified by the fluid cavity, thus permitting the fluid ejection.

This analysis suggests that the upper limit of working fluid viscosities able to be ejected by squeeze type ejectors is on the order of 100 mPas. Large computational times prohibit a comprehensive multi-parameter optimization of squeeze ejector geometries to further refine the viscosity limit. However, as the considered 12.3 mm geometry lies close to the ideal case with the driving section being a half wavelength shorter than the fluid cavity, one could not expect significant increases to the maximum pressure gradient magnitude were additional geometries to be considered.

6.6 Concluding remarks on squeeze type ejectors

A coupled electro-mechanical model was applied to understand the ejection of high viscosity working fluids by squeeze type ejectors. The acoustic response of the realized ejector devices examined by Bogy and Talke were characterized and performance was shown to heavily depend on the placement of the driven section along the mode shape of the fluid cavity. For strong coupling between different ejector sections (transducer, spacers, and the horn) and the generation of large pressure gradient magnitudes for a given driving condition, a point on the particle velocity mode shape with a large amplitude must lie on the interface between the driven and spacer sections. By comparing the maximum pressure gradient magnitude produced by the ejectors against an estimated pressure gradient threshold value required for ejectability, it was shown that ejection of working fluids with greater than 100 mPas viscosity is unlikely to

be possible. This value agrees with the experimental values seen in Sun et al.[93] The inability of squeeze ejectors to generate a sufficiently large pressure gradient magnitude to eject high viscosity working fluids was shown to extend across a broad range of geometric parameters of the ejector, namely the total length, driven length ratio, capillary inner radius, and transducer thickness. Application of the developed analytical model to squeeze type fluid ejectors thus indicates that such ejectors could not generate greater pressure gradient magnitudes as compared to horn-based ultrasonic atomizers, and would therefore unable to extend the range of fluid viscosities that can be ejected by the ultrasonic atomizers relying on pressure waves to produce a driving force for atomization.

CHAPTER 7: CONCLUSIONS AND RECOMMENDATIONS FOR FUTURE WORK

This dissertation presented the development of a series of coupled electro-mechanical models for micromachined fluid ejectors of increasing complexity, and these models' applications to horn-based ultrasonic atomizers and squeeze type ejectors aiming at understanding their performance with high viscosity working fluids. The analytical models have been shown to accurately predict the acoustic field in fluid ejectors while incorporating the dominant sources of viscous dissipation in fluid cavity acoustic field due to the acoustic boundary layer and bulk attenuation in various operating regimes. In addition, the acoustics of the ejectors was coupled to the piezoelectric transducer behavior for various embodiments (planar quasi-1D and cylindrical), resulting in a complete electromechanical model of atomizers. The closed-form analytical solution of the ejector models was developed for a number of practically realizable designs, thus providing a computationally efficient means to analyze the effect of high viscosity working fluids on the operation of fluid ejectors.

The models were developed by decomposing the ejectors into component parts, developing models for each component, and coupling the component models together via appropriate boundary conditions according to the specific ejector design. Through comparison to finite-element simulations and experimental data from literature, the model was shown to accurately reproduce the acoustic response of fluid ejectors. Original contributions have been made in the development of analytical ejector models (Chapter 3) as well as understanding the acoustic response of various ejector geometries (Chapters 4 and 6). Description of the ejector acoustic response was done in parallel with

device optimization for operation with high viscosity working fluids (Chapters 4 and 5). Application of the analytical ejector models and comparison against the "ejectability" pressure gradient threshold allowed us to establish an upper limit on the working fluid viscosity able to be ejected by ejectors within the limits of considered designs and geometries.

While substantially advancing the current state-of-the-art in the field, the device analytical models were formulated using certain assumptions about the behavior of the fluid cavity acoustic field, namely a one dimensional pressure/velocity fields and linear acoustics. To more generally characterize the behavior of micromachined fluid ejectors, investigation of the following model modifications is recommended for future research:

1. *Retention of both the Radial and Axial Shear Stress Components in Model Formulation:* The development of closed form analytical solutions required that the components of the viscous shear stress be treated individually based on the operating regime in which each was the dominant source of viscous dissipation. While the viscous dissipation due to the boundary layer is the largest source of acoustic energy loss in geometries bounded by walls, bulk attenuation still occurs especially at higher frequencies as the wave propagates in the axial direction. Moreover, for high working fluid viscosities, the magnitude of losses due to bulk attenuation can still be large in absolute terms. Inclusion of both terms in the model would more accurately account for viscous dissipation, but would require the use of numerical solution methods as closed form analytical solutions would no longer be permitted.

2. *Consideration of a Two-Dimensional Acoustic Field in the Fluid Cavity:* The development of closed form analytical solutions for the fluid cavity acoustic field assumed a quasi-one-dimensional acoustic field in the axial direction, allowing for only a small variation in the axial particle velocity to match the no slip condition at the wall. As the operating frequency for micromachined fluid ejectors is increased, the wavelength in the fluid cavity would eventually become comparable to the diameter of the fluid cavity causing the one dimensional acoustic field assumption to break down. This is a particular concern as the horn entrance diameters become large. Consideration of two-dimensional effects would allow larger in size and more complex in shape fluid cavity geometries to be considered which have the potential for large volume velocity concentration in viscous fluids.
3. *Inclusion of Nonlinear Wave Propagation in the Fluid Cavity Acoustic Field:* During the formulation of the analytical models, the nonlinear terms were eliminated as they were assumed to be small compared to the linear terms. When the amplitude of the fluid cavity acoustic field becomes large this assumption will no longer hold. Any substantial increases to the fluid cavity acoustic field, particularly in horn-based ultrasonic atomizers when driven with high input velocities/displacements, may produce a sufficiently large amplitude acoustic field that nonlinear effects must be considered for an accurate representation of the ejector acoustic response.

The analytical model for horn-based ultrasonic atomizers was applied in Chapter 4 to understand the acoustic response of the devices when loaded with working fluids of

increasing viscosity. An exhaustive optimization was conducted of the atomizer geometry to yield the maximum pressure gradient producible by the device. By the application of the pressure gradient threshold required for ejection, it was shown that horn-based ultrasonic atomizers are only capable of producing a large enough pressure gradient magnitude to eject working fluids with viscosities on the order of 100 mPas. The ejection of higher viscosity working fluids, which was demonstrated experimentally in the literature, are not predicted by the model and requires additional work to understand fully. Based on the need to resolve the discrepancy between the predictions of the analytical model and experimental measurements, the following areas are recommended for future research:

1. *Further Study of the Pressure Gradient Magnitude Required to Eject Working Fluids as a Function of Working Fluid Properties:* A more accurate estimate of the pressure gradient threshold obtained through a detailed understanding of the fluid mechanics at the horn aperture would reduce the uncertainty surrounding the current order of magnitude estimate. The refined value could be applied to understand if changes in the fluid mechanics at the horn aperture reduce the pressure gradient threshold to enable the ejection of high viscosity working fluids. The value could also be applied to better optimize each given ejector geometry for operation with the targeted working fluid.
2. *Further Study of the Working Fluid Heating Effects:* Previous experimental work with horn-based ultrasonic atomizers did not capture the transient working fluid temperature that could be the enabling ejection mechanism for high viscosity fluids through lowering of the working fluid viscosity. Direct measurements of

the working fluid temperature are required to better understand this mechanism. Moreover, a record of the time delay between the powering of the atomizer and the start of ejection is necessary to understand the temperature increase that occurs prior to fluid ejection.

In Chapter 5, potential modifications to the geometry of horn-based ultrasonic atomizers were investigated in order to increase the pressure gradient magnitude produced by the atomizer. Two different designs were analyzed, both utilizing a low viscosity working fluid in the reservoir coupling the transducer to the horn filled with the high viscosity fluid to be ejected. The first geometry consisted of a uniform cross section reservoir and the second geometry of an additional acoustic horn in place of the reservoir for greater concentration of the volume velocity imparted by the transducer. It was shown that with available working fluids of desperate viscosities, such as water and glycerol, that any increase in ejector performance would be marginal and not provide any meaningful increase to the working fluid viscosity able to be ejected. The considered geometric modifications were limited by the assumptions built into the analytical models, such as quasi-one-dimensional behavior and a slow change of cross-sectional area along the ejector length. However, numerous additional modifications can be envisioned, which cannot be directly handled by the developed models. As such, the following areas are recommended for future research:

1. *Incorporation of a Solid Secondary Horn to Concentrate Volume Velocity:* The poor performance of the secondary acoustic horn was attributed to the reduction in the fluid cavity impedance at the transducer surface. Use of a solid secondary horn rather than a liquid horn (i.e. silicon) should increase the fluid cavity

acoustic impedance seen by the transducer, as well as should reduce the viscous dissipation in the fluid cavity due to the lower attenuation in the solid medium. Inclusion of a solid horn would require the development of a model which could describe the two-dimensional affects present in solids as well as the coupling between compression and shear wave modes.

2. *Use of Multiple, Fluid Filled Horn in Series:* Multiple acoustic horns would permit a greater amplification factor of the input driving condition. Such structures have demonstrated a performance benefit in the atomization of low viscosity liquids, but still need to be evaluated for fluids of high viscosity.[123] Inclusion of multiple horns would require the development of a model which could describe the sudden change in area between horn components and the resulting two-dimensional acoustic field.
3. *Additional Driving Mechanisms to Increase the Energy in the Fluid Cavity Acoustic Field:* While minimization of viscous dissipation in the fluid cavity is important to achieving overall large pressure levels in the cavity, the pressure amplitude and thus the pressure gradient at the ejection aperture is ultimately governed by the amount of energy delivered by the transducer and transmitted to the ejection point. The present analysis has shown that a fluid ejector with a single, optimized transducer imparts insufficient energy to the acoustic field for the large amplitudes required to eject viscous fluids. Additional driving mechanisms must be considered if a larger energy is to be imposed on the fluid cavity to elevate the pressure gradient magnitude to the extent that high viscosity fluids can be ejected.

The acoustic response of squeeze type ejectors was analyzed in Chapter 6. The generated pressure gradient magnitude at the nozzle aperture was evaluated as a function the main ejector geometric parameters – ejector length, driven section length, and radius – and was shown to depend primarily on the interface location between the driven (active/wave generation) and the spacer (passive/wave propagation) sections to achieve an optimal component coupling and transmission of acoustic energy from the transducer to the ejection point at the nozzle aperture. Using the pressure gradient threshold required for ejection, it was shown that squeeze type ejectors are only capable of produce a large enough pressure gradient magnitude to eject working fluids with viscosity on the order of 100 mPas. However, due to the excessive computational time requirement, the investigation of squeeze type atomizers did not optimize the device across multiple geometric and operating parameters simultaneously for finding a global optimum in evaluating the ejectability of high viscosity working fluids. While such an optimization investigation is not expected to significantly alter the presented findings, the following areas are suggested for further study:

1. *A Computationally Efficient Means to Optimize Squeeze Ejectors for Use with High Viscosity Working Fluids:* The optimization of squeeze ejectors is limited by the computational resources required to conduct the optimization. The geometry and limited number of parameters of horn-based ultrasonic atomizers permitted the development of an efficient optimization routine. However, the increase number of components and geometric parameters of squeeze type ejectors greatly increases the complexity of the optimization process. Thus, a computational algorithm which minimizes computation

while consider considering the full variation of squeeze ejector geometries is an important avenue for further work to be able to conduct the global multi-parameter optimization efficiently.

2. *Inclusion of Transducer Elasticity as Part of the Capillary Wall:* The presented analysis neglects the change in the elasticity of the wall due to the presence of the transducer, considering only the effect of elastic properties of the capillary itself. A better representation of the true behavior of the wall can be achieved by the development of an effective wall elasticity model, which would account for the effect of both the capillary and transducer thicknesses and different elastic properties through the use of thick walled cylinder approximations.

3. *Inclusion of Planar Transducers/Additional Driving Mechanisms to Increase the Energy in the Acoustic Field:* As it was found for horn-based ultrasonic atomizers, the pressure gradient magnitude produced by squeeze type ejectors is also ultimately limited by the energy imparted by the driving mechanism to the fluid cavity. Further increases to the pressure gradient magnitude require either a change in the main driving mechanism or the inclusion of additional driving mechanisms of the fluid cavity. The most straightforward of these would be to include in squeeze ejectors a planar transducer at the fluid cavity inlet. Analysis of such a hybrid design is possible, but would require substantial modifications of the current model to include both driving transducers and the use a superposition between the fields created by the transducers with the assumption that linear acoustics remains valid even for

the large amplitudes of the pressure waves due to dual transducer pumping.

APPENDIX A: MATERIAL PROPERTIES UTILIZED IN THE ANSYS AND ANALYTICAL MODELS

The material properties need in the analytical models and ANSYS simulations are given in Tables A.1 to A.5. Properties for each of the considered working fluids, structural solids, and piezoelectric ceramics are provided. The elastic and piezoelectric properties for the piezoelectric transducer (PZT-855) were obtained from APC International, Inc and from Auld.[104, 116]

The reference directions for the piezoelectric transducers vary based on the transducer geometry. The component directions for each geometry are given in Table A.1.

Table A.1: Component directions for the piezoelectric transducer properties for the planar and annular geometries

Component direction	Planar transducer	Annular transducer
1	X-direction	Azimuthal direction
2	Z-direction	Axial direction
3	Y-direction	Radial direction

Table A.2: Properties used to model silicon in the ANSYS simulations and analytical models.[124]

Material	Property	Value
Silicon	Young's modulus, E	150×10^9 N/m^2
	Poisson's ratio, ν	0.21
	Mass density, ρ	2330 kg/m^3
	Damping coefficient, γ	6×10^{-9}

Table A.3: Properties used to model nickel in the analytical models[125]

Material	Property	Value
Nickel	Young's modulus, E	200×10^9 N/m^2

Table A.4: Properties used to model lead zirconate titanate (PZT-5) in the ANSYS simulations and analytical models.

Material	Property	Value
PZT-5	Young's modulus in the unpolarized direction, E_p	6.06×10^{10} N/m^2
	Young's modulus in the polarized direction, E_z	4.83×10^9 N/m^2
	Poisson's ratio (unpolarized/polarized), ν_p	0.290
	Poisson's ratio (polarized/unpolarized), ν_{zp}	0.408
	Shear modulus in the polarized direction, G_{zp}	1.149×10^{10} N/m^2
	Mass density, ρ	7500 kg/m^3
	Piezoelectric stress constant relating charge applied in the polarized direction to the stress in the polarized direction, e_{33}	29.99 C/m^2
	Piezoelectric constant relating charge applied in the polarized direction to stress in the unpolarized direction, e_{31}	-5.377 C/m^2
	Piezoelectric constant relating charge applied in the unpolarized direction to the generated shear stress, e_{15}	17.028 C/m^2
	Relative permittivity in the unpolarized direction, $\varepsilon_{r,p}$	3400
	Relative permittivity in the polarized direction, $\varepsilon_{r,z}$	3130
	Damping Coefficient, γ	1×10^{-9}
	Mechanical quality factor, Q_m	60
	Loss tangent, $\tan\delta$	2.0×10^{-2}

Table A.5: Properties used to model the working fluids in the ANSYS simulations and analytical models[2, 117, 126, 127]

Material	Property	Value
Water	Mass density, ρ_0	998 kg/m^3
	Speed of sound, c	1481 m/s
	Dynamic viscosity, μ	1.00x10^{-3} Pas
Glycol	Mass density, ρ_0	1113 kg/m^3
	Speed of sound, c	1658 m/s
	Dynamic viscosity, μ	3.00x10^{-2} Pas
Glycerol	Mass density, ρ_0	1261 kg/m^3
	Speed of sound, c	1920 m/s
	Dynamic viscosity, μ	1.4 Pas

APPENDIX B: TECHNICAL DETAILS OF THE SIMULATIONS PERFORMED IN ANSYS

Additional details for each of the ANSYS simulations is provided here. Each component of the models – the piezoelectric transducer, the fluid cavity, and the silicon nozzle – are individually discussed.

Modeling the piezoelectric transducer

ANSYS solves the stress-charge form of the constitutive equations for piezoelectric behavior, given as:

$$\boldsymbol{T} = \boldsymbol{c_E} \cdot \boldsymbol{S} - \boldsymbol{e^t} \cdot \boldsymbol{E} \quad \text{B.1}$$

$$\boldsymbol{D} = \boldsymbol{e} \cdot \boldsymbol{S} + \boldsymbol{\epsilon_s} \cdot \boldsymbol{E} \quad \text{B.2}$$

where **T** is the stress matrix in the piezoelectric element, $\boldsymbol{c_E}$ is the stiffness matrix at constant electric field, $\boldsymbol{S}$ is the strain matrix, **E** is the electric field matrix, **D** is the displacement, $\boldsymbol{e}$ is the piezoelectric stress matrix, $\boldsymbol{e^t}$ is the transpose of the piezoelectric stress matrix, and $\boldsymbol{\epsilon_s}$ is the permittivity matrix at constant strain. [104]

As outlined by Meacham, additional matrix manipulations are required due to the assumptions built into the program for the planar transducer.[1] The piezoelectric stress and stiffness matrices are given in references usually ordered as x, y, z, yz, xz, xy. ANSYS assumes an input order of x, y, z, xy, yz, and xz, which requires the interchanging of rows when inputting parameters. ANSYS also requires that axisymmetric geometries be modeled in the XY plane with the y-axis being the symmetric axis and transducer polarization in the Y direction. However, Equations B.1 and B.2 are for material polarized in the z-direction. To polarize the transducer in the

correct direction, the second and third rows and fourth and six rows of the piezoelectric stress and stiffness matrices must be interchanged. The matrix columns must also be modified; the stiffness matrix also requires the second and third columns and fourth and six columns be switched; the piezoelectric stress matrix requires only the second and third columns be exchanged.

For the annular piezoelectric transducer, polarization is in the radial direction corresponding to the x-direction in ANSYS. Given the outlined manipulations for the planar transducer, correct alignment of the transducer properties in ANSYS can be attained by rotating the property matrices 90° about the z-axis. Details for the rotation procedure are given by Auld.[104]

Modeling the fluid cavity

As previously mentioned in Chapter 3, the fluid cavity is modeled using two-dimensional

FLUID79 acoustic elements. The element type is a legacy element type models the fluid as a structural element with mass, stiffness, and damping matrices. The inclusion of a damping matrix in the formulation of the element sets it apart from the traditional FLUID29 and FLUID30 elements used for acoustic analyzes which assume losses wave propagation. Due to the geometric restrictions associated with the element type, all elements must be rectangular. The slope of the nozzle is therefore represented as a series of steps, sufficiently small so as to not influence the acoustic field at the upper frequency of interest.

The damping matrix can utilized to include the effects of bulk attenuation through the DMPR property. Whereas damping would otherwise be zero, the DMPR property adds an amount of damping proportional to the amplitude of the acoustic field at the interfaces between elements. To set the DMPR property, the classical attenuation coefficient (α_s) is calculated for every frequency and the DMPR programmed using the MP command. However, the DMPR property cannot be set as a frequency independent value and must be updated for every considered frequency. As damping is a material property which can only be set before the solution command and cannot be updated once attached to an element type, this requires that the model be restarted for every considered frequency. Once the solution for the fluid cavity is obtained for the first frequency, the necessary parameters are written to disk, the program is automatically cleared, the model remeshes with and updated damping matrix, and the solution obtained again for the next frequency of interest.

Modeling the nozzle

The silicon horn is modeled as SOLID182. This is a standard solid element and required no special treatment in the developed models.

APPENDIX C: DEFINITION OF COMMONLY USED SYMBOLS

Latin Symbols

Symbol	Definition
A, B, C, D	Complex amplitude coefficients
A	Cross-sectional area
B/A	Nonlinearity parameter
c	Speed of sound
c_p	Specific heat capacity at constant pressure
c_v	Specific heat capacity at constant volume
c_{nm}^E	Piezoelectric stiffness at constant electric field in the direction indicated by n,m
c_{nm}^D	Piezoelectric stiffness at constant displacement in the direction indicated by n,m
d	Displacement imposed on the exterior of the driven glass capillary
E	Young's modulus
e_{nm}	Piezoelectric stress constant in the direction indicated by n,m
F	Force
f	Frequency; source driver amplitude
h_{nm}	Transmitting constant in the direction indicated by n,m
h	Capillary wall thickness
I	Electric current
j	Imaginary unit
k	Wavenumber in the fluid cavity
k_{cond}	Thermal conductivity
l	Length
m	Mass
$\dot{m}$	Mass flow rate
P	Total pressure; acoustic pressure
P_0	Ambient pressure
Q_m	Transducer mechanical quality factor

R, R_i, R_o	Radius; inner radius; outer radius
r	Radial position
S	Cross-sectional area
T	Temperature
t	Time
V	Voltage
V_z	Axial volume velocity
v_z, v_r	Axial velocity; radial velocity
v_w	Radial velocity at the wall
w_0	Maximum component of the displacement spectral density imposed on the capillary wall
x_{rt}	Shock distance
Z_c	Transducer characteristic impedance
Z	Mechanical impedance
z	Axial position; acoustic impedance

Greek Symbols

Symbol	Definition
α_s	Spatial attenuation coefficient
α_T	Viscosity thermal fitting parameter
β	Wavenumber in the transducer; nonlinearity parameter
δ	Linearity constant
$\tan(\delta)$	Loss tangent
ϵ	Nondimensional wavenumber
ϵ_r	Relative permittivity of free space
ϵ_0	Permittivity of free space
ϵ_{33}^s	Clamped dielectric constant
μ	Dynamic viscosity
ν	Kelvin function order constant
ρ	Density
σ	Stress, surface tension

ϕ	Velocity potential
ω_r	Signal repeat rate

Nondimensional Groups

Symbol	Definition
Eu	Euler number
Go	Goldberg number
Ma	Mach number
Na	Nahme number
R_a	Displacement ratio
R_c	Dispersion ratio
R_d	Diameter ratio
Re	Particle speed Reynolds number
Re^*	Sound speed Reynolds number
St	Strouhal number
We	Weber Number

BIBLIOGRAPHY

[1] J. M. Meacham, "A micromachined ultrasonic droplet generator: Design, fabrication, visualization, and modeling," Ph.D. 3233561, Georgia Institute of Technology, United States -- Georgia, 2006.

[2] D. B. Bogy and F. E. Talke, "Experimental and Theoretical Study of Wave Propagation Phenomena in Drop-on-Demand Ink Jet Devices," *IBM Journal of Research and Development,* vol. 38, pp. 314-321, 1984.

[3] J. Meacham, C. Ejimofor, S. Kumar, F. Degertekin, and A. Fedorov, "Micromachined ultrasonic droplet generator based on a liquid horn structure," *Review of Scientific Instruments,* vol. 75, pp. 1347-1352, 2004.

[4] K. Liang, "Analytic model for 1-D axisymmetric piezoelectric transducers," *2002 Ieee Ultrasonics Symposium Proceedings, Vols 1 and 2,* pp. 1149-1152, 2002.

[5] S. J. Ford, M. J. Routley, R. Phaal, and D. R. Probert, "The industrial emergence of commercial inkjet printing," *European Journal of Innovation Management,* vol. 17, pp. 126-143, 01 / 01 / 2014.

[6] H. Wijshoff, "The dynamics of the piezo inkjet printhead operation," *Physics Reports,* vol. 491, pp. 77-177, 2010.

[7] P. Calvert, "Printing Cells," *Science,* p. 208, 2007.

[8] R. E. Saunders, J. E. Gough, and B. Derby, "Delivery of human fibroblast cells by piezoelectric drop-on-demand inkjet printing," *Biomaterials,* vol. 29, pp. 193-203, 01 / 01 / 2008.

[9] T. Xu, C. A. Gregory, P. Molnar, X. Cui, T. Boland, S. Jalota, *et al.*, "Viability and electrophysiology of neural cell structures generated by the inkjet printing method," *Biomaterials,* vol. 27, pp. 3580-3588, 07 / 01 / 2006.

[10] M. Schumacher, U. Deisinger, G. Ziegler, F. Uhl, and R. Detsch, "Static and dynamic cultivation of bone marrow stromal cells on biphasic calcium phosphate scaffolds derived from an indirect rapid prototyping technique," *Journal of Materials Science: Materials in Medicine,* vol. 21, pp. 3039-3048, 11 / 01 / 2010.

[11] P. J. Tarcha, D. Verlee, H. W. Hui, J. Setesak, B. Antohe, D. Radulescu, *et al.*, "The application of ink-jet technology for the coating and loading of drug-eluting stents," *Annals of Biomedical Engineering,* vol. 35, pp. 1791-1799, 10 / 01 / 2007.

[12] V. G. Zarnitsyn, J. M. Meacham, M. J. Varady, C. H. Hao, F. L. Degertekin, and A. G. Fedorov, "Electrosonic ejector microarray for drug and gene delivery," *Biomedical Microdevices,* vol. 10, pp. 299-308, Apr 2008.

[13] G. Su, P. W. Longest, and R. M. Pidaparti, "A novel micropump droplet generator for aerosol drug delivery: Design simulations," *Biomicrofluidics,* vol. 4, pp. 44108-44108, 2010.

[14] S. Wagner, D. Sawitzky, B. Christ, G. Dues, and P. Frey, "Assessment of the biological performance of the needle-free injector INJEX using the isolated porcine forelimb," *British Journal of Dermatology,* vol. 150, pp. 455-461, 03 / 01 / 2004.

[15] T. P. Forbes, R. B. Dixon, D. C. Muddiman, F. L. Degertekin, and A. G. Fedorov, "Characterization of Charge Separation in the Array of Micromachined

UltraSonic Electrospray (AMUSE) Ion Source for Mass Spectrometry," *Journal of the American Society for Mass Spectrometry,* vol. 20, pp. 1684-1687, Sep 2009.

[16] T. P. Forbes, F. L. Degertekin, and A. G. Fedorov, "Electrochemical ionization and analyte charging in the Array of Micromachined UltraSonic Electrospray (AMUSE) ion source," *Journal of Electroanalytical Chemistry,* vol. 645, pp. 167-173, Jul 2010.

[17] T. H. J. Van Osch, J. Perelaer, U. S. Schubert, and A. W. M. De Laat, "Inkjet printing of narrow conductive tracks on untreated polymeric substrates," *Advanced Materials,* vol. 20, pp. 343-345, 01 / 18 / 2008.

[18] J. Z. Wang, Z. H. Zheng, H. Sirringhaus, H. W. Li, and W. T. S. Huck, "Dewetting of conducting polymer inkjet droplets on patterned surfaces," *Nature Materials,* vol. 3, pp. 171-176, 03 / 01 / 2004.

[19] J. H. Cho, J. Lee, Y. Xia, T. P. Lodge, C. D. Frisbie, B. Kim, *et al.*, "Printable ion-gel gate dielectrics for low-voltage polymer thin-film transistors on plastic," *Nature Materials,* vol. 7, pp. 900-906, 11 / 16 / 2008.

[20] A. Rida, L. Yang, R. Vyas, and M. M. Tentzeris, "Conductive inkjet-printed antennas on flexible low-cost paper-based substrates for RFID and WSN applications," *IEEE Antennas and Propagation Magazine,* vol. 51, pp. 13-23, 01 / 01 / 2009.

[21] J. Hiller, J. D. Mendelsohn, and M. F. Rubner, "Reversibly erasable nanoporous anti-reflection coatings from polyelectrolyte multilayers," *Nature Materials,* vol. 1, pp. 59-63, 09 / 01 / 2002.

[22] A. Kamyshny, M. Ben-Moshe, S. Aviezer, and S. Magdassi, "Ink-jet printing of metallic nanoparticles and microemulsions," *Macromolecular Rapid Communications,* vol. 26, pp. 281-288, 02 / 21 / 2005.

[23] S. B. Fuller, E. J. Wilhelm, and J. M. Jacobson, "Ink-jet printed nanoparticle microelectromechanical systems," *Journal of Microelectromechanical Systems,* vol. 11, pp. 54-60, 02 / 01 / 2002.

[24] B. De Heij, B. Van Der Schoot, N. F. De Rooij, H. Bo, and J. Hess, "Characterization of a fL droplet generator for inhalation drug therapy," *Sensors and Actuators, A: Physical,* vol. 85, pp. 430-434, 08 / 25 / 2000.

[25] B. Derby, "Inkjet Printing of Functional and Structural Materials: Fluid Property Requirements, Feature Stability, and Resolution," *Annual Review of Materials Research,* vol. 40, pp. 395-414, 2010.

[26] M. M. Gepp and et al., "Dispensing of very low volumes of ultra high viscosity alginate gels: a new tool for encapsulation of adherent cells and rapid prototyping of scaffolds and implants," *Biotechniques,* vol. 46, p. 31, 2009.

[27] P. J. Bártolo, *Stereolithography Materials, Processes and Applications*. Springer Science+Business Media LLC: Boston, MA, 2011.

[28] J. M. Meacham, A. O'Rourke, Y. Yang, A. G. Fedorov, F. L. Degertekin, and D. W. Rosen, "Micromachined Ultrasonic Print-Head for Deposition of High-Viscosity Materials," *Journal of Manufacturing Science and Engineering - Transactions of the ASME,* vol. 132, 2010.

[29] H. Liu, *Science and engineering of droplets : fundamentals and applications / by Huimin Liu*: Park Ridge, N.J. : Noyes Publications ; Norwich, N.Y. : William Andrew Pub., c2000., 2000.

[30] E. J. Lavernia and Y. Wu, *Spray atomization and deposition / Enrique J. Lavernia and Yue Wu*: Chichester ; New York : John Wiley, c1996., 1996.

[31] D. V. Rosato, D. V. Rosato, and M. G. Rosato, *Injection molding handbook [electronic resource] / edited by Dominick V. Rosato, Donald V. Rosato, Marlene G. Rosato*: Boston : Kluwer Academic Publishers, c2000. 3rd ed., 2000.

[32] A. Aliseda, E. J. Hopfinger, J. C. Lasheras, D. M. Kremer, A. Berchielli, and E. K. Connolly, "Atomization of viscous and non-newtonian liquids by a coaxial, high-speed gas jet. Experiments and droplet size modeling," *International Journal of Multiphase Flow,* vol. 34, pp. 161-175, 02 / 01 / 2008.

[33] D. Jang, D. Kim, and J. Moon, "Influence of Fluid Physical Properites on Ink-Jet Printability," *Langmuir,* vol. 25, pp. 2629-2635, 2009.

[34] G. D. Martin, S. D. Hoath, I. M. Hutchings, and Iop, "Inkjet printing - the physics of manipulating liquid jets and drops," in *Conference on Engineering in Physics - Synergy for Success*, London, ENGLAND, 2006.

[35] M. Nakamura, S. Iwanaga, C. Henmi, K. Arai, and Y. Nishiyama, "Biomatrices and biomaterials for future developments of bioprinting and biofabrication," *Biofabrication,* vol. 2, 2010.

[36] G. Cummins and M. P. Y. Desmulliez, "Inkjet printing of conductive materials: a review," *Circuit World,* vol. 38, pp. 193-213, 2012.

[37] B.-J. de Gans, P. C. Duineveld, and U. S. Schubert, "Inkjet printing of polymers state of the art and future developments," *Advanced Materials,* vol. 16, pp. 203-213, 2004.

[38] H. P. Le, "Progress and trends in ink-jet printing technology," *Journal of Imaging Science and Technology,* vol. 42, pp. 49-62, 01 / 01 / 1998.

[39] Hewlett-Packard. (2014, May 31). *Advantages of HP thermal inkjet technology*. Available: http://h10088.www1.hp.com/cda/gap/display/main/index.jsp?zn=gap&cp=20000-13698-13855-14056%5E203738_4041_100__

[40] Canon. (2013, May 31). *The Technology Inside: Inkjet Print Heads*. Available: http://www.learn.usa.canon.com/resources/articles/2013/ipf_inkjet_printheads_technology.htmlp

[41] B. H. Kim, S. I. Kim, J. C. Lee, S. J. Shin, and S. J. Kim, "Dynamic characteristics of a piezoelectric driven inkjet printhead fabricated using MEMS technology," *Sensors and Actuators a-Physical,* vol. 173, pp. 244-253, Jan 2012.

[42] J. M. Lai, J. D. Lin, and K. Linliu, "Numerical investigation of the effect of a transducer pulse on the microfluidic control of a piezoelectric printhead," *Journal of Micro/ Nanolithography, MEMS, and MOEMS,* vol. 9, 07 / 01 / 2010.

[43] H. C. Wu, T. R. Shan, W. S. Hwang, and H. J. Lin, "Study of micro-droplet behavior for a piezoelectric inkjet printing device using a single pulse voltage pattern," *Materials Transactions,* vol. 45, pp. 1794-1801, May 2004.

[44] S. Y. Wu, Y. He, J. Z. Fu, and H. F. Shao, *Design and fabrication of a piezoelectric bend mode drop-on-demand inkjet printhead with interchangeable nozzle* vol. 819, 2013.

[45] W. Sim, S. J. Park, C. Park, Y. Yoo, Y. Kim, J. Joung, *et al.*, "Analysis of the droplet ejection for piezoelectric-driven industrial inkjet head," 2006, pp. 528-533.

[46] A. S. Yang and W. M. Tsai, "Ejection process simulation for a piezoelectric microdroplet generator," *Journal of Fluids Engineering-Transactions of the Asme,* vol. 128, pp. 1144-1152, Nov 2006.

[47] Epson. (2014, May 31). *What is Micro Piezo Technology?* Available: http://global.epson.com/innovation/printing_technology/micro_piezo_technology/

[48] H. J. Lin, H. C. Wu, T. R. Shan, and W. S. Hwang, "The effects of operating parameters on micro-droplet formation in a piezoelectric inkjet printhead using a double pulse voltage pattern," *Materials Transactions,* vol. 47, pp. 375-382, Feb 2006.

[49] R. M. Verkouteren and J. R. Verkouteren, "Inkjet metrology II: Resolved effects of ejection frequency, fluidic pressure, and droplet number on reproducible drop-on-demand dispensing," *Langmuir,* vol. 27, pp. 9644-9653, 08 / 02 / 2011.

[50] H. Y. Gan, X. Shan, B. K. Lok, T. Eriksson, and Y. C. Lam, "Reduction of droplet volume by controlling actuating waveforms in inkjet printing for micro-pattern formation," *Journal of Micromechanics and Microengineering,* vol. 19, 01 / 01 / 2009.

[51] E. Q. Li, Q. Xu, J. Sun, J. Y. H. Fuh, Y. S. Wong, and S. T. Thoroddsen, "Design and fabrication of a PET/PTFE-based piezoelectric squeeze mode drop-on-demand inkjet printhead with interchangeable nozzle," *Sensors and Actuators, A: Physical,* vol. 163, pp. 315-322, 09 / 01 / 2010.

[52] P. Shin, J. Sung, and M. H. Lee, "Control of droplet formation for low viscosity fluid by double waveforms applied to a piezoelectric inkjet nozzle," *Microelectronics Reliability,* vol. 51, pp. 797-804, 04 / 01 / 2011.

[53] C. H. Lee and A. Lal, "Single microdroplet ejection using an ultrasonic longitudinal mode with a PZT/tapered glass capillary," *IEEE Transactions on Ultrasonics, Ferroelectrics, and Frequency Control,* vol. 51, pp. 1514-1522, 11 / 01 / 2004.

[54] M. Technologies. (2014, May 31). *Products Overview*. Available: http://www.microfab.com/index.php?option=com_content&view=article&id=10&Itemid=12

[55] F. Barreras, H. Amaveda, and A. Lozano, "Transient high-frequency ultrasonic water atomization," *Experiments in Fluids,* vol. 33, pp. 405-413, Sep 2002.

[56] J. Y. Ju, Y. Yamagata, H. Ohmori, and T. Higuchi, "High-frequency surface acoustic wave atomizer," *Sensors and Actuators A-Physical,* vol. 145, pp. 437-441, Jul-Aug 2008.

[57] S. Elrod, B. Hadimioglu, B. Khuriyakub, E. Rawson, E. Richley, C. Quate*, et al.*, "Nozzleless droplet formation with focused acoustic beams," *Journal of Applied Physics,* vol. 65, 1989.

[58] S. C. Tsai, Y. L. Song, T. K. Tseng, Y. F. Chou, W. J. Chen, and C. S. Tsai, "High-Frequency, Silicon-Based Ultrasonic Nozzles Using Multiple Fourier Horns," *IEEE Transactions on Ultrasonics, Ferroelectrics, and Frequency Control,* vol. 51, pp. 277-285, 2004.

[59] J. M. Meacham and et al, "Droplet formation and ejection from a micromachined ultrasonic droplet generator: Visualization and scaling," *Physics of Fluids,* vol. 17, 2005.

[60] T. P. Forbes, F. L. Degertekin, and A. G. Fedorov, "Multiplexed operation of a micromachined ultrasonic droplet ejector array," *Review of Scientific Instruments,* vol. 78, 2007.
[61] J. M. Meacham, M. J. Varady, D. Esposito, F. L. Degertekin, and A. G. Fedorov, "Micromachined ultrasonic atomizer for liquid fuels," *Atomization and Sprays,* vol. 18, pp. 163-190, 2008.
[62] L. Margolin, *Ultrasonic droplet generation jetting technology for additive manufacturing an initial investigation*, 2007.
[63] D. Rosen, L. Margolin, and S. Vohra, "Printing high-viscosity fluids using ultrasonic droplet generation," *Solid Freeform Fabrication Symposium,* 2008.
[64] T. P. Forbes, F. L. Degertekin, and A. G. Fedorov, "Droplet charging regimes for ultrasonic atomization of a liquid electrolyte in an external electric field," *Physics of Fluids,* vol. 23, p. 10, Jan 2011.
[65] P. K. Notz, A. U. Chen, and O. A. Basaran, "Satellite drops: Unexpected dynamics and change of scaling during pinch-off," *Physics of Fluids,* vol. 13, pp. 549-552, 2001.
[66] S. Hoath, I. Hutchings, G. Martin, T. Tuladhar, M. Mackley, and D. Vadillo, "Links between ink rheology, drop-on-demand jet formation, and printability," *Journal of Imaging Science and Technology,* vol. 53, 2009.
[67] L. E. Kinsler, A. R. Frey, A. B. Coppens, and J. V. Sanders, "Chapter 8 - Absorption and Attenuation of Sound," in *Fundamentals of acoustics*, ed: New York : Wiley, c2000. 4th ed., 2000.
[68] L. E. Kinsler, A. R. Frey, A. B. Coppens, and J. V. Sanders, *Fundamentals of Acoustics*: Wiley and Sons, 1999.
[69] D. T. Blackstock, *Fundamentals of Physical Acoustics*: Wiley & Sons Inc, 2000.
[70] A. D. Pierce, "Chapter 10 - Effects of Viscosity and Other Dissipative Processes," in *Acoustics: An introduction to its physical principles and applications*. vol. 4th ed., ed New York: New York, NY: Acoustical Society of America, 1994.
[71] R. L. Panton, *Incompressible flow / Ronald L. Panton*: Hoboken, New Jersey : John Wiley and Sons, Inc., [2013] Fourth edition., 2013.
[72] J. F. Dijksman, "Hydrodynamics of Small Tubular Pumps," *Journal of Fluid Mechanics,* vol. 139, pp. 173-191, 1984.
[73] H. Tijdeman, "Propagation of Sound Waves in Cylindrical Tubes," *Journal of Sound and Vibration,* vol. 39, pp. 1-33, 1975.
[74] B. P. Bogert, "Classical Viscosity in Tubes and Cavities of Large Dimensions," *Journal of the Acoustical Society of America,* vol. 22, pp. 432-437, 1950.
[75] R. F. Lambert, "Wall Viscosity and Heat Conduction Losses in Rigid Tubes," *Journal of the Acoustical Society of America,* vol. 23, pp. 480-481, 1951.
[76] R. Beatty, "Boundary layer attenuation of higher order modes in rectangular and circular tubes," *The Journal of the Acoustical Society of America,* vol. 22, p. 5, 1950.
[77] H. F. Olson, "Chapter 5 - Acoustical Elements," in *Elements of Acoustical Engineering*, ed New York: D. Van Nostrand Company, Inc., 1940.
[78] E. Eisner, "Complete Solutions of the ``Webster" Horn Equation," *The Journal of the Acoustical Society of America,* vol. 41, pp. 1126-1146, 1967.

[79] G. Amza and D. Drimer, "Design and Construction of Solid Concentrators for Ultrasonic Energy," *Ultrasonics,* vol. 14, pp. 223-226, 1976.
[80] G. W. Stewart, "The performance of conical horns," *Physical Review,* vol. 16, pp. 313-326, Oct 1920.
[81] L. G. Merkulov and A. V. Kharitonov, "Theory and analysis of sectional concentrators," *Soviet physics, Acoustics.,* vol. 5, pp. 183-190, 1959.
[82] D. Donskoy and B. Cray, "Acoustic particle velocity horns," *The Journal of the Acoustical Society of America,* vol. 131, 2012.
[83] A. Lal and R. M. White, "Silicon microfabricated horns for power ultrasonics," *Sensors and Actuators a-Physical,* vol. 54, pp. 542-546, Jun 1996.
[84] X. D. Li, C. Schemel, U. Michel, and F. Thiele, "Aximuthal sound mode propagation in axisymmetric flow ducts," *AIAA Journal,* vol. 42, p. 9, 2004.
[85] M. Utsumi, "An analytical method for expansion chambers with continuously varying cross-sectional area," *Journal of vibration and acoustics,* vol. 126, p. 10, 2004.
[86] S. Rienstra, "Webster's horn equation revisted," *Siam Journal of Applied Mathematics,* vol. 65, pp. 1981-2004, 2006.
[87] J. Agullo, A. Barjau, and D. Keefe, "Acoustic propagation in flaring, axisymmetric horns: I. A new family of unidimensional solutions," *Acta Acustica,* vol. 85, pp. 278-284, 1999.
[88] D. Keefe and A. Barjau, "Acoustic propagation in flaring, axisymmetric horns: II Numerical results, WKB theory, and viscothermal effects," *Acta Acustica,* vol. 85, pp. 285-293, 1999.
[89] Y. F. Liu, M. H. Tsai, Y. F. Pai, and W. S. Hwang, "Control of droplet formation by operating wavefore for inks with various viscosities in piezolectric inkjet printing," *Applied Physics A,* vol. 111, pp. 509-516, 2013.
[90] J. Tai, H. Y. Gan, Y. N. Liang, and B. K. Lok, "Control of droplet formation in inkjet printing using ohnesorge number," presented at the 10th IEEE Electronics Packaging and Technology Conference, 2008.
[91] I. Raman, M. Syafiq, N. Sa'ude, M. Ibrahim, and M. S. Wahab, "Viscosity effect on piezoelectric actuated nozzle in generating micro droplet," *Advanced Materials Research,* vol. 626, pp. 415-419, 2013.
[92] B. W. Jo, A. Lee, K. H. Ahn, and S. J. Lee, "Evaluation of jet performance in drop-on-demand (DOD) inkjet printing," *Korean Journal of Chemical Engineering,* vol. 26, pp. 339-348, 2009.
[93] J. Sun, J. H. Ng, Y. H. Fuh, Y. S. Wong, H. T. Loh, and Q. Xu, "Comparison of micro-dispensing performance between micro-valve and piezoelectric printhead," *Microsystem Technologies-Micro-and Nanosystems-Information Storage and Processing Systems,* vol. 15, pp. 1437-1448, Sep 2009.
[94] B. V. Antohe and D. B. Wallace, "Acoustic phenomena in a demand mode piezoelectric ink jet printer," *Journal of Imaging Science and Technology,* vol. 46, pp. 409-414, Sep-Oct 2002.
[95] T. W. Shield, D. B. Bogy, and F. E. Talke, "A Numerical Comparison of One-Dimensional Fluid Jet Models Applied to Drop-on-Demand Printing," *Journal of Computational Physics,* vol. 67, pp. 327-347, Dec 1986.

[96] F. X. Pan, J. Kubby, and J. K. Chen, "Numerical simulation of fluid-structure interaction in a MEMS diaphragm drop ejector," *Journal of Micromechanics and Microengineering,* vol. 12, pp. 70-76, Jan 2002.
[97] P. H. Chen, H. Y. Peng, H. Y. Liu, S. L. Chang, T. I. Wu, and C. H. Cheng, "Pressure response and droplet ejection of a piezoelectric inkjet printhead," *International Journal of Mechanical Sciences,* vol. 41, pp. 235-248, Feb 1999.
[98] G. Percin and B. T. Khuri-Yakub, "Piezoelectrically actuated flextensional micromachined ultrasound droplet ejectors," *IEEE Transactions on Ultrasonics, Ferroelectrics and Frequency Control,* vol. 49, pp. 756-766, 2002.
[99] G. Perçin, L. Levin, and B. T. Khuri-Yakub, "Piezoelectrically actuated droplet ejector," *Review of Scientific Instruments,* vol. 68, pp. 4561-4563, 12 / 01 / 1997.
[100] K. F. Teng, "A Mathematical Model of Impulse Jet Mechanism," *Mathematical and Computer Modelling,* vol. 11, pp. 751-753, 1988.
[101] J. F. Dijksman, "Hydro-acoustics of piezoelectrically driven ink-jet print heads," *Flow Turbulence and Combustion,* vol. 61, pp. 211-237, 1998.
[102] P. Grassia, "The design of a droplet ejector," *Journal of Fluids Engineering-Transactions of the Asme,* vol. 121, pp. 658-664, Sep 1999.
[103] E. L. Kyser, L. F. Collins, and N. Herbert, "Design of an Impulse Ink Jet," *Journal of Applied Photographic Engineering,* vol. 7, pp. 73-79, 1981.
[104] B. A. Auld, "Chapter 8 - Piezoelectricity," in *Acoustic fields and waves in solids*, ed: Malabar, Fla. : R.E. Krieger, 1990.
2nd ed., 1990.
[105] S. Sherrit, S. P. Leary, B. P. Dolgin, and Y. Bar-Cohen, "Comparison of the Mason and KLM equivalent circuits for piezoelectric resonators in the thickness mode," in *1999 Ieee Ultrasonics Symposium Proceedings, Vols 1 and 2*, S. C. Schneider, M. Levy, and B. R. McAvoy, Eds., ed New York: Ieee, 1999, pp. 921-926.
[106] P. D. Edmonds, *Ultrasonics / edited by Peter D. Edmonds*: New York : Academic Press, 1981., 1981.
[107] D. Ensminger, *Ultrasonics: fundamentals, technology, applications - 2nd ed., rev. and expanded*: Dekker, 1988.
[108] "ANSYS Inc," vol. 15.0, ed. Canonsburg, PA, 2014.
[109] G. W. McMahon, "Performance of Open Ferroelectric Ceramic Cylinders in Underwater Transducers," *Journal of the Acoustical Society of America,* vol. 36, p. 528, 03// 1964.
[110] L. E. Kinsler, A. R. Frey, A. B. Coppens, and J. V. Sanders, "Chapter 10 - Pipes, Resonators, and Filters," in *Fundamentals of acoustics*, ed: New York : Wiley, c2000. 4th ed., 2000.
[111] "Chapter 9: Thin Cylinders and Shells," *Mechanics of Materials Volume 1,* pp. 198-214, 1/1/1997 1997.
[112] M. Abramowitz and I. A. Stegun, *Handbook of mathematical functions, with formulas, graphs, and mathematical tables, edited by Milton Abramowitz and Irene A. Stegun*: New York, Dover Publications [1965], 1965.
[113] D. T. Blackstock, "Chapter 7 - Horns," in *Fundamentals of physical acoustics*, ed: New York : Wiley, c2000., 2000.

[114] A. F. Stevenson, "Exact and Approximate Equations for Wave Propagation in Acoustic Horns," *Journal of Applied Physics,* vol. 22, pp. 1461-1463, 1951.
[115] V. Pagneux, N. Amir, and J. Kergomard, "A study of wave propagation in varying cross-section waveguides by modal decomposition .1. Theory and validation," *Journal of the Acoustical Society of America,* vol. 100, pp. 2034-2048, Oct 1996.
[116] A. P. C. International. (2011, June 30). *Physical and Piezoelectric Properties of APC Materials* [Website]. Available: http://www.americanpiezo.com/
[117] (2012, May 30). *Dow Chemical OPTIM™ Synthetic Glycerine - Viscosity*. Available: http://www.dow.com/safechem/optim/optim-advantage/physical-properties/viscosity.htm
[118] C. Rauwendaal, *Polymer extrusion*, 4th ed. ed. Cincinnati, OH :: Hanser Gardner Publications, 2001.
[119] E. toolbox. (2014, July 3). *Thermal conductivity common liquids*. Available: http://www.engineeringtoolbox.com/thermal-conductivity-liquids-d_1260.html
[120] E. Weissten. (July 3). *Conical Frustum*. Available: http://mathworld.wolfram.com/ConicalFrustum.html
[121] M. F. Hamilton and D. T. Blackstock, *Nonlinear acoustics / edited by Mark F. Hamilton and David T. Blackstock*: San Diego, CA : Academic Press, c1998., 1998.
[122] "Goldberg's Number Influence on the Validity Domain of the Quasi-Linear Approximation of Finite Amplitude Acoustic Waves," ed: INTECH Open Access Publisher, 2012-03-07., 2012.
[123] S. Tsai, C. Cheng, N. Wang, Y. Song, C. Lee, and C. Tsai, "Silicon-Based Megahertz Ultrasonic Nozzles for Production of Monodisperse Micrometer-Sized Droplets," *IEEE Transactions on Ultrasonics, Ferroelectrics, and Frequency Control,* vol. 56, pp. 1968-1979, 2009.
[124] M. J. Madou, *Fundamentals of microfabrication : the science of miniaturization / Marc J. Madou*: Boca Raton : CRC Press, c2002. 2nd ed., 2002.
[125] T. Fritz, M. Griepentrog, W. Mokwa, and U. Schnakenberg, "Determination of Young's modulus of electroplated nickel," *Electrochimica Acta,* vol. 48, p. 3029, 2003.
[126] L. E. Kinsler, *Fundamentals of acoustics / Lawrence E. Kinsler ... [et al.]*: New York : Wiley, c2000. 4th ed., 2000.
[127] E. Jungermann and N. Sonntag, *Glycerine: A Key Cosmetic Ingredient*: Marcel Dekker, 1991.